Electron spins in few-electron lateral quantum dots

Electron spins in few-electron lateral quantum dots

Proefschrift

ter verkrijging van de graad van doctor
aan de Technische Universiteit Delft,
op gezag van de Rector Magnificus prof. dr. ir. J. T. Fokkema,
voorzitter van het College voor Promoties,
in het openbaar te verdedigen ten overstaan van een commissie,
door het College voor Promoties aangewezen,

op dinsdag 8 november 2005 om 10.30 uur

door

Laurens Henry WILLEMS VAN BEVEREN

natuurkundig ingenieur
geboren te Assen.

Dit proefschrift is goedgekeurd door de promotor:
Prof. dr. ir. L. P. Kouwenhoven

Samenstelling van de promotiecommissie:

Rector Magnificus,	voorzitter
Prof. dr. ir. L. P. Kouwenhoven	Technische Universiteit Delft, promotor
Prof. dr. ir. J. E. Mooij	Technische Universiteit Delft
Prof. dr. ir. B. J. van Wees	Universiteit Groningen
Prof. dr. G. E. W. Bauer	Technische Universiteit Delft
Dr. T. Fujisawa	NTT Basic Research Laboratories, Japan
Dr. ir. L. M. K. Vandersypen	Technische Universiteit Delft
Dr. M. J. A. de Dood	Universiteit Leiden
Prof. dr. ir. B. J. Thijsse	Technische Universiteit Delft, reservelid

Published by: L. H. Willems van Beveren

Printed by: Cendris, Delft

Cover design: Atomic force micrograph of a few-electron lateral quantum dot

An electronic version of this thesis, including colour figures, is available at:
http://www.library.tudelft.nl/dissertations/

Casimir Ph.D. Series, Delft-Leiden, 2005-04

ISBN: 90-859-3004-9

Copyright © 2005 by L. H. Willems van Beveren

All rights reserved. No part of the material protected by this copyright notice may be reproduced or utilized in any form or by any means, electronic or mechanical, including photocopying, recording or by any information storage and retrieval system, without permission from the author.

Printed in the Netherlands

Preface

During a traineeship at the University of Tokyo in 2001, as part of my M.Sc. Applied Physics at the University of Groningen, I became aware of the close collaboration between the NTT Basic Research Laboratories in Japan and the Delft University of Technology. The nice experiments with quantum dots attracted my attention (maybe even as much as the long nights in Rappongi) and soon after I returned to The Netherlands I applied for a Ph.D. position in Delft. In the middle of October 2001 I actually started in the quantum transport (QT) group of Leo Kouwenhoven and Hans Mooij, working as an experimental researcher on electron spins in few-electron lateral quantum dots. This thesis describes the results of four years of experimental research in this group.

The quantum dot devices that were measured in Delft so far, had all been fabricated in Japan, forming the basis of a strong collaboration with the research group in NTT. However because of practicality, it was decided to transfer the fabrication process to Delft. Therefore in the beginning of 2002 I went with Ronald Hanson to NTT (after celebrating New Year in Kuala Lumpur) to learn all the details concerning the fabrication of lateral quantum dot devices. After three months of hard work in one of the many NTT cleanrooms I came back to Delft with a lot of devices and fabrication skills. The measurements of these devices led to a number of scientific results presented throughout this thesis. In the mean time I started the fabrication process at DIMES in Delft as well, together with several students. After solving a lot of technical problems we managed to produce the first working few-electron quantum dot devices in the Delft cleanroom. From that point onwards, the focus of my research shifted more towards the cryogenic measurements of these devices, in particular the experiment to manipulate a single electron spin by electron spin resonance.

At this point I want to thank Seigo Tarucha and Yoshiro Hirayama for their hospitality which enabled me to spent several months working at NTT. Here I was supervised by Toshiaki Hayashi and Toshimasa Fujisawa. I really enjoyed working together and learning from you. Furthermore, I thank Tadashi Saku for growing heterostructure wafers and Mike Stopa for the discussions about the self-consistent simulations of the quantum dot devices. During my stay in NTT the people of the ERATO project, the members of the 'Butsuden G' group and the international trainees were always there for me, even outside the lab, to join karaoke parties or to explore the Japanese countryside.

During the four years I spent in QT I really enjoyed working as a member of the spin-qubit team. This experience allowed me to improve myself not only on my fabrication skills, but also on the level of scientific knowledge, presentation and publication techniques. To be able to give a talk about your research on international conferences, after many days of hard work in the lab, is very satisfying.

Since this research has been carried out in a team, I owe much to everybody who contributed to the results. First of all, I thank my supervisor and promotor Leo Kouwenhoven for giving me the chance to do a Ph.D. in his group. Because of his funding skills there was always the possibility to buy new equipment when needed, join international workshops, et cetera. Throughout my Ph.D. I could benefit enormously from the quantum dot knowledge of Jeroen Elzerman and Ronald Hanson, my predecessors. Thank you for your patience on explaining the many questions I had. Next, I would like to thank Lieven Vandersypen, our expert on quantum information theory, for always trying to make our research become more effective and efficient. The weekly group meetings in the library surely contributed to this and your organization skills are a good example for many of us. The several months that David DiVincenzo and Josh Folk joined us were fun and I enjoyed the discussions we had on all sorts of topics. As time passed by, the next generation Ph.D. students Frank Koppens and Ivo Vink smoothly joined the team and are currently working on very interesting experiments. It was fun working with you guys, keep up the good work! More recently, Tristan Meunier started in the team as Post-Doc to spent his Marie Curie fellowship money and Katja Nowack started as fresh Ph.D. student. I have no doubt that your time in QT will become a success. There have been a bunch of undergraduate students working in our team over the last few years and their contribution is greatly appreciated and therefore their names should not be forgotten: Joris Wijpkema, Jabob Greidanus, Jort Wever, Benoit Witkamp, Ivo Vink, Wouter Naber and more recently Christo Buizert and Klaas-Jan Tielrooij.

The people in DIMES assisted me a lot during the time I spent in the cleanroom. I would like to thank in particular Marc Zuiddam and Emile van der Drift for useful discussions and efforts to continuously improve on the usage facilities. Arnold van Run helped enormously with debugging software errors related to the introduction of the new electron beam pattern generator. From Matthias Kroug I got a lot of support in the sputter deposition and characterization of superconducting films.

We had great support from theorists in Delft and from outside: Siggi Erlingsson, Miriam Blaauboer, Oleg Jouravlev, Yuli Nazarov, Björn Trauzettel, Daniel Loss, Hans-Andreas Engel, Guido Burkard and Vitaly Golovach. Useful simulations on our devices have been carried out by Lingxiao Zhang and Jean-Pierre Leburton.

Naturally I want to thank all former and present group members of QT since they surely have helped to create a very pleasant and stimulating atmosphere and I hope to see you again soon. I would like to thank especially Hannes Majer for his hospitality when I was visiting New Haven and Wilfred van der Wiel for teaching me how to survive in Japan. Thank you Floris Zwanenburg and Floor Paauw for to make sure to exercise at least twice a week at the sports center. The combination of experimental research and sports turned out to be a great success. I have enjoyed playing in the Monday evening football competition with all of its ups and downs. We did a great job in promoting QT on the annual sports day by beating MB in the finales again. Also the two race biking trips to Egmond aan Zee were an unforgettable experience. I am grateful for the good coffee in QT thanks to the initiative of Jorden van Dam and Hubert Heersche. From the group formerly known as NF I would like to thank: Frank Meijer, Ruth de Boer, Hon Tin Man, Alberto Morpurgo, Jian-Rong Gao and Teun Klapwijk.

Last but not least I want to thank the current and former staff members of QT: Raymond Schouten, Bram van der Enden, Leo Lander, Leo Dam, Wim Schot, Willem den Braver, Kees Harmans and Masscha van Oossanen for all the work on the electronics, the sample holders, the pumps and evaporators, the helium-supply and all other help. Yuki Nakagawa and Ria van Heeren - van der Kramer, thank you both for all the paperwork and your concerns. Finally, I thank my family for all their understanding and support.

Laurens Willems van Beveren
Delft, September 2005

Contents

1 Introduction **1**
- 1.1 Motivation 1
- 1.2 Quantum computing 3
- 1.3 Electron spin as a quantum bit 5
- 1.4 Outline of this theis 8
- References 9

2 Fabrication of few-electron lateral quantum dot devices **11**
- 2.1 The GaAs/AlGaAs heterostructure 12
- 2.2 Lithography 15
  - 2.2.1 Optical lithography 16
  - 2.2.2 Electron beam lithography 17
- 2.3 Fabrication of lateral quantum dot devices 20
  - 2.3.1 Sample preparation 21
  - 2.3.2 Alignment markers 22
  - 2.3.3 Mesa etching 22
  - 2.3.4 Ohmic contacts 24
  - 2.3.5 Fine gates 26
  - 2.3.6 Electron cyclotron resonance 27
  - 2.3.7 Large gates 27
  - 2.3.8 Coplanar stripline 27
  - 2.3.9 Dielectric layers 31
  - 2.3.10 Sample finalization 34
- 2.4 Gate design of few-electron quantum dots 34
- 2.5 Device stability and bias cooling 37
- 2.6 Conclusions 39
- References 40

3 Theory and measurement techniques **45**
- 3.1 Quantum dots 45

3.1.1 Constant Interaction model 46
3.1.2 Spin configurations in few-electron quantum dots 50
3.2 Measurement setup 53
3.3 Quantum Point Contact as charge detector 59
3.4 Double dot charge stability diagram 61
3.5 Real-time observation of single-electron tunneling 62
3.6 Conclusions 64
References 65

4 Spin filling of a quantum dot derived from excited-state spectroscopy 67
4.1 Introduction 68
4.2 Zeeman splitting and spin filling 68
4.3 Device characteristics 71
4.4 N=0↔1 transition 72
4.5 N=1↔2 transition 73
4.6 N=2↔3 transition 74
4.7 N=3↔4 transition 75
4.8 N=4↔5 transition 76
4.9 Conclusions 76
References 76

5 Zeeman energy and spin relaxation of a single electron 81
5.1 Introduction 82
5.2 Zeeman energy 82
5.3 Measuring the spin relaxation time 85
5.4 Spin relaxation measurement using single-step pulses 85
5.5 Spin relaxation measurement using double-step pulses 88
5.6 Back-action of the QPC 90
References 90

6 Excited-state spectroscopy on a nearly closed quantum dot via charge detection 93
6.1 Introduction 94
6.2 Tuning the tunnel barriers 94
6.3 Excited-state spectroscopy for $N = 1$ 97
6.4 Excited-state spectroscopy for $N = 2$ 99
References 101

7 Single-shot read-out of a single electron spin using a difference in energy 103
7.1 Measuring electron spin in quantum dots 104
7.2 Two-level pulse technique 105
7.3 Tuning the quantum dot into the read-out configuration 107
7.4 Single-shot read-out of one electron spin 109
7.5 Measurement fidelity 112
References 114

8 Single-shot read-out of two-electron spin states using spin-dependent tunnel rates 117
8.1 Single-shot spin read-out using spin-dependent tunnel rates 118
8.2 Measurement visibility of the read-out 120
8.3 Single-shot read-out of the two-electron spin states 121
8.4 Magnetic field dependence of the triplet-to-singlet relaxation . . . 124
8.5 Read-out of nearly degenerate states 125
8.6 Conclusions 127
References 127

9 Current status and future directions for electron spin-based quantum computing 129
9.1 Introduction 130
  9.1.1 Qubit 130
  9.1.2 Initialization 132
  9.1.3 Read-out 133
  9.1.4 Coherence 134
  9.1.5 Universality 137
  9.1.6 Summary of the current status 139
9.2 Single-spin rotations 139
  9.2.1 On-chip generation of the oscillating magnetic field 140
  9.2.2 Detection of Continuous Wave ESR 141
  9.2.3 Detection of pulsed ESR 143
9.3 Two-spin experiments 145
  9.3.1 Two-spin quantum gate: SWAP 145
9.4 Conclusions 146
References 147

A Fabrication recipes 151
A.1 Alignment markers 151

- A.2 Mesa etching 152
- A.3 Ohmic contacts 153
- A.4 Fine gates 154
- A.5 Large gate / CPS and ESR wire 155
- A.6 Dielectric layers 156
  - A.6.1 SiO / SiO_2 156
  - A.6.2 PMGI / SF7 157
  - A.6.3 HSQ / FOx-12 158
  - A.6.4 Calixarene 159

Summary **161**

Samenvatting **165**

Curriculum Vitae **169**

List of publications **171**

Chapter 1

Introduction

'If I have seen further, it is by standing on the shoulders of giants.' [1]

1.1 Motivation

Classical mechanics is a mathematical framework developed by the english scientist and philosopher Isaac Newton [1642-1726]. In 1687 Newton published his famous work the *Principia Mathematica*, in which he showed how gravity produces the forces and movements of all that we see in the world, from the motions of the planets to the falling of an apple from a tree. In contrast to the other great thinkers before, whose theories were largely couched in philosophical terms, and never verified by systematic experimental testing as is popular today, Newton pioneered the use of experiment to validate physical theories, which is the key idea in the scientific method. The behavior of electricity and magnetism was studied by Faraday, Ohm, and others. In 1855, Maxwell unified the two phenomena into a single theory of electromagnetism, described by Maxwell's equations. A prediction of this theory was that light is an electromagnetic wave. Virtually all physical phenomena in our everyday macroscopic world can be described correctly by Newton's laws governing classical mechanics and Maxwell's equations describing electromagnetism. However, it was at the end of the nineteenth century that one started to realize that classical theory is not applicable at the atomic scale.

In the beginning of the 20th century Planck, Einstein, Bohr, and others developed quantum theories by introducing discrete energy levels to explain various anomalous experimental results regarding the behavior of small particles and light

---

[1] Sir Isaac Newton.

(photo-electric effect and the stability of atoms) that could not be explained by classical theories. In 1925, Heisenberg and 1926, Schrödinger and Dirac formulated quantum mechanics, which explained the preceding quantum theories and successfully describes the behavior of matter at small distance scales, i.e. the microscopic world with high accuracy.

In quantum mechanics, the outcomes of physical measurements are inherently probabilistic; the theory describes the calculation of these probabilities. It ascribes to all particles a wave function, responsible for intriguing effects such as energy quantization and interference. The particle-wave duality is beautifully demonstrated by Young's double-slit experiment using an electron source in stead of light [1]. Quantum mechanics also provided the theoretical tools for condensed matter physics, which studies the physical behavior of solids and liquids, including phenomena such as crystal structures, semiconductivity, and superconductivity. The pioneers of condensed matter physics include Bloch, who created a quantum mechanical description of the behavior of electrons in crystal structures in 1928.

These days, the computer chip industry is about to experience the same transition as science did in the early 20th century. As transistors are made smaller and smaller, a world is entered that does not obey the classical laws of physics. Certainly, the famous Moore's law [2], which states that the number of transistors on integrated circuits (a rough measure of computer processing power) doubles every 18 months, will not hold any longer when transistors reach the size of individual atoms [3]. Indeed, gate leakage currents due to quantum-mechanical tunneling and intrinsic current fluctuations due to the charge quantization already pose one of the most difficult hurdles for further decreasing the transistor size.

Rather than viewing the quantum-mechanical behaviour as a problem, we might also ask ourselves whether it is possible to actually use quantum mechanics for computing. One approach is to integrate a quantum property in a classical computing scheme. For example, the field of *spintronics* aims to use the spin degree of freedom of electrons as a carrier of classical information (bits) [4]. Alternatively, we might try to build a computer that exploits the unique features of quantum mechanics to perform computations that are not possible classically: a true *quantum computer*.

The research described in this thesis constitutes a first step towards a small-scale quantum computer where the spins of electrons serve as quantum bits, the basic building blocks of a quantum computer. In the next sections, the concept of quantum computing is explained, and the basic ingredients for implementing quantum bits with electron spins confined in quantum dots are outlined.

1.2 Quantum computing

In 1982, Richard Feynman speculated [5] that quantum systems might be able to perform certain tasks more efficiently than would be possible in classical systems. Important theoretical breakthroughs in the 1980s and 1990s have led to a realistic idea of what a quantum computer should look like. Before we continue discussing the quantum computer, we need to understand two important concepts from quantum mechanics: superpositions and entanglement.

Unlike a classical two-level system, which is always either in state 0 or in state 1, a quantum two-level system can be in an arbitrary *superposition* of states $|0\rangle$ and $|1\rangle$: $\alpha|0\rangle+\beta|1\rangle$, where $|\alpha|^2+|\beta|^2=1$. The evolution of this system is deterministic, as it is governed by a first-order differential equation – the Schrödinger equation. However, coupling this quantum system to a measurement apparatus forces it into one of the possible measurement eigenstates in an apparently non-deterministic way: the particular measurement outcome is random, only the probability for each outcome can be determined [6]. In the case of the above superposition state, the probability for measuring $|0\rangle$ is $|\alpha|^2$, and for $|1\rangle$ is $|\beta|^2$. The question of what exactly constitutes a measurement, which seems to be closely related to the transition from quantum to classical behaviour, is not fully understood [7].

The second property of quantum mechanics that is needed is one which has sprouted controversy for many years: *entanglement*. By interacting with each other, two quantum two-level systems can become entangled, which means that we can not fully describe one system independently of the other. For example, the state $(|01\rangle-|10\rangle)/\sqrt{2}$ gives a complete description of the whole system, but the two subsystems do not have a definite state. Due to this strong connection between the two systems, a measurement made on one, which forces it into one of the two states $|0\rangle$ or $|1\rangle$, immediately influences the state of the other, even though it may be arbitrarily far away. People have questioned whether it is not just a lack of our knowledge of some 'hidden variable' that hinders the prediction of a measurement outcome. However, measurements on so-called EPR pairs of photons (named after a landmark thought experiment by Einstein, Podolsky and Rosen [8]) have clearly shown that the non-local correlations between the photons are significantly larger than permitted by any local hidden-variable theory [9, 10]. Thus, entanglement is real, and constitutes one of the essential resources for quantum computing [11].

Using the concepts of superposition and entanglement, we now give a simplified view of the difference between a classical and a quantum computer in Fig. 1.1. A one-bit classical computer is a machine that takes one input value, 0 or 1, and computes the corresponding output value, $f(0)$ or $f(1)$. A quantum computer with one quantum bit (or 'qubit') could take as an input value a superposition of $|0\rangle$ and $|1\rangle$, and due to the linearity of quantum mechanics the output would be a superposition of $F|0\rangle$ and $F|1\rangle$. So, in a sense it has performed two calculations in a single step. For a two-qubit system, the gain becomes even more significant: now the input can be a superposition of four states, so the quantum computer can perform four calculations in one step. The operation on many input states simultaneously is termed 'quantum parallelism' and is at the heart of quantum computing. In fact, it can be proved [12] that the computing power of a quantum computer scales exponentially with the number of qubits, whereas this scaling is only linear for a classical computer.

It might appear that a fundamental problem has been overlooked: according to quantum mechanics, a superposition of possible measurement outcomes can only exist before it is measured, and the measurement gives only one actual outcome. The exponential computing power thus appears inaccessible. However, by using carefully tailored quantum algorithms, an exponential speed-up can be achieved for some problems such as factoring integers [13] or simulating a quantum system [14]. For other tasks, such as searching a database, a quadratic speed-up is possible [15]. Using such quantum algorithms, a quantum computer can indeed be far more efficient than a classical one, performing tasks that a classical computer could not possibly finish before the sun will burn up the earth.

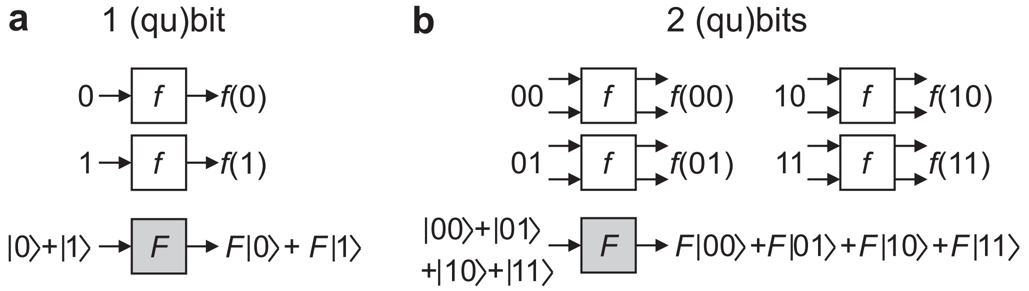

Figure 1.1: Difference between a classical and a quantum computer. **(a)** To determine the function f for the two possible input states 0 and 1, a one-bit classical computer needs to evaluate the function twice, once for every input state. In contrast, a one-qubit quantum computer can have a superposition of $|0\rangle$ and $|1\rangle$ as an input, to end up in a superposition of the two output values, $F|0\rangle$ and $F|1\rangle$. It has taken only half the number of steps as its classical counterpart. **(b)** Similarly, a two-qubit quantum computer needs only a quarter of the number of steps that are required classically. The computing power of a quantum computer scales exponentially with the number of qubits, for a classical computer the scaling is only linear.

The concepts of quantum superposition and entanglement also allow the realization of quantum teleportation of photonic [16] and atomic states [17, 18]. Quantum teleportation provides a means to transport quantum information efficiently from one location to another, without the physical transfer of the associated quantum-information carrier. This is achieved by using non-local correlations of previously distributed, entangled quantum bits and the transmission of some classical information. Quantum teleportation plays an important rule in the field of quantum cryptography as it provides a communication system which can always detect eavesdropping [19]. This is because measurements on the quantum carrier of information disturb it and so leave traces. As thinking about quantum algorithms has only barely begun, it is not unreasonable to assume that more applications of quantum computing will be discovered in the future.

Another fundamental issue is the interaction of the quantum system with the (uncontrolled) environment, which inevitably disturbs the desired quantum evolution. This process, known as 'decoherence', results in errors in the computation. Additional errors are introduced by imperfections in the quantum operations that are applied. All these errors propagate, and after some time the state of the computer will be significantly different from what it should be. It would seem that this prohibits any long computations, making it impossible for a quantum computer to use its exponential power for a non-trivial task. Fortunately, it has been shown that methods to detect and correct any errors exist [20, 21], keeping the computation on track. Of course, such methods only help if the error rate is small enough, since otherwise the correction operations create more errors than they remove. This sets a so-called 'accuracy threshold' [22, 23], which is currently believed to be around 10^{-4}. If the error per quantum operation is smaller than this threshold, any errors can be corrected and an arbitrarily long computation is possible.

Due to the development of quantum algorithms and error correction, quantum computation is feasible from a theoretical point of view. The challenge is building an actual quantum computer with a sufficiently large number of coupled qubits. Probably, more than a hundred qubits will be required for useful computations, but a system of about thirty qubits might already be able to perform valuable simulations of quantum systems.

1.3 Electron spin as a quantum bit

Any quantum two-level system can in principle function as a qubit, but for a scalable quantum computer a number of additional features are required [24].

Essentially, we have to reconcile the conflicting demands of good access to the quantum system (in order to perform fast and reliable operations or measurements) with sufficient isolation from the environment (for long coherence times). Current state-of-the-art is a seven-bit quantum computer, built up from the nuclear spins of molecules in a liquid solution. In this system, Shor's factoring algorithm has been demonstrated on the number 15 using nuclear magnetic resonance (NMR) techniques [25]. Practical limitations do not allow the NMR approach to be scaled up to more than about ten qubits. Therefore, many other implementations are currently being studied (a frequently updated overview of the progress on the different implementations can be found at Ref. [26]).

Typically, microscopic systems such as atoms or ions have good coherence properties, but are not easily accessible or scalable; on the other hand, larger systems such as solid-state devices can be accessed and scaled more easily, but often lack a long coherence time. A solid-state device with a long coherence time would represent the best of both worlds.

Precisely such a system was proposed by Loss and DiVincenzo [27] in 1997: the spin orientation of a single electron trapped in a semiconductor quantum dot. We outline the basic ingredients of this proposal below.

An electron spin can point 'up' or 'down' with respect to an external magnetic field. These eigenstates, $|\uparrow\rangle$ and $|\downarrow\rangle$, correspond to the two basis states of the qubit.

The electron is trapped on a quantum dot, which is basically a small electrically defined box with a discrete energy spectrum. The quantum dots that we use are defined by metal 'gate' electrodes on top of a semiconductor (GaAs/AlGaAs) heterostructure (see Fig. 1.2). At the interface between GaAs and AlGaAs, conduction band electrons accumulate that can only move in the lateral direction. Applying negative voltages to the gates locally depletes this two-dimensional electron gas underneath. The resulting gated quantum dots are very controllable and versatile systems, which can be manipulated and probed electrically. With the external magnetic field, B, we can tune the Zeeman splitting, $\Delta E_Z = g\mu_B B$, where $g \approx -0.44$ is the g-factor of GaAs, and $\mu_B = 9.27 \times 10^{-24}$ J/T is the Bohr magneton. In this way, we can control the energy levels of the qubit.

To perform single-qubit operations, we can apply a microwave magnetic field on resonance with the Zeeman splitting, i.e. with a frequency $f = \Delta E_Z/h$, where h is Planck's constant. The oscillating magnetic component perpendicular to the static magnetic field B results in a spin nutation. By applying the oscillating field for a fixed duration, a superposition of $|\uparrow\rangle$ and $|\downarrow\rangle$ can be created. This magnetic technique is known as electron spin resonance (ESR).

Two-qubit operations can be carried out purely electrically, by varying the

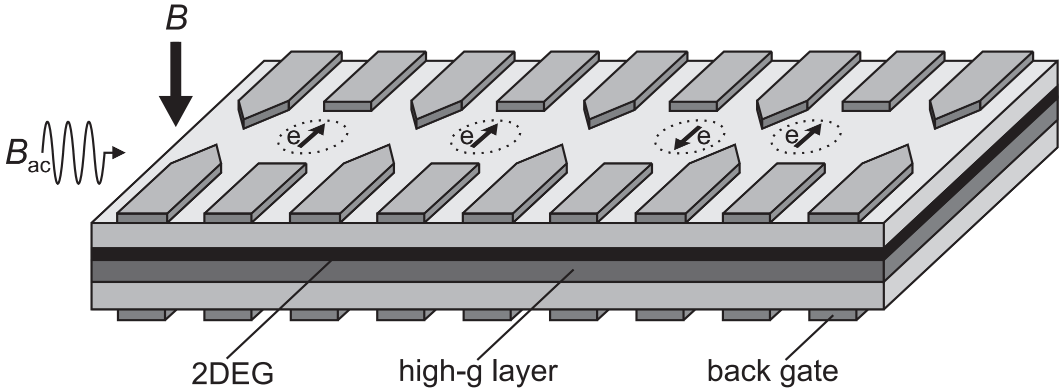

Figure 1.2: Schematic picture of the electron spin quantum computer as proposed by Loss and DiVincenzo [27]. The array of metal electrodes on top of a semiconductor heterostructure, containing a two-dimensional electron gas (2DEG) below the surface, defines a number of quantum dots (dotted circles), each holding a single electron spin (arrow). A magnetic field, B, induces a Zeeman splitting between the spin-up and spin-down states of each electron spin. The spin state is controlled either via an oscillating magnetic field, B_{ac} (on resonance with the Zeeman splitting), or via an oscillating electric field created with the back gates, which can pull the electron wavefunction into a layer with a large g-factor. Coupling between two spins is controlled by changing the voltage on the electrodes between the two dots. (Adapted from Ref. [27].)

gate voltages that control the potential barrier between two dots. It has been shown [27] that the system of two electron spins on neighboring dots, S_1 and S_2, coupled via a tunnel barrier, can be mapped onto the Heisenberg exchange Hamiltonian $H = J\vec{S_1} \cdot \vec{S_2}$. The strength of this interaction, J, depends on the wave function overlap of the electrons and can be controlled electrically. By turning the two-spin interaction on for a certain well-defined time, the two electron spins can be swapped or even entangled. With combinations of arbitrary single-spin rotations and the two-spin interaction, any quantum gate can be implemented [27].

A last crucial ingredient is a method to read out the state of the spin qubit. This implies measuring the spin orientation of a single electron – a daunting task, since the electron spin magnetic moment is exceedingly small (equal to the Bohr magneton μ_B). Therefore, an indirect spin measurement is proposed [27]. First the spin orientation of the electron is correlated with its position, via 'spin-to-charge conversion'. Then an electrometer is used to measure the position of the charge, thereby revealing its spin. In this way, the problem of measuring the spin orientation has been replaced by the much easier measurement of charge.

The ideas of Loss and DiVincenzo have led to an enormous research effort aiming at implementing the different parts of the proposal. Currently, among the most active players in this rapidly moving field are the groups of prof. S. Tarucha (Tokyo University, Japan), dr. T. Fujisawa and dr. Y. Hirayama (NTT Basic Research Labs, Japan), Prof. J. P. Kotthaus (LUM München, Germany), prof. C. M. Marcus and Prof. R. Westervelt (Harvard University, USA), prof. M. A. Kastner (MIT, USA), and prof. D. Goldhaber-Gordon (Stanford University, USA).

Finally, it should be stressed that our efforts to create a spin qubit are not purely application-driven. If we have the ability to control and read out a single electron spin, we are in a unique position to study the interaction of the spin with its environment. This may lead to a better understanding of decoherence, and will also allow us to study the semiconductor environment using the spin as a probe.

1.4 Outline of this theis

This thesis describes a series of experiments aimed at understanding and controlling single electron spins confined in semiconducting lateral quantum dots, with the long-term goal of creating of a small-scale quantum computer.

We start in chapter 2 with a detailed description of the fabrication process of few-electron lateral quantum dot devices. These devices form the hardware for all the experimental results shown in this thesis. Here we specifically discuss the coplanar stripline structure for guiding high-frequency signals on-chip and the use of dielectric layers.

Next (chapter 3) we explain the basic theory of quantum dots and the measurement techniques applied in this work, including the hardware for the experiments on electron spins that is developed: a (double) quantum dot circuit with a voltage-tunable number of electrons, with an integrated charge detector formed by a quantum point contact (QPC).

Then, in chapter 4, we investigate the ground state spin configuration of a quantum dot containing 1-5 electrons at large in-plane magnetic fields by measurements of electron transport through the dot. In chapter 5, we use again an in-plane magnetic field to directly detect the Zeeman splitting of a single electron. Furthermore, by using fast voltage pulses, we find a lower bound on the spin relaxation time of 50 μs.

In chapter 6 to chapter 8, we use the charge detector for measurements in the regime of very weak dot-lead coupling, where we can resolve single-electron tunnel events in real time. First, a novel method is presented for finding the relevant dot parameters in this regime (chapter 6). Then, we demonstrate one of the key ingredients for a quantum computer: single-shot read-out of the spin states. To convert the spin information to charge information, we have exploited the spin-dependent energy (chapter 7), and spin-dependent tunnel rates (chapter 8), achieving a measurement visibility of more than 80%. Both for a single spin and for the two-electron spin states, we find that the relaxation can be very slow (relaxation times up to milliseconds). We find a strong magnetic field dependence that hints at spin-orbit interaction as the dominant relaxation mechanism.

The current status of the field and the remaining issues are discussed in the concluding chapter 9. Also, detailed measurement schemes for single-spin rotations and the two-spin SWAP operation are proposed.

References

[1] C. Jönsson, Zeitschrift für Physik **161**, 454 (1961).

[2] G. E. Moore, Electronics **38**, 114 (1965).

[3] For up-to-date information and prospects, see the International Technology Roadmap for Semiconductors at http://public.itrs.net/.

[4] S. A. Wolf *et al.*, Science **294**, 1488 (2001).

[5] R. P. Feynman, in *The Feynman Lectures on Computation*, edited by R. W. Allen and T. Hey, (Perseus Publishing, 2000).

[6] R. P. Feynman, in *The Feynman Lectures on Physics*, Vol. 3 (Addison Wesley, 1970).

[7] V. B. Braginsky and F. Y. Khalili, *Quantum Measurement*, (Cambridge University Press, 1992).

[8] A. Einstein, B. Podolsky and N. Rosen, Phys. Rev. **47**, 777 (1935).

[9] A. Aspect, P. Grangier and G. Roger, Phys. Rev. Lett. **49**, 91 (1982).

[10] J. S. Bell, *Physics* **1**, 195 (1964); S. J. Freedman and J. F. Clauser, Phys. Rev. Lett. **28**, 938 (1972).

[11] M. A. Nielsen and I. L. Chuang, *Quantum Computation and Quantum Information*, (Cambridge University Press, Cambridge, England, 2000).

[12] D. Deutsch, Proc. Roy. Soc. Lond. **A400**, 97 (1985).

[13] P. W. Shor, 'Algorithms for quantum computation: discrete logarithms and factoring', in *Proceedings of 35th Annual Symposium on Foundations of Computer Science* (IEEE Press, 1994).

[14] S. Lloyd, Science **273**, 1073 (1996).

[15] L. K. Grover, Phys. Rev. Lett. **79**, 325 (1997).

[16] D. Bouwmeester *et al.*, Nature **390**, 575 (1997).

[17] M. Riebe, *et al.*, Nature **429**, 734 (2004).

[18] M. D. Barrett, *et al.*, Nature **429** 737 (2004).

[19] A. K. Ekert, Phys. Rev. Lett. **67**, 661 (1991).

[20] P. W. Shor, in *Proceedings of 37th Annual Symposium on Foundations of Computer Science*, (IEEE Press, 1996).

[21] A. M. Steane, Phys. Rev. Lett. **77**, 793 (1996).

[22] A. Y. Kitaev, 'Quantum error correction with imperfect gates', in *Quantum Communication, Computing, and Measurement*, edited by A. S. Holevo, O. Hirota and C. M. Caves, (Plenum Press, 1997).

[23] D. Aharonov and M. Ben-Or, quant-ph/9906129 (1999).

[24] D. P. DiVincenzo, Fortschr. Phys. **48**, 771 (2000).

[25] L. M. K. Vandersypen *et al.*, Nature **414**, 883 (2001).

[26] Quantum Information Science and Technology roadmapping project, available at http://qist.lanl.gov/.

[27] D. Loss and D. P. DiVincenzo, Phys. Rev. A **57**, 120 (1998).

Chapter 2

Fabrication of few-electron lateral quantum dot devices

L. H. Willems van Beveren, R. Hanson, F. H. L. Koppens,
J. J. Wever, W. J. M. Naber, I. T. Vink,
L. P. Kouwenhoven and L. M. K. Vandersypen

In this chapter, we report in detail the fabrication process of lateral quantum dot devices. This process was developed in the NTT Basic Research Laboratories and optimized with respect to sample yield and device application in the Delft Institute of MicroElectronics and Submicron technology (DIMES). The basis for all these devices is the GaAs/AlGaAs heterostructure wafer which will be discussed first. Next, a general introduction to optical and electron beam lithography is given, followed by a complete description of all fabrication steps involved. We then show the results of the implementation of dielectric layers and on-chip (superconducting) coplanar striplines. Finally, we show the gate design of several few-electron lateral quantum dots and discuss the issue of device stability. The recipe for the fabrication process can be found in the Appendix of this thesis.

2.1 The GaAs/AlGaAs heterostructure

All lateral quantum dot devices reported in this thesis are fabricated out of silicon (Si) doped GaAs/AlGaAs heterostructures. These heterostructures are semiconducting wafers where layers of gallium arsenide (GaAs) and aluminum gallium arsenide (AlGaAs) are stacked in a specific way (see Fig. 2.1a). GaAs is a III-V compound semiconductor material composed of the element gallium (Ga) from column III and the element arsenic (As) from column V of the periodic table of the elements. AlGaAs is obtained when a fraction of Ga ions in GaAs is substituted by aluminum (Al) ions, also from column III of the periodic table of elements.

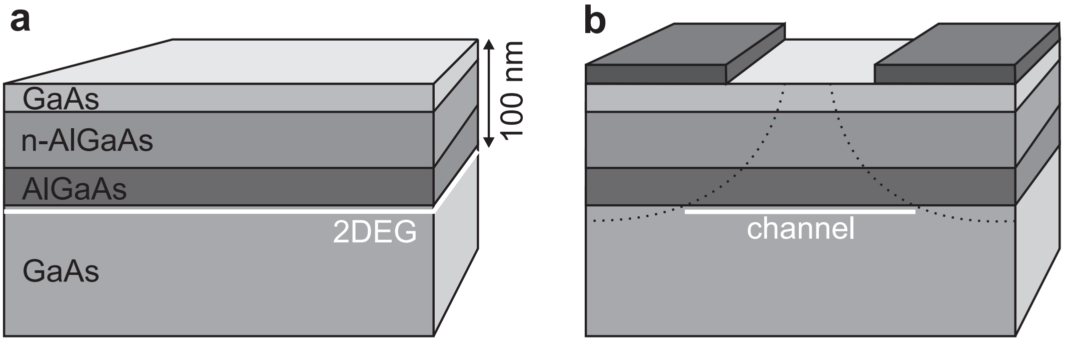

Figure 2.1: Confining electrons in a semiconductor. **(a)** Semiconductor heterostructure containing a 2DEG (indicated in white) approximately 100 nm below the surface, at the interface between GaAs and AlGaAs. The electrons in the 2DEG result from Si donors in the n-AlGaAs layer. (The thickness of the different layers is not to scale.) **(b)** By applying negative voltages to the metal electrodes on the surface of the heterostructure, the underlying 2DEG can be locally depleted. In this way, electrons can be confined to one or even zero dimensions.

The GaAs and AlGaAs layers are grown on top of each other by the technique of molecular beam epitaxy (MBE). MBE produces near-perfect crystalline layers of extreme purity with atomically sharp transitions between layers. If necessary, dopants can easily be implanted during the growth process. The heterostructures are usually grown in the [100] direction. As the [100], the [010] and the [001] directions are equivalent for GaAs (see Fig. 2.2a), we generalize these growth directions as <100> and the subsequent growth planes as {100}, according to the index system for crystal planes [1]. In Fig. 2.2b the surface of the heterostructure wafer is indexed by (100) and the generalized cleavage planes of the heterostructure correspond to {110}. For this particular crystallographic orientation we can easily break the heterostructure wafer along the primary (OF) and secondary flat (IF) directions.

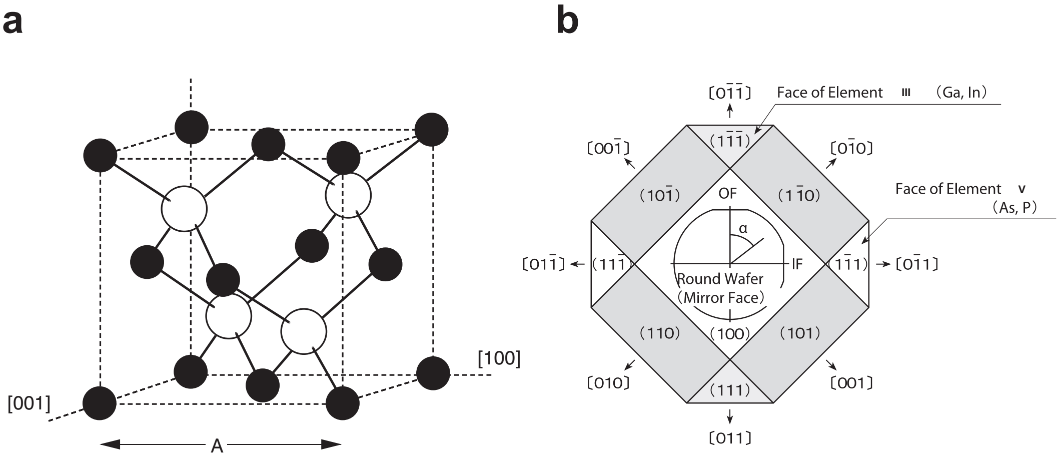

Figure 2.2: **(a)** Unit cube of the GaAs crystal with a lattice constant A of 5.65 Å. Black (white) balls indicate the Ga (As) atoms, respectively. GaAs has a crystal configuration which is known as the 'zincblende' structure and is composed of two sublattices, each face centered cubic. **(b)** Top view of the crystallographic faces of a (100) grown wafer of GaAs or InP, indexed by Miller indices. The primary (OF) and secondary flats (IF) located in the circumference of the wafer indicate the type and orientation of the crystal.

The bandgap of GaAs ΔE_g (1.42 eV) can be increased by substituting a fraction of Ga atoms by Al atoms, thereby changing the crystal composition from GaAs to $\mathrm{Al}_x\mathrm{Ga}_{1-x}\mathrm{As}$. Usually an Al fraction of x=0.3 is substituted, resulting in a bandgap of 1.79 eV. Therefore if GaAs and $\mathrm{Al}_{0.3}\mathrm{Ga}_{0.7}$ As are stacked in a heterostructure, the result is a bandgap mismatch ΔE_C at the interface of these two materials as shown in Fig. 2.3. When subsequently Si-dopants are implanted in the $\mathrm{Al}_{0.3}\mathrm{Ga}_{0.7}\mathrm{As}$ donor region (typically $1{\times}10^{18}$ cm^{-3} dopants in 65 nm AlGaAs), free electrons will accumulate at the heterojunction in a triangular-shaped quantum well which resides typically 90 nm below the surface [2]. We will refer to $\mathrm{Al}_{0.3}\mathrm{Ga}_{0.7}\mathrm{As}$ as AlGaAs from this point on and drop the indices for convenience. The electrons in this well are strongly confined in the growth direction, forming discrete states. The electrons are only allowed to move in the plane of the interface, where they form a so called two-dimensional electron gas (2DEG) [3]. The conduction and valence band of a modulation-doped [4] heterostructure are also schematically shown in Fig. 2.3. A practical difficulty is that we need to know the charge density to solve Poisson's equation and deduce the energy bands, but we can not calculate the density of free carriers until we know the energy bands. Thus the calculation has to be performed self-consistently [5]. Here the bandgap mismatch ΔE_C is given by the difference in electron affinity

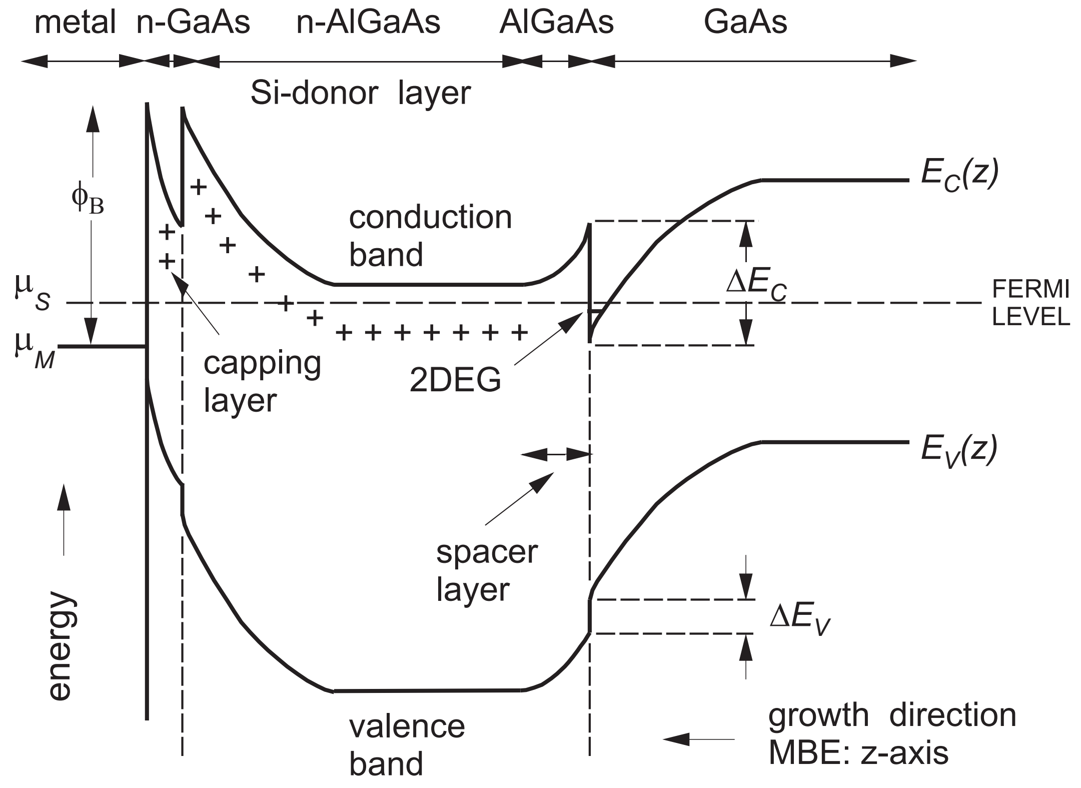
metal
n-GaAs
n-AlGaAs
AlGaAs
GaAs
Si-donor layer
ϕ_B
μ_S
μ_M
conduction band
$E_C(z)$
ΔE_C
FERMI LEVEL
capping layer
2DEG
$E_V(z)$
spacer layer
ΔE_V
energy
valence band
growth direction MBE: z-axis

Figure 2.3: Energy band diagram through the layers of a gated GaAs/AlGaAs heterostructure, as can be found by solving Poisson's equation self-consistently. The Si-doping region is indicated with a '+' sign. The alignment of the Fermi level in the semiconductor crystal implies that no net charge transport takes place in the growth direction (diffusive equilibrium condition). Note that the triangular well in the conduction band is absent in the valence band.

between GaAs and undoped AlGaAs. The discontinuity in the valence band follows from $\Delta E_V = \Delta E_g - \Delta E_C$.

The 2DEG is usually separated about 20 nm from the n-AlGaAs donor region by an undoped AlGaAs 'spacer' layer. This separation allows for an extremely high mobility of the electrons in the 2DEG, because scattering with the Si donors is reduced significantly. At 4.2 K the 2DEG has a typical mobility and electron density of $10^5 - 10^6$ cm^2/Vs and $\sim 3 \times 10^{15}$ m^{-2}, respectively. Therefore GaAs/AlGaAs heterostructures are often referred to as high electron mobility transistor (HEMT) wafers. The relatively low electron density results in a large Fermi wavelength ($\sim$ 40 nm) and a large screening length, which allows us to locally deplete the 2DEG with an electric field.

This electric field is created by applying voltages to metal gate electrodes fabricated on top of the heterostructure (Fig. 2.1b). The gate voltage V_g is related to the chemical potential in the metal and the semiconductor as $eV_g = \mu_S - \mu_M$ (see Fig. 2.3). The Schottky barrier Φ_B formed at the metal-semiconductor junction ensures that no charge is leaking into the heterostructure. The steep slope of the conduction band at the metal-semiconductor interface arises from the high charge density in the surface states. This charge must be balanced by that from the donors, and most of the donors are needed to neutralize the Schottky barrier; only a small fraction contributes to electrons in the 2DEG. Ionized donor regions cause the conduction band to curve whereas charge neutral regions leave the conduction band unaffected. For details concerning ionized and non-ionized donor regions, see Ref. [39].

If the gate voltage is made too positive, or the AlGaAs donor layer is too thick or too highly doped, the minimum in the conduction band within the doped AlGaAs layer falls below the Fermi level and a second population of electrons appears in this region. This is called parallel conduction [6] and interferes with the controllability of the quantum dot, since the 2DEG is now almost perfectly screened from the surface gate.

2.2 Lithography

Lithography is the process for creating patterns on a surface [7]. From the Greek lithos (stone) and graphy (writing), lithography literally means ‘writing on rocks’. Our lateral quantum dot devices are fabricated by the technique of electron beam (e-beam) lithography. The e-beam lithography technique is required to define metal electrodes on top of a GaAs/AlGaAs heterostructure with lateral dimensions of $\sim$ 50 nm. By applying negative voltages on these tiny electrodes (fine gates), we confine electrons in the 2DEG to form a ‘dot’ of electrons (see Fig. 2.4).

Normally for patterns larger than a few μm, optical lithography is used since it is much faster than e-beam lithography. However there are some drawbacks of the optical lithography process. First, for each different writing step a separate photomask is required, making it difficult to switch designs on a fast time scale. Second, the alignment mechanism of the optical lithography set-up in DIMES was not really suited for our very small wafer pieces. Third, the lift-off with photoresist was usually poor (all metal comes off or the metal does not come off at the places where it should) and not reproducible. The exact reasons are not yet fully understood. Since the e-beam pattern generator (EBPG) in DIMES could easily handle large exposure areas, we modified the fabrication process such that all optical lithography steps were replaced by e-beam lithography. This resulted in several improvements. First, the e-beam lithography process allowed for very

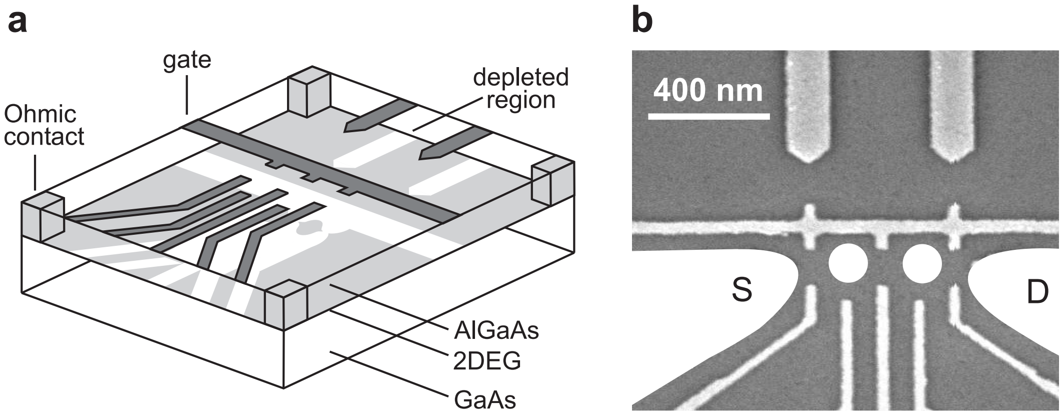

Figure 2.4: Lateral quantum dot device defined by metal surface electrodes. **(a)** Schematic view of a device. Negative voltages applied to metal gate electrodes (dark gray) lead to depleted regions (white) in the 2DEG (light gray). Ohmic contacts (light gray columns) enable bonding wires (not shown) to make electrical contact to the 2DEG reservoirs. **(b)** Scanning electron microscope image of an actual device, showing the gate electrodes (light gray) on top of the surface (dark gray). The two white dots indicate two quantum dots, connected via tunable tunnel barriers to a source (S) and drain (D) reservoir, indicated in white. The two upper gates can be used to create two quantum point contacts, in order to detect changes in the number of electrons on the dot, as will be explained in chapter 3 (Device fabricated by Ronald Hanson and Laurens Willems van Beveren at NTT Basic Research Labs.)

precise alignment to a set of markers defined on the semiconductor surface. Second, it resulted in a higher reliability of the lift-off process. This might be related to the more homogeneous thickness of the e-beam resist (no edge bead) and its enhanced robustness against both high temperatures and outgassing during the evaporation process. Finally, due to the combination of two e-beam resists with different sensitivities, an undercut profile in the resist mask can be realized, facilitating the lift-off process. Both optical and e-beam lithography techniques have been used and will be discussed now.

2.2.1 Optical lithography

In case of optical lithography a positive tone photosensitive resist layer is deposited on the cleaned surface of a heterostructure with a typical thickness of 1-2 μm. We have tried both near-UV and deep-UV optical lithography. With the latter technique it is possible to pattern finer structures because of the reduced wavelength of the light used. As photoresist we have used both S1813 (similar to AZ-1400) and AZ-5214E (option for image reversal) with (diluted) developers

AZ-351 and developer concentrate. We have also tried developing S1813 with MF-321 (metal ion free) but this was less successful than the (diluted) developer concentrate. Usually no photoresist adhesion promoter, like HMDS primer, was needed.

To improve the lift-off procedure of evaporated metals it is possible to increase the undercut of the photoresist layer, similar as in Fig. 2.5b, by immersing the sample for a few minutes in (mono)chlorobenzene right after the optical exposure and before the actual developing step. The chlorobenzene chemically modifies the upper part of the photoresist layer causing it to be less soluble in the developing stage. In this way a pronounced undercut profile can be created in the resist layer. Even with this chlorobenzene soak, the lift-off was not always reproducible.

2.2.2 Electron beam lithography

Polymethyl methacrylate (PMMA) has been used for many years as the high resolution resist of choice in electron beam lithography [8]. PMMA is a positive-tone [9] resist with a molecular weight varying between 50k and 2.2M (atomic mass units) and is commercially available, e.g. at MicroChem. PMMA with a molecular weight of 950k (950PMMA) is used for our (high resolution) applications. In general, lower molecular weight resists are more sensitive to exposure and dissolve faster in a solvent developer. With 950PMMA and small beam diameters, it has been possible to reproducibly fabricate gates with a lateral size of 20-40 nm. In order to spin coat thin 950PMMA layers, the 950PMMA is diluted in chlorobenzene (2% by weight) to reduce the viscosity.

There are several factors in evaluating a high resolution resist. One of them is the ‘contrast’ and is usually defined as the maximum slope in the normalized resist thickness versus log(dose) graph. The contrast of a resist becomes higher as the molecular weight of the PMMA increases. Therefore, high-contrast resist like 950PMMA yields well-defined profiles in dense patterns. However, the ultimate resolution achievable in a resist is not predetermined merely from the contrast. The developer selection is just as important as the resist due to the fact that contrast is also a function of the developer. A more fundamental and less controllable factor that determines the ultimate resolution is related to the interaction of the e-beam (effective spot size is ~ 3 nm) with the resist and the substrate, as we will see later.

The resist layer that is used in the e-beam lithography process depends on the structure that is fabricated, in particular the thickness of the metal that is to be deposited and the lateral dimension of the structure. For the small surface electrodes that define the quantum dot, a single layer of PMMA resist with a thickness of 90 nm gave the best results. Two different types of PMMA resist were used for this purpose. The first resist was 950PMMA (2%) from MicroChem. The second resist was the chemically amplified PMMA based resist OEBR-1000 (100 cp) with a typical molecular weight of 600k (source: Tokyo Ohka Kogyo). The OEBR-1000 (100 cp) was diluted by addition of OFPR-800, in a ratio of 1:2. Both resists gave similar results.

For larger patterns with a metal thickness larger than 60 nm, a bilayer system of resists was used. The bottom layer is a 350 nm thick copolymer resist denoted as P(MAA-MAA) [10]. P(MAA-MAA) is a mixture of PMMA and 17.5% methacrylic acid (MAA) and is diluted in ethyl-L-lactate (8.5%). The top layer is a 90 nm thick resist of 950PMMA (2%). The copolymer resist has a lower molecular weight as compared to 950PMMA (2%) which results in a higher sensitivity and dissolution rate in solvent developers. This allows for the formation of an undercut of the bottom resist layer, facilitating the lift-off process. This is important when thick layers of metal are to be evaporated or in case of (isotropic) sputter deposition, where the side-walls of the resist get easily covered by the material used.

The e-beam lithography process is depicted in Fig. 2.5. First a pattern is defined by writing with a focused electron beam in an electron-sensitive resist (Fig. 2.5a). In DIMES a Leica e-beam pattern generator EBPG 5HR100 FEG (EBPG5) was used for this purpose. The standard acceleration voltage of the electrons is 100 kV to obtain small beam diameters. The high acceleration voltage also minimizes forward scattering of the electrons in the resist. The EBPG5 was also operated at 50 kV to see the effect of acceleration voltage on the (electron backscatter mediated) lift-off process of the small surface gates. However, no large differences were found.

When the primary electrons hit the substrate they return back in the resist as secondary electrons (resulting from inelastic scattering events), causing additional exposure over large lateral distances (typical spatial range $\sim$ 10 μm for GaAs substrates). This process is known as ‘backscattering’ and is believed to be the main contributor to the resolution limit of PMMA. Resist exposure comes mainly from secondary electrons with an energy below 1 keV. The substrate plays an important role in the energy distribution of secondary electrons. This is evident when we compare the exposure dose of a resist film on a Si substrate which is approximately twice as high as the exposure dose (of the same resist) on a GaAs substrate. This exposure dose increase is primarily due to the reduced backscattering in the Si material. However, the advantage of writing small patterns on GaAs substrates is that an undercut in the bottom layer of resist (Fig. 2.5b) is automatically created by exposure from backscattered electrons, facilitating the

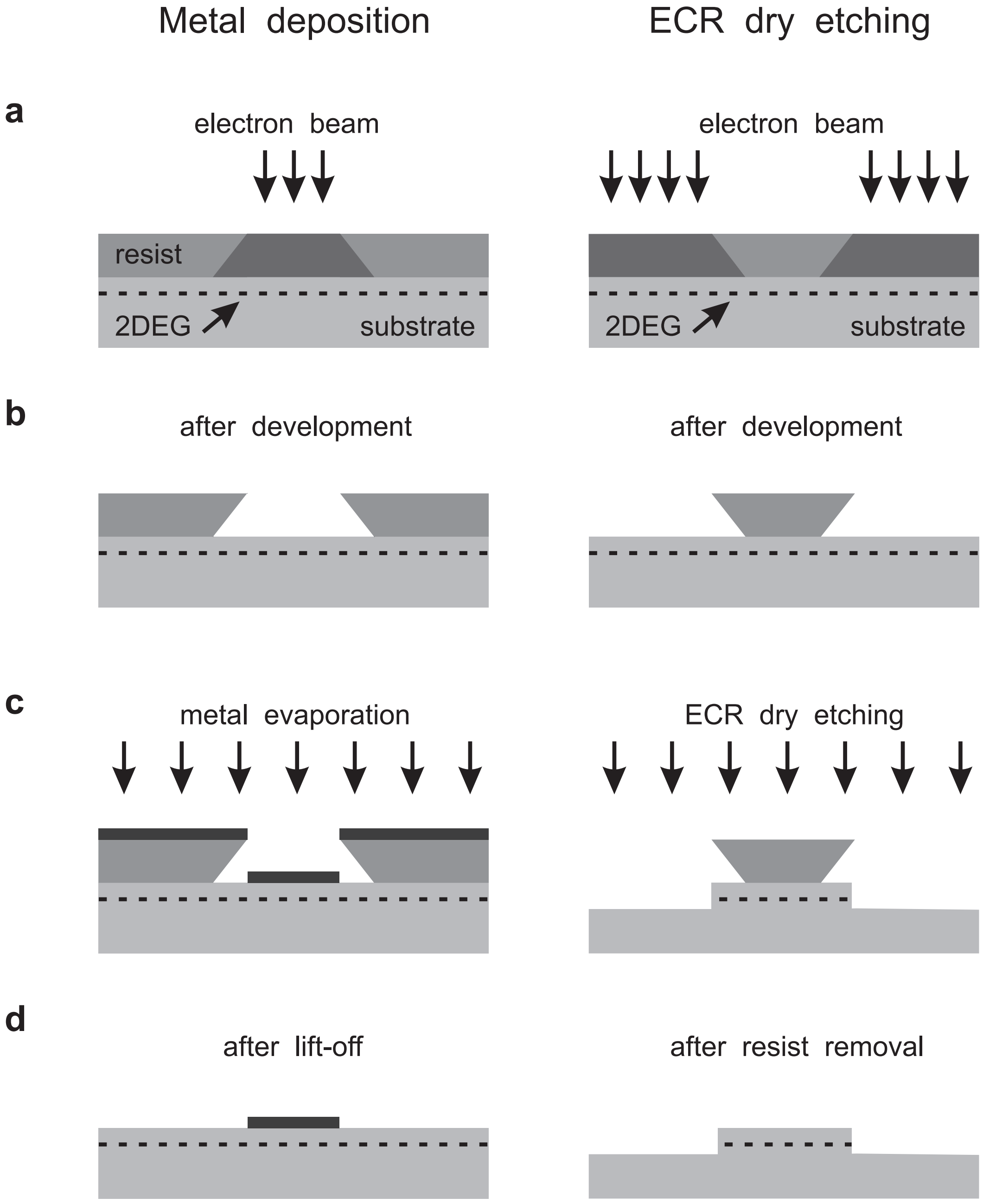
Metal deposition
ECR dry etching
a
electron beam
electron beam
resist
2DEG
substrate
2DEG
substrate
b
after development
after development
c
metal evaporation
ECR dry etching
d
after lift-off
after resist removal

Figure 2.5: Electron beam lithography process to define either metal electrodes or to etch the surface of the heterostructure wafer. Note that even for a single 950PMMA layer, backscattered electrons give rise to an undercut in the resist profile which enhances the lift-off process for metallic gates. **(a)** Write a pattern in the resist layer with an electron beam. **(b)** Resist profile after development of the exposed resist. **(c)** Metal evaporation or dry etching by electron cyclotron resonance (ECR). **(d)** After removing the resist in acetone either a metal electrode or a mesa (etched region) remains.

lift-off process. This is why even single layers of resist can be used in the lift-off process of the fine gates.

For highly dense patterns, the proximity effect needs to be considered. Here backscattered electrons from the writing of adjacent patterns cause additional exposure of the resist. The proximity effect is responsible for the increase of the size of the exposed resist and therefore limits the resolution of the patterns to be written. Low-energy e-beam lithography in the range of 1-10 keV would strongly suppress the proximity effect [11]. Since the penetration depth of electrons is smaller for lower energies, the number of backscattered electrons from the substrate is reduced. Furthermore, the irradiation damage of the underlying substrate is potentially minimized.

The e-beam locally breaks up the polymer chains in the resist, so-called bond scission, such that the exposed parts can be removed by a developer. The overall performance of a developer is characterised by sensitivity, contrast, exposure dose latitude, roughness and ultimate resolution. It is commonly found that an improvement in resist sensitivity is accompanied by a decrease in contrast, for example, increasing the MIBK ratio in MIBK / IPA from 1:3 to 1:1 doubles the sensitivity but almost halves the contrast. The resolution of a resist-developer system depends on contrast, therefore a developer of very high sensitivity, but of very low contrast, is not suitable for nanolithography. The developer used is a mixture of isopropanol (IPA) and methyl isobutyl ketone (MIBK) in a 1:3 MIBK / IPA ratio. The developing process is stopped by rinsing the chip in pure IPA.

In the next step, the sample is either fully covered with metal by evaporation or is dry etched by the technique of electron cyclotron resonance (ECR) (see Fig. 2.5c). In the ECR process (see section 2.3.6) the GaAs substrate is etched only on the places that are not covered by PMMA resist. The e-beam resist itself is hardly affected by ECR etching. In the final lift-off step, the remaining resist (with the unwanted metal film in case of evaporation) is removed by an acetone spray. The result is a metal electrode or an etched mesa (Fig. 2.5d).

2.3 Fabrication of lateral quantum dot devices

The fabrication process of lateral quantum dot devices consists of a series of steps. At first the heterostructure wafer is cut and its surface cleaned. Then a marker pattern is fabricated to align to in the next steps. In the third step a mesa is etched in the wafer to isolate the surface gates from the ohmic contacts to the 2DEG which are formed by depositing a gold-germanium alloy (AuGe) followed by rapid thermal annealing. In the fifth step the small surface electrodes are defined. These determine the actual size and design of the quantum dot. At this point an optional dry etching step is possible for isolating regions of 2DEG without the use surface electrodes. In the sixth step the fine gates are connected to bonding pads by a large gate pattern. The fabrication of a microwave line running next to the quantum dot can be incorporated in the sixth step. However, in case of a microwave line on top of the quantum dot, an additional step is required involving the deposition of a dielectric layer, electrically isolating the fine gate pattern from the coplanar stripline. The result of the first six fabrication steps is illustrated in Fig. 2.6.

In all of the fabrication steps e-beam lithography is used. The smallest structures of the quantum dot devices have a lateral dimension of about 20 nm, much smaller than the size of dust particles in normal air. Therefore the fabrication is performed in a class 10k cleanroom that maintains less than ten thousand particles larger than 0.5 μm in each cubic foot of air space. In addition the cleanroom is temperature and humidity controlled.

2.3.1 Sample preparation

First, 10 by 14 mm sized pieces are cut out of a GaAs/AlGaAs heterostructure wafer using a diamond scriber (model RV-129 from ATV Technology). A sharp diamond pen indents the surface of the wafer and perpendicular lines are drawn that follow the cleavage axis of the wafer. Then the wafer is flipped upside down and can easily be broken along the indented lines when one pushes gently with a tweezer on the backside. Apart from the GaAs/AlGaAs heterostructure, pieces of wafer are cut out of a semi-insulating GaAs wafer. These pieces serve as dummy material to test each fabrication step before applied to the samples from the valuable GaAs/AlGaAs heterostructure wafer. Here we assume that the fabrication process of semi-insulating GaAs and GaAs/AlGaAs heterostructure wafers give similar results.

On each piece of wafer (chip) there is space to fabricate up to 56 (7 rows by 8 columns) devices that each have a size of 1.1 by 1.3 mm. Therefore the total area the pattern on the chip spans is 7.7 by 10.4 mm. It is convenient to cut the chips on which the devices are fabricated a bit bigger than the total pattern size, a few mm on each side, to have some extra space to mount the chip in the machines and for handling them with tweezers. The extra space also ensures a uniform resist profile, such that the lithography is not affected by an edge bead that is usually formed near the edges of the chip. After fabrication the quantum dot devices are taken out of the chip in a similar manner. It is therefore necessary to have a lateral scribing resolution that is comparable to the separation between the individual devices; about 80 μm in our case.

Throughout the whole fabrication process, it is extremely important to work with a clean surface of the heterostructure. Any kind of particles on the surface of the wafer will affect the homogeneity of the resist films. Also, the adhesion of deposited materials to the semiconductor wafer may be reduced. Therefore the wafer is cleaned before every step in the following way. First the surface of the wafer is cleaned by rinsing it in acetone for several minutes. Acetone is a good solvent for many organic materials. The acetone is then removed from the surface by rinsing the sample in isopropanol (IPA) or in de-mineralized water, after which the sample should be blown dry using nitrogen (N_2) gas. To remove water residues from the surface the sample is dried in a convection oven or on a hot plate at a temperature of about 200°C for several minutes.

2.3.2 Alignment markers

Here we place a marker pattern on the surface of the heterostructure, oriented along the cleavage planes of the wafer (black regions in Fig. 2.6a). The marker pattern consists of a series of 20 μm square markers and is used to align the chip in each e-beam lithography step. This alignment can be done automatically by the EBPG5 within 50 nm for markers separated by 1 mm. Within the same marker pattern, each of the 56 devices is labeled with a letter code from AA to GH.

A resist combination of copolymer MMA (17.5%) MAA (8%) and 950PMMA (2%) is used to define the marker pattern with a thickness of 50/150 nm Ti/Au. The visibility of the markers in the EBPG5 is ensured by the large backscattering of electrons from the Au atoms. The Au layer should also not be fabricated too thin for this reason of contrast.

2.3.3 Mesa etching

It is important to realize that in our fabrication scheme all the bonding pads on the chip, except for the microwave line, are identical. Therefore the bonding pads for the surface electrodes are connected to the 2DEG, just as those for the ohmic contacts. Without etching a mesa all these bonding pads will be shorted via the 2DEG. The etching of the mesa is not necessary if the bonding pads for the surface gates are electrically isolated from the 2DEG.

Etching the GaAs/AlGaAs heterostructure is used to electrically isolate conducting regions on the chip, in particular the gate electrodes and the ohmic contacts to the 2DEG (next process step). This isolation is guaranteed when all

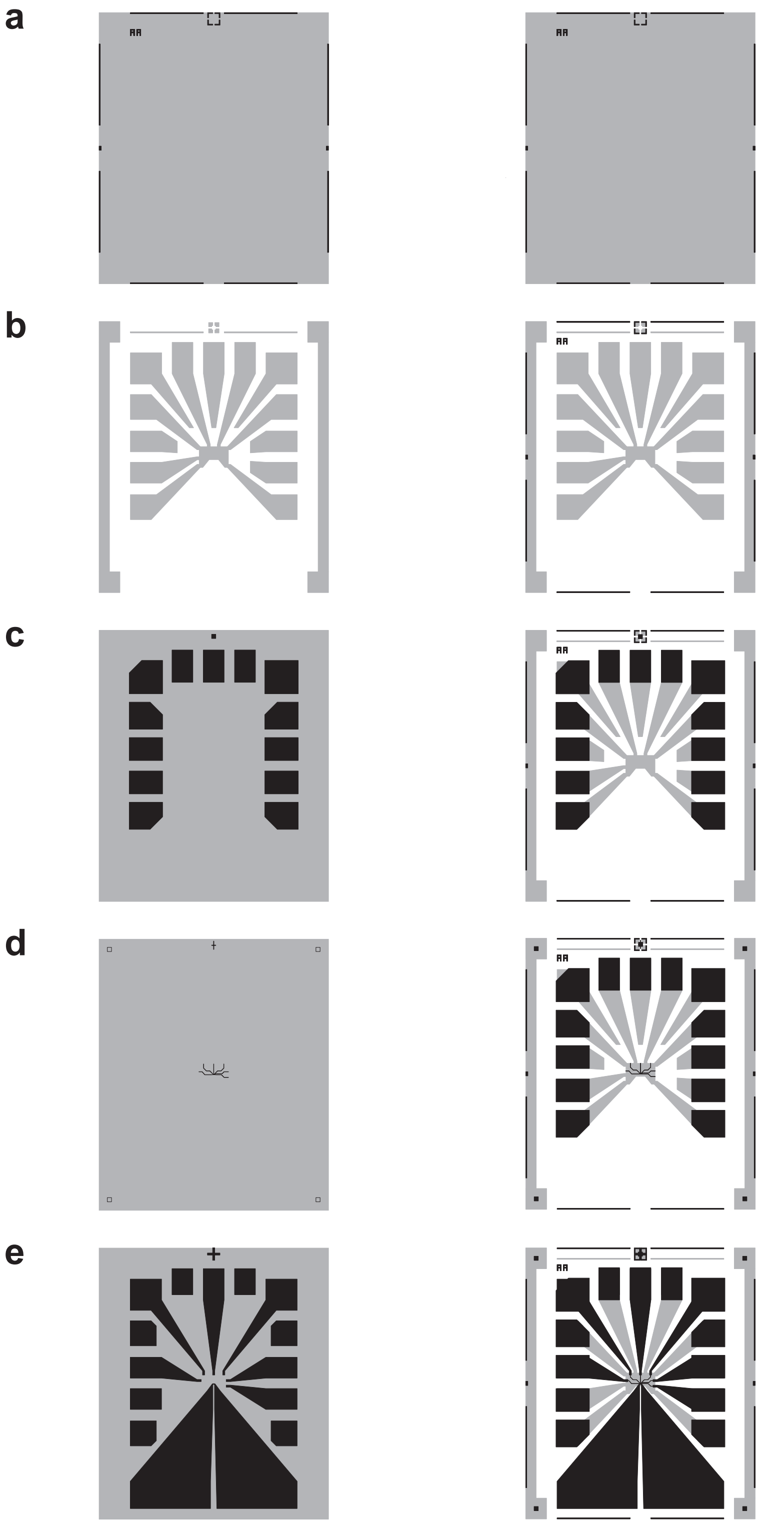

Figure 2.6: Fabrication steps for lateral quantum dot devices. The result of each individual fabrication step (left) and applied sequentially (right). **(a)** Patterning of Ti/Au alignment markers (black). **(b)** Wet etching the mesa structure (grey). **(c)** Patterning Ni/AuGe/Ni ohmic contacts (black). **(d)** Patterning the Ti/Au fine gate structure (black). **(e)** Patterning the Ti/Au or NbTiN large gate pattern including the CPS structure at the bottom of the chip (black).

the Si donors in the n-AlGaAs layer are removed in the etching process, since they provide the electrons to form the 2DEG. However, in practice we always etch a little bit deeper than the 2DEG and thereby remove also the AlGaAs spacer layer. This is more practical for δ-doped heterostructures where the Si donors reside in a narrow region of n-AlGaAs close to the 2DEG.

The regions that remain unaffected by the wet etching process form a conducting area, referred to as the 'mesa' (grey region in Fig. 2.6b). A second motivation for etching the substrate is to reduce the capacitive coupling to the 2DEG when high frequency signals are applied to surface gates or on-chip waveguides.

As an etching mask, a single layer of 950PMMA (2%) is used. It is important to invert the design file of the mesa, since 950PMMA (2%) is a positive tone resist. Directly after development the resist layer thickness should be measured in order to determine the etch depth before removing the resist layer. This enables one to etch more in case the wafer is not etched deep enough. Just before the wet etching, the surface of the wafer is cleaned in diluted sulphuric acid to remove native oxides from the GaAs surface, which may affect the etching process. It was found that the resist was not affected during the etching process. The chip is etched in a solution of H_2O_2:H_2SO_4:H_2O mixed in a ratio of 1:5:25. The etching liquid was kept at a constant temperature of 10°C (au bain-marie) in a temperature controlled cooling bath. The etching rate of GaAs is 3 nm/sec and can be increased by raising the temperature. Usually, 40-50 seconds of etching resulted in a depth of 120-150 nm. It should be noted that the layers of AlGaAs have a higher etching speed than GaAs. The etching liquid is prepared by adding 4 ml of H_2O_2 to 120 ml of 1:5 H_2SO_4:H_2O. Directly after mixing of these liquids an exothermic reaction takes place, heating up the etching liquid. Therefore it is best to wait several minutes before starting the etching process to obtain a stable etching speed. The etching process is stopped by rinsing the chip in demi-water.

2.3.4 Ohmic contacts

Good electrical contacts to the 2DEG are realized by rapid thermal annealing (RTA) surface electrodes, 100 by 100 μm each, made out of a sandwich of nickel (Ni) and gold-germanium (AuGe). Deposition of the Ni and AuGe layers was achieved first by thermal evaporation (resistance heating). Here the AuGe alloy can easily be evaporated using a tungsten (W) boat, but the Ni needs to be evaporated in an Al_2O_3-coated boat as it tends to form an alloy with W during the evaporation process. This even caused the uncoated W boat to break several times. A much better control of the deposition process was obtained using an evaporator where the target materials, Ni and AuGe, were placed in carbon (C) crucibles and heating took place by an electron beam.

In the RTA process, Ni/AuGe/Ni (5/150/25 nm) surface electrodes are heated from 20°C to 440°C in 42 seconds and kept at this temperature for 60 seconds, followed by a cool down in one minute to 80°C. The wafer to be heated is placed on a quartz glass tray which slides into a quartz glass tube in a oven. Two banks of lamps, one above the tube and one below it, provide the source of energy for heating the wafer. The RTA process takes place in a controlled hydrogen (H_2) / nitrogen (N_2) atmosphere to prevent oxidation. During the RTA, the electrodes melt and diffuse deeply into the heterostructure wafer and form an ohmic contact to the 2DEG (see [12] and references therein). The incorporation of Ge atoms plays a crucial role here, since these provide dopants in the GaAs region near the metal interface thereby reducing the heterostructure barrier that is formed between the metals and the semiconductor. The RTA process results in typical resistances per contact of several tens of kΩ at room temperature, and $\sim$kΩ at 4.2 K for devices that have been wet etched. The wet etching process slightly increases the series resistance between two ohmic contacts because the aspect ratio of the current channel, defined by the mesa, is increased. This effect has been observed at room temperature. At 4.2 K the series resistance is dominated by the contact resistance of the ohmic contacts.

The Ni/AuGe/Ni surface electrodes are patterned by e-beam lithography (bilayer resist), evaporation and subsequent lift-off (black region in Fig. 2.6c). The primary Ni layer improves the uniformity of the contacts and enhances the adhesion of the electrodes to the GaAs substrate, facilitating the wire bonding process. The AuGe eutectic used is composed of 88-12 wt% Au-Ge. A thin capping layer of GaAs (5 nm) is usually grown on top of the AlGaAs layer to complete the MBE process. The GaAs capping layer reduces the Schottky barrier because of its smaller bandgap compared to AlGaAs. Most of our heterostructures have a Si-doped capping layer (typically a donor density of 1.5×10^{18} cm^{-3} in a 10 nm thick GaAs cap), which reduces the Schottky barrier even further to improve the contact to the 2DEG. The Si-doped capping layer also protects the AlGaAs donor layer from surface oxidation and depletion. However, a too high doping concentration results in unwanted parallel conduction channels in the n-AlGaAs layer. Moreover, the surface gates that deplete the 2DEG rely on the presence of a Schottky barrier and to prevent leaking, the Schottky barrier should not be too small.

2.3.5 Fine gates

In this fabrication step the fine gate pattern and additional alignment markers are written (small black areas in Fig. 2.6d). To a large extent the fine gate pattern defines the properties of the quantum dot devices. It defines the position and size of the tunnel barriers and quantum point contacts. However, the fabrication procedure of the fine gate pattern is the same for any given gate design. A single layer of resist is spin coated for this purpose (either 3:2 OEBR-1000 (100 cp) / OFPR-800 or 950PMMA (2%)), to a thickness of about 90 nm. In case of a resist bilayer, a too large undercut in the copolymer bottom layer caused the walls of the resist to collapse after development. The fine gate pattern is written with an exposure dose that is slightly higher compared to the other e-beam lithography steps to compensate for a reduction in proximity effect (due to the small exposure area). For the same reason, the plunger gates of the quantum dot are usually written with a higher exposure dose (130%) than the other gates. The gate pattern of the quantum dot is defined in the center of the mesa.

After cleaning the surface of the heterostructure in diluted sulphuric acid, we evaporate the metal for the fine gates. The metal gates consist of a thin (10 nm) sticking layer of titanium (Ti), followed by a 20 nm layer of gold (Au) on top. It is important to deposit the layer of reactive Ti with a high evaporation rate to reduce the formation of TiO_x which affects the adhesion. In addition to developing in standard 1:3 MIBK / IPA, we have tested the unconventional 3:7 water / IPA developer. It was shown that water / IPA improves sensitivity by nearly 40%, and contrast by nearly 20%, compared to standard 1:3 MIBK / IPA developer [13].

To improve the metal-semiconductor contact the developed chip is rinsed in diluted sulphuric acid (1:5 H_2SO_4 / H_2O), prior to evaporation, in order to remove native oxides from the GaAs surface. Moreover, to enhance the adhesion of metals to the GaAs surface, a plasma stripping process is employed directly after developing to remove organic contaminants (also known as a ‘de-scum’), e.g. PMMA remnants. In the NTT cleanroom, a reactive ozone plasma was used to strip the chip surface at an elevated temperature of 200°C. However, in the DIMES cleanroom a damage-free oxygen plasma was used to strip the chip surface at room temperature. However, since stripping in an oxygen plasma introduces oxides at the surface it is recommended to perform the acid rinse after the stripping process has been completed.

It is important that the lift-off is done very carefully as this is a critical step. There are two signatures of a bad lift-off. The first is characterized by missing parts of the fine gates (too much metal comes off). The second is characterized by metal connections between surface electrodes (too little or no metal comes off). Good results were obtained when the evaporated sample is kept in an acetone bath for several hours. Subsequently, acetone is sprayed onto the surface of the heterostructure from different directions to lift-off the unwanted metal from the sample.

2.3.6 Electron cyclotron resonance

For some experiments it is desirable to isolate the quantum dot with source and drain contacts from the remaining part of the 2DEG without the use of depletion gates. One can isolate regions of 2DEG by locally removing the Si donors in the AlGaAs layer. This is achieved by electron beam lithography in combination with electron cyclotron resonance (ECR) dry etching [14], a technique employing BCl_3 plasma chemistry. The e-beam lithography (EBL) / ECR technique is shown in Fig. 2.5. The advantage of ECR etching over wet etching is that it allows for a very high resolution (set by the EBL process) due to the highly anisotropic properties of the etching process. Furthermore ECR etching minimizes damage to the 2DEG as compared to reactive ion etching (RIE), due to its low ion energy (controlled by wafer biasing).

2.3.7 Large gates

The large gate pattern electrically connects the tiny surface gates of the quantum dot to large pads on the outside of the chip necessary for wire bonding. Since these bonding pads lie outside the central mesa it is necessary to evaporate a thick layer of metal in order to overcome the height step of the mesa. A conventional bilayer of resists is used to deposit a 50 nm thick layer of Ti, followed by a 150 nm thick layer of Au (black region in Fig. 2.6e). It might be a good idea to finish the evaporation process with a layer of gold-palladium (AuPd) since this material is harder than Au and thereby enhances the wire bonding process.

2.3.8 Coplanar stripline

In order to couple AC magnetic fields to the quantum dot, a coplanar stripline (CPS) is fabricated on-chip (see Fig. 2.7). In the ESR experiment the frequency of the AC signal corresponds to the Larmor precession of an electron spin in a magnetic field, which is completely determined by the g-factor of GaAs and the static magnetic field applied. A few Tesla of magnetic field requires AC signals of several GHz, i.e. in the microwave regime. A CPS consists of two

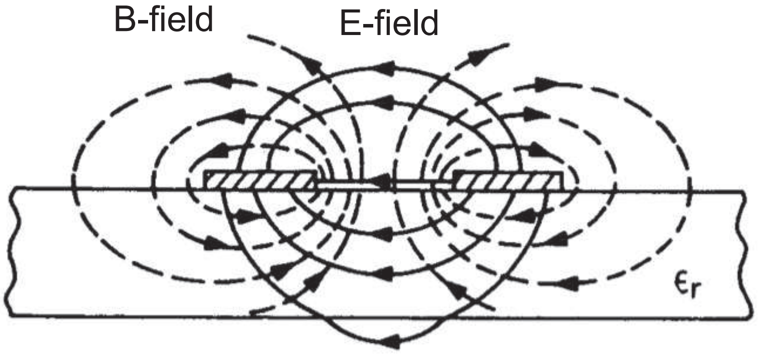

Figure 2.7: Side-view of a coplanar stripline (CPS) structure on a dielectric material. The electric (solid lines) and magnetic fields (dashed lines) are plotted.

parallel sheets of metal on the surface of a dielectric layer and is designed to carry electromagnetic fields in a large bandwidth over long distances. The two sheets of metal confine the electromagnetic field lines similarly as in the case of a coax cable. By shorting the two sheets of the CPS close to the quantum dot, a local source of magnetic flux is created (see Fig. 2.9). The CPS itself is designed to match the 50 Ω impedance of the coax line in the dilution refrigerator to minimize power loss due to reflections. The connection from coax cable to the CPS is made by wire bonding the inner and outer conductor of the coax to the two sheets of metal on the chip. It is important to minimize the length of the bond wires and to maximize the number of bonds to reduce the total inductance of the transition.

To maximize the coupling of the AC magnetic field to the electron spin, the short is to be placed as close to the quantum dot as possible. A shorted CPS can be fabricated in the same step as the large gate pattern (see Fig. 2.6e). Here the CPS structure is fabricated directly next to the quantum dot. First a 500 nm thick OEBR-1000 (200 cp) resist layer is spun followed by 90 nm thick layer of 950PMMA (2%) [15]. Then either a 50/400 nm thick layer of Ti/Au or a 320 nm thick film of superconductor niobium-titanium nitride (NbTiN) is deposited. The Au film has a typical room temperature resistivity of 2.2 $\mu\Omega$ cm. The NbTiN layer was deposited by reactive DC-magnetron sputtering of (Nb,Ti) in an argon (Ar) / nitrogen (N_2) atmosphere [16]. To increase the AC magnetic field generated, the thickness of the Ti/Au or NbTiN film can be made thicker such as to increase the maximum current flowing through the shorted CPS. However, the skin effect [17] sets an upper bound for this thickness.

The reason for implementing NbTiN is to increase the coupling of the microwave signals to the quantum dot by minimizing ohmic losses in the material of the stripline [18]. Since the quantum dot is operated in strong magnetic fields, a superconductor with a critical field of several Tesla is required. At the same time the superconductor should have a large critical current, as this is the relevant parameter for the AC field generated. The maximum supercurrent that can be transported for type-I superconductors is very small; a relatively weak external magnetic field exceeds the critical field thereby destroying superconductivity. However, NbTiN fulfills both these requirements.

NbTiN is a type-II compound superconductor with a critical temperature T_c of 15 K and a bandgap of 5.2 meV. Therefore, below T_c, NbTiN is expected to transport microwave signals with negligible losses up to the bandgap frequency (THz regime) [19]. NbTiN does not show the extreme brittleness as niobium nitride (NbN) and is therefore easy applicable in the fabrication process for RF devices. The 320 nm thick NbTiN film has a normal state resistivity of about 110 $\mu\Omega$ cm and in the superconducting state a typical supercurrent density of about 10^5 A/cm^2 is expected, even in a magnetic field of $\sim$ 5 T [20]. Considering the stripline geometry (smallest cross-section), we expect a maximum supercurrent of about 640 μA. The series resistance of the shorted CPS was found to be 90 Ω at room temperature and 50 Ω at 20 mK, above I_{c2} (see Fig. 2.8(a) and (c)).

Characteristic of a type-II superconductor is the existence of a mixed state, where magnetic flux partially penetrates the superconductor to form vortices (flux tubes). The lower and upper boundaries of this mixed state are given by two critical field values, referred to as H_{c1} and H_{c2}. The vortices repel each other and form a triangular lattice referred to as the Abrikosov lattice. The vortices interact with the supercurrent flow leading to finite dissipation if the flux line lattice starts moving. However, if we have a strong hysteresis, caused by impurities and defects in the material, a current will flow without moving the vortices if the force exerted on them is not strong enough to set them in motion. The superconductor will support a current without dissipation.

The properties of a superconductor in the GHz regime are difficult to measure with a conventional measurement set-up. Therefore we have performed four-terminal DC measurements of a shorted CPS made of NbTiN as a function of magnetic field (45° angle). The results of these measurements are shown in Fig. 2.8(a)-(d). These results clearly show the presence of a mixed state which is an indication that the vortices have difficulties moving (vortex pinning). For a fixed magnetic field, a pure supercurrent is observed up to a critical current we refer to as I_{c1}. Beyond I_{c1} the state of the superconductor enters a regime of small, but finite dissipation referred to as the ‘flux flow regime’. The flux flow regime is characterized by a resistivity that is linear in magnetic field. Next, at a critical current I_{c2} the superconductor resistivity suddenly increases at the

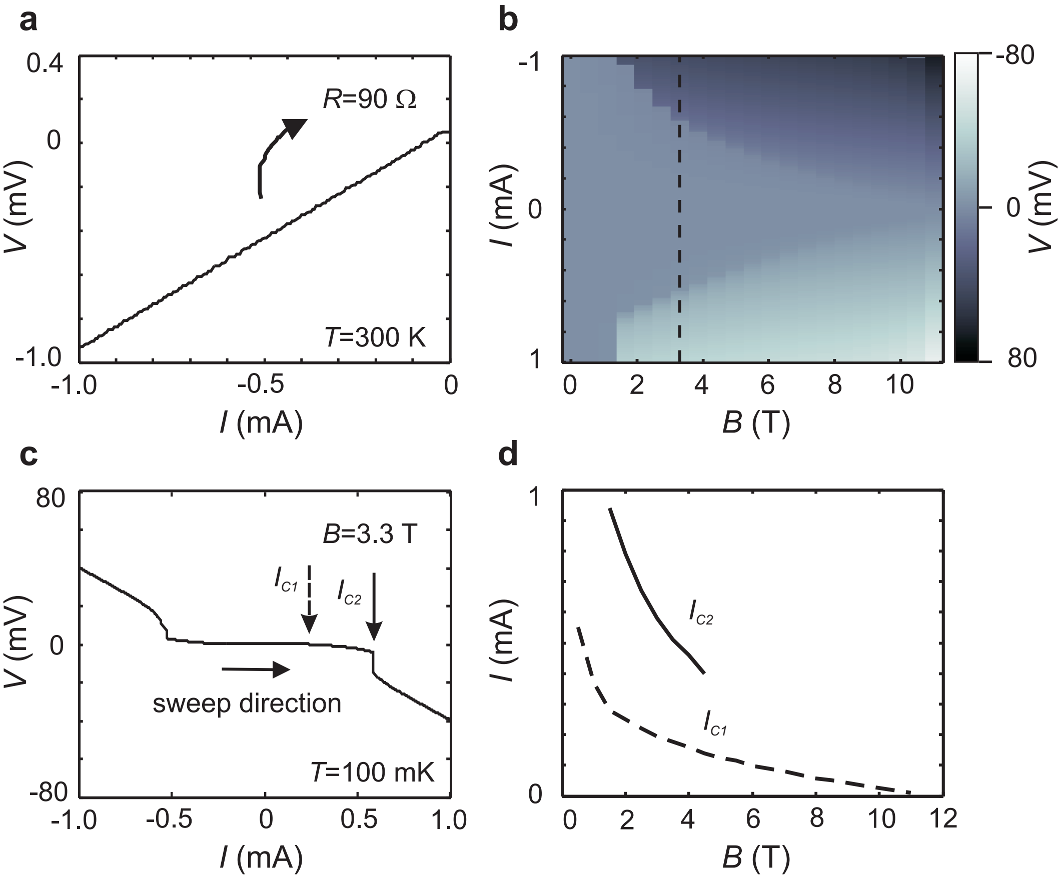

Figure 2.8: **(a)** Voltage versus current measurement of a NbTiN CPS at room temperature. The normal state resistance of the CPS structure, R, is 90 Ω. **(b)** Similar measurement as a function of magnetic field at a temperature T of 100 mK. Below T_c the NbTiN film is superconducting for currents smaller than the critical current $I_c(B)$. The superconducting gap is clearly visible and decreases for higher values of the magnetic field. **(c)** Voltage versus current trace taken from **(b)** (vertical dashed line) at $B = 3.3$ T. Three regions can be distinguished: a pure non-dissipative state bound by I_{c1}, a flux-flow state with small but finite dissipation (between I_{c1} and I_{c2}) and a normal state for currents larger than I_{c2}. The current is swept from -1 mA to 1 mA. Note that the switch from the superconducting state to the normal state occurs suddenly as compared to the reverse transition. **(d)** Magnetic field dependence of the critical currents I_{c1} and I_{c2} as defined in **(c)**. For zero magnetic field supercurrents of 6 mA were measured. Note that the sample is oriented at an angle of 45° with respect to the magnetic field, allowing the formation of vortices in the thin film.

transition to the normal state [21]. The critical current I_{c1} is 550 μA at 0.5 T and decreases to 30 μA at 10 T. The critical current I_{c2} is 900 μA at 1 T and decreases to 500 μA at 3.3 T. Both I_{c1} and I_{c2} decrease as the magnetic field

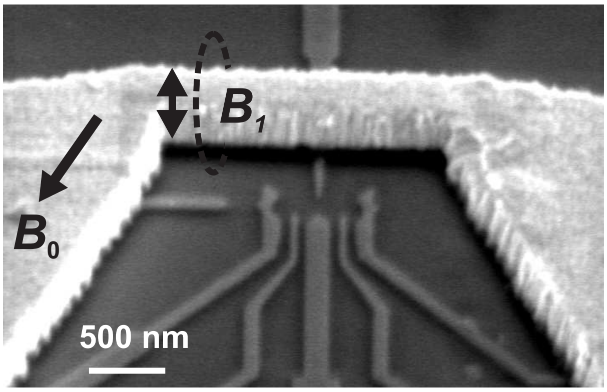

Figure 2.9: Scanning electron microscope image of a double quantum dot device designed for electron spin resonance experiments. A QPC charge detector coupled to the QD on the left is used for single-shot spin detection. A 50/450 nm thick Ti/Au wire is patterned on top of a locally defined dielectric film (calixarene). The wire that shorts the CPS structure provides magnetic flux to the double dot when current biased. Here the short is shifted upwards to visualize the fine gate pattern of the quantum dot. When the shorted CPS is placed directly on top of the dot the electron spin resonance configuration can be realized either with a perpendicular or in-plane static magnetic field (device fabricated by F. H. L. Koppens and K.-J. Tielrooij in DIMES).

is increased. This can be explained by the stronger Lorentz force acting on the vortices so that the flux flow state sets in at an earlier stage. The parallel field dependence of the NbTiN film still has to be investigated.

In order to further increase the magnetic field coupling to the quantum dot, the shorted CPS can be fabricated directly on top of the quantum dot separated by a thin dielectric layer to prevent a shortcut between the surface gates and the CPS metal (see section 2.3.9). Simulations in Microwave Studio (a 3D electromagnetic field solver) indicate that the highest magnetic fields are formed inside the loop formed by the CPS and the short [22].

2.3.9 Dielectric layers

A dielectric layer is a material that is electrically insulating and prevents conducting materials from coming into contact, allowing for smaller separations and therefore higher capacitances. There are two reasons why it is interesting to integrate dielectric layers with our quantum dot devices. First, it allows us to increase the coupling of the AC magnetic field to the electron spin by placing the CPS in very close vicinity to the quantum dot [23]. Second, this particular configuration provides AC magnetic fields that point in the plane of the 2DEG, such that the ESR condition can be satisfied for both perpendicular and in-plane static magnetic fields. For this to succeed, the dielectric material has to be compatible with e-beam lithography, a cryogenic environment and should electrically isolate the metal structures above and below the dielectric layer.

Several types of dielectric material were tested: i) sputtered SiO_2 and evaporated SiO, ii) PMGI / SF7 resist iii) negative tone hydrogen silsesquioxane (HSQ) and finally iv) negative tone calixarene resist. To characterize these dielectric materials a sandwich structure is fabricated on semi-insulating GaAs substrates consisting of a thin bottom electrode of Ti/Au, a dielectric film and a thick top electrode of Ti/Au. The dielectric layers were measured at room temperature and at 4.2 K. Next we discuss the results of the measurements of these dielectric materials.

SiO / SiO$_2$

Standard e-beam lithography and deposition techniques were used to pattern single dielectric layers of SiO and SiO_2. The quality of these films (defects, cracks) and the adhesion to the GaAs substrate were poor. Also the lift-off process of the top electrode was problematic in most cases. Moreover, transport measurements showed that the SiO layer was leaking substantially. No further fabrication tests were carried out to solve some of the above mentioned problems.

PMGI / SF7

MicroChem PMGI / SF7 resist consists of polydimethylglutarimide polymer with proprietary solvent blends and is virtually insoluble in typical photoresist solvents. Therefore i-line, deep UV and e-beam resists can be placed on top of PMGI without intermixing. In a bilayer configuration the developing process for 950PMMA (2%) and PMGI are completely independent and the undercut in the resist is variable. Dielectric layers of PMGI were easily patterned and had a good adhesion to the substrate. First a bottom layer of PMGI is spun directly on top of a a surface electrode defined on the GaAs substrate. Then a 950PMMA (2%) imaging resist layer is spin coated, baked and finally exposed and developed in order to remove the PMGI locally. The PMGI layer is developed in MF-321 (or 322). In this way well defined films of PMGI were made in a reproducible way. In the next step, the Ti/Au top electrode is fabricated by standard bilayer lithography. However the acetone, used in the lift-off process of the top electrode, turned out to be incompatible with the PMGI film, resulting in missing PMGI layers after lift-off. In our process, the PMGI / SF7 resist was not chemically resistant enough against acetone and therefore fails to be employed as a useful dielectric. As was recently found out, mixing of several types of PMGI resist increases the chemical resistance against acetone.

HSQ / FOx-12

HSQ is a flowable oxide spin-on dielectric that is compatible with e-beam and optical lithography [24]. HSQ is available in a liquid solution of MIBK (FOx-12) and has a dielectric constant of 2.9. First a 100 nm layer of FOx-12 is spin coated. During the pre-bake on a hot plate, the carrier solvent is removed and the film melts. After e-beam exposure (550 μC/cm^2) the unexposed regions are removed by MF 322 developer. The HSQ dielectric layers were very reproducible and a coplanar stripline could easily be fabricated on top without any adhesion problems. However, room temperature and 4K probe station measurements revealed severe leakage currents through the dielectric layer. The origin of the leakage might be related to defects (pinholes) in the spin coated resist.

Calixarene

Calixarene [25] is an organic material and can be dissolved in chlorobenzene [26]. Solutions of 2.5 and 5 % (by weight) were made by adding 1 and 2 gram of calixarene to 39 grams of chlorobenzene respectively. Since calixarene does not easily dissolve in chlorobenzene the solution is mixed for several days on a hot plate. Then samples containing a Ti/Au bottom electrode were spin coated after filtering the calixarene solution and baked in an oven. Extremely smooth films of approximately 50 nm thickness could easily be realized. After calixarene exposure to the e-beam it was developed by dipping the samples in xylene to remove the unexposed areas. To stop the developing process, the sample is rinsed in IPA. The exposure dose of calixarene is 7500 μC/cm^2, about 10 times higher as compared to standard PMMA resist. The large exposure dose increases the writing time substantially, but is necessary to let the calixarene molecules cross-link with each-other sufficiently to form a solid layer [27]. It was found that the large exposure dose, required for fabricating the calixarene film, does not destroy the 2DEG underneath and QPC noise measurements of these devices do not show a noticeable degradation of the sample stability. A Ti/Au (40/110 nm) top electrode was then deposited to be able to measure the leakage current through the dielectric films.

From current versus voltage measurements in a 4 K probe station a resistance of a few kΩ was extracted for a single layer of calixarene with a thickness of 50 nm. The resistance increased for samples with a 75 nm thick calixarene layer to values between MΩ-GΩ, comparable to the substrate resistance. The current voltage relation sometimes shows a linear response, but often the leakage current is suppressed for small source drain voltage applied.

Samples where two calixarene layers were spun and baked on top of each-other isolated even better and a resistance on the order of a GΩ was extracted. Here, the substrate conductivity of semi-insulating GaAs substrates sets an upper bound to the measured resistance of the calixarene bilayer. Substrate conductivity was identified by shining light on the substrate while measuring the leakage current through the calixarene bilayer. The electrically isolation of the calixarene layers are very promising for our application. Moreover, since calixarene has a very low thermal conductance it may prevent local heating from the ESR wire to the quantum dot. In this case the dissipated energy can not directly be absorbed by the underlying substrate and needs to be transported by the ESR wire.

2.3.10 Sample finalization

After the fabrication process is completed the quantum dot devices are taken out of the chip by a diamond scriber as explained before. The individual devices are then fixed on a plastic sample plate with two component glue. The sample plate with sample is subsequently glued on a copper sample holder [28]. Wire bonding is used to make electrical connection from the sample plate to the bonding pads on the device. The bonds to the device are either formed by ball bonding of gold (Au) wire or by wedge bonding of aluminum (Al) wire. Finally a copper (Cu) cap is put on the sample holder for protection and to screen electromagnetic fields.

2.4 Gate design of few-electron quantum dots

The proposal by Loss and DiVincenzo [29] to use single electron spins in quantum dots as quantum bits, describes an optimal combination of the single-electron charge degree of freedom (for convenient manipulation using electrical voltages) and the spin degree of freedom (which is believed to have a long coherence time, essential for encoding quantum information). For the control of one-electron quantum states by electrical voltages, the first requirement is to realize an appropriate quantum dot circuit containing just a single conduction electron.

Single-electron quantum dots have been created in self-assembled structures [30] and in small vertical pillars defined by etching [31]. Recently, realization of few-electron dots in semiconductor nanowires [32] and carbon nanotubes [33] has also been reported. The disadvantage of these types of quantum dots is that they are hard to integrate into circuits with a controllable coupling between the elements, although integration of vertical quantum dot structures is currently being pursued [34, 35]. Alternatively, we can use a system of lateral quantum dots defined in a two-dimensional electron gas (2DEG) by surface gates on top of a semiconductor heterostructure [36]. Here, integration of multiple dots is straightforward, by simply increasing the number of gate electrodes. In addition, the tunnel coupling between the dots can be tuned *in situ*, since it is controlled by the gate voltages. The challenge is to reduce the number of electrons to one per quantum dot. This has long been impossible, since reducing the electron number tends to be accompanied by a decrease in the tunnel coupling, resulting in a current too small to be measured. However, by proper design of the surface gate geometry the decrease of the tunnel coupling can be compensated for.

In 2000, Ciorga *et al.* reported measurements on the first lateral few-electron quantum dot [37]. Their device made use of two types of gates specifically designed to have different functionalities. The gates of one type were big and largely enclosed the quantum dot. The voltages on these gates determine the dot potential. The other type of gate was thin and just reached up to the barrier region. The voltage on this gate has a very small effect on the dot potential, and it can be used almost independently to set the tunnel barrier. The combination of the two gate types allows the dot potential (and thereby electron number) to be changed over a wide range while keeping the tunnel rates high enough for measuring electron transport through the dot.

Since 2001, we have fabricated and measured several few-electron single and double quantum dots, of four different designs A-D, shown in Fig. 2.10a-d. These designs share the different gate functionalities explained above. The first two types, A and B (Fig. 2.10a-b), have only been used once as few-electron *single* dots. In both cases, one of the gate electrodes was not functioning, which prevented us from testing if these devices also function as few-electron *double* dots. In design A (Fig. 2.10a), two gates coming from the top end in small circles (the 'eyes'). These gates were meant to make the dot confinement potential steeper, by applying a positive voltage to them (up to $\sim$ 0.5 V). The gates were not effective, and were left out in later designs.

In the second quantum dot design (Fig. 2.10b), the narrow 'plunger' gates approach the dot more from the sides, rather than from below, making the dots more symmetric. In this way, they are further away from the central tunnel barrier, reducing the effect they have on the tunnel rate. Also, the gate coming from the top of the picture was made thinner, in order to make the tunnel barriers more easily controllable [37]. This device was easily tunable.

In design C (Fig. 2.10c) quantum point contacts (QPCs) were added to serve as charge detectors. The QPCs were placed close to the dots, thus ensuring a good charge sensitivity. To create space for the QPCs, the plunger gates were again set as in the first design. Two devices with this gate design have functioned as a few-electron double dot, and several others as few-electron single dots.

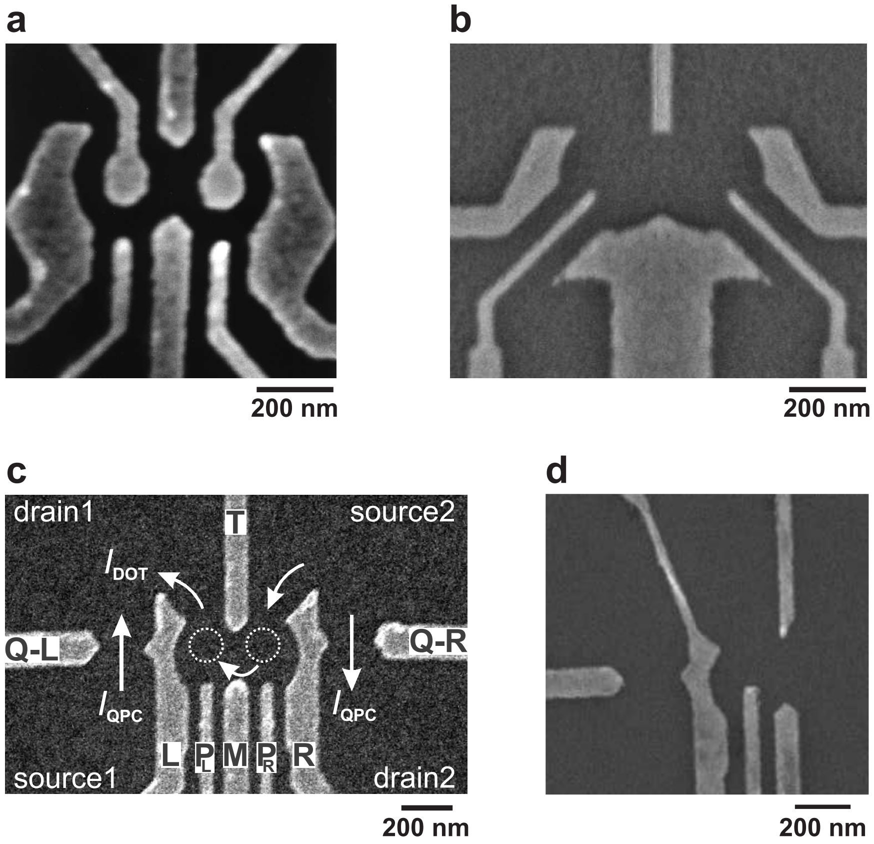

Figure 2.10: Scanning electron microscope images of few-electron quantum dot devices measured in Delft, showing the metal gate electrodes (light) on top of a GaAs/AlGaAs heterostructure (dark). **(a)** Design A. This device was used only as a few-electron *single* dot. Due to the similarity of the image to characters from the Japanese 'Gundam' animation, this has become known as the Gundam design. (The device was fabricated by Wilfred van der Wiel at NTT Basic Research Laboratories.) **(b)** Design B. This design was used only once as a few-electron *single* dot. (This device was fabricated by Wilfred van der Wiel and Ronald Hanson at NTT Basic Research Laboratories.) **(c)** Design C, with two extra side gates to form two quantum point contacts (QPCs). Devices having this design were operated many times as a single dot, and twice as a few-electron *double* dot. White dotted circles indicate the two quantum dots, white arrows show the possible current paths. A bias voltage, V_{DOT}, can be applied between source 2 and drain 1, leading to current through the dot(s), I_{DOT}. A bias voltage, V_{SD1} (V_{SD2}), between source 1 (source 2) and drain 1 (drain 2), yields a current, I_{QPC}, through the left (right) QPC. (This device was fabricated by Ronald Hanson and Laurens Willems van Beveren at NTT Basic Research Laboratories.) **(d)** Design D. In this design the lead for the QPC is separated from the dot lead by extending one of the gates. Devices of this type were operated many times as a single dot. (This device was fabricated by Wouter Naber and Laurens Willems van Beveren in DIMES in Delft.)

In design C, the QPC and the dot share one lead, which makes it inconvenient to perform transport measurements through the dot and at the same time measure the current through the QPC. To solve this problem, we have created separate leads for the dot and the QPC in design D (Fig. 2.10d) by extending the side gate all the way to the edge of the 2DEG mesa. Also, the plunger gates were extended to increase the capacitive coupling to electrons in the dot.

2.5 Device stability and bias cooling

A severe experimental difficulty that is not related to the measurement setup, but is intrinsic to the device itself, is the problem of 'charge switching': fluctuating charges in the semiconductor environment that modulate the electrostatic potential landscape in the 2DEG. Charge switching shows up in measurements as fluctuations in the position of a Coulomb peak, or as sudden jumps in the QPC-current. Changes in impurity configurations and in the charge states of electronic traps are examples of such fluctuations. These fluctuations are also referred to as 'switching noise'.

The origin of switching noise in our devices is not clear. Most likely it originates from traps in the AlGaAs donor layer that capture or release electrons during the the time of a measurement. One possible source of charge switching is the DX center [38]. The presence of DX centers in GaAs/AlGaAs heterostructures is well-known but the physical mechanisms leading to switching noise are poorly understood. In particular their large ionization energy (deep trap) makes it questionable whether DX centers contribute to switching noise at very low temperatures. Relevant or not, the presence of DX centers in the wafer can be probed by recording the electron density in the 2DEG (Shubnikov-de Haas) before and after exposing the wafer to optical light. If the electron density is modified drastically after the light exposure at 4.2 K, it means that the DX centers have released their bound electrons by the process of photo-ionization. If on the other hand the electron density in the 2DEG stays approximately the same, the amount of DX centers is expected to be minimal.

The frequency of the charge fluctuations can differ enormously. In some samples, switching occurs on a time scale of seconds, making only the most trivial measurements possible, whereas in other samples no major switching is visible on a time scale of hours. It is not clear what exactly determines the stability. It certainly depends on the heterostructure, as some wafers are clearly better than others. A number of growth parameters could be important, such as the Al concentration in the AlGaAs, the doping density and method, the thickness

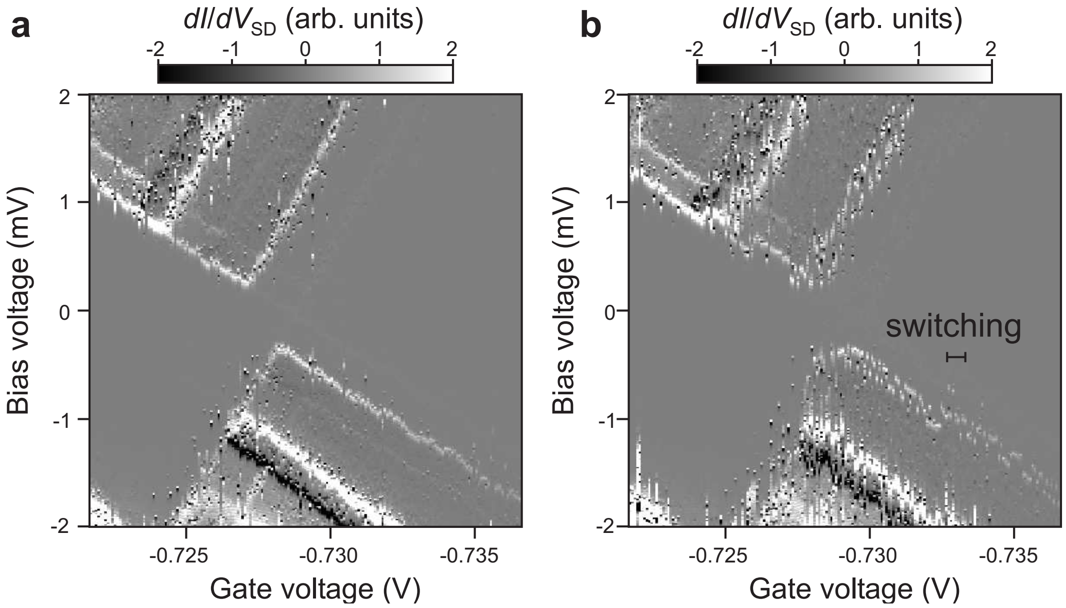

Figure 2.11: Charge switching in a large-bias measurement in the few-electron regime, for B = 12 T. **(a)** Differential conductance, dI/dV_{SD} (in grayscale), as a function of bias voltage and gate voltage. This measurement is considered reasonably stable. **(b)** Identical measurement, taken immediately after (a). A single two-level fluctuator has become active, causing the effective gate voltage to fluctuate between two values at any position in the figure, and leading to an apparent splitting of all the lines. This is considered a measurement of poor stability.

of the spacer layer between the n-AlGaAs and GaAs, the depth of the 2DEG below the surface, and many more. Recently, we have started a collaboration with the group of Prof. W. Wegscheider in Regensburg to grow and characterize heterostructures in which some of these parameters are systematically varied, hoping to gain insight in the factors that determine device stability. Noise spectra of QPC's indicate that the Al concentration in the AlGaAs layer plays an important role for the stability of the heterostructure.

Even for the same heterostructure, some devices show less charge switching than others. The reasons for this are not clear. There are reports that stability is improved if the sample is cooled down slowly, while applying a positive voltage on all gates that are going to be used in the experiment (commonly referred to as 'bias cooling'). This procedure effectively 'freezes in' a negative charge around the gates, such that less negative gate voltages are sufficient to define the quantum dot at low temperatures. Most samples described in this thesis have been cooled down from room temperature to 4.2 K slowly (in one to two days) with all gates grounded. Others have been cooled down faster, or with +280 mV on the gates.

Recently new insights were obtained for the underlying mechanisms of switching noise [39]. It was found that bias cooling with positive gate voltages reduces charge switching in a QPC. A model was proposed in which the noise originates from the leakage current of electrons tunneling through the Schottky barrier under the gate into the doped AlGaAs layer. If this hypothesis is correct, the key to reducing switching noise would be to keep the barrier opaque under experimental conditions.

As long as we can not suppress the charge fluctuations, finding a stable device will involve an element of luck: Fig. 2.11 shows two Coulomb diamonds that were measured during one night, immediately after each other, under identical conditions. The measurement in Fig. 2.11a shows reasonably stable behavior, but in Fig. 2.11b the effects of an individual two-level fluctuator are visible. This particular fluctuator remained active for a week, until the sample was warmed up.

Switching has made all experiments we performed more difficult, and has made some experiments that we wanted to perform impossible. Better control over heterostructure stability might become essential for the increasingly difficult steps towards creating quantum dot spin qubits.

Besides bias cooling, another solution for the problem of switching noise (depending on its origin) might be the realization of a thin insulating layer (tunnel barrier) between the gates and the GaAs substrate in order to suppress electron tunneling into the doping layer. The insulating layer could be formed by oxidation of a thin evaporated layer of aluminum (Al_2O_3) followed by the evaporation of a layer of gold (Au) on top. The latter is required to assure a good electrical contact between the fine gate pattern and the large gate pattern (native oxide forms on aluminum films).

2.6 Conclusions

We have presented in detail the fabrication process of lateral quantum dot devices. Several improvements to increase the device yield have been successfully implemented. First, by replacing the optical lithography steps by e-beam lithography. Second, by modifying the deposition technique for evaporation of the ohmic contacts: from electrical resistance heating to e-beam heating. Next, we have shown how QPC based charge detectors and CPS structures (next to the dot) can easily be integrated and do not require additional fabrication steps. CPS structures of normal metal Ti/Au and superconductor NbTiN have both been fabricated successfully.

Furthermore, we investigated the implementation of several types of dielectric material to fabricate devices where the shorted CPS is defined directly above the quantum dot. Here, an additional fabrication step is required to define the dielectric layer. The electrically insulating properties of calixarene look very promising for this purpose. Finally we presented gate designs of several few-electron single and double quantum dot devices with integrated QPC charge detectors and discussed the importance of bias cooling on the device stability.

We thank T. Fujisawa, T. Hayashi, T. Saku, Y. Hirayama, E. van der Drift, M. Zuiddam, A. van Run, B. Rousseeuw, M. Kroug, T. M. Klapwijk, W. Wegscheider and B. van der Enden for valuable discussions and help.

References

[1] C. Kittel, in *Introduction to solid state physics*, (John Wiley & Sons, 1996), p. 12-15.

[2] Usually the doping profile of the heterostructure is engineered such that only the lowest sub-band in the quantum well is occupied by electrons. This condition is satisfied when the Fermi level at the heterojunction is just above the energy of the first bound state.

[3] *HEMTs and HBTs: Devices, Fabrication and Circuits*, F. Ali and A. Gupta, Editors, (Artech House, Boston, 1991).

[4] The silicon (Si) donors in the AlGaAs region can be implanted either by modulation doping or δ-doping. In the first case, the Si-dopants are distributed homogeneously over the AlGaAs layer (except for the spacer layer). In the case of δ-doping, the Si-dopants are implanted in a very thin sheet (typically less than 10 nm) just before the AlGaAs spacer layer. The latter technique makes it possible to grow heterostructures with the 2DEG very close to the surface. At the same time it allows for enhanced electron mobility of the 2DEG as scattering in the donor layer is reduced.

[5] M. Stopa, Phys. Rev. B **54**, 13767 (1996).

[6] Parallel conduction channels can be found by performing longitudinal magnetoresistance measurements at 4.2 K. One signature is a term proportional to B^2 in the Hall effect at small fields; another is that the minima in the Shubnikov-de Haas effect do not fall to zero at large fields. In our experiments we have used heterostructures which do not have parallel conduction channels.

[7] *Handbook of Microlithography, Micromachining and Microfabrication*, P. Rai-Choudhury, Editor, (SPIE Press, Bellingham - Washington, 1997). Detailed information can be found on-line at this url: http://www.cnf.cornell.edu/cnf_spietoc.html.

[8] R. E. Howard and D. E. Prober, in *VLSI Electronics: Microstructure Science*, edited by N. G. Einspruch (Academic, New York, 1982), Vol. 5, p. 146.

[9] In a positive-tone resist, also called a positive resist, the material in the irradiated area is removed, which results in an image with a pattern identical with that on the mask. In a negative-tone resist, also called a negative resist, the non-irradiated area is removed, which results in an image that is the reverse of that on the mask.

[10] R. E. Howard *et al.*, IEEE Trans. Electron. Dev. ED **28** 1378 (1981).

[11] P. A. Peterson *et al.*, J. Vac. Sci. Technol. B **10**, 3088 (1992).

[12] A. G. Baca *et al.*, Thin Solid Films **308-309**, 599 (1997).

[13] S. Yasin *et al.*, Microelectronic Engineering **61-62**, 745 (2002).

[14] See, for details, D. M. Manos and D. L. Flamm, in *Plasma Etching-An Introduction*, (New York: Academic, 1989).

[15] Near the end of the coplanar stripline, the gap between the two metallic strips becomes very small and the proximity effect can easily interfere with the lithography process. At first, the step size (resolution) and spot diameter of the e-beam were reduced in order to suppress the proximity effect. However, since this makes the writing time very long as well, the copolymer was replaced by a less sensitive resist: 350PMMA (7%) or the even better OEBR-1000 (200 cp) which has a molecular weight of about 600k.

[16] J. A. Thornton and A. S. Penfold, in *Thin film processes*, edited by J. L. Vossen, (Academic Press, New York, 1978).

[17] The skin effect is a phenomenon which occurs when high frequency currents are sent through a conducting medium. Beyond a specific frequency the current density becomes non-uniform such that all the current flows through a thin sheet at the edges of the conductor. Alternatively, for a fixed frequency, the skin depth determines whether the conductor is affected by the skin effect or not. The skin depth can be calculated by the formula $\delta = \frac{1}{\sqrt{\pi\mu\sigma f}}$, where μ is the permeability, σ the conductivity and f is the frequency. Associated to this skin depth is the sheet or surface resistance for a normal metal $R_s = \frac{1}{\delta\sigma} = \sqrt{\frac{\pi\mu f}{\sigma}}$ and for a superconductor $R_s = \frac{2}{\delta\sigma_n}(\frac{\lambda}{\delta})^3 = 2\sigma_n(\pi\mu f)^2\lambda^3$, valid

when $\lambda \ll \delta$ (λ is the London penetration depth), as in T. P. Orlando and K. A. Delin, in *Foundations of applied Superconductivity*, (Addison-Wesley Publishing Company, 1991).

[18] B. D. Jackson *et al.*, Appl. Phys. Lett. **79**, 436 (2001).

[19] The ideal DC properties of superconductors are governed by the flow of lossless supercurrent within an equilibrium state of the system. However, the response of a superconductor to a high-frequency current results in a finite amount of dissipation. At any nonzero frequency the conductivity has a real part (resistance) and an imaginary part (capacitive and/or inductive), related to the density of normal and superconducting electrons, respectively. See R. L. Kautz, J. Appl. Phys. **49**, 309 (1978); Page 69 of M. Tinkham, in *Introduction to Superconductivity*, (McGraw Hill, 1975).

[20] M. Cyrot and D. Pavuna *Introduction to superconductivity and high-T_c materials*, (World Scientific, 1992).

[21] Actually, above H_{c2} and up to $H_{c3} = 1.69 H_{c2}$, a superconducting sheath persists on surfaces parallel to the applied field. This phenomenon is called 'surface superconductivity'.

[22] Microwave Studio is a high frequency 3D electromagnetic field simulator. A frequency domain solver in combination with a finite element method calculates electric and magnetic fields around lumped elements in the far and near-field, including conductor surface losses and skin effect.

[23] The magnetic field amplitude at a point a distance r from an infinitely long wire carrying a current I can be derived easily from the Biot-Savart law and has a magnitude $B = \mu_0 I/2\pi r$ and its direction is given by the right-hand rule: point the thumb of your right hand in the direction of the current, and your fingers indicate the direction of the circular magnetic field lines around the wire.

[24] H. Namatsu *et al.*, J. Vac. Sci. Technol. B **16**, 69 (1998).

[25] The chemical name of the calixarene used is 4-methyl-1-acetoxycalix(6)arene and was ordered at TCI America, U.S. subsidiary of Tokyo Kasei Kogyo. See http://www.tciamerica.com/.

[26] J. Fujita *et al.*, Appl. Phys. Lett. **68**, 1297 (1996).

[27] A new high resolution, high sensitive calixarene resist, referred to as CMC4, was recently developed recently by Tokuyama and NEC together. This resist allowed the fabrication of a 5-nm-gate world-smallest transistor operating at

room temperature. See M. Ishida *et al.*, Jpn. J. Appl. Phys. **42**, 3913 (2003); H. Sailer *et al.*, J. Vac. Sci. Technol. B **22**, 3485 (2004).

[28] To fix the device to the sample plate, two component (1:1) silver filled epoxy H20E from Epo-Tek is used. The glue is especially designed for wire bonding, has a short curing cycle (15 minutes at 120°C) and a high electrical conductivity. To fix the sample plate on the sample holder we rather use the electrically insulating two component glue High Super 5 from Cemedine, which has the nice property to soften again upon heating. This allows us to replace sample holders if needed without affecting the bond wire connections.

[29] D. Loss and D. P. DiVincenzo, Phys. Rev. A **57**, 120 (1998).

[30] P. M. Petroff, A. Lorke, and A. Imamoglu, Phys. Today, **46**, (2001).

[31] L. P. Kouwenhoven, D. G. Austing and S. Tarucha, Rep. Prog. Phys. **64** (6), 701 (2001).

[32] M. T. Bjork *et al.*, Nano Lett. **4** (9), 1621 (2004).

[33] P. Jarillo-Herrero *et al.*, Nature **429**, 389 (2004).

[34] K. Ono *et al.*, Science **297**, 1313 (2002).

[35] T. Hatano *et al.*, Phys. Rev. Lett. **93**, 066806 (2004).

[36] L. P. Kouwenhoven *et al.*, in *Mesoscopic Electron Transport*, edited by L. L. Sohn, L. P. Kouwenhoven and G. Schön, NATO Advanced Study Institutes, Ser. E, Vol. **345** (Kluwer, Dordrecht, Boston, 1997), pp. 105-214.

[37] M. Ciorga *et al.*, Phys. Rev. B **61**, R16315 (2000).

[38] J. H. Davies, *The physics of low-dimensional semiconductors*, (Cambridge University Press, Cambridge, 1998).

[39] M. Pioro-Ladrière *et al.*, cond-mat/0503602v2.

Chapter 3

Theory and measurement techniques

3.1 Quantum dots

A quantum dot is simply a small box that can be filled with electrons. The box is coupled via tunnel barriers to a source and drain reservoir, with which particles can be exchanged (see Fig. 3.1). By attaching current and voltage probes to these reservoirs, we can measure the electronic properties of the dot. The dot is also coupled capacitively to one or more 'gate' electrodes, which can be used to tune the electrostatic potential of the dot with respect to the reservoirs. When the size of the dot is comparable to the wavelength of the electrons that occupy it, the system exhibits a discrete energy spectrum, resembling that of an atom. As a result, quantum dots behave in many ways as *artificial atoms* [1].

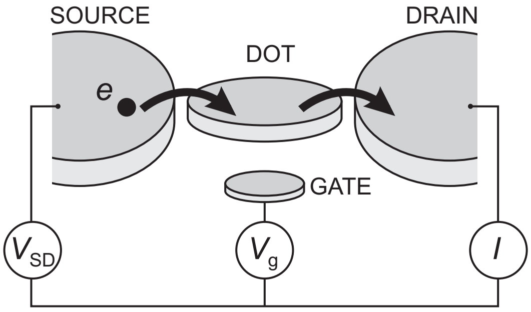

Figure 3.1: Schematic picture of a quantum dot in a lateral geometry. The quantum dot (represented by a disk) is connected to source and drain contacts via tunnel barriers, allowing the current through the device, I, to be measured in response to a bias voltage, V_{SD} and a gate voltage, V_g.

Parts of this chapter has been published in Physical Review B **67**, 161308 (2003).

Because a quantum dot is such a general kind of system, there exist quantum dots of many different sizes and materials: for instance single molecules trapped between electrodes, metallic or superconducting nanoparticles, self-assembled quantum dots, semiconductor lateral or vertical dots, and also semiconducting nanowires or carbon nanotubes between closely spaced electrodes. In this thesis, we focus on lateral (gated) semiconductor quantum dots [2]. These lateral devices allow all relevant parameters to be controlled *in situ*.

In this thesis, two different ways are used to probe the behavior of electrons on a quantum dot. We can measure the current due to transport of electrons through the dot, and we can use an electrometer to detect changes in the number of electrons on the dot. These experiments are conveniently understood using the constant interaction (CI) model [2].

3.1.1 Constant Interaction model

The CI model makes two important assumptions. First, the Coulomb interactions among electrons in the dot, and between electrons in the dot and those in the environment, are parameterized by a single, constant capacitance, C. This capacitance can be thought of as the sum of the capacitances between the dot and the source, C_S, the drain, C_D, and the gate, C_g: $C = C_S + C_D + C_g$. Second, the discrete energy spectrum can be described independently of the number of electrons on the dot. Under these assumptions the total energy of a N-electron dot in the ground state with the source-drain voltage, V_{SD}, applied to the source (and the drain grounded), is given by

$$U(N) = \frac{[-|e|(N - N_0) + C_S V_{SD} + C_g V_g]^2}{2C} + \sum_{n=1}^{N} E_n(B) \tag{3.1}$$

where $-|e|$ is the electron charge and N_0 the number of electrons in the dot at zero gate voltage, which compensates the positive background charge originating from the donors in the heterostructure. The terms $C_S V_{SD}$ and $C_g V_g$ can change continuously and represent the charge on the dot that is induced by the bias voltage (through the capacitance C_S) and by the gate voltage V_g (through the capacitance C_g), respectively. The last term of Eq. 3.1 is a sum over the occupied single-particle energy levels $E_n(B)$, which are separated by an energy $\Delta E_n = E_n - E_{n-1}$. These energy levels depend on the characteristics of the confinement potential. Note that, within the CI model, only these single-particle states depend on magnetic field, B.

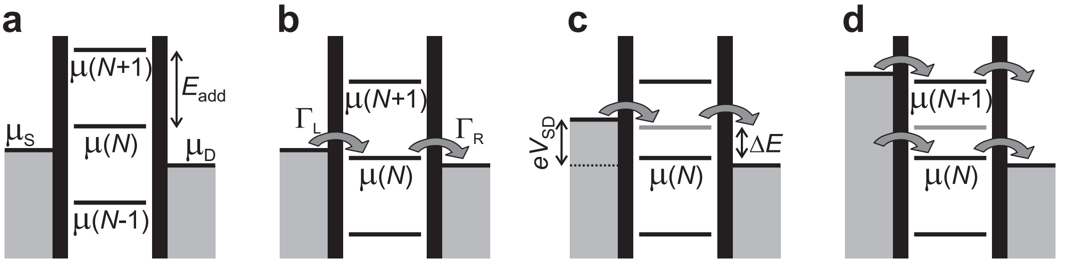

Figure 3.2: Schematic diagrams of the electrochemical potential of the quantum dot for different electron numbers. **(a)** No level falls within the bias window between μ_S and μ_D, so the electron number is fixed at $N-1$ due to Coulomb blockade. **(b)** The $\mu(N)$ level is aligned, so the number of electrons can alternate between N and $N-1$, resulting in a single-electron tunneling current. The magnitude of the current depends on the tunnel rate between the dot and the reservoir on the left, Γ_L, and on the right, Γ_R. **(c)** Both the ground-state transition between $N-1$ and N electrons (black line), as well as the transition to an N-electron excited state (gray line) fall within the bias window and can thus be used for transport (though not at the same time, due to Coulomb blockade). This results in a current that is different from the situation in (b). **(d)** The bias window is so large that the number of electrons can alternate between $N-1$, N and $N+1$, i.e. two electrons can tunnel onto the dot at the same time.

To describe transport experiments, it is often more convenient to use the electrochemical potential. The electrochemical potential of the dot is by definition the energy required for adding the Nth electron to the dot:

$$\begin{aligned}\mu(N) &\equiv U(N) - U(N-1) = \\ &= (N - N_0 - \frac{1}{2})E_C - \frac{E_C}{|e|}(C_S V_{SD} + C_g V_g) + E_N \end{aligned} \tag{3.2}$$

where $E_C = e^2/C$ is the charging energy. This expression denotes the transition between the N-electron ground state and $N-1$-electron ground state. To avoid confusion when also excited states play a role, we will sometimes use a more explicit notation: the electrochemical potential for the transition between the $N-1$-electron state $|a\rangle$ and the N-electron state $|b\rangle$ is then denoted as $\mu_{a\leftrightarrow b}$, and is defined as $U_b - U_a$.

The electrochemical potential for the transitions between ground states with a different electron number N is shown in Fig. 3.2a. The discrete levels are spaced by the so-called addition energy:

$$E_{add}(N) = \mu(N+1) - \mu(N) = E_C + \Delta E. \tag{3.3}$$

The addition energy consists of a purely electrostatic part, the charging energy E_C, plus the energy spacing between two discrete quantum levels, ΔE. Note that ΔE can be zero, when two consecutive electrons are added to the same spin-degenerate level.

Of course, for transport to occur, energy conservation needs to be satisfied. This is the case when an electrochemical potential level falls within the 'bias window' between the electrochemical potential (Fermi energy) of the source (μ_S) and the drain (μ_D), i.e. $\mu_S \geq \mu \geq \mu_D$ with $-|e|V_{SD} = \mu_S - \mu_D$. Only then can an electron tunnel from the source onto the dot, and then tunnel off to the drain without losing or gaining energy. The important point to realize is that since the dot is very small, it has a very small capacitance and therefore a large charging energy – for typical dots $E_C \approx$ a few meV. If the electrochemical potential levels are as shown in Fig. 3.2a, this energy is not available (at low temperatures and small bias voltage). So, the number of electrons on the dot remains fixed and no current flows through the dot. This is known as Coulomb blockade.

The Coulomb blockade can be lifted by changing the voltage applied to the gate electrode. This changes the electrostatic potential of the dot with respect to that of the reservoirs, shifting the whole 'ladder' of electrochemical potential levels up or down. When a level falls within the bias window, the current through the device is switched on. In Fig. 3.2b $\mu(N)$ is aligned, so the electron number alternates between $N-1$ and N. This means that the Nth electron can tunnel onto the dot from the source, but only after it tunnels off to the drain can another electron come onto the dot again from the source. This cycle is known as single-electron tunneling.

By sweeping the gate voltage and measuring the current, we obtain a trace as shown in Fig. 3.3a. At the positions of the peaks, an electrochemical potential level is aligned with the source and drain and a single-electron tunneling current flows. In the valleys between the peaks, the number of electrons on the dot is fixed due to Coulomb blockade. By tuning the gate voltage from one valley to the next one, the number of electrons on the dot can be precisely controlled. The distance between the peaks corresponds to $E_C + \Delta E$, and can therefore give information about the energy spectrum of the dot.

A second way to lift Coulomb blockade is by changing the source-drain voltage, V_{SD} (see Fig. 3.2c). In general, we change the electrochemical potential of only one of the reservoirs, and keeping the other one fixed. This increases the bias window and also 'drags' the electrochemical potential of the dot along, due to the capacitive coupling to the source. Again, a current can flow only when an electrochemical potential level falls within the bias window. When V_{SD} is increased so much that both the ground state as well as an excited state transition fall within the bias window, there are two paths available for electrons tunneling through the dot. In general, this will lead to a change in the current, enabling us to perform energy spectroscopy of the excited states. How exactly the current changes depends on the tunnel rates of the two paths [3].

Usually, we measure the current or differential conductance (the derivative of the current with respect to the source-drain bias) while sweeping the bias voltage, for a series of different values of the gate voltage. Such a measurement is shown schematically in Fig. 3.3b. Inside the diamond-shaped region, the number of electrons is fixed due to Coulomb blockade, and no current flows. Outside the diamonds, Coulomb blockade is lifted and single-electron tunneling can take place (or for larger bias voltages even double-electron tunneling is possible, see Fig. 3.2d). Excited states are revealed as changes in the current, i.e. as peaks or dips in the differential conductance. From such a 'Coulomb diamond' the energy of excited states as well as the charging energy can be read off directly.

The simple model described above explains successfully how quantization of charge and energy leads to effects like Coulomb blockade and Coulomb oscillations. Nevertheless, it is too simplified in many respects. For instance, the model considers only first-order tunneling processes, in which an electron tunnels first from one reservoir onto the dot, and then from the dot to the other reservoir. But when the tunnel rate between the dot and the leads, Γ, is increased, higher-order tunneling via virtual intermediate states becomes important. Such processes are known as 'cotunneling'. Furthermore, the simple model does not take into account the spin of the electrons, thereby excluding for instance exchange effects.

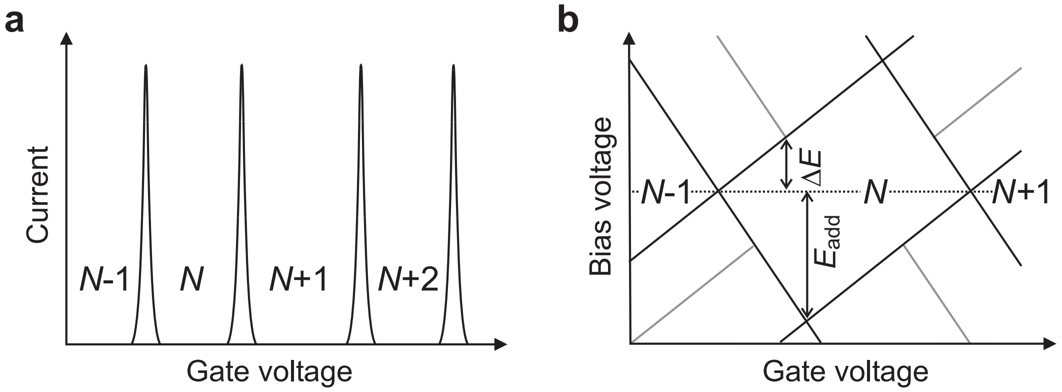

Figure 3.3: Transport through a quantum dot. **(a)** Coulomb peaks in current versus gate voltage in the linear-response regime. **(b)** Coulomb diamonds in differential conductance, dI/dV_{SD}, versus V_{SD} and V_g, up to large bias. The edges of the diamond-shaped regions (black) correspond to the onset of current. Diagonal lines emanating from the diamonds (gray) indicate the onset of transport through excited states.

3.1.2 Spin configurations in few-electron quantum dots

The fact that electrons carry spin determines the electronic states of the quantum dot, in quite the same way as it does in real atoms. In fact, a group of physicists that pioneered measurements on few-electron (vertical) dots, have established a periodic system of elements in two dimensions [1]. In the simplest case – a dot containing just a single electron (artificial Hydrogen)– spin leads to a splitting of all orbitals into Zeeman doublets, with the ground state corresponding to the electron spin pointing up (↑), i.e. parallel to the magnetic field, and the excited state to the spin pointing down (↓), i.e. antiparallel to the magnetic field. The difference between the corresponding energy levels $E_\uparrow$ and $E_\downarrow$ is given by the Zeeman energy, $\Delta E_Z = g\mu_B B$, which is approximately 25 μeV/T in GaAs.

For two electrons in a quantum dot (artificial Helium), the situation is more complicated. For a Hamiltonian without spin-orbit coupling terms (which is true to a good approximation for our system), the two-electron state is the product of the orbital and spin state. Since electrons are fermions, the total two-electron state has to be anti-symmetric under exchange of the two particles. Therefore, if the orbital part is symmetric, the spin state must be anti-symmetric, and if the spin part is anti-symmetric, the orbital state must be symmetric. The anti-symmetric two-spin state is the spin singlet $|S\rangle$:

$$|S\rangle = \frac{|\uparrow\downarrow\rangle - |\downarrow\uparrow\rangle}{\sqrt{2}} \tag{3.4}$$

which has total spin $S = 0$. The symmetric two-spin states are the so-called spin triplets ($|T_+\rangle$, $|T_0\rangle$ and $|T_-\rangle$):

$$|T_+\rangle = |\uparrow\uparrow\rangle \qquad |T_0\rangle = \frac{|\uparrow\downarrow\rangle + |\downarrow\uparrow\rangle}{\sqrt{2}} \qquad |T_-\rangle = |\downarrow\downarrow\rangle \tag{3.5}$$

which have total spin $S = 1$ and a quantum number m_s (corresponding to the spin z-component) of 1, 0, and -1, respectively. In a finite magnetic field, the three triplet states are split by the Zeeman splitting, ΔE_Z.

Even at zero magnetic field, the energy of the two-electron system depends on its spin configuration, through the requirement of anti-symmetry of the total state. If we consider just the two lowest orbitals, ε_0 and ε_1, then there are six possibilities to fill these with two electrons (Fig. 3.4). At zero magnetic field [4], the two-electron ground state is always the spin singlet with both electrons on the lowest orbital (Fig. 3.4a), and the lowest excited states are then the three spin triplets (Fig. 3.4b–d). The energy gain of T_0 with respect to the excited spin singlet S_1 (Fig. 3.4e) is known as the exchange energy. It essentially results from the fact that electrons in the triplet states tend to avoid each other, reducing

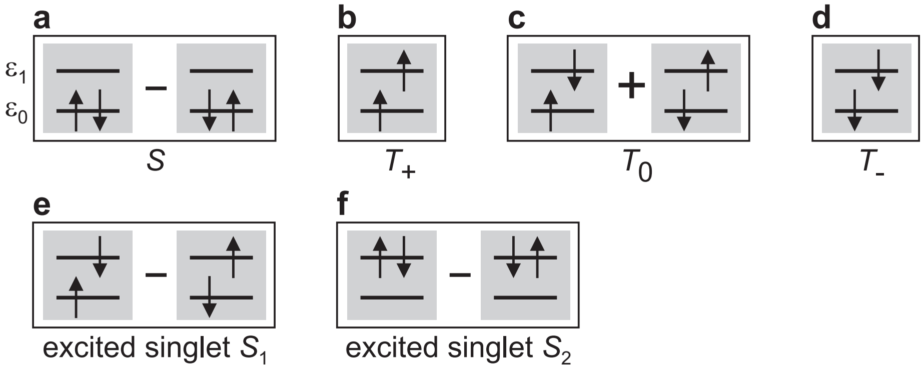

Figure 3.4: Schematic energy diagrams depicting the spin states of two electrons occupying two spin degenerate single-particle levels (ε_0 and ε_1). **(a)** Spin singlet, which is the ground state at zero magnetic field. **(b)–(d)** Lowest three spin triplet states, $|T_+\rangle$, $|T_0\rangle$ and $|T_-\rangle$, which have total spin $S = 1$ and quantum number $m_s = +1$, 0 and -1, respectively. In finite magnetic field, the triplet states are split by the Zeeman energy. **(e)** Excited spin singlet state, S_1. The energy difference between S_1 and the triplet state T_0 is the exchange energy. **(f)** Highest excited spin singlet state, S_2.

their mutual Coulomb energy. As the Coulomb interaction is very strong, the exchange energy can be quite large (a few 100 μeV) [5].

In the presence of a magnetic field, the energies of the lowest singlet and triplet states (Fig. 3.4a–d) can be expressed as (choosing the zero of energy conveniently, $\mu_{0\leftrightarrow\uparrow}=E_\uparrow$ and $\mu_{0\leftrightarrow\downarrow}=E_\downarrow=E_\uparrow+\Delta E_Z$, as in [6]):

$$\begin{aligned}
E_S &= E_\uparrow + E_\downarrow + E_C = 2E_\uparrow + \Delta E_Z + E_C \\
E_{T_+} &= 2E_\uparrow + E_{ST} + E_C \\
E_{T_0} &= E_\uparrow + E_\downarrow + E_{ST} + E_C = 2E_\uparrow + E_{ST} + \Delta E_Z + E_C \\
E_{T_-} &= 2E_\downarrow + E_{ST} + E_C = 2E_\uparrow + E_{ST} + 2\Delta E_Z + E_C.
\end{aligned}$$

Figure 3.5a shows the possible transitions between the one-electron spin-split orbital ground state and the two-electron states. We have omitted the transitions $\uparrow\leftrightarrow T_-$ and $\downarrow\leftrightarrow T_+$ since these require a change in the spin z-component of more than 1/2 and are thus spin-blocked [7]. From the energy diagram we can deduce the electrochemical potential ladder, which is shown in Fig. 3.5b. Note that $\mu_{\uparrow\leftrightarrow T_+} = \mu_{\downarrow\leftrightarrow T_0}$ and $\mu_{\uparrow\leftrightarrow T_0} = \mu_{\downarrow\leftrightarrow T_-}$. Consequently, the *three* triplet states lead to only *two* resonances in first order transport through the dot.

For more than two electrons, the spin states can be much more complicated (see chapter 4). However, in some cases and for certain magnetic field regimes they might be well approximated by a one-electron Zeeman doublet (when N is odd) or by two-electron singlet or triplet states (when N is even). But there are

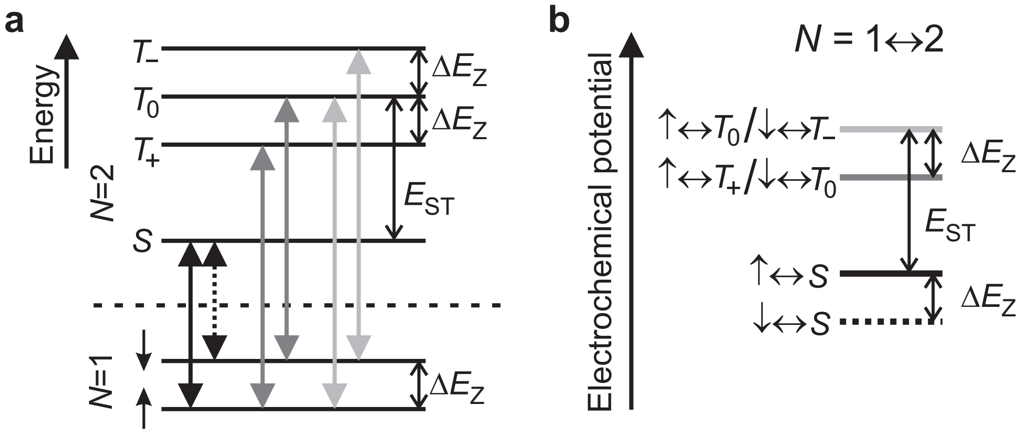

Figure 3.5: One- and two-electron states and transitions at finite magnetic field. **(a)** Energy diagram for a fixed gate voltage. By changing the gate voltage, the one-electron states (below the dashed line) shift up or down relative to the two-electron states (above the dashed line). The six transitions that are allowed (i.e. not spin-blocked) are indicated by vertical arrows. **(b)** Electrochemical potentials for the transitions between one- and two-electron states. The six transitions in (a) correspond to only four different electrochemical potentials. By changing the gate voltage, the whole ladder of levels is shifted up or down.

still differences – for instance, if $N > 2$ the ground state at zero field can be a spin triplet, due to Hund's rule [8].

The eigenstates of a two-electron double dot (artificial Hydrogen molecule) are also spin singlets and triplets. We can again use the diagrams in Fig. 3.4, but now the single-particle eigenstates ε_0 and ε_1 represent the symmetric and anti-symmetric combination of the lowest orbital on each of the two dots, respectively. Due to tunneling between the dots, with tunneling matrix element t, ε_0 (the 'bonding state') and ε_1 (the 'anti-bonding state') are split by an energy $2t$. By filling the two states with two electrons, we again get a spin singlet ground state and a triplet first excited state (at zero field). However, the singlet ground state is not purely S (Fig. 3.4a), but also contains a small admixture of the excited singlet S_2 (Fig. 3.4f). The admixture of S_2 depends on the competition between inter-dot tunneling and the Coulomb repulsion, and serves to lower the Coulomb energy by reducing the double occupancy of the dots [9].

If we focus only on the singlet ground state and the triplet first excited states, then we can describe the two spins $\vec{S_1}$ and $\vec{S_2}$ by the Heisenberg Hamiltonian, $H = J\vec{S_1}\cdot\vec{S_2}$. Due to this mapping procedure, J is now defined as the energy difference between the triplet state T_0 and the singlet ground state, which depends on the details of the double dot orbital states. From a Hund-Mulliken calculation [10],

J is approximately given by $4t^2/U + V$, where U is the on-site charging energy and V includes the effect of the long-range Coulomb interaction. By changing the overlap of the wave functions of the two electrons, we can change t and therefore J. Thus, control of the inter-dot tunnel barrier would allow us to perform operations such as swapping or entangling two spins.

We finally remark on the orbital part of the electron wave function in the dot. The confinement potential of semiconductor quantum dots is to a good approximation a parabolic well. Indeed, experiments on vertical dots have shown excellent agreement between the orbital wave functions in the dots and the single-particle Fock-Darwin states [1]. The Fock-Darwin states can therefore be very helpful in explaining effects that arise from the spatial form of the electron wave function in the dot (e.g. the fact that different orbitals can have a very different tunnel coupling to the reservoir).

3.2 Measurement setup

Dilution refrigerator

To resolve small energies such as the Zeeman splitting, the sample has to be cooled down to temperatures well below a Kelvin. We use an Oxford Kelvinox 300 dilution refrigerator, which has a base temperature of about 10 mK, and a cooling power in excess of 300 μW (at 100 mK). The sample holder is connected to a cold finger and placed in a copper can (36 mm inner diameter) in the bore of a superconducting magnet that can apply a magnetic field up to 16 T.

Measurement electronics

A typical measurement involves applying a source-drain voltage over (a part of) the device, and measuring the resulting current as a function of the voltages applied to the gates. The electrical circuits for the voltage-biased current measurement and for applying the gate voltages are shown in Fig. 3.6 and Fig. 3.7, respectively. The most important parts of the measurement electronics – i.e. the current-to-voltage (I-V) converter, isolation amplifier, voltage source and digital-to-analog convertors (DACs) – were all built by Raymond Schouten at Delft University. The underlying principle of the setup is to isolate the sample electrically from the measurement electronics. This is achieved via optical isolation at both sides of the measurement chain, i.e. in the voltage source, the isolation amplifier, as well as the DACs. In all these units, the electrical signal passes through analog optocouplers, which first convert it to an optical signal using an LED, and then convert the optical signal back using a photodiode. In

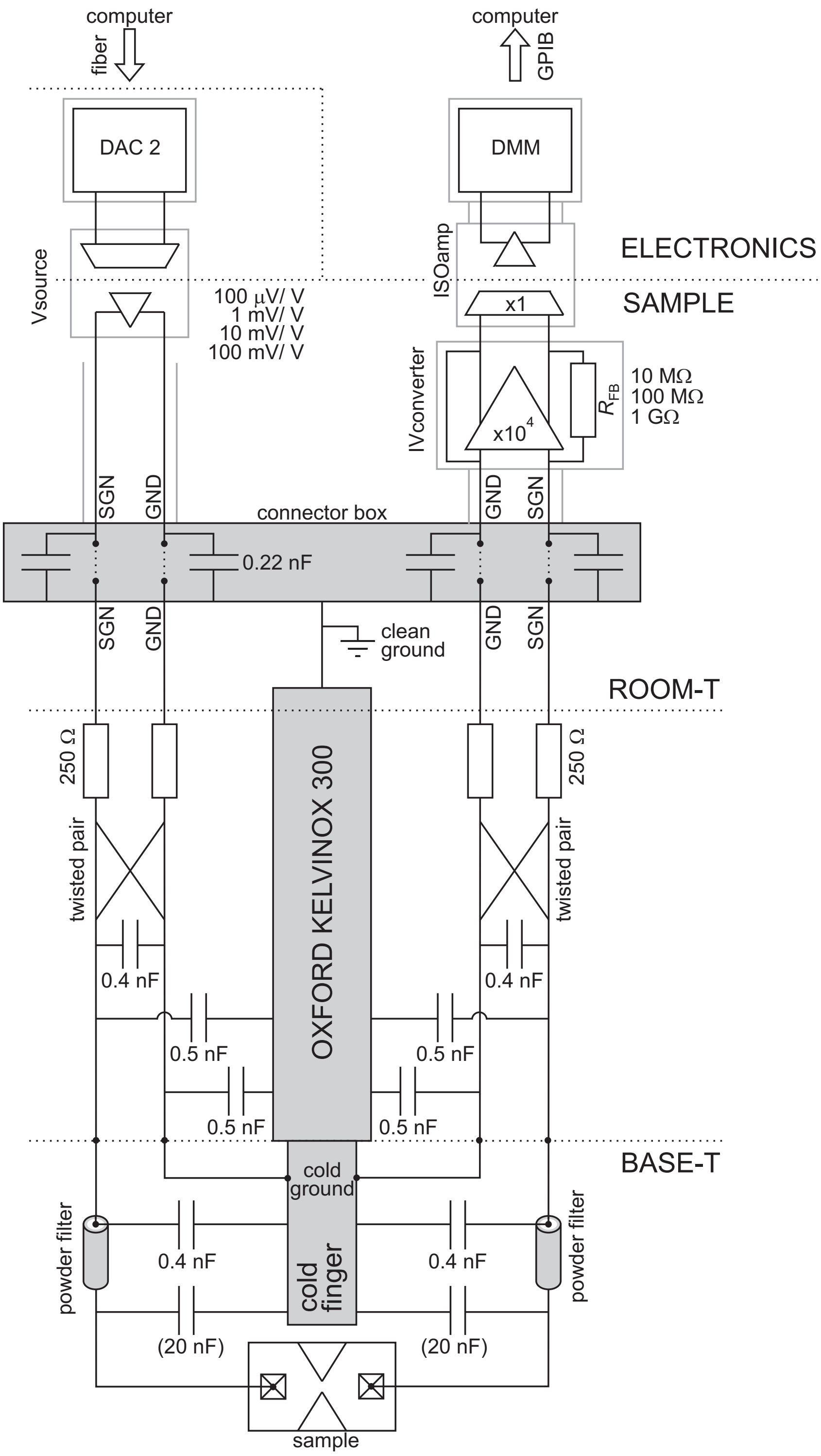
computer
fiber
computer
GPIB
DAC 2
DMM
ELECTRONICS
SAMPLE
Vsource
ISOamp
x1
100 µV/ V
1 mV/ V
10 mV/ V
100 mV/ V
IVconverter
x10^4
R_FB
10 MΩ
100 MΩ
1 GΩ
SGN
GND
GND
SGN
connector box
0.22 nF
SGN
GND
GND
SGN
clean ground
ROOM-T
OXFORD KELVINOX 300
250 Ω
250 Ω
twisted pair
twisted pair
0.4 nF
0.4 nF
0.5 nF
0.5 nF
0.5 nF
0.5 nF
BASE-T
cold ground
powder filter
powder filter
0.4 nF
0.4 nF
cold finger
(20 nF)
(20 nF)
sample

Figure 3.6: Electrical circuit for performing a voltage-biased current measurement. Elements shown in gray are connected to ground. Gray lines indicate the shielding of the measurement electronics and wires.

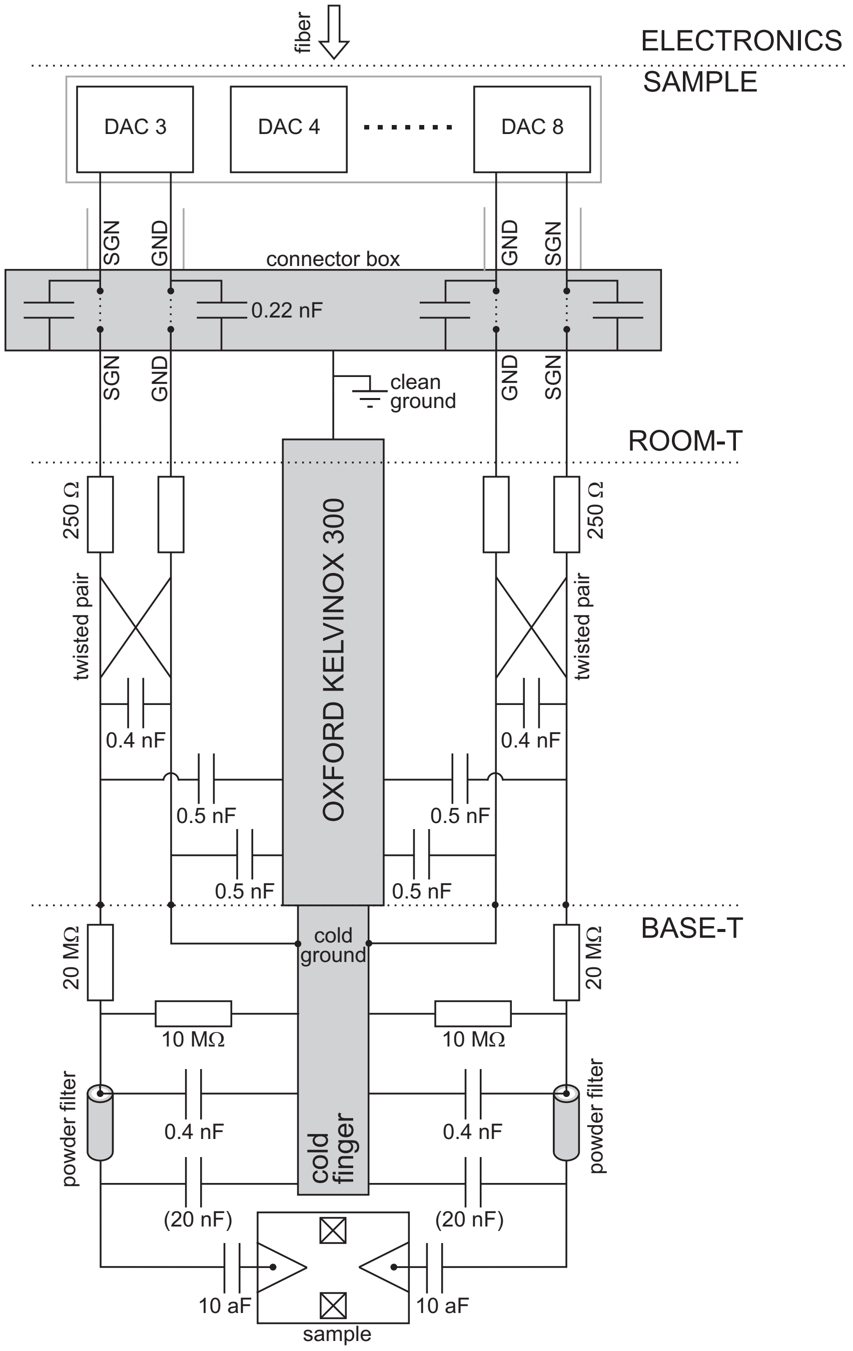
fiber
ELECTRONICS
SAMPLE
DAC 3
DAC 4
DAC 8
SGN
GND
GND
SGN
connector box
0.22 nF
SGN
GND
GND
SGN
clean
ground
ROOM-T
250 Ω
250 Ω
OXFORD KELVINOX 300
twisted pair
twisted pair
0.4 nF
0.4 nF
0.5 nF
0.5 nF
0.5 nF
0.5 nF
BASE-T
20 MΩ
cold
ground
20 MΩ
10 MΩ
10 MΩ
powder filter
0.4 nF
0.4 nF
cold
finger
powder filter
(20 nF)
(20 nF)
10 aF
10 aF
sample

Figure 3.7: Electrical circuit for applying DC voltages to the gate electrodes. Elements shown in gray are connected to ground. Gray lines indicate the shielding of the measurement electronics and wires.

this way, there is no galvanic connection between the two sides. In addition, all circuitry at the sample side is analog (even the DACs have no clock circuits or microprocessors), battery-powered, and uses a single clean ground (connected to the metal parts of the fridge) which is separated from the ground used by the 'dirty' electronics. All these features help to eliminate ground loops and reduce interference on the measurement signal.

Measurements are controlled by a computer running LabView. It sends commands via a fiber link to two DAC-boxes, each containing 8 digital-to-analog convertors, and powered by a specially shielded transformer. Most of the DACs are used to generate the voltages applied to the gate electrodes (typically between 0 and -5 V). One of the DACs controls the source-drain voltage for the device. The output voltage of this DAC (typically between +5 and -5V) is sent to a voltage source, which attenuates the signal by a factor 10, 10^2, 10^3 or 10^4 and provides optical isolation. The attenuated voltage is then applied to one of the ohmic contacts connected to the source reservoir of the device.

The resulting current coming from the drain reservoir is fed to a low-noise I-V converter. In this thesis we use two types, depending on the desired bandwidth. The first one (used in chapters 4, 5, sections 3.3 and 3.4, is designed for low-frequency measurements. It has a bandwidth of about 1 kHz, and a noise floor of $\sim$ 5 fA/Hz$^{1/2}$. The feedback resistance can be set to 10 MΩ, 100 MΩ or 1GΩ, with an input resistance that is a factor 10^3 or 10^4 smaller (for the 'low noise' or 'low input resistance' setting, respectively). The faster I-V converter, used in section 3.5, chapter 6, 7 and 8 has a bandwidth of about 150 kHz, and a current noise of $\sim$ 1 pA/Hz$^{1/2}$ at 100 kHz. The feedback resistance is 10 MΩ, corresponding to an input resistance of 1.3 kΩ.

The signal from the I-V converter is then sent to an isolation amplifier, to provide optical isolation and possibly gain. Again we can choose a low-frequency version (up to $\sim$ 1 kHz) or a high-frequency one (up to $\sim$ 300 kHz). The voltage from the isolation amplifier is finally measured by a digital multimeter (Keithley 2700) and sent to the computer via GPIB interface. Alternatively, we can use a lock-in amplifier (Stanford EG&G 5210) if the signal to be measured is periodic, or an ADwin Gold module for very fast measurements (up to 2.2×10^6 14-bit samples per second).

Measurement wires

To make contact to the sample, 2×12 twisted pairs of wires run from two connector boxes at room temperature all the way down to the 'cold finger' at base temperature. The diameter and material of these wires is chosen to minimize the heat load on the mixing chamber. From room temperature to 1 Kelvin, 2×9 pairs consist of manganine wires (100 μm diameter), and 2×3 pairs of copper wires (90 μm diameter). From 1 Kelvin to the mixing chamber, superconducting 'Niomax' wires (50 μm diameter) are used. From the mixing chamber to the bottom of the cold finger, where thermal conductivity is no longer a constraint, we have standard copper wires. At base temperature, one wire of each twisted pair is connected to 'cold ground' (i.e. the cold finger), which is electrically connected to clean ground via the metal parts of the fridge.

All wires are thermally anchored to the fridge, by carefully wrapping them around copper posts, at several temperature stages (4 K, 1 K, $\sim$ 100 mK and $\sim$ 10 mK). At room temperature, the resistance of the wires is about 250 Ω or 150 Ω for the manganine or copper wires, respectively. At low temperature it is about 50 Ω. The wires have various parasitic capacitances to their twisted partner and to ground, as indicated in Fig. 3.6 and Fig. 3.7.

Filtering

The wires connect the device to the measurement electronics at room temperature, so they have to be carefully filtered to avoid that the electrons in the sample heat up due to spurious noise and interference. Several filtering stages are required for different frequency ranges (see Fig. 3.6 and Fig. 3.7). In the connector box at room temperature, all wires are connected to ground via 0.22 nF 'feedthrough capacitors'. At base temperature, all signal wires run through 'copper powder filters' [11]. These are copper tubes filled with copper powder, in which 4 signal wires with a length of about 2 meters each are wound. The powder absorbs the high-frequency noise very effectively, leading to an attenuation of more than -60 dB from a few 100 MHz up to more than 50 GHz [12].

To remove the remaining low-frequency noise, we solder a 20 nF capacitor between each signal wire and the cold finger ground. In combination with the $\sim$ 100 Ω resistance of the wires, this forms a low-pass RC filter with a cut-off frequency of about 100 kHz (even 10 kHz for the wire connected to the I-V converter, due to its input resistance of about 1.3 kΩ). These filters are used for the wires connecting to ohmic contacts (although they were taken out to perform some of the high-bandwidth measurements described in this thesis). For the wires connecting to gate electrodes, a 1:3 voltage divider is present (consisting of a 20 MΩ resistance in the signal line and a 10 MΩ resistance to ground). In this way, the gate voltages are filtered by a low-pass RC filter with a cut-off frequency of about 1 Hz. By combining all these filters, the electrons in the sample can be cooled to an effective temperature below 100 mK (if no extra heat loads such as coaxial cables are present).

High-frequency signals

High-frequency signals can be applied to gate electrodes via two coaxial cables. They consist of three parts, connected via standard 2.4 mm Hewlett Packard connectors (specified up to 50 GHz). From room temperature to 1 Kelvin, a 0.085 inch semi-rigid Be-Cu (inner and outer conductor) coaxial cable is used. From 1 Kelvin to the mixing chamber, we use 0.085 inch semi-rigid superconducting Nb coax cables. From the mixing chamber to the sample holder, flexible tin plated Cu coaxial cables are present. The coaxes are thermally anchored at 4 K, 1 K, $\sim$ 800 mK, $\sim$ 100 mK and base temperature, by clamping each cable firmly between two copper parts. To thermalize also the inner conductor of the coax, we use Hewlett Packard 8490D attenuators (typically -20 dB) at 1 K. These attenuators cannot be used at the mixing chamber, as they tend to become superconducting below about 100 mK. We have also tried using Inmet 50EH attenuators at the mixing chamber, but these showed the same problem. The 2.4 mm, DC-40 GHz attenuators of Weinschel (model 84) behaved normally at mixing chamber temperatures. It is believed that also attenuators with NiCr as resistor material stay normal at these temperatures.

To generate the high-frequency signals, we use a microwave source (Hewlett Packard 83650A) that goes up to 50 GHz; a pulse generator (Hewlett Packard 8133A), which generates simple 10 ns to 1 μs pulses with a rise time of 60 ps; and an arbitrary waveform generator (Sony Tektronix AWS520), which can generate more complicated pulses with a rise time of about 1 ns. With the cables described above, the fastest pulse flank we can transmit to the sample is about 200 ps. Microwave signals are transmitted with about 10 dB loss at 30 GHz.

Special care needs to be given to the connection from the coaxial cable to the chip, in order to minimize reflections. The sample holder we use, has an SMA connector that can be connected to the 2.4 mm coaxial cable in the dilution refrigerator. At the other end, the pin of the SMA connector sticks through a small hole in the chip carrier / sample plate. This allows it to be soldered to a metal pad on the chip carrier, from which we can then bond to the chip. This sample holder is used to apply pulses or microwave signals to a gate electrode.

For certain experiments, such as Electron Spin Resonance (see chapter 9), very large microwave signals are needed. To minimize on-chip reflections, we then use a waveguide. The signal and ground planes of the waveguide are connected by bonding wires to the inner and outer conductor of a 2.4 mm coaxial cable. Half of this cable has been sawed off, to allow bonding on a flat surface.

3.3 Quantum Point Contact as charge detector

As an alternative to measuring the current through the quantum dot, we can also measure the charge on the dot using one of the QPCs [13, 14]. To demonstrate this functionality, we first define only the left dot (by grounding gates R and P_R), and use the left QPC as a charge detector. The QPC is formed by applying negative voltages to $Q-L$ and L. This creates a narrow constriction in the 2DEG, with a conductance, G, that is quantized when sweeping the gate voltage V_{Q-L}. The last plateau (at $G = 2e^2/h$) and the transition to complete pinch-off (i.e. $G = 0$) are shown in Fig. 3.8a. We tune the QPC to the steepest point ($G \approx e^2/h$), where the QPC-conductance has a maximum sensitivity to changes in the electrostatic environment, including changes in the charge of the nearby quantum dot.

To change the number of electrons in the left dot, we make gate voltage V_M more negative (see Fig. 3.8b). This reduces the QPC current, due to the capacitive coupling from gate M to the QPC constriction. In addition, the changing gate voltage periodically pushes an electron out of the dot. The associated sudden change in charge lifts the electrostatic potential at the QPC constriction, resulting in a step-like feature in I_{QPC} (see the expansion in Fig. 3.8b, where the linear background is subtracted). This step indicates a change in the electron number. So, even without passing current through the dot, I_{QPC} provides information about the charge on the dot.

To enhance the charge sensitivity we apply a small modulation (0.3 mV at 17.7 Hz) to V_M and use lock-in detection to measure dI_{QPC}/dV_M [14]. The steps in I_{QPC} now appear as dips in dI_{QPC}/dV_M. Figure 3.8c shows the resulting dips, as well as the corresponding Coulomb peaks measured in the current through the dot. The coincidence of the Coulomb peaks and dips demonstrates that the QPC indeed functions as a charge detector. The height of the current step induced by a change in electron occupation, $\Delta I_{QPC,e}$, is $\sim$ 50 pA in Fig. 3.8b. We typically find $\Delta I_{QPC,e}$ to be 1-2% of the total current. The unique advantage of QPC charge detection is that it provides a signal even when the tunnel barriers of the dot are so opaque that I_{DOT} is too small to be measured [13, 14]. This allows us to study quantum dots even when they are virtually isolated from the reservoirs. This is demonstrated in Fig. 3.8d, where the tunnel coupling between the dot and the leads is so weak that the Coulomb peaks are not resolved anymore. Even in this regime, the QPC can track the transitions in electron number. We will explore this functionality in more detail in chapter 6.

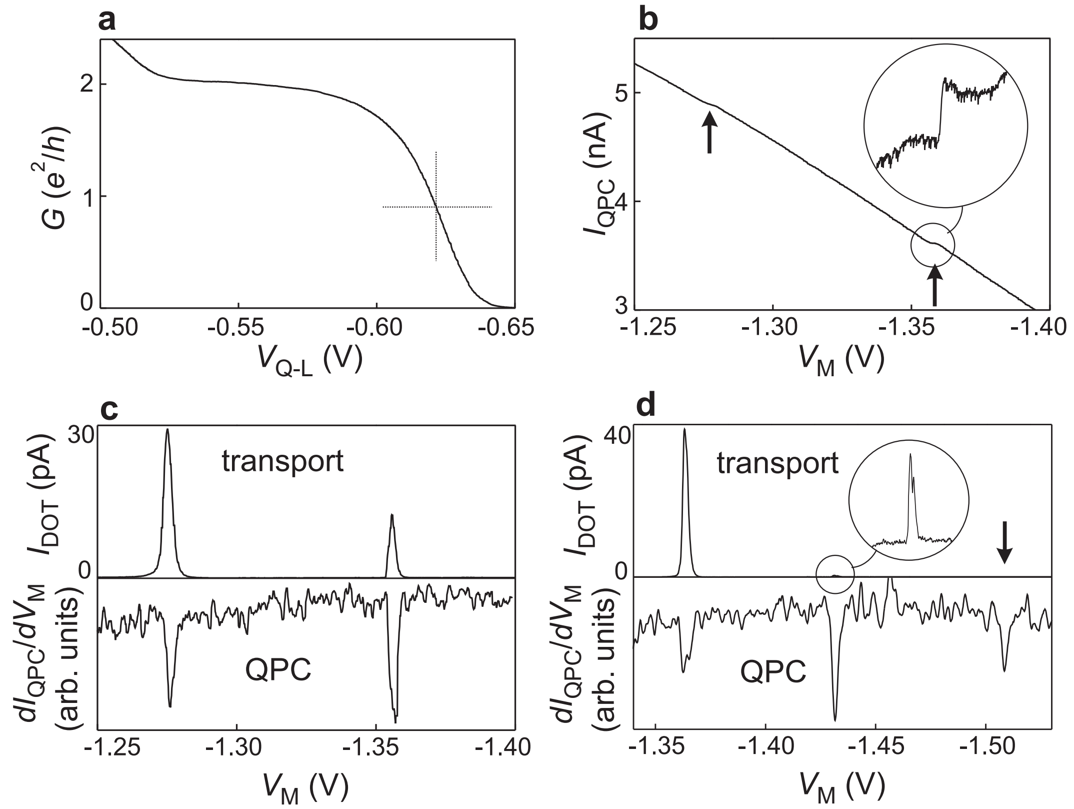

Figure 3.8: Operating the QPC as a charge detector of a single dot. **(a)** Conductance, G, of the left QPC versus gate voltage, V_{Q-L}, showing the last quantized plateau (at $G = 2e^2/h$) and the transition to complete pinch-off ($G = 0$). The QPC is set to the point of highest charge sensitivity, at $G \approx e^2/h$ (indicated by the dashed cross). **(b)** Current through the left QPC, I_{QPC}, versus left-dot gate voltage, V_M, with $V_{SD1} = 250$ μV and $V_{SD2} = V_{DOT} = 0$. Steps indicated by arrows correspond to changes in the number of electrons on the left dot. Encircled inset: the last step ($\sim$ 50 pA high), with the linear background subtracted. **(c)** Comparison between transport and charge detection measurements. Upper panel: Coulomb peaks measured in transport current through the left dot, with $V_{DOT} = 100$ μV and $V_{SD1} = V_{SD2} = 0$. Lower panel: changes in the number of electrons on the left dot measured with the left QPC, with $V_{SD1} = 250$ μV and $V_{SD2} = V_{DOT} = 0$). **(d)** Measurements as in (c), but in the regime of very weak dot-lead coupling. In the lower panel, charge detection shows an electron transition around -1.5 V, indicated by the arrow, whereas the Coulomb peak is not resolved in the transport measurement (upper panel). (Because the signal in (d) is a numerical derivate of I_{QPC} some dips show a much worse signal-to-noise ratio than in (c), where the signal is obtained using a lock-in technique.)

3.4 Double dot charge stability diagram

The QPC can also detect changes in the charge configuration of the *double* dot. To demonstrate this, we use the QPC on the right to measure dI_{QPC}/dV_L versus V_L and V_{P_R} (Fig. 3.9a), where V_L controls (mainly) the number of electrons on the left dot, and V_{P_R} (mainly) that on the right. Dark lines in the figure signify a dip in dI_{QPC}/dV_L, corresponding to a change in the total number of electrons on the double dot. Together these lines form the so-called 'honeycomb' diagram [15, 16]. The almost-horizontal lines correspond to a change in the number of electrons on the left dot, whereas almost-vertical lines indicate a change in the electron number on the right.

In the upper left region the 'horizontal' lines are not present, even though the QPC can still detect changes in the charge, as demonstrated by the presence of the 'vertical' lines. We conclude that in this region the *left* dot contains zero electrons. Similarly, a disappearance of the 'vertical' lines occurs in the lower right region, showing that here the *right* dot is empty. In the upper right region, the absence of lines shows that here the *double* dot is completely empty. This is indicated by the electron occupation numbers '00'.

We are now able to identify the exact charge configuration of the double dot in every honeycomb cell, by simply counting the number of 'horizontal' and 'vertical' lines that separate it from the '00' region. In Fig. 3.9b the first few honeycomb cells are labelled according to their charge configuration, with e.g. the label '21' meaning 2 electrons in the left dot and 1 on the right.

Besides the dark lines, also short bright lines are visible, signifying a peak in dI_{QPC}/dV_L. These bright lines correspond to an electron being transferred from one dot to the other, with the total electron number remaining the same. (The fact that some charge transitions result in a dip in dI_{QPC}/dV_L and others in a peak, derives from the fact that we use the QPC on the *right* and apply the modulation to the gate on the *left*. When an electron is pushed out of the double dot by making V_L more negative, the QPC opens up and dI_{QPC}/dV_L displays a dip. When V_L pushes an electron from the left to the right dot, the QPC is closed slightly, resulting in a peak.)

The visibility of all lines in the honeycomb pattern demonstrates that the QPC is sufficiently sensitive to detect *all* charge transitions in the double quantum dot. Generally, we find the QPC on the right side to be about a factor of 2 more sensitive to changes in the electron number on the right dot than to changes in the electron number on the left dot.

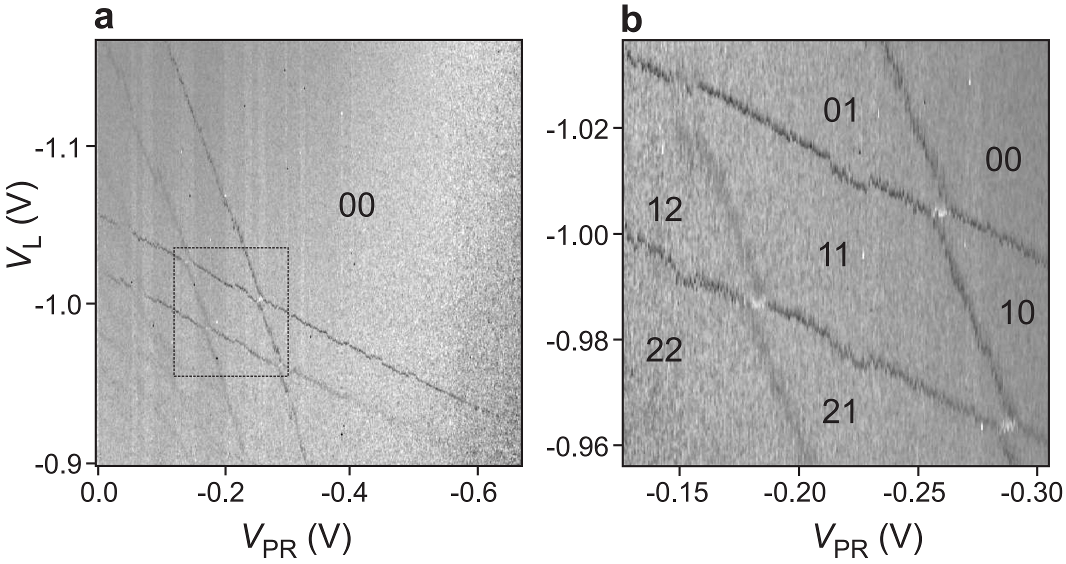

Figure 3.9: Using the QPC to measure the charge configuration of a double quantum dot in the few-electron regime. **(a)** dI_{QPC}/dV_L (in grayscale) versus V_L and V_{P_R}, with $V_{SD2} = 100\ \mu$V and $V_{SD1} = V_{DOT} = 0$. A small modulation (0.3 mV at 17.77 Hz) is applied to V_L, and the resulting modulation in I_{QPC} is measured with a lock-in amplifier to give dI_{QPC}/dV_L directly. The label '00' indicates the region where the double dot is completely empty. In the bottom left corner the dark lines are poorly visible. Here the tunnel rates to the reservoirs are quite large, leading to smearing of the steps in the QPC current, and therefore to smaller dips in dI_{QPC}/dV_L. **(b)** Zoom-in of Fig. 3.9a, showing the 'honeycomb' diagram for the first few electrons in the double dot. The black labels indicate the charge configuration, with '21' meaning 2 electrons in the left dot and 1 on the right.

3.5 Real-time observation of single-electron tunneling

If the time between tunnel events is longer than the time needed to determine the number of electrons on the dot – or equivalently: if the bandwidth of the charge detection exceeds the tunnel rate – electron tunneling can be observed in real-time. In our setup, the measured current noise integrated from dc is comparable to the current step induced by an electron tunneling on or off the dot ($\Delta I_{QPC,e}$) for a bandwidth of 80 kHz, and 2.5 times smaller than $\Delta I_{QPC,e}$ around 40 kHz [18]. These numbers correspond to a QPC voltage bias of 1 mV. A larger voltage bias is found to influence the tunneling statistics, possibly due to photon-assisted tunneling. We set the cut-off frequency of the external low-pass filter at 40 kHz, so we should see clear steps in time traces of the QPC current, corresponding to

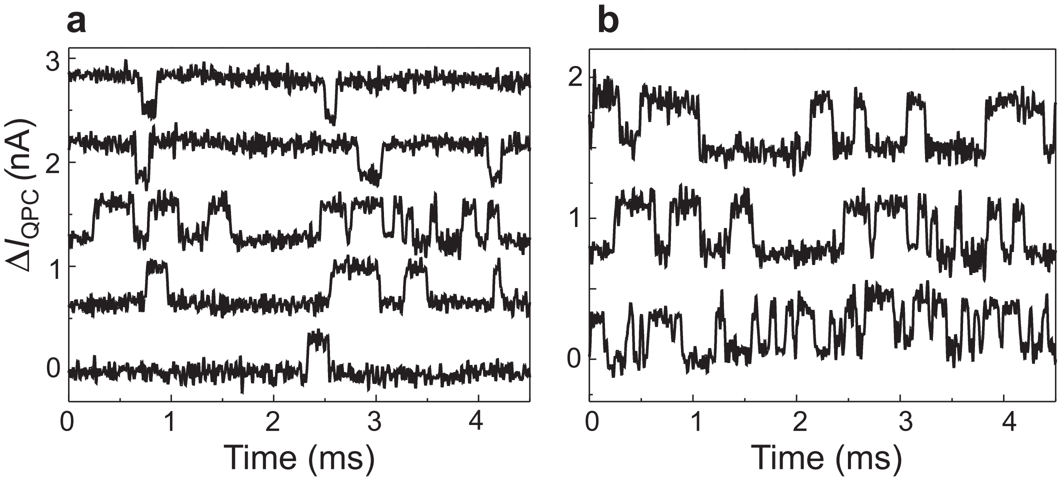

Figure 3.10: Measured changes in the QPC current, ΔI_{QPC}, with the electrochemical potential in the dot and in the reservoir nearly equal. ΔI_{QPC} is 'high' and 'low' for 0 and 1 electrons on the dot respectively (QPC bias $V_{SD2} = 1$ mV; the steps in ΔI_{QPC} are ≈ 300 pA). The small roll of the baseline is at 50 Hz. Traces are offset for clarity. **(a)** The dot potential is lowered from top to bottom. **(b)** The tunnel barrier is lowered from top to bottom.

single electrons tunneling on or off the dot.

We use a one-electron single dot defined by gates T, M and R (see Fig. 2.10c), and tune the tunnel barriers such that the dot is virtually isolated from the lead that is connected to the QPC channel path. In this regime, the dot is operated as a charge box, coupled to only one reservoir. Next, the electrochemical potential in the dot is aligned with the electrochemical potential in the reservoir. Now the electron can *spontaneously* tunnel back and forth between the dot and the lead, and the QPC current should exhibit a random telegraph signal (RTS). This is indeed what we observe experimentally (Fig. 3.10). In order to ascertain that the RTS really originates from electron tunnel events between the dot and the reservoir, we verify that (1) the dot potential relative to the Fermi level determines the fraction of the time an electron resides in the dot (Fig. 3.10a) and (2) the dot-lead tunnel barrier sets the RTS frequency (Fig. 3.10b). The shortest steps that clearly reach above the noise level are about $8\,\mu$s long. This is consistent with the 40 kHz filter frequency, which permits a rise time of $8\,\mu$s.

We can also *induce* tunnel events by pulsing the dot potential using fast voltage pulses on the plunger gate, so N predictably changes from 0 to 1 and back to 0. The response of the QPC current to such a pulse contains two contributions (Fig. 3.11a). First, the shape of the pulse is reflected in ΔI_{QPC}, as the pulse gate couples capacitively to the QPC. Second, some time after the pulse is started, an

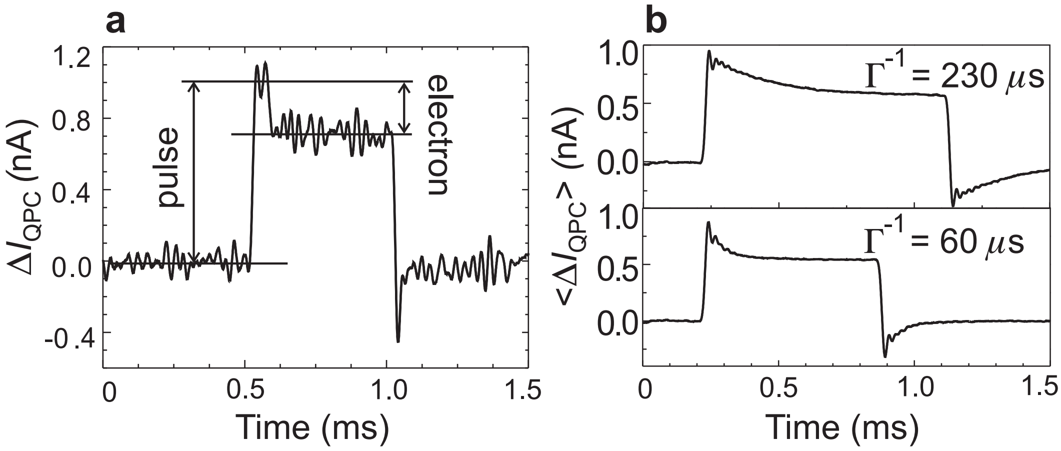

Figure 3.11: (a) Measured changes in the QPC current, ΔI_{QPC}, when a pulse is applied to gate P_R, near the degeneracy point between 0 and 1 electrons on the dot (V_{SD2} = 1 mV). (b) Average of 286 traces as in (a). The top and bottom panel are taken with a different setting of gate M. The damped oscillation following the pulse edges is due to the 8th-order 40 kHz filter used.

electron tunnels into the dot and ΔI_{QPC} goes down by about 300 pA. Similarly, ΔI_{QPC} goes up by 300 pA when an electron leaves the dot, some time after the pulse ends. We observe that the time before tunneling takes place is randomly distributed, and obtain a histogram of this time simply by averaging over many single-shot traces (Fig. 3.11b). The measured distribution decays exponentially with the tunnel time, characteristic of a Poisson process. The average time before tunneling corresponds to Γ^{-1}, and can be tuned by adjusting the tunnel barrier.

3.6 Conclusions

In this chapter, the theory for electron transport through quantum dots and the details of the measurement setup have been presented. Next, the operation of a QPC charge detector is explained and demonstrated by measuring the double dot charge stability and real-time observation of single-electron tunneling.

We thank T. Fujisawa, T. Hayashi, T. Saku, Y. Hirayama, C. J. P. M. Harmans and B. van der Enden and for valuable discussions and help. This work was supported by the Specially Promoted Research Grant-in-Aid for Scientific Research, from the Ministry of Education, Culture, Sports, Science and Technology in Japan, the DARPA-QUIST program (DAAD19-01-1-0659), and the Dutch Organisation for Fundamental Research on Matter (FOM).

References

[1] L. P. Kouwenhoven, D. G. Austing and S. Tarucha, Rep. Prog. Phys. **64** (6), 701 (2001).

[2] L. P. Kouwenhoven *et al.*, in *Mesoscopic Electron Transport*, edited by L. L. Sohn, L. P. Kouwenhoven and G. Schön, (Kluwer, Series E **345**, 1997), p.105-214.

[3] R. Hanson *et al.*, in *Proceedings of the 39th Rencontres de Moriond*; see also cond-mat/0407793.

[4] N. W. Ashcroft and N. D. Mermin, *Solid State Physics*, (New York Saunders, 1974).

[5] S. Tarucha *et al.*, Phys. Rev. Lett. **84**, 2485 (2000).

[6] R. Hanson *et al.*, Phys. Rev. B **70**, 241304(R) (2004).

[7] D. Weinmann, W. Häusler and B. Kramer, Phys. Rev. Lett. **74**, 984 (1995).

[8] S. Tarucha *et al.*, Phys. Rev. Lett. **77**, 3613 (1996).

[9] V. N. Golovach and D. Loss, Europhys. Lett. **62**, 83 (2003).

[10] G. Burkard, D. Loss and D. P. DiVincenzo, Phys. Rev. B **59**, 2070 (1999).

[11] J. M. Martinis, M. H. Devoret and J. Clarke, Phys. Rev. B **35**, 4682 (1987).

[12] K. Bladh *et al.*, Rev. Sci. Instr. **74**, 1323 (2003).

[13] M. Field *et al.*, Phys. Rev. Lett. **70**, 1311 (1993).

[14] D. Sprinzak *et al.*, Phys. Rev. Lett. **88**, 176805 (2002).

[15] H. Pothier *et al.*, Europhys. Lett. **17**, 249 (1992).

[16] W. G. van der Wiel *et al.*, Rev. Mod. Phys. **75**, 1 (2003); see also cond-mat/0205350v2.

[17] A. W. Rushforth *et al.*, Phys. Rev. B **69**, 113309 (2004).

[18] L. M. K. Vandersypen *et al.*, Appl. Phys. Lett. **85**, 4394 (2004).

Chapter 4

Spin filling of a quantum dot derived from excited-state spectroscopy

L. H. Willems van Beveren, R. Hanson, I. T. Vink,
F. H. L. Koppens, L. P. Kouwenhoven and L. M. K. Vandersypen

We study the spin filling of a semiconductor quantum dot using excited-state spectroscopy in a strong magnetic field. The field is oriented in the plane of the two-dimensional electron gas in which the dot is electrostatically defined. By combining the observation of Zeeman splitting with our knowledge of the absolute number of electrons, we are able to determine the ground state spin configuration for one to five electrons occupying the dot. For four electrons, we find a ground state spin configuration with total spin $S = 1$, in agreement with Hund's first rule. The electron g-factor is observed to be independent of magnetic field and electron number.

This chapter has been published in New J. Phys. **7**, 182 (2005). Part of *Focus on Solid State Quantum Information*. The article has been chosen for publication in IOP Select.

4.1 Introduction

A single electron spin confined in a semiconductor quantum dot (QD) is considered a promising candidate for the implementation of a qubit [1, 2]. Also the joint spin state of N electrons on a single dot may be used for quantum computation schemes. For instance, as long as the N-electron ground state has spin $S = 1/2$, it can be used in a similar way as the spin of a single electron. Furthermore, proposals exist for encoding a qubit in two specific spin states of three electrons in a single dot, and for controlling this qubit fully electrically [3]. Therefore, it is important to understand the interaction of multiple electron spins confined in a quantum dot, and specifically the spin configuration of the ground state. This can be done by studying spin filling, i.e. by determining the spin of successive electrons that are added to the dot, starting from zero electrons.

Quantum dots defined in pillars etched from a GaAs/AlGaAs double-barrier heterostructure (“so-called vertical” QDs) have been studied extensively, showing spin filling obeying Hund’s rule [4], triplet-singlet ground state transitions [5], and a dependence of spin filling on the anisotropy of the confinement potential [6]. Furthermore, zero magnetic field addition spectra have revealed an atomic-like shell structure induced by a two-dimensional harmonic potential. Therefore these devices are commonly referred to as “artificial atoms”. The addition spectrum of few-electron quantum dots, defined electrostatically within a two-dimensional electron gas (2DEG) by means of surface gates (so-called “lateral” QDs), has also been studied [7]. Although a two-electron singlet-triplet ground state transition has been observed in these systems [8], evidence for a shell structure and spin filling obeying Hund’s rule has not yet been found.

Here we study the spin filling of a few-electron lateral quantum dot by performing excited-state spectroscopy at a fixed magnetic field $B_{||}$ of 10 T, applied parallel to the 2DEG. First we explain in detail our general method for determining spin filling. Then the device characteristics and settings are described. Finally we apply the method in order to determine spin filling for five successive transitions in the electron number, starting from an empty dot.

4.2 Zeeman splitting and spin filling

The method for determining spin filling is based on the facts that any single orbital can be occupied by at most two electrons, and that these electrons must have anti-parallel spins, due to the Pauli exclusion principle. Therefore, as we add one electron to a dot containing N electrons, there are only two scenarios possible: (I) the electron moves into an empty orbital, or (II) it moves into an orbital that already holds one electron. We will now show that (in a high magnetic field) for the transition from the N-electron ground state, GS(N), to the (N+1)-electron ground state, GS(N+1), these two scenarios always correspond to the addition of a spin-up electron and a spin-down electron respectively.

We first consider case I where an electron enters an empty orbital. In a strong magnetic field $B_{||}$, spin-up electrons have a lower energy than spin-down electrons [9] due to the Zeeman splitting $\Delta E_Z = |g| \, \mu_B B_{||}$, where $\mu_B = 58 \, \mu$eV/T is the Bohr magneton. Therefore, if the orbital is empty, addition of a spin-up electron is energetically favored and thus takes the dot from GS(N) to GS(N+1). In contrast, addition of a spin-down electron takes the dot from GS(N) to the (N+1)-electron excited state, ES(N+1), which lies ΔE_Z higher in energy.

Next we look at case II, where an electron moves into an orbital with already one electron present. The electron that already occupies the orbital has spin-up if the dot is in GS(N), as explained above. Therefore, the electron added in the transition from GS(N) to GS(N+1) must have spin-down in order to satisfy the Pauli exclusion principle. A spin-up electron can only be added to the same orbital if the first electron is spin-down, i.e. when the dot starts from ES(N), ΔE_Z higher in energy than GS(N). Thus, addition of a spin-up electron corresponds to a transition from ES(N) to GS(N+1).

Comparing the two cases, we see that in case I, where a spin-up electron is added, there is an (N+1)-electron ES separated from GS(N+1) by ΔE_Z, while in case II, where a spin-down electron is added, there is a N-electron ES, separated from GS(N) by ΔE_Z. Thus, the spin filling has a one-to-one correspondence with the excited-state spectrum [10].

We can discriminate between cases I and II by looking at electron transport through the dot as a function of the voltage bias (V_{SD}) applied between source and drain contacts, and gate voltage. Fig.4.1 (a) and (b) schematically show the expected result of such a measurement for cases I and case II respectively. Lines in the differential conductance dI/dV_{SD} indicate where electron transitions involving ground and excited states become energetically accessible. The transition from GS(N) to GS(N+1) is only allowed in the V-shaped region spanned by the two solid lines in dI/dV_{SD} that intersect at $V_{SD} = 0$. These lines thus form the edges of the Coulomb blockaded (CB) region. The onset of the transition from GS(N) to ES(N+1), as in case I, appears as a line terminating at the edge of the (N+1)-electron CB region, at point P in Fig.4.1(a). In contrast, the onset of the transition from ES(N) to GS(N+1), as in case II, appears as a line terminating at the edge of the N-electron CB region, at point Q in Fig.4.1 (b).

Thus, if we see a line at a distance ΔE_Z from the edge of the CB region and terminating at the (N+1)-electron CB region, we have case I. Here a spin-up

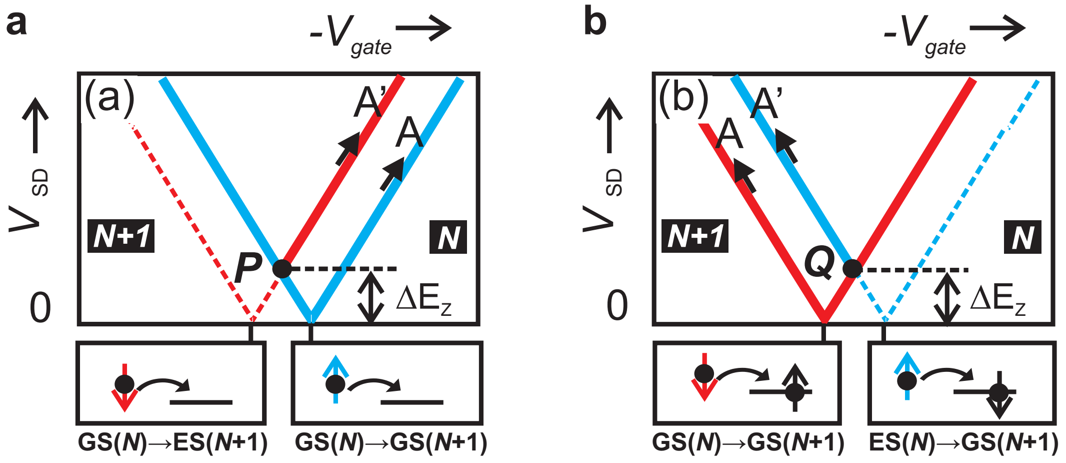

Figure 4.1: Schematic representation of excited-state spectra for case I (a) and case II (b). Shown is the differential conductance dI/dV_{SD} as a function of V_{SD} and gate voltage V_{gate} in the presence of a strong in-plane magnetic field. The lines indicate where the transitions depicted in the corresponding diagrams become energetically accessible. Current can only flow in the V-shaped region defined by the GS(N) to GS(N+1) transition (line A); outside this region the dot is in Coulomb blockade and the number of electrons on the dot is fixed. When a transition involving an ES becomes accessible, the current changes, leading to an extra line in dI/dV_{SD} (line A'). In case I, this line terminates at the (N+1)-electron CB region (point P in (a)), whereas in case II the line terminates at the N-electron CB region (point Q in (b)). Each of the excited-state spectra is symmetric with respect to V_{SD}. Therefore, the spectra for $V_{SD} < 0$ can be obtained by rotating the shown spectra about the V_{gate} axis.

electron is added to the dot. In contrast, if there is a line at a distance ΔE_Z from the CB region that terminates at the N-electron CB region, we have case II, where a spin-down electron is added to the dot.

The main requirement for this method is the ability to identify the Zeeman splitting in the excited-state spectrum. In GaAs/AlGaAs lateral quantum dots Zeeman splitting has already been observed in several experiments [11, 12, 13, 14]. We emphasize that the method is valid regardless of the spin S of the ground states involved, as long as the addition of one electron changes the spin of the ground state by $|\Delta S| = 1/2$ [15]. We now utilize this method to determine the change in spin at subsequent electron transitions in a lateral GaAs quantum dot containing zero to five electrons.

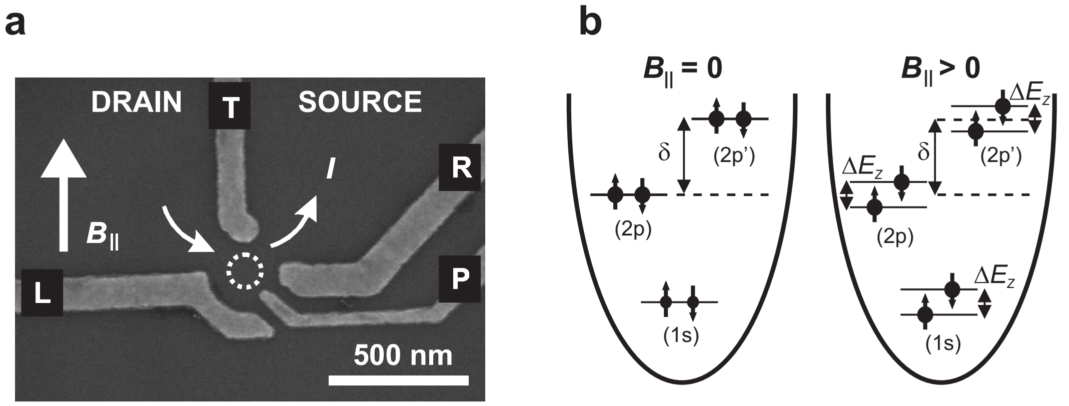

Figure 4.2: (a) Scanning electron micrograph of the device showing Ti/Au gate electrodes lying on top of a GaAs/AlGaAs heterostructure. The gate electrodes can locally deplete the 2DEG when negatively biased. Gate electrodes L, R and T are used to form the quantum dot, indicated by the white dashed circle. Gate electrode P is left floating. (b) Level structure of a quantum dot with anisotropic parabolic confinement in zero and finite magnetic field. Two electrons with opposite spin can occupy the orbital states (1s), (2p) and (2p'). The latter two orbitals are separated in energy by δ due to anisotropy of the confinement potential.

4.3 Device characteristics

The lateral quantum dot is defined by Ti/Au gate electrodes patterned on top of a Si modulation doped GaAs/Al$_x$Ga$_{1-x}$As heterostructure ($x = 0.265$), containing a high mobility 2DEG 60 nm below the surface, see Fig.4.2 (a). Annealing of Ni/AuGe/Ni contacts provides electrical contact to the source and drain reservoirs in the 2DEG. The 2DEG has an electron density $n_s = 4.0 \times 10^{15}$ m^{-2}. This sample was cooled down with +266 mV on each of the surface gates in order to reduce background charge fluctuations [16]. The voltage on gate electrode T, V_T, is used to vary the electrochemical potential of the dot in each of the excited-state spectra. A magnetic field is applied parallel to the 2DEG to minimize additional lateral confinement and to exclude Landau level formation. All measurements are performed in a dilution refrigerator at base temperature $T = 15$ mK.

We tune the quantum dot to the few-electron regime at $B_{||} = 0$ T. We identify the 0↔1 electron transition by the absence of further electron transitions in sweeping the gate voltages to more negative values under large applied source-drain voltage [17]. Then we track the 0↔1 electron transition as the magnetic field is swept to $B_{||} = 10$ T.

The charging energy of the dot, E_C, is 4.8 meV (for adding a second electron to a one-electron dot). For $N = 1$, the level spacing from the orbital ground state to the first orbital excited state is 1.7 meV (data not shown). The level spacing between the first and second orbital excited state is considerably smaller, 0.8 meV. This implies that the confinement potential of the dot has no circular symmetry as in [18]. We nevertheless adopt the nomenclature from Refs. [17, 18] to denote the lowest orbital states in our quantum dot as (1s), (2p), etcetera. In fact, we shall see that the data is well explained by assuming an anisotropic confinement potential in the dot, where the two-fold orbital degeneracy of the first excited state (2p) is lifted. This gives rise to a level structure as shown in Fig.4.2 (b), in which the two (2p)-like orbitals, now denoted (2p) and (2p'), are offset by an amount $\delta = 0.8$ meV. In lateral quantum dots, the spacing between successive orbitals is found to be dependent on gate voltage (and thus electron number) [8, 19, 20]; generally, the level spacing decreases as the size of the dot is increased (which is needed to allow more electrons on the dot). Therefore, we also expect the value of δ to decrease as we increase the number of electrons on the dot.

We set the tunnel rate of the incoming barrier Γ_L much smaller than the tunnel rate for the outgoing barrier Γ_R. As a result, in all of the excited-state spectra shown, the intensity of the lines involving transitions to or from excited states is enhanced when they run from bottom left to top right. In turn, the intensity of the lines involving excited states and running from top left to bottom right is suppressed [21]. Thus, lines corresponding to transitions from GS(N) to ES(N+1) (line A' in Fig.4.1 (a)) are most easily observed for $V_{SD} > 0$, while lines corresponding to transitions from ES(N) to GS(N+1) (line A' in Fig.4.1 (b)) are most easily seen for $V_{SD} < 0$.

4.4 N=0↔1 transition

The excited-state spectrum obtained around the 0↔1 transition is shown in Fig.4.3 (a). Clearly two parallel lines are observed, A and A'. The separation between these lines increases linearly with $B_{||}$, and thus corresponds to the Zeeman splitting. From the spacing between lines A and A' (to be precise, from the value of V_{SD} at point P), we extract $\Delta E_Z = 0.16 \pm 0.01$ meV at 10 T. Since A' terminates in the $N = 1$ CB region, the electron added to the empty dot to form the $N = 1$ GS has spin-up (see Fig.4.1 (a)), as expected.

In Fig.4.3 (b) the Zeeman energy ΔE_Z at the 0↔1 transition is plotted versus applied magnetic field in the range from 5.5 to 14 T. For $B_{||} < 5.5$ T we cannot clearly resolve the Zeeman splitting from the spectroscopy data. As a reference, the Zeeman splitting ΔE_Z expected for bulk GaAs is plotted with $|g_0| = 0.44$ [22] (dashed black line). Clearly the g-factor we extract from Fig.4.3 (b) is independent of field. Linear fitting of the data points results in a g-factor value of 0.27 ± 0.02. This value is lower than the bulk value of GaAs. Deviations of the g-factor from g_0 in quantum dots and possible explanations for this effect have been reported before [11, 12, 13].

4.5 N=1↔2 transition

Next we tune the dot to the 1↔2 electron transition. At zero magnetic field the ground state for a two-electron quantum dot is always a spin singlet state $|S\rangle$, where two electrons with opposite spin occupy the lowest orbital and the total spin $S = 0$ [23]. We expect that this is still true for an in-plane field of 10 T, as the Zeeman energy is much smaller than the zero-field singlet-triplet energy separation [14].

The dI/dV_{SD} data obtained for the 1↔2 electron transition is shown in Fig.4.4 (a). Two lines A and A' separated by 0.16 ± 0.01 meV are visible, for $V_{SD} < 0$. This is exactly the energy scale of the Zeeman splitting found for the 0↔1 transition. Because A' terminates in Q at the edge of the $N = 1$ CB region (and not at the edge of the $N = 2$ CB region), we conclude that the transition from GS(1) to the GS(2) involves adding a spin-down electron. The spin-down electron pairs with the spin-up electron already present in the (1s) orbital to form a two-electron singlet state $|S\rangle$, as illustrated in the left diagram of Fig.4.4 (b).

For the color scale chosen, parts of line A are difficult to observe. Therefore dashed yellow lines are added as a guide to the eye. For $V_{SD} > 0$, line A' is also hardly visible. Its position is indicated by a black dashed line. The absence of this latter line is caused by the asymmetry of the tunnel barriers, as explained earlier. For the same reason, the lines B-B' and C-C' are hardly visible for $V_{SD} < 0$. Line A is weaker than line A' because in a strong magnetic field spin-up electrons generally couple better to the source and drain reservoirs than spin-down electrons, even if the magnetic field is applied in the plane of the 2DEG [24].

The lines B-B' correspond to the onset of transitions involving the three triplet states. These lines too are separated by the Zeeman splitting; B and B' involve transport of spin-up and spin-down electrons respectively [14]. The distance between A and B' gives the singlet-triplet energy splitting E_{ST}, 0.56 ± 0.02 meV. The data also shows a third set of parallel lines with the same spacing, C-C'. The fact that the pair of lines C-C' have a different intensity than the pair of lines

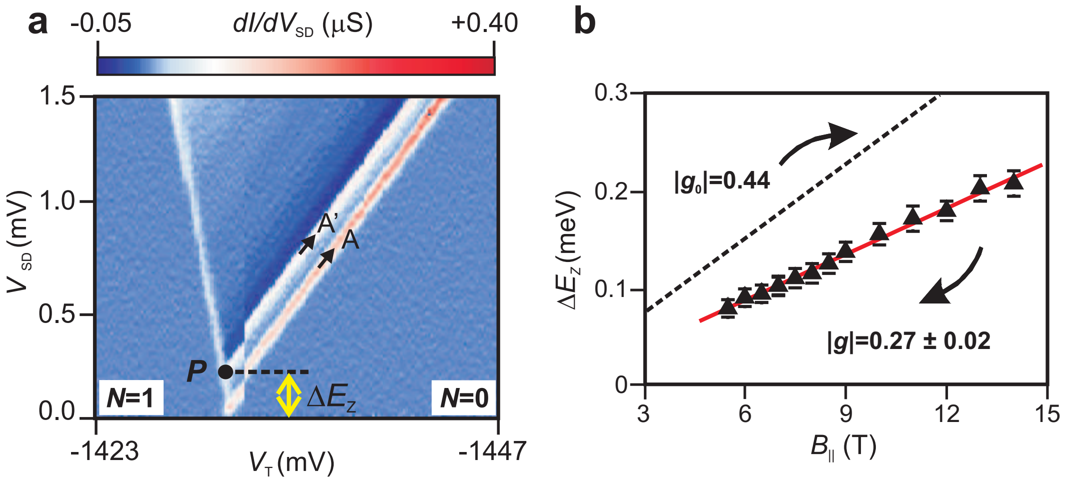

Figure 4.3: (a) Color scale plot of the differential conductance dI/dV_{SD} as a function of V_{SD} and gate voltage V_T near the 0↔1 electron transition, at $B_{||}$ = 10 T. Zeeman splitting of the orbital ground state is clearly observed (A-A'). The vertical shift in the data near V_T=-1430 mV is caused by a background charge rearrangement in the environment of the dot. (b) Extracted Zeeman splitting ΔE_Z at the 0↔1 electron transition as a function of $B_{||}$. A linear fit of ΔE_Z (red curve) results in $|g| = 0.27 \pm 0.02$. The dashed black line corresponds to the Zeeman splitting in bulk GaAs, where $g_0 = -0.44$.

B-B' suggests that different orbitals are involved. We believe that the lines C-C' correspond to transitions to and from triplet states with one electron in the (2p') orbital instead of in the (2p) orbital. Here, the offset between the (2p) and (2p') orbitals, δ, is 0.52 meV (B'-C'), somewhat smaller than the value at the 0↔1 electron transition.

4.6 N=2↔3 transition

Next we move on to the 2↔3 electron transition. We have seen that the two-electron ground state is a singlet state $|S\rangle$, where two electrons with opposite spin occupy the (1s) orbital. When a third electron is added, it has to occupy a different orbital in order to satisfy the Pauli exclusion principle.

The dI/dV_{SD} data we find is shown in Fig.4.5 (a). We notice several important features. A first pair of lines, A-A', is split by 0.17 ± 0.01 meV, the Zeeman splitting. Since these lines terminate at the edge of the $N = 3$ CB region, the transition from GS(2) to GS(3) involves adding a spin-up electron. The three-electron ground state then corresponds to the situation where the third electron (with spin-up) occupies the orbital (2p), as shown in the left diagram of Fig.4.3 (b).

A second set of Zeeman split lines, B-B', runs parallel to the lines A and A', with smaller amplitude. The separation between both sets of transitions, δ, is 0.34 meV. In our spin filling picture, the lines B and B' correspond to electron transitions where the third electron occupies the (2p') orbital, as in the right diagram of Fig.4.3 (b). The value of δ we find here is smaller than at the 1↔2 electron transition, as expected from our earlier considerations.

4.7 N=3↔4 transition

In Fig.4.6 (a) we show the excited-state spectrum for the 3↔4 electron transition. Ignoring spin-exchange interactions, one expects a four-electron dot with total spin $S = 0$, where two electrons occupy the (1s) orbital and two electrons occupy the (2p) orbital. This implies that a spin-down electron must be added to a three-electron dot in the GS in order to reach the $N = 4$, $S = 0$ state.

However, the data in Fig.4.6 (a) indicates that the fourth electron added to the dot has spin-up, because the line A', separated from line A by the Zeeman splitting ($\Delta E_Z = 0.17 \pm 0.01$ meV), terminates at the edge of the $N = 4$ CB region. Since both the third and fourth electron have spin-up, they occupy different orbitals, (2p) and (2p'), as shown in the left diagram of Fig.4.6 (b). The $N = 4$ ground state thus has $S = 1$. This $N = 4$ ground state can be understood when we take into account the exchange interaction K_{ab} between the spins in the (2p) and (2p') orbital and the terms C_{aa} and C_{ab}, representing the direct Coulomb energy when the two spins are in the same or in a different orbital state respectively [17]. $S = 1$ spin filling is favored when $K_{ab} + |C_{aa} - C_{ab}| > \delta$.

This particular spin configuration of the $N = 4$ ground state is related to Hund's first rule, which states that a shell of degenerate orbitals will, as much as possible, be filled by electrons with parallel spins, up to the point where the shell is half filled. Exchange energy K_{ab} (causing a lowering of the Coulomb energy when spins align parallel in different orbitals) reduces the total energy and favors the $S = 1$ state. This state can only exist when the offset beteen the (2p) orbitals, δ, is small compared to the exchange energy and the difference in direct Coulomb energy terms [6].

4.8 N=4↔5 transition

As we have seen, the four-electron ground state has a total spin $S = 1$, in agreement with Hund's first rule. When the fifth electron is added the total spin of the system is expected to change back from $S = 1$ to $S = 1/2$ because of spin pairing in the (2p) orbital. A less likely option for the transition from GS(4) to GS(5) is that the fifth electron tunnels into the next empty orbital.

In Fig.4.7 (a) we show the excited-state spectrum for the 4↔5 electron transition. Indeed, the transition from GS(4) to GS(5) corresponds to adding an electron with spin-down, as the line A' terminates at the edge of the $N = 4$ CB region (as before, some of the lines are hardly visible; their position is indicated by yellow dashed lines). The resulting spin configuration for five electrons is indicated in the left diagram of Fig.4.7 (b). The added spin-down electron occupies the (2p) orbital. The Zeeman splitting extracted from the data ($V_{SD} < 0$) is $\Delta E_Z = 0.17 \pm 0.01$ meV.

4.9 Conclusions

We have determined the spin filling of a few-electron lateral quantum dot containing one up to five electrons in a parallel magnetic field of 10 T. The spin filling was extracted without magnetic field sweeps, by looking at the position of the excited spin state in the spectroscopy data. The Zeeman splitting is equal for all orbitals and independent of the number of electrons on the dot. The ground state of a four-electron dot is a $S = 1$ Hund state. Field dependence of the Zeeman splitting for the 0↔1 electron transition yields a field independent g-factor value of 0.27 ± 0.02.

This work was supported by the Dutch Science Foundation NWO/FOM, the DARPA-QUIST program, the ONR, the International Cooperative Research Project (ICORP) and the EU-RTN network on spintronics. We gratefully acknowledge fabrication support from W. J. M. Naber and valuable discussions with J. M. Elzerman.

References

[1] D. Loss and D. P. DiVincenzo, Phys. Rev. A **57**, 120 (1998).

[2] D. P. DiVincenzo, Nature **408**, 339 (2000).

[3] J. Kyriakidis *et al.*, Phys. Rev. B **71**, 125332 (2005).

[4] S. Tarucha *et al.*, Phys. Rev. Lett. **77**, 3613 (1996).

[5] S. Tarucha *et al.*, Phys. Rev. Lett. **84**, 2485 (2000).

[6] S. Tarucha *et al.*, Appl. Phys. A **71**, 367 (2000).

[7] M. Ciorga *et al.*, Phys. Rev. B **61**, R16315 (2000).

[8] J. Kyriakidis *et al.*, Phys. Rev. B **66**, 035320 (2002).

[9] Since the g-factor in GaAs is negative, the electron spin is aligned with the magnetic moment of the electron, and spin-up (aligned with the magnetic field) has a lower energy than spin-down.

[10] D. H. Cobden *et al.*, Phys. Rev. B **81**, 681 (1998).

[11] R. Hanson *et al.*, Phys. Rev. Lett. **91**, 196802 (2003).

[12] R. M. Potok *et al.*, Phys. Rev. Lett. **91**, 016802 (2003).

[13] A. Kogan *et al.*, Phys. Rev. Lett. **93**, 166602 (2004).

[14] R. Hanson *et al.*, Phys. Rev. B **70**, 241304 (2004).

[15] If $|\Delta S| > 1/2$, the $(N{+}1)$-electron GS cannot be reached from the N-electron GS by adding a single electron, leading to a spin blockade of electron transport through the dot, see D. Weinmann *et al.*, Phys. Rev. Lett. **74**, 984 (1995).

[16] M. Pioro-Ladrière *et al.*, cond-mat/0503602.

[17] L. P. Kouwenhoven *et al.*, Rep. Prog. Phys. **64** (6), 701 (2001).

[18] C. G. Darwin, Proc. Cambridge. Philos. Soc. **27**, 86 (1930); V. Fock, Z. Phys. **47**, 446 (1928).

[19] A. Kogan *et al.*, Phys. Rev. B **67**, 113309 (2003).

[20] D. M. Zumbühl *et al.*, Phys. Rev. Lett. **93**, 256801 (2004).

[21] T. Hayashi *et al.*, Phys. Stat. Sol. B **238**, 262 (2003).

[22] C. Weisbuch and C. Hermann, Phys. Rev. B **15**, 816 (1977).

[23] N. W. Ashcroft and N. D. Mermin,*Solid State Physics*, (New York Saunders, 1974).

[24] R. Hanson *et al.*, in *Proceedings of the 39th Rencontres de Moriond*; see also cond-mat/0407793.

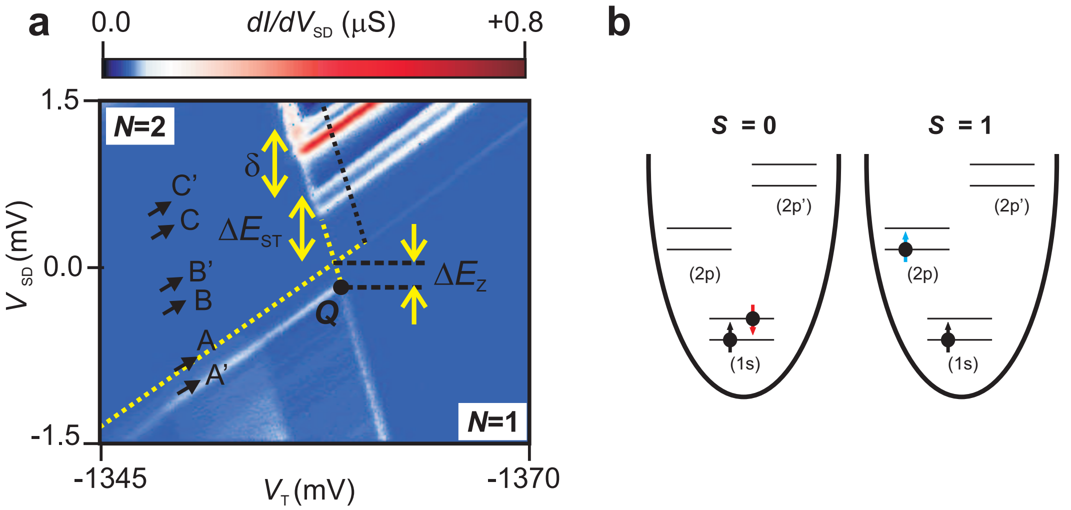

Figure 4.4: (a) Color scale plot of the differential conductance dI/dV_{SD} as a function of V_{SD} and gate voltage V_T near the 1↔2 electron transition, at $B_{||} = 10$ T. (b) *Left*: Ground state spin configuration for a two-electron dot. A spin-down electron (red) is added and pairs with the spin-up electron already present, to form a singlet state $|S\rangle$ with total spin $S = 0$. *Right*: Spin configuration of an excited state. The second spin-up electron occupies the (2p) orbital to form a two-electron triplet state $|T\rangle$ with total spin $S = 1$. When the second spin-up electron occupies the (2p') orbital an excited triplet state is formed.

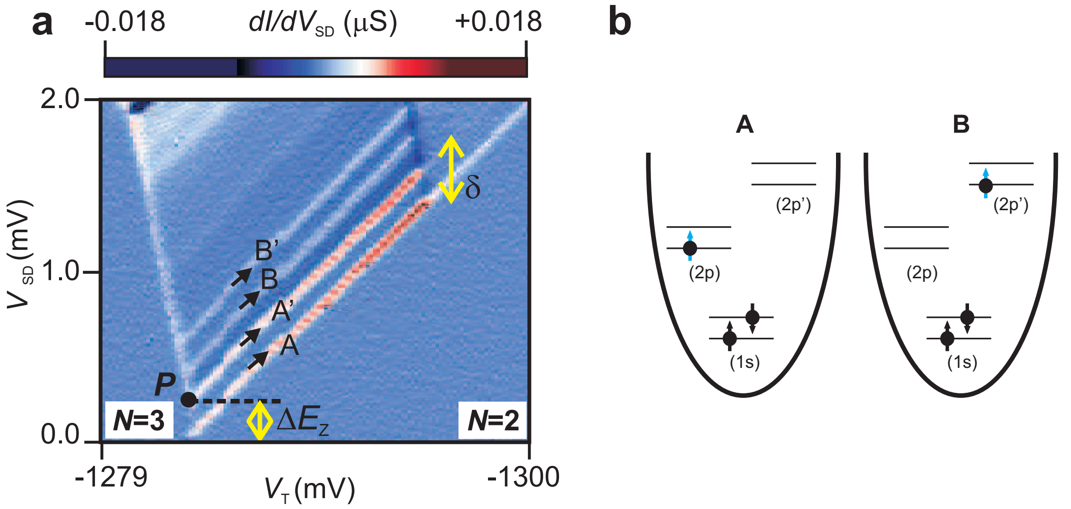

Figure 4.5: (a) Color scale plot of the differential conductance dI/dV_{SD} as a function of V_{SD} and gate voltage V_T near the 2↔3 electron transition, at $B_{||} = 10$ T. (b) *Left*: Ground state spin configuration for a three-electron dot. *Right*: Spin configuration of the excited state that can be reached starting at line B in (a).

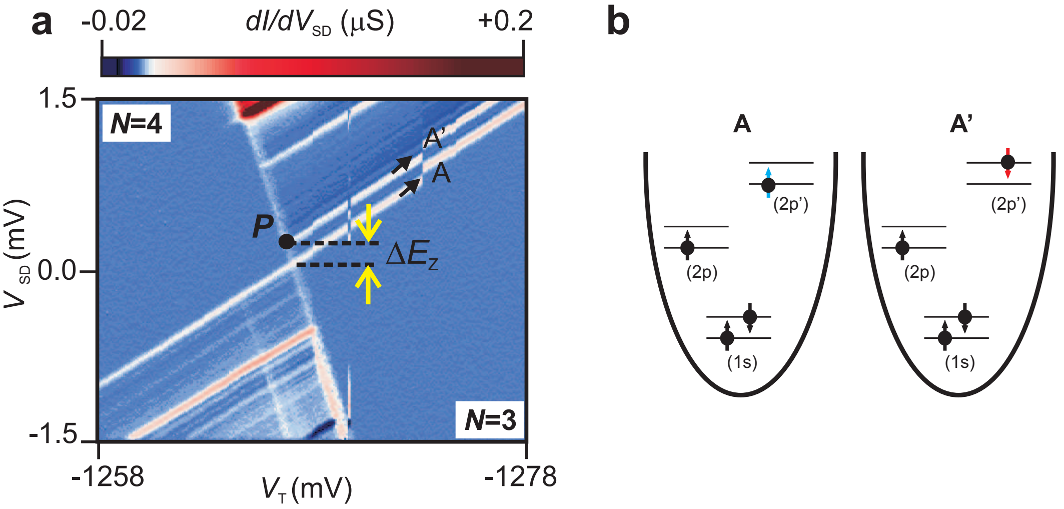

Figure 4.6: (a) Color scale plot of the differential conductance dI/dV_{SD} as a function of V_{SD} and gate voltage V_T near the 3↔4 electron transition, at $B_{||} = 10$ T. (b) *Left*: Ground state spin configuration of the four-electron dot ($S = 1$). *Right*: Spin configuration of one possible spin-excited state, where the (2p') orbital is occupied by a spin-down electron.

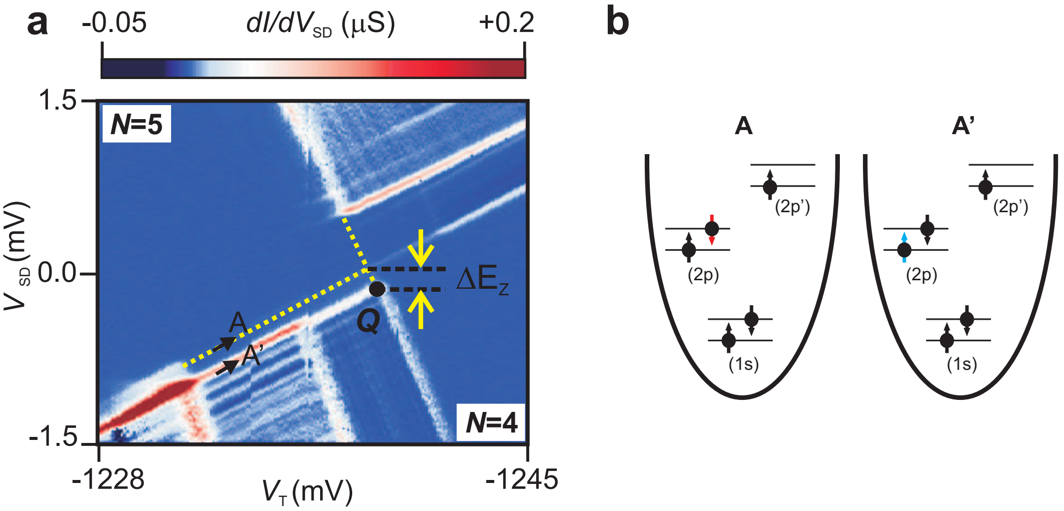

Figure 4.7: (a) Color scale plot of the differential conductance dI/dV_{SD} as a function of V_{SD} and gate voltage V_T near the 4↔5 electron transition, at $B_{||} = 10$ T. (b) *Left*: Ground state spin configuration of a five-electron dot. *Right*: Spin configuration of the spin-excited state. In both cases, the total spin is $S = 1/2$.

Chapter 5

Zeeman energy and spin relaxation of a single electron

R. Hanson, B. Witkamp, L. M. K. Vandersypen,
L. H. Willems van Beveren, J. M. Elzerman
and L. P. Kouwenhoven

In this chapter, we study the spin states of a single electron confined in a quantum dot. In a magnetic field, applied parallel to the two-dimensional electron gas in which the quantum dot is defined, Zeeman splitting of the orbital states is directly observed by measurements of electron transport through the dot. By applying short voltage pulses, we can populate the excited spin state with one electron and monitor relaxation of the spin. We find a lower bound on T_1 of 50 μs at 7.5 T, only limited by our signal-to-noise ratio. A continuous measurement of the charge on the dot has no observable effect on the spin relaxation.

This chapter has been published in Physical Review Letters **91**, 196802 (2003).

5.1 Introduction

The electron spin states in quantum dots (QDs) are expected to be very stable, because the zero-dimensionality of the electron states in QDs leads to a significant suppression of the most effective 2D spin-flip mechanisms [1]. Relaxation between Zeeman sublevels in closed GaAs QDs is expected to be dominated by hyperfine interaction with the nuclei at magnetic fields below 0.5 T [3] and by spin-orbit interaction at higher fields [4]. At 1 T, theory predicts a T_1 of 1 ms in GaAs [4].

For comparison, in n-doped self-assembled InAs QDs containing one resident electron, pump-probe photoluminescence measurements gave a single-electron spin relaxation time of 15 ns (at B=0 T, T= 10 K) [5]. In undoped self-assembled InAs QDs, the exciton polarization is frozen throughout the exciton lifetime, giving a relaxation time >20 ns [6].

Electrical measurements of the single-electron spin relaxation time have up to now remained elusive. In vertical QDs, where electrical measurements on a single electron were reported almost a decade ago [7], it has been difficult to directly resolve the Zeeman splitting of orbitals [8]. As demonstrated in chapter **??**, the one-electron regime was also reached in single [9] and double lateral GaAs QDs [10], which are formed electrostatically within a two-dimensional electron gas (2DEG) by means of surface gates.

In this chapter we study the spin states of a one-electron lateral QD directly, by performing energy spectroscopy and relaxation measurements. We observe a clear Zeeman splitting of the orbital states in electron transport measurements through the QD, and find no signature of spin relaxation in our experimental time window, leading to a lower bound on T_1 of 50 μs. This lower bound is two to three orders of magnitude longer than spin relaxation times observed in bulk n-type GaAs [11], GaAs quantum wells [12] and InAs QDs [5].

5.2 Zeeman energy

The quantum dot is defined in a GaAs/Al$_{0.3}$Ga$_{0.7}$As heterostructure, containing a 2DEG 90 nm below the surface with an electron density $n_s = 2.9 \times 10^{11}$ cm^{-2} (Fig. 5.1a). A magnetic field (0-14 T) is applied parallel to the 2DEG. All measurements are performed in a dilution refrigerator at base temperature T = 20 mK.

We tune the device to the few-electron regime and identify the 0↔1 electron transition by the absence of further transitions under applied source-drain voltage up to 10 mV. The electron number is confirmed by using the nearby QPC as a charge detector [14, 10, 15]. We find a charging energy of 2.4 meV and an orbital

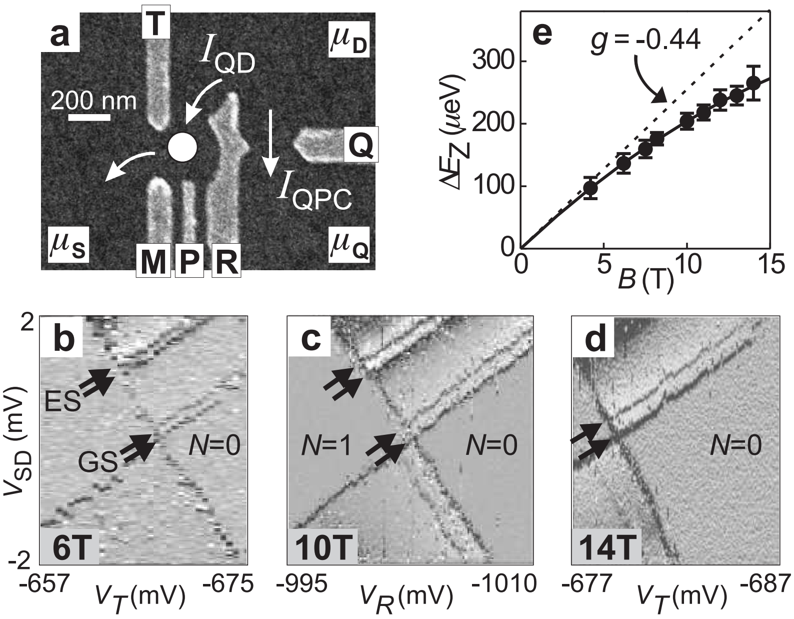

Figure 5.1: **(a)** Scanning Electron Micrograph of the metallic surface gates [13]. Gates M, R and T are used to form the quantum dot indicated by a white circle. Additionally, gate Q can be used to form a quantum point contact (QPC). To apply high-frequency signals, gate P is connected to a coaxial cable. Currents through the dot, I_{QD}, and through the QPC, I_{QPC}, are measured as a function of applied bias voltage, $V_{SD} = (\mu_S - \mu_D)/e$ and $V_{QD} = (\mu_Q - \mu_D)/e$ respectively. **(b)-(d)** Differential conductance dI_{QD}/dV_{SD} as a function of V_{SD} and gate voltage near the 0↔1 electron transition, at parallel magnetic fields of 6, 10 and 14 T. Darker corresponds to larger dI_{QD}/dV_{SD}. The zero-field spin degeneracy of both the ground state (GS) and the first orbital excited state (ES) is lifted by the Zeeman energy as indicated by arrows. **(e)** Extracted Zeeman splitting ΔE_Z as a function of B. At high fields a clear deviation from the bulk GaAs g-factor of -0.44 (dashed line) is observed.

level spacing of 1.1 meV at $B = 0$ T.

In a parallel magnetic field, the electron states acquire a Zeeman energy shift, which causes the orbital levels to split by $\Delta E_Z = g\mu_B B$ [16]. Figs. 5.1b-d show stability diagrams [7] around the 0↔1 electron transition, measured at $B = 6$ T, 10 T and 14 T. A clear Zeeman splitting of both ground and first orbital excited state is seen directly in this spectroscopy measurement [17]. (Because of the large asymmetry in the tunnel barriers, the visibility of the Zeeman splitting is very different for positive and for negative bias [18].) Using this measurement technique, we can extract the value of the Zeeman splitting ΔE_Z. In Fig. 5.1e, ΔE_Z is plotted as a function of B. At high fields a clear deviation from the bulk GaAs g-factor of -0.44 (dashed line) is observed.

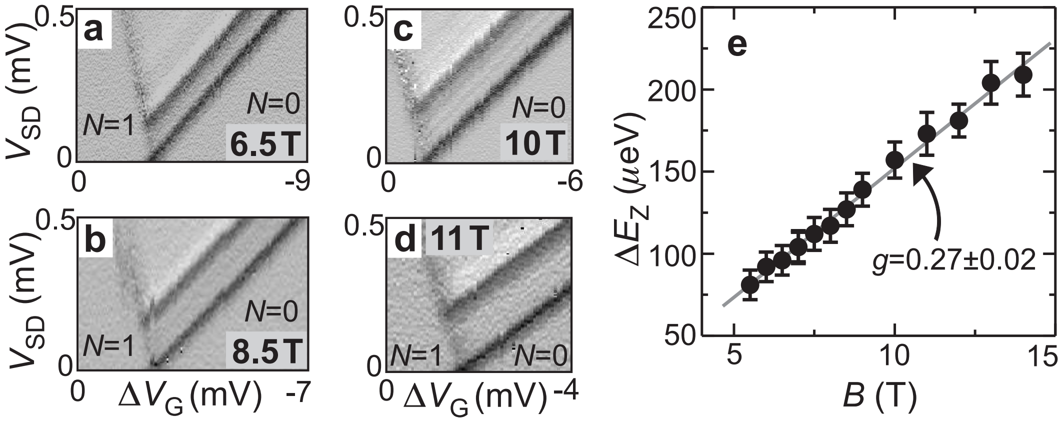

Figure 5.2: (a)-(d) High source-drain bias measurements similar to Fig. 5.1(b)-(d) on a different heterestructure, with a 2DEG 60 nm below the surface, for in-plane magnetic fields of (a) 6.5 T, (b) 8.5 T, (c) 10 T, and (d) 11 T. **(e)** Extracted Zeeman splitting ΔE_Z as a function of B. The value of $|g|$ is 0.27 for all fields.

A least-squares fit of the data to a second-order polynomial, which extrapolates with negligible deviation to the origin, gives

$$|g| = (0.43 \pm 0.04) - (0.0077 \pm 0.0020)\, B\ (T)\ , \tag{5.1}$$

similar to early measurements on 2DEGs [19]. If we force the fit to be linear in B, we get $|g|=0.29 \pm 0.01$, with a zero-field splitting $\Delta E_{Z,B=0}$=$(34 \pm 6)\mu$eV.

For comparison, we present similar measurements on a different heterostructure, where the 2DEG is 60 nm below the surface. Figure 5.2a-d show high source-drain bias measurements around the 0↔1 electron transition for different in-plane magnetic fields. The extracted B-dependence of ΔE_Z is given in Fig. 5.2e. The value of the g-factor, $|g| = 0.27 \pm 0.02$, is significantly smaller than the bulk value. Furthermore, in contrast to the data in Fig. 5.1e, there is no dependence on magnetic field.

Factors which can influence the magnetic field dependence of the g-factor include: (1) extension of the electron wave function into the $Al_{0.3}Ga_{0.7}As$ region, where $g = +0.4$ [20, 21], (2) thermal nuclear polarization, which decreases the effective magnetic field through the hyperfine interaction [22], (3) dynamic nuclear polarization due to electron-nuclear flip-flop processes in the dot, which enhances the effective magnetic field [22], (4) the nonparabolicity of the GaAs conduction band [20] and (5) the spin-orbit coupling [23]. Factors 2 and 3 can not explain our data, since they do not depend on the heterostructure. More experiments are needed to separate the other effects, e.g. by measuring the dependence of the g-factor on the orientation of the in-plane magnetic field [23]. However, this is outside the scope of this research. In the remaining part of the chapter, we will use the device shown in Fig. 5.1a.

5.3 Measuring the spin relaxation time

The two spin states $|\uparrow\rangle$ (lowest energy) and $|\downarrow\rangle$ can be used as the basis states of a quantum bit [24, 25]. In order to perform quantum operations and to allow sufficient time for read-out of the quantum bit, it is necessary that the spin excited state $|\downarrow\rangle$ be stable. We investigate this by measuring the relaxation time from $|\downarrow\rangle$ to $|\uparrow\rangle$. By applying short pulses to gate P, we can modulate the potential of the dot and thus the position of the energy levels relative to the electrochemical potentials of the leads, μ_S and μ_D. This enables us to populate the spin excited state $|\downarrow\rangle$ and monitor relaxation to $|\uparrow\rangle$. The applicability of various pulse methods for measuring the spin relaxation time depends on two timescales. If the relaxation rate W $(=1/T_1)$ is at least of the same order as the outgoing tunnel rate Γ_D, i.e. $W \geq \Gamma_D$, we can determine T_1 by applying single-step pulses. This method has previously been used to measure the relaxation time between orbital levels in a QD (~10 ns) [2]. In the other limit, $W < \Gamma_D$, a more elaborate method using double-step pulses is needed [2]. We proceed as follows. First, we apply single-step pulses to show that $W < \Gamma_D$. Then we apply double-step pulses to measure T_1. All data shown are taken at $B = 7.5$ T, and reproduced at 14 T. At fields below 6 T the Zeeman splitting is too small to be resolved in pulse experiments. The bias voltage is always much smaller than the charging energy, thus allowing at most one electron on the dot.

5.4 Spin relaxation measurement using single-step pulses

The single-step pulses are schematically depicted in Fig. 5.3a. Fig. 5.3b shows current traces for different amplitudes of the pulses. Transport of electrons through the ground state takes place when $|\uparrow\rangle$ lies in the bias window (i.e. $\mu_S > E_\uparrow > \mu_D$). When we apply single-step pulses, this condition is met at two different values of the gate voltage V_T and therefore the Coulomb peak splits in two. Fig. 5.3c shows the positions of the energy levels during the two phases of the pulse for the left peak in Fig. 5.3b. Here, electrons flow from source to drain during the "high" phase of the pulse. Similarly, Fig. 5.3e corresponds to the right peak in Fig. 5.3b, where ground state transport occurs during the "low" phase of the

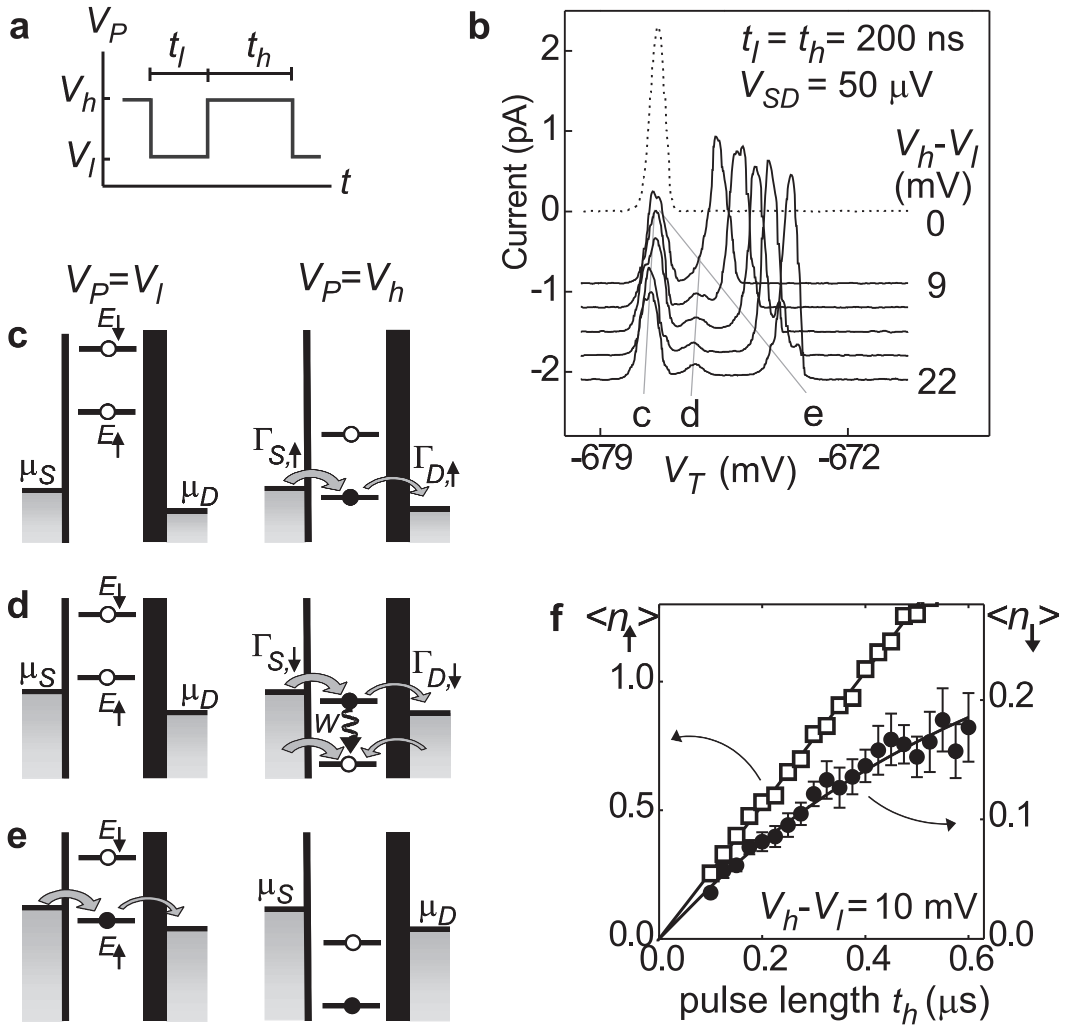

Figure 5.3: One-electron spin relaxation studied using single-step pulses at 7.5T. **(a)** Schematic waveform of the pulse train (rise/fall time of 0.2 ns). **(b)** Current traces under applied pulses, offset for clarity. **(c)-(e)** Diagrams showing the position of the energy levels during the two phases of the pulse for three different gate voltage settings, corresponding to the three peaks in (b). **(f)** Average number of electrons tunneling per cycle ($=I(t_l+t_h)/e$) through the ground state $<n_\uparrow>$, as in (c), and through the excited state $<n_\downarrow>$, as in (d), vs. pulse length t_h. The $<n_\uparrow>$ shows no decay, as expected for a stable current, whereas $<n_\downarrow>$ saturates. However, this saturation is not due to spin relaxation (see text).

pulse. When the pulse amplitude exceeds the Zeeman splitting ($\approx$160 μeV), an extra current peak becomes clearly visible. This peak is due to transient transport via the spin-down state $|\downarrow\rangle$ during the "high" phase of the pulse (Fig. 5.3d). The transient current flows until $|\uparrow\rangle$ becomes occupied and Coulomb blockade prohibits other electrons to enter the dot. Occupation of $|\uparrow\rangle$ can happen either via tunneling of an electron from the leads into $|\uparrow\rangle$ when the dot is empty, or by spin relaxation from $|\downarrow\rangle$ to $|\uparrow\rangle$. For both these processes, the probability to have occurred increases with time. Therefore, the number of electrons tunneling via $|\downarrow\rangle$ per cycle, $<n_\downarrow>$, saturates with increasing pulse length t_h. In particular, if the tunnel rate Γ_S through the incoming barrier is much larger than the tunnel rate Γ_D through the outgoing barrier, i.e. $\Gamma_S \gg \Gamma_D$ [26], it can be shown that [18, 27]

$$<n_\downarrow> \simeq A\Gamma_{D,\downarrow}(1-e^{-Dt_h})/D \ , \tag{5.2}$$

where $A \simeq \Gamma_{S,\downarrow}/(\Gamma_{S,\uparrow}+\Gamma_{S,\downarrow})$ is the injection efficiency into $|\downarrow\rangle$, and $\Gamma_{D,\downarrow}$ is the tunnel rate from $|\downarrow\rangle$ to the drain (see Fig. 5.3c-d). The saturation rate D is the sum of W, the spin relaxation rate from $|\downarrow\rangle$ to $|\uparrow\rangle$, and $(1–A)\Gamma_{D,\downarrow}$, which accounts for direct tunneling into $|\uparrow\rangle$:

$$D = W + (1–A)\Gamma_{D,\downarrow} \ . \tag{5.3}$$

By measuring $<n_\downarrow>$ for different pulse widths t_h, we can find D and $A\Gamma_{D,\downarrow}$ using Eq. (5.2). Together with the value of A, which can be extracted from large-bias measurements without pulses, we can determine the spin-relaxation rate W=$1/T_1$ via Eq. (5.3).

In Fig. 5.3f we show the average number of tunneling electrons per cycle for the stable current, $<n_\uparrow>$, and for the transient current, $<n_\downarrow>$. Clearly, $<n_\uparrow>$ increases linearly with pulse length, whereas $<n_\downarrow>$ saturates, as expected. From fitting $<n_\downarrow>$ to Eq. (5.2) we find D=(1.5 ± 0.2) MHz and $A\Gamma_{D,\downarrow}$=(0.47 ± 0.09) MHz. Furthermore, A=(0.28 ± 0.05), leading to $(1–A)\Gamma_{D,\downarrow}$=(1.2 ± 0.3) MHz and W=(0.30± 0.35) MHz. Averaging over similar measurements, using different tunnel rates and t_l, leads to W=(0.20± 0.25) MHz.

We conclude that the spin relaxation rate (W<0.5 MHz) is much smaller than the tunnel rates ($\Gamma_S \gg \Gamma_D \approx 1.6$ MHz). This means that the decay of the transient current is dominated by direct injection into $|\uparrow\rangle$, and therefore the single-step pulse method can only provide a weak lower bound on T_1. To circumvent this, we decouple the read-out stage from the relaxation stage by inserting an extra pulse step. This way, an electron can only tunnel out of the dot *after* the waiting time, enabling us to directly measure the relaxation probabilities as a function of waiting time [2], as explained below.

5.5 Spin relaxation measurement using double-step pulses

The schematic waveform of the double-step pulses is shown in Fig. 5.4a. Applying these pulses results in current traces as in Fig. 5.4b. Figs. 5.4c-e depict the energy levels for the $|\downarrow\rangle$ current peak indicated in Fig. 5.4b at the three different stages of the pulse cycle. First the dot is emptied (Fig. 5.4c). In the second stage (Fig. 5.4d), an electron tunnels into either $|\downarrow\rangle$ or $|\uparrow\rangle$. Again, due to the charging energy only one electron can occupy the dot. The probability that it enters $|\downarrow\rangle$, A, does not depend on the pulse lengths, which are the only parameters we change. If the electron entered $|\downarrow\rangle$, the probability that it has *not* relaxed to $|\uparrow\rangle$ after t_h is exp(-t_h/T_1) (we assume exponential decay).

Finally (Fig. 5.4e), if the electron is in $|\downarrow\rangle$, it can tunnel out, but only to the drain. In contrast, if the electron is in $|\uparrow\rangle$, it can tunnel out to either the source or the drain when the cycle is restarted (Fig. 5.4c). Similarly, electrons entering the dot originate from the source or the drain (Fig. 5.4d). Assuming that Γ_S/Γ_D is constant throughout the cycle, the average current generated by electrons leaving the dot during the "low" phase of the pulse train (Fig. 5.4c) is zero. Therefore the current only consists of electrons that entered $|\downarrow\rangle$ and have not relaxed during t_h:

$$I = ef_{rep} <n_\downarrow> = \; ef_{rep}CA\, e^{(-t_h/T_1)}, \tag{5.4}$$

where f_{rep} is the pulse repetition frequency and C a constant accounting for the tunnel probability in the read-out stage. We determine $<n_\downarrow>$ for different t_h. Normalized to the value for t_h=0, it is a direct measure of spin relaxation:

$$\frac{<n_\downarrow>_{t_h=t}}{<n_\downarrow>_{t_h=0}} = \frac{CA\, e^{(-t/T_1)}}{CA\, e^{(-0/T_1)}} = \frac{P_\downarrow(t)}{P_\downarrow(0)} = e^{(-t/T_1)}\ . \tag{5.5}$$

To be able to extract reliable peak heights from the very small currents, we average over many traces. Examples of averaged curves are shown in Fig. 5.4f for t_h=1, 2.5 and 4 μs. In Fig. 5.4g, data extracted from these and similar curves are plotted as a function of t_h, up to 7.5 μs. Longer waiting times result in unmeasurably small currents ($I \propto 1/t_h$). The two data sets shown were taken with different gate settings (and thus different tunnel rates) and different t_m. As a guide to the eye, lines corresponding to an exponential decay with decay times $\tau = 10\,\mu$s, $\tau = 30\,\mu$s and $\tau = \infty$ are included. There is no clear decay visible. We fit the data in Fig. 5.4g and similar data, and average the resulting relaxation

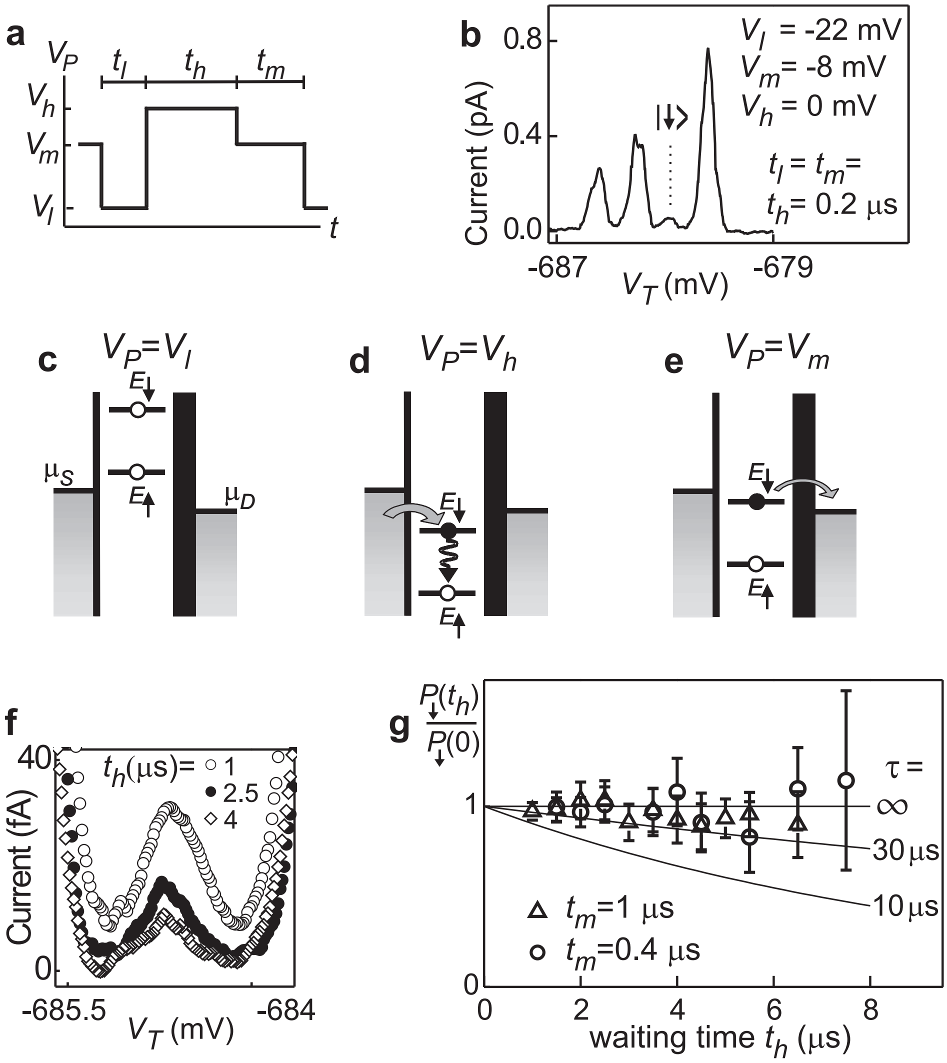

Figure 5.4: One-electron spin relaxation studied using double-step pulses at 7.5T. **(a)** Schematic waveform of the pulse train (rise/fall time of 1.5 ns). **(b)** Typical pulse-excited current trace. The three main peaks correspond to a stable current flowing via $|\uparrow\rangle$ when $|\uparrow\rangle$ is in the bias window during one of the three stages of the waveform. The small peak is due to transient current via $|\downarrow\rangle$ for $V_P = V_m$ [28]. **(c)-(e)** Diagrams depicting the energy levels during the three stages of the pulse for the $|\downarrow\rangle$-peak shown in (b). **(c)** The dot is emptied during a time t_l. **(d)** Both $|\uparrow\rangle$ and $|\downarrow\rangle$ lie below the electrochemical potentials of the leads and an electron can tunnel into the $|\downarrow\rangle$; other possible tunnel processes are not indicated since they do not contribute to the current (see text). We allow the electron to relax for a time t_h. **(e)** Now $|\downarrow\rangle$ lies in the bias window. Only if the electron has spin-down it can tunnel out and contribute to current. **(f)** Averaged $|\downarrow\rangle$ current peaks for t_h=1, 2.5 and 4 μs with t_m=0.4 μs (for data in (f) and (g) t_l=t_h). **(g)** The probability $P_\downarrow(t_h)/P_\downarrow(0)$ that the spin did *not* decay during the waiting time t_h.

rates. From an error analysis we find a lower bound of $T_1 > 50\ \mu$s. We emphasize that, since we do not observe a clear signature of relaxation in our experimental time window, T_1 might actually be much longer.

5.6 Back-action of the QPC

The lower bound we find for T_1 is much longer than the time needed for read-out of the quantum bit using proposed spin-to-charge conversion schemes [25]. In these schemes, spin-dependent tunneling events correlate the charge on the dot to the initial spin state. A subsequent charge measurement thus reveals information on the spin. This can de done in our device using the QPC located next to the QD (see Fig. 5.1a) [10].

An interesting question is how much the stability of the spin states is affected by such charge measurements. We have studied this by sending a large current through the QPC, set at maximum charge sensitivity, and repeating the T_1 measurements. The drain lead is shared by the QPC- and the QD-current, which causes some peak broadening and limits the experimental window. However, even for a very large current of ~20 nA through the QPC ($\mu_Q - \mu_D = 500\,\mu eV$), we still do not find a measurable decay of the spin. For comparison, we can measure the charge on the QD within 50 μs using a QPC current of only 10 nA [29]. Taking these measurements together shows that, by using spin-to-charge conversion, it should be possible to perform single-shot spin readout in this device. In chapter 7 we will proceed on this path.

We thank T. Fujisawa, S. Tarucha, T. Hayashi, T. Saku, Y. Hirayama, S. I. Erlingsson, Y. V. Nazarov, O. N. Jouravlev, S. De Franceschi, D. Gammon and R. N. Schouten for discussions and help. This work was supported by the DARPA-QUIST program.

References

[1] A. V. Khaetskii and Y. V. Nazarov, Phys. Rev. B **61**, 12639 (2000).

[2] T. Fujisawa *et al.*, Nature (London) **419**, 278 (2002).

[3] S. I. Erlingsson and Y. V. Nazarov, Phys. Rev. B **66**, 155327 (2002).

[4] A. V. Khaetskii and Y. V. Nazarov, Phys. Rev. B **64**, 125316 (2001).

[5] S. Cortez *et al.*, Phys. Rev. Lett. **89**, 207401 (2002).

[6] M. Paillard *et al.*, Phys. Rev. Lett. **86**, 1634 (2001).

[7] For a review on few-electron vertical QDs, see L. P. Kouwenhoven, D. G. Austing and S. Tarucha, Rep. Prog. Phys. **64** (6), 701 (2001).

[8] S. Sasaki, D. G. Austing and S. Tarucha, Physica B **256**, 157-160 (1998); J. Könemann, P. König, R. J.Haug, Physica E **13**, 675 (2002).

[9] M. Ciorga *et al.* , Phys. Rev. B **61**, R16315 (2000).

[10] J. M. Elzerman *et al.*, Phys. Rev. B. **67**, 161308(R) (2003).

[11] J. M. Kikkawa and D. D. Awschalom, Phys. Rev. Lett. **80**, 4313 (1998).

[12] Y. Ohno *et al.*, Phys. Rev. Lett. **83**, 4196 (1999).

[13] For clarity, we have hidden the surface gates that are not used in the experiments. The complete gate structure can be found in Ref. [10].

[14] M. Field *et al.*, Phys. Rev. Lett. **70**, 1311 (1993).

[15] D. Sprinzak *et al.*, Phys. Rev. Lett. **88**, 176805 (2002).

[16] J. Weis *et al.*, Surface Science 305, 664 (1994).

[17] Similar values for $|g|$ below 9 T are reported by R. M. Potok *et al.*, Phys. Rev. Lett. **91**, 016802 (2003).

[18] T. Fujisawa, Y. Tokura and Y. Hirayama, Physica B **298**, 573-579 (2001).

[19] M. Dobers, K. v. Klitzing and G. Weimann, Phys. Rev. B **38**, 5453 (1988).

[20] M. J. Snelling *et al.*, Phys. Rev. B **44**, 11345 (1991).

[21] G. Salis *et al.*, Nature (London) **414**, 619 (2001).

[22] See, e.g., *Optical Orientation*, edited by F. Meier and B. P. Zakharchenya, (North-Holland, 1984).

[23] V. I. Fal'ko, B. L. Altschuler and O. Tsyplyatev, cond-mat/0501046 (2005).

[24] D. Loss and D. P. DiVincenzo, Phys. Rev. A **57**, 120 (1998).

[25] L. M. K. Vandersypen *et al.*, in *Quantum Computing and Quantum Bits in Mesoscopic Systems* (Kluwer Academic, New York, 2003); quant-ph/0207059.

[26] The condition $\Gamma_S \gg \Gamma_D$ is easily achieved by tuning the different gate voltages.

[27] T. Fujisawa, Y. Tokura and Y. Hirayama, Phys. Rev. B **63**, R081304 (2001).

[28] The $|\downarrow\rangle$ peak for V_h appears at the same voltage on T as the $|\uparrow\rangle$ peak belonging to V_m.

[29] L. M. K. Vandersypen *et al.*, Appl. Phys. Lett. **85**, 4394 (2004).

Chapter 6

Excited-state spectroscopy on a nearly closed quantum dot via charge detection

J. M. Elzerman, R. Hanson, L. H. Willems van Beveren,
L. M. K. Vandersypen and L. P. Kouwenhoven

In this chapter, we demonstrate a method for measuring the discrete energy spectrum of a quantum dot connected very weakly to a single lead. A train of voltage pulses applied to a metal gate induces tunneling of electrons between the quantum dot and a reservoir. The effective tunnel rate depends on the number and nature of the energy levels in the dot made accessible by the pulse. Measurement of the charge dynamics thus reveals the energy spectrum of the dot, as demonstrated for a dot in the few-electron regime.

This chapter has been published in Applied Physics Letters **84**, 4617 (2004).

6.1 Introduction

Few-electron quantum dots are considered as qubits for quantum circuits, where the quantum bit is stored in the spin or orbital state of an electron in a single or double dot. The elements in such a device must have functionalities such as initialization, one- and two-qubit operations and read-out [1]. For all these functions it is necessary to have precise knowledge of the qubit energy levels. Standard spectroscopy experiments involve electron transport through the quantum dot while varying both a gate voltage and the source-drain voltage [2]. This requires that the quantum dot be connected to two leads with a tunnel coupling large enough to obtain a measurable current [3].

Coupling to the leads unavoidably introduces decoherence of the qubit: even if the number of electrons on the dot is fixed due to Coulomb blockade, an electron can tunnel out of the dot and be replaced by another electron through a second-order tunneling process, causing the quantum information to be irretrievably lost. Therefore, to optimally store qubits in quantum dots, higher-order tunneling has to be suppressed, i.e. the coupling to the leads must be made as small as possible. Furthermore, real-time observation of electron tunneling, important for single-shot read-out of spin qubits via spin-to-charge conversion, also requires a small coupling of the dot to the leads. In this regime, current through the dot would be very hard or even impossible to measure. Therefore an alternative spectroscopic technique is needed, which does not rely on electron transport through the quantum dot.

Here we present spectroscopy measurements using charge detection. Our method resembles experiments on superconducting Cooper-pair boxes and semiconductor disks which have only one tunnel junction so that no net current can flow. Information on the energy spectrum can then be obtained by measuring the energy for adding an electron or Cooper-pair to the box, using a single-electron transistor (SET) operated as a charge detector [4, 5, 6]. We are interested in the excitation spectrum for a given number of electrons on the box, rather than the addition spectra. We use a quantum point contact (QPC) as an electrometer [7] and excitation pulses with repetition rates comparable to the tunnel rates to the lead, to measure the discrete energy spectrum of a nearly isolated one- and two-electron quantum dot.

6.2 Tuning the tunnel barriers

The quantum dot and QPC are defined in the two-dimensional electron gas (2DEG) in a GaAs/$\mathrm{Al_{0.27}Ga_{0.73}As}$ heterostructure by dc voltages on gates T, M, R

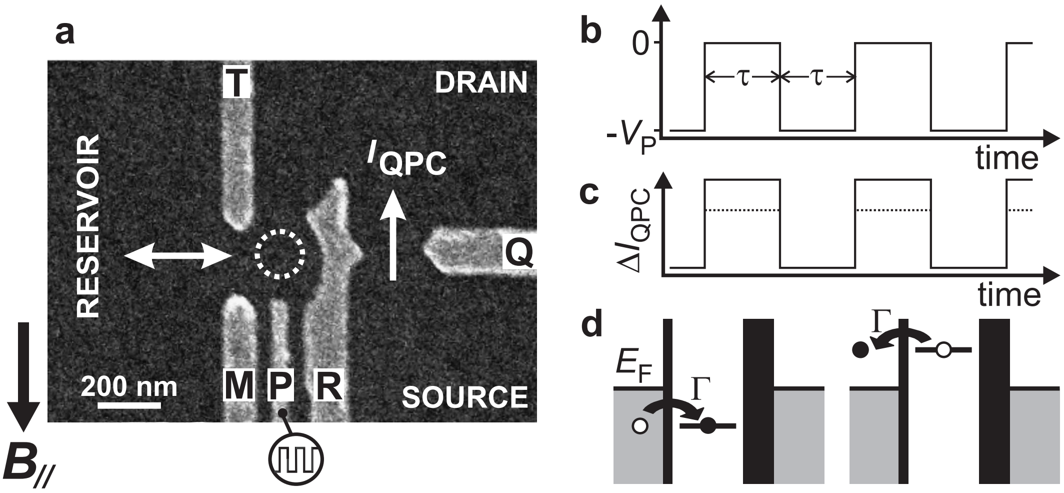

Figure 6.1: QPC response to a pulse train applied to the plunger gate. **(a)** Scanning electron micrograph of a quantum dot and quantum point contact, showing only the gates used in the present experiment (the complete device is described in ref. [8]) and section 2.4. **(b)** Pulse train applied to gate P. **(c)** Schematic response in QPC current, ΔI_{QPC}, when the charge on the dot is unchanged by the pulse (solid line) or increased by one electron charge during the 'high' stage of the pulse (dashed). **(d)** Schematic electrochemical potential diagrams during the high (left) and low (right) pulse stage, when the ground state is pulsed across the Fermi level in the reservoir, E_F.

and Q (Fig. 6.1a). The dot's plunger gate, P, is connected to a coaxial cable, to which we can apply voltage pulses (rise time 1.5 ns). The QPC charge detector is operated at a conductance of about e^2/h with source-drain voltage $V_{SD} = 0.2$ mV. All data are taken with a magnetic field $B_{//} = 10$ T applied in the plane of the 2DEG, at an effective electron temperature of about 300 mK.

We first describe the procedure for setting the gate voltages such that tunneling in and out of the dot take place through one barrier only (i.e. the other is completely closed), and the remaining tunnel rate be well controlled. For gate voltages far away from a charge transition in the quantum dot, a pulse applied to gate P (Fig. 6.1b) modulates the QPC current via the cross-capacitance only (solid trace in Fig. 6.1c). Near a charge transition, the dot can become occupied with an extra electron during the high stage of the pulse (Fig. 6.1d). The extra electron on the dot reduces the current through the QPC. The QPC response to the pulse is thus smaller when tunneling takes place (dotted trace in Fig. 6.1c). We denote the amplitude of the difference between solid and dotted traces as the 'electron response'.

Now, even when tunneling is allowed energetically, the electron response is only non-zero when an electron has sufficient time to actually tunnel into the dot

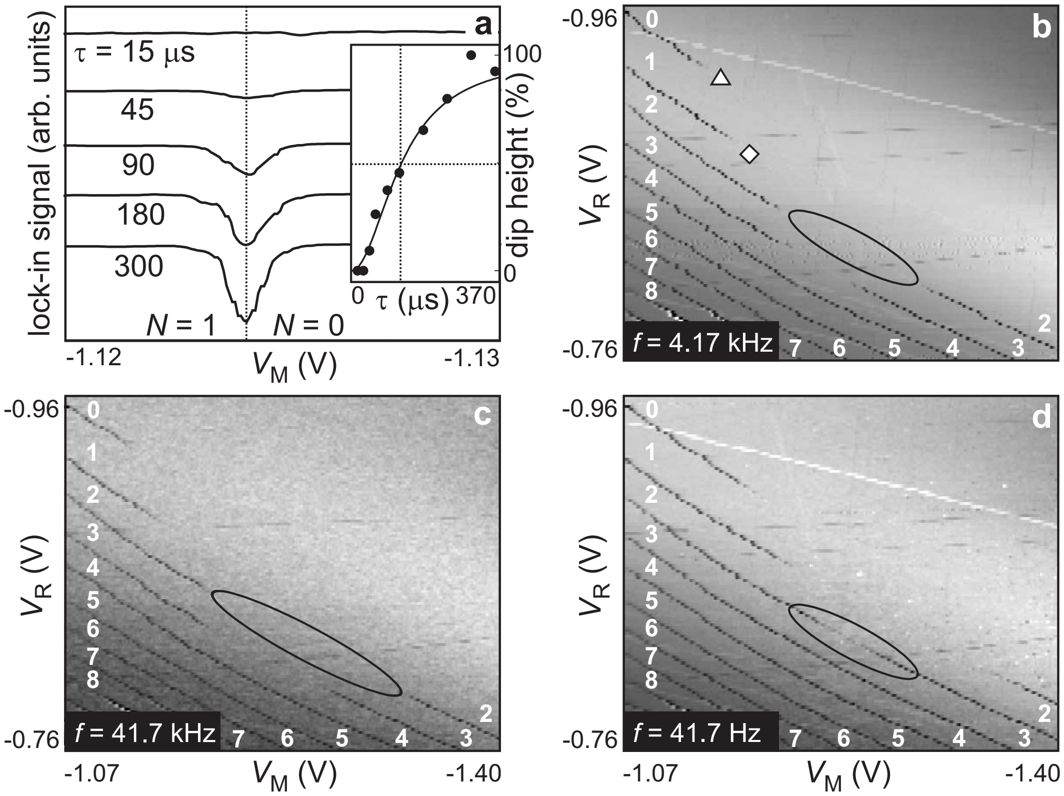

Figure 6.2: Lock-in detection of electron tunneling. **(a)** Lock-in signal at $f = 1/(2\tau)$ versus V_M for different pulse times, τ, with $V_P = 1$ mV. The dip due to the electron response disappears for shorter pulses. (Individual traces have been lined up horizontally to compensate for a fluctuating offset charge, and have been given a vertical offset for clarity.) (Inset) Height of the dip versus τ, as a percentage of the maximum height (obtained at long τ). Circles: experimental data. Dashed lines indicate the pulse time ($\tau \approx 120$ μs) for which the dip size is half its maximum value. Solid line: calculated dip height using $\Gamma = (40\ \mu\text{s})^{-1}$. **(b)** Lock-in signal in grayscale versus V_M and V_R for $V_P = 1$ mV and $f = 4.17$ kHz. Dark lines correspond to dips as in (a), indicating that the electron number changes by one. White labels indicate the absolute number of electrons on the dot. **(c)** Same plot as in (b), but with larger pulse repetition frequency ($f = 41.7$ kHz). **(d)** Same plot as in (b), but with smaller pulse repetition frequency ($f = 41.7$ Hz).

during the pulse time, τ. By measuring the electron response as a function of τ, we can extract the tunnel rate, Γ, as demonstrated in Fig. 6.2a. We apply a pulse train to gate P with equal up and down times, so the repetition rate is $f = 1/(2\tau)$ (Fig. 6.1b). The QPC response is measured using lock-in detection at frequency f [9], and is plotted versus the dc voltage on gate M. For long pulses (lowest curves) the traces show a dip, which is due to the electron response when crossing the zero-to-one electron transition. Here, $f \ll \Gamma$ and tunneling occurs quickly on the scale of the pulse duration. For shorter pulses the dip gradually disappears. We find analytically (see the Appendix in [10]) that the dip height is proportional to $1 - \pi^2/(\Gamma^2\tau^2 + \pi^2)$, so the dip height should equal half its maximum value when $\Gamma\tau = \pi$. From the data (inset to Fig. 6.2a), we find that this happens for $\tau \approx 120$ μs, giving $\Gamma \approx (40\ \mu\text{s})^{-1}$. Using this value for Γ in the analytical expression given above, we obtain the solid line in the inset to Fig. 6.2a, which nicely matches the measured data points.

We explore several charge transitions in Fig. 6.2b, which shows the lock-in signal in grayscale for $\tau = 120$ μs, i.e. $f = 4.17$ kHz. The slanted dark lines correspond to dips as in Fig. 6.2a. From the absence of further charge transitions past the topmost dark line, we obtain the absolute electron number starting from zero. In the top left region of Fig. 6.2b, the right tunnel barrier (between gates R and T) is much more opaque than the left tunnel barrier (between M and T). Here, charge exchange occurs only with the left reservoir (indicated as 'reservoir' in Fig. 6.1a). Conversely, in the lower right region charge is exchanged only with the drain reservoir. In the middle region, indicated for the two-to-three electron transition by an ellipse, both barriers are too opaque and no charge can flow into or out of the dot during the 120 μs pulse; consequently the electron response becomes zero and thus the dark line disappears. For shorter pulses, i.e. larger pulse repetition frequency, the region where the dark line disappears becomes wider (ellipse in Fig. 6.2c). For longer pulses the dark line reappears (Fig. 6.2d). By varying the voltages on gates M and R, we can thus precisely set the tunnel rate to the left or right reservoir for each charge transition.

6.3 Excited-state spectroscopy for $N = 1$

For spectroscopy measurements on a one-electron dot, we set the gate voltages near the zero-to-one electron transition at the point indicated as $\triangle$ in Fig. 6.2b. At this point, the dot is operated as a charge box, with all tunnel events occurring through just a single barrier. The pulse repetition rate is set to 385 Hz, so that the dip height is half its maximum value. The electron response is then very sensitive to changes in the tunnel rate, which occur when an excited state becomes accessible for tunneling.

Fig. 6.3a shows the electron response for a pulse amplitude larger than was used for the data in Fig. 6.2. The dip now exhibits a shoulder on the right side (indicated by 'b'), which we can understand as follows. Starting from the right ($N = 0$), the dip develops as soon as the ground state (GS) is pulsed across the

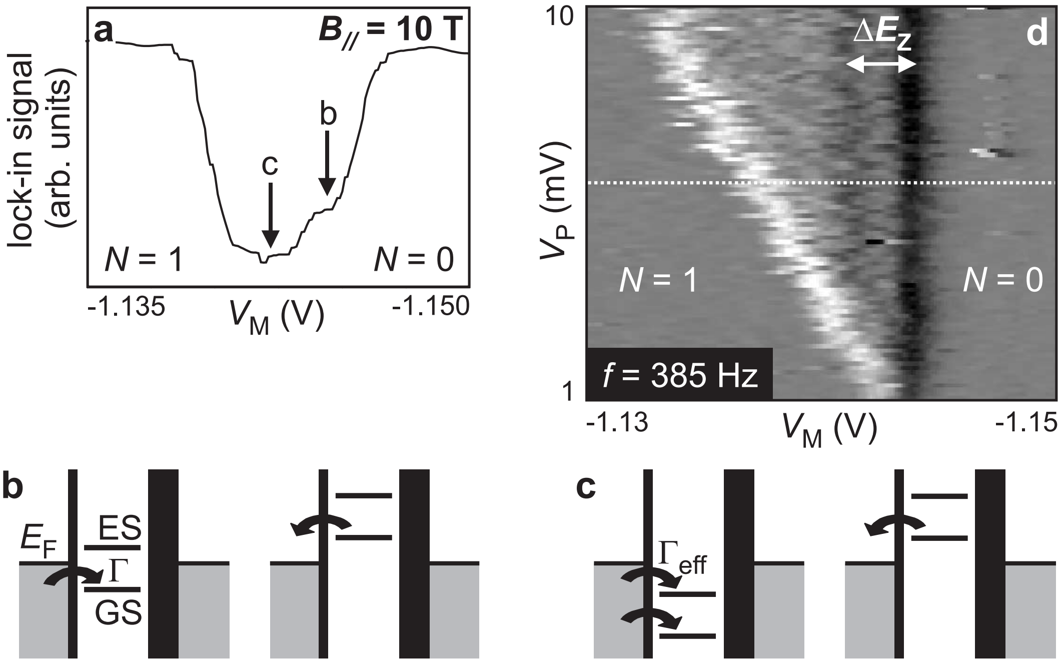

Figure 6.3: Excited-state spectroscopy in a one-electron dot. **(a)** Lock-in signal at $f = 385$ Hz versus V_M, with $V_P = 6$ mV. The dip is half the maximum value (obtained at low f and small V_P) from which we conclude that $\Gamma \approx 2.4$ kHz. **(b)** Schematic electrochemical potential diagrams for the case that only the GS is pulsed across E_F. **(c)** Idem when both the GS and an ES are pulsed across E_F. **(d)** Derivative of the lock-in signal with respect to V_M, plotted as a function of V_M and V_P (individual traces have been lined up to compensate for a fluctuating offset charge). The curve in (a) is taken at the dotted line. The Zeeman energy splitting between the one-electron GS (spin-up) and first ES (spin-down) is indicated by ΔE_Z.

Fermi level E_F and an electron can tunnel into the dot (Fig. 6.3b). As V_M is made less negative, we reach the point where both the GS and an excited state (ES) are pulsed across E_F (Fig. 6.3c). The effective rate for tunneling on the box is now the sum of the rate for tunneling in the GS and for tunneling in the ES, and as a result the dip becomes deeper (the electron response increases). When V_M is made even less negative, the one-electron GS lies below E_F during both stages of the pulse, so there is always one electron on the dot. The electron response is now zero and the dip ends.

The derivative of a set of curves as in Fig. 6.3a is plotted in Fig. 6.3d. Three lines are observed. The right vertical, dark line corresponds to the right flank of the dip in Fig. 6.3a, the onset of tunneling to the GS. The slanted bright line corresponds to the left flank of the dip in Fig. 6.3a (with opposite sign in the derivative) and reflects the pulse amplitude. The second, weaker, but clearly visible dark vertical line represents an ES. The distance between the two vertical lines is proportional to the energy difference between GS and ES.

We identify the ground and first excited state observed in this spectroscopy experiment as the spin-up and spin-down state of a single electron on the quantum dot. For $B_{//} = 10$ T, the Zeeman energy is about 0.21 meV [11], while the excitation energy of the first orbital excited state is of order 1 meV. The distance between the two vertical lines can, in principle, be converted to energy and directly provide the spin excitation energy. However, it is difficult to determine independently the conversion factor between gate voltage and energy in this regime of a nearly closed quantum dot. Instead we take the measured Zeeman splitting from an earlier transport measurement [11] and deduce the conversion factor from gate voltage to energy, $\alpha = 105$ meV/V. This value will be used below, to convert the two-electron data to energy.

6.4 Excited-state spectroscopy for $N = 2$

Fig. 6.4a shows pulse spectroscopy data for the one-to-two electron transition, taken with the gate settings indicated by $\diamond$ in Fig. 6.2b. The rightmost vertical line corresponds to transitions between the one-electron GS (spin-up) and the two-electron GS (spin singlet) only. As V_P is increased above 5 mV, the two-electron ES (spin triplet) also becomes accessible, leading to an enhanced tunnel rate [12]. This gives rise to the left vertical line, and the distance between the two vertical lines corresponds to the singlet-triplet energy splitting ΔE_{ST}. Converted to energy, we obtain $\Delta E_{ST} = 0.49$ meV.

Excitations of the one-electron dot can be made visible at the one-to-two electron transition as well, by changing the pulse frequency to 1.538 kHz (Fig. 6.4b). This is too fast for electrons to tunnel if only the GS is accessible, so the rightmost line almost vanishes. However, a second slanted line becomes visible (indicated by the arrow in Fig. 6.4b), corresponding not to an increased tunnel rate into the dot (due to an $N = 2$ ES), but to an increased tunnel rate out of the dot (due to an $N = 1$ ES). Specifically, if the pulse amplitude is sufficiently large, either the spin-up or the spin-down electron can tunnel out of the two-electron dot. This is explained schematically in Fig. 6.4c and d.

Similar experiments at the transition between two and three electrons, and for tunnel rates to the reservoir ranging from 12 Hz to 12 kHz, yield similar excitation spectra.

This work demonstrates that an electrometer such as a QPC can reveal not only the charge state of a quantum dot, but also its tunnel coupling to the outside

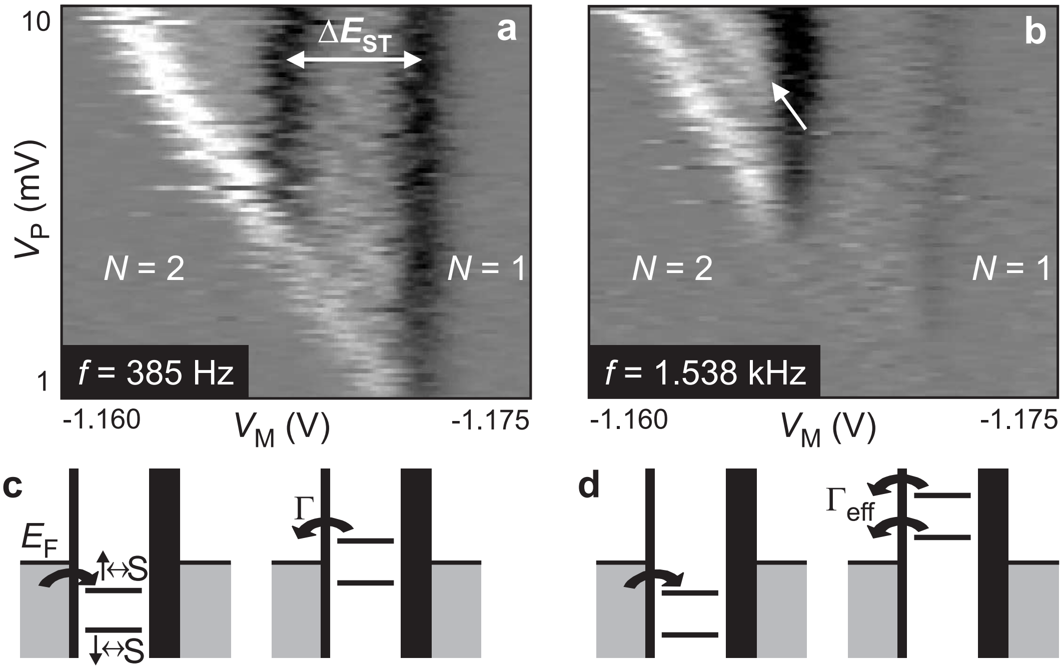

Figure 6.4: Excited state spectroscopy in a two-electron dot. **(a)** Similar to Fig. 6.3d, but for the one-to-two electron transition. Again, $f = 385$ Hz. We clearly observe the singlet-triplet splitting ΔE_{ST} (individual traces in (a) and (b) have been lined up). **(b)** Same experiment but with $f = 1.538$ kHz, which increases the contrast for excited states. An extra slanted line appears (arrow), corresponding to the $N = 1$ ES, spin-down. **(c)** Schematic electrochemical potential diagram for the case that only the spin-down electron can leave from the two-electron GS (spin singlet). This occurs to the left of the bright line indicated by the arrow in (b). **(d)** Idem when either the spin-up or the spin-down electron can leave from the spin singlet. This occurs to the right of the arrow in (b), and leads to a larger effective tunnel rate.

world and the energy level spectrum of its internal states. We can thus access all the relevant properties of a quantum dot, even when it is almost completely isolated from the leads.

We thank T. Fujisawa, S. Tarucha, T. Hayashi, T. Saku, Y. Hirayama and R. N. Schouten for useful discussions and experimental help. This work was supported by the DARPA-QUIST program, the ONR and the EU-RTN network on spintronics.

References

[1] D. Loss and D. P. DiVincenzo, Phys. Rev. A **57**, 120 (1998).

[2] L. P. Kouwenhoven *et al.*, in Mesoscopic Electron Transport, v. 345 of NATO Advanced Study Institutes, Ser. E: Applied Sciences, L. L. Sohn, L. P. Kouwenhoven and G. Schön, Eds., (Kluwer Academic, Dordrecht, 1997).

[3] M. Ciorga *et al.*, Phys. Rev. B **61**, R16315 (2000).

[4] P. Lafarge *et al.*, Zeitschrift für Physik B, **85**, 327 (1991).

[5] R. C. Ashoori *et al.*, Phys. Rev. Lett. **68**, 3088 (1992).

[6] K. W. Lehnert *et al.*, Phys. Rev. Lett. **90**, 027002 (2003).

[7] M. Field *et al.*, Phys. Rev. Lett. **70**, 1311 (1993).

[8] J. M. Elzerman *et al.*, Phys. Rev. B **67**, R161308 (2003).

[9] D. Sprinzak *et al.*, Phys. Rev. Lett. **88**, 176805 (2002).

[10] R. Hanson, Ph.D. thesis '*Electron spins in semiconductor quantum dots*', ISBN 90-901-9134-8, Delft University of Technology (2005).

[11] R. Hanson *et al.*, Phys. Rev. Lett. **91**, 196802 (2003).

[12] The expected Zeeman splitting of the triplet state is not resolved here.

Chapter 7

Single-shot read-out of a single electron spin using a difference in energy

J. M. Elzerman, R. Hanson, L. H. Willems van Beveren,
B. Witkamp, L. M. K. Vandersypen and L. P. Kouwenhoven

Spin is a fundamental property of all elementary particles. Classically it can be viewed as a tiny magnetic moment, but a measurement of an electron spin along the direction of an external magnetic field can have only two outcomes [1]: parallel or anti-parallel to the field. This discreteness reflects the quantum mechanical nature of spin. Ensembles of many spins have found diverse applications ranging from magnetic resonance imaging [2] to magneto-electronic devices [3], while individual spins are considered as carriers for quantum information. Read-out of single spin states has been achieved using optical techniques [4], and is within reach of magnetic resonance force microscopy [5]. However, electrical read-out of single spins [6, 7, 8, 9, 10, 11, 12, 13] has so far remained elusive. Here, we demonstrate electrical single-shot measurement of the state of an individual electron spin in a semiconductor quantum dot [14]. We use spin-to-charge conversion of a single electron confined in the dot, and detect the single-electron charge using a quantum point contact; the spin measurement visibility is $\sim 65\%$. Furthermore, we observe very long single-spin energy relaxation times (up to ~ 0.85 ms at a magnetic field of 8 Tesla), which are encouraging for the use of electron spins as carriers of quantum information.

This chapter has been published in Nature **430**, 431 (2004).

7.1 Measuring electron spin in quantum dots

In quantum dot devices, single electron charges are easily measured. Spin states in quantum dots, however, have only been studied by measuring the average signal from a large ensemble of electron spins [17, 18, 19, 20, 21, 22]. In contrast, the experiment presented here aims at a single-shot measurement of the spin orientation (parallel or antiparallel to the field, denoted as spin-$\uparrow$ and spin-$\downarrow$, respectively) of a particular electron; only one copy of the electron is available, so no averaging is possible. The spin measurement relies on spin-to-charge conversion [20, 21] followed by charge measurement in a single-shot mode [15, 16]. Fig. 7.1a schematically shows a single electron spin confined in a quantum dot (circle). A magnetic field is applied to split the spin-$\uparrow$ and spin-$\downarrow$ states by the Zeeman energy. The dot potential is then tuned such that if the electron has spin-$\downarrow$ it will leave, whereas it will stay on the dot if it has spin-$\uparrow$. The spin state has now been correlated with the charge state, and measurement of the charge on the dot will reveal the original spin state.

This concept is implemented using a structure [23] (Fig. 7.1b) consisting of a quantum dot in close proximity to a quantum point contact (QPC). The quantum dot is used as a box to trap a single electron, and the QPC is operated as a charge detector in order to determine whether the dot contains an electron or not. The quantum dot is formed in the two-dimensional electron gas (2DEG) of a GaAs/AlGaAs heterostructure by applying negative voltages to the metal surface gates M, R, and T. This depletes the 2DEG below the gates and creates a potential minimum in the centre, that is, the dot (indicated by a dotted white circle). We tune the gate voltages such that the dot contains either zero or one electron (which we can control by the voltage applied to gate P). Furthermore, we make the tunnel barrier between gates R and T sufficiently opaque that the dot is completely isolated from the drain contact on the right. The barrier to the reservoir on the left is set [24] to a tunnel rate $\Gamma \approx (0.05 \text{ ms})^{-1}$. When an electron tunnels on or off the dot, it changes the electrostatic potential in its vicinity, including the region of the nearby QPC (defined by R and Q). The QPC is set in the tunnelling regime, so that the current, I_{QPC}, is very sensitive to electrostatic changes [25]. Recording changes in I_{QPC} thus permits us to measure on a timescale of about 8 μs whether an electron resides on the dot or not [26]. In this way the QPC is used as a charge detector with a resolution much better than a single electron charge and a measurement timescale almost ten times shorter than $1/\Gamma$.

The device is placed inside a dilution refrigerator, and is subject to a magnetic field of 10 T (unless noted otherwise) in the plane of the 2DEG. The measured

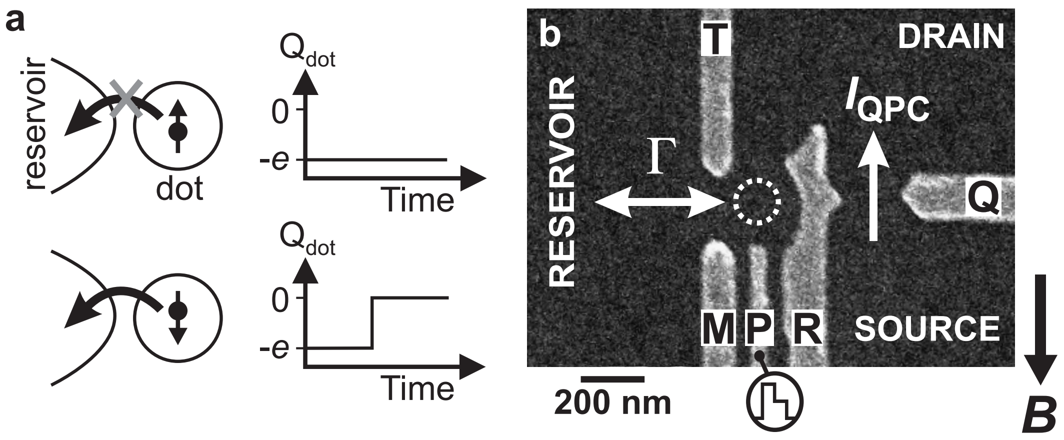

Figure 7.1: Spin-to-charge conversion in a quantum dot coupled to a quantum point contact. **(a)** Principle of spin-to-charge conversion. The charge on the quantum dot, Q_{dot}, remains constant if the electron spin is ↑, whereas a spin-↓ electron can escape, thereby changing Q_{dot}. **(b)** Scanning electron micrograph of the metallic gates on the surface of a GaAs/$Al_{0.27}Ga_{0.73}As$ heterostructure containing a two-dimensional electron gas (2DEG) 90 nm below the surface. The electron density is 2.9×10^{15} m^{-2}. (Only the gates used in the present experiment are shown, the complete device is described in Ref. [23].) Electrical contact is made to the QPC source and drain and to the reservoir via Ohmic contacts. With a source-drain bias voltage of 1 mV, I_{QPC} is about 30 nA, and an individual electron tunnelling on or off the dot changes I_{QPC} by $\sim$ 0.3 nA. The QPC-current is sent to a room temperature current-to-voltage convertor, followed by a gain 1 isolation amplifier, an AC-coupled 40 kHz SRS650 low-pass filter, and is digitized at a rate of 2.2×10^6 samples/s. With this arrangement, the step in I_{QPC} resulting from an electron tunnelling is clearly larger than the rms noise level, provided it lasts at least 8 μs. A magnetic field, B, is applied in the plane of the 2DEG.

Zeeman splitting in the dot [21], $\Delta E_Z \approx 200\mu$eV, is larger than the thermal energy (25 μeV) but smaller than the orbital energy level spacing (1.1 meV) and the charging energy (2.5 meV).

7.2 Two-level pulse technique

To test our single-spin measurement technique, we use an experimental procedure based on three stages: 1) empty the dot, 2) inject one electron with unknown spin, and 3) measure its spin state. The different stages are controlled by voltage pulses on gate P (Fig. 7.2a), which shift the dot's energy levels (Fig. 7.2c). Before the pulse the dot is empty, as both the spin-↑ and spin-↓ levels are above the Fermi energy of the reservoir, E_F. Then a voltage pulse pulls both levels below

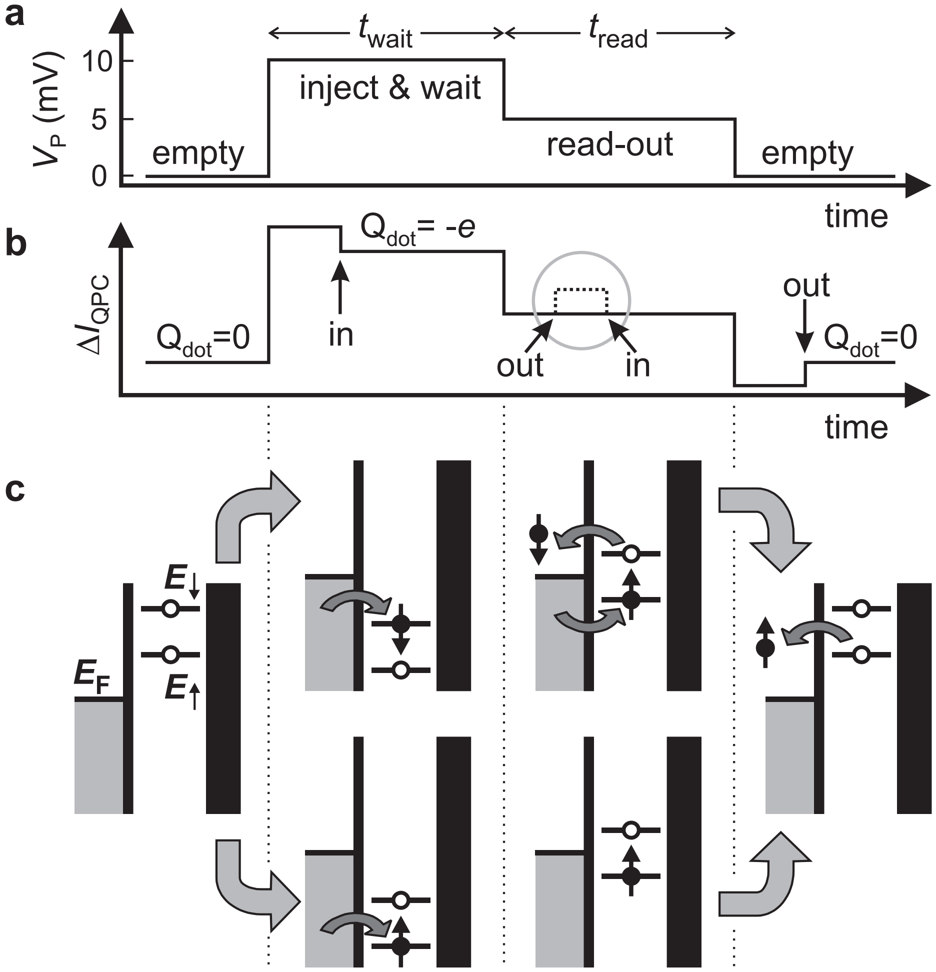
a
V_P (mV)
10
5
0
t_{wait}
t_{read}
inject & wait
empty
read-out
empty
time
b
ΔI_{QPC}
Q_{dot}= -e
Q_{dot}=0
in
out
in
out
Q_{dot}=0
time
c
$E_\downarrow$
E_F
$E_\uparrow$

Figure 7.2: Two-level pulse technique used to inject a single electron and measure its spin orientation. **(a)** Shape of the voltage pulse applied to gate P. The pulse level is 10 mV during t_{wait} and 5 mV during t_{read} (which is 0.5 ms for all measurements). **(b)** Schematic QPC pulse-response if the injected electron has spin-↑ (solid line) or spin-↓ (dotted line; the difference with the solid line is only seen during the read-out stage). Arrows indicate the moment an electron tunnels into or out of the quantum dot. **(c)** Schematic energy diagrams for spin-↑ ($E_\uparrow$) and spin-↓ ($E_\downarrow$) during the different stages of the pulse. Black vertical lines indicate the tunnel barriers. The tunnel rate between the dot and the QPC-drain on the right is set to zero. The rate between the dot and the reservoir on the left is tuned to a specific value, Γ. If the spin is ↑ at the start of the read-out stage, no change in the charge on the dot occurs during t_{read}. In contrast, if the spin is ↓, the electron can escape and be replaced by a spin-↑ electron. This charge transition is detected in the QPC-current (dotted line inside grey circle in (b)).

E_F. It is now energetically allowed for an electron to tunnel onto the dot, which will happen after a typical time $\sim \Gamma^{-1}$. The particular electron can have spin-$\uparrow$ (shown in the lower diagram) or spin-$\downarrow$ (upper diagram). (The tunnel rate for spin-$\uparrow$ electrons is expected to be larger than that for spin-$\downarrow$ electrons [27], i.e. $\Gamma_\uparrow > \Gamma_\downarrow$, but we do not assume this a priori.) During this stage of the pulse, lasting t_{wait}, the electron is trapped on the dot and Coulomb blockade prevents a second electron to be added. After t_{wait} the pulse is reduced, in order to position the energy levels in the read-out configuration. If the electron spin is $\uparrow$, its energy level is below E_F, so the electron remains on the dot. If the spin is $\downarrow$, its energy level is above E_F, so the electron tunnels to the reservoir after a typical time $\sim \Gamma_\downarrow^{-1}$. Now Coulomb blockade is lifted and an electron with spin-$\uparrow$ can tunnel onto the dot. This occurs on a timescale $\sim \Gamma_\uparrow^{-1}$ (with $\Gamma = \Gamma_\uparrow + \Gamma_\downarrow$). After t_{read}, the pulse ends and the dot is emptied again.

The expected QPC-response, ΔI_{QPC}, to such a two-level pulse is the sum of two contributions (Fig. 7.2b). First, due to a capacitive coupling between pulse-gate and QPC, ΔI_{QPC} will change proportionally to the pulse amplitude. Thus, ΔI_{QPC} versus time resembles a two-level pulse. Second, ΔI_{QPC} tracks the charge on the dot, i.e. it goes up whenever an electron tunnels off the dot, and it goes down by the same amount when an electron tunnels on the dot. Therefore, if the dot contains a spin-$\downarrow$ electron at the start of the read-out stage, ΔI_{QPC} should go up and then down again. We thus expect a characteristic step in ΔI_{QPC} during t_{read} for spin-$\downarrow$ (dotted trace inside grey circle). In contrast, ΔI_{QPC} should be flat during t_{read} for a spin-$\uparrow$ electron. Measuring whether a step is present or absent during the read-out stage constitutes our spin measurement.

7.3 Tuning the quantum dot into the read-out configuration

To perform spin read-out, V_M has to be fine-tuned so that the position of the energy levels with respect to E_F is as shown in Fig. 7.2c. To find the correct settings, we apply a two-level voltage pulse and measure the QPC-response for increasingly negative values of V_M (Fig. 7.3a). Four different regions in V_M can be identified (separated by white dotted lines), with qualitatively different QPC-responses. The shape of the typical QPC-response in each of the four regions (Fig. 7.3b) allows us to infer the position of $E_\uparrow$ and $E_\downarrow$ with respect to E_F during all stages of the pulse (Fig. 7.3c).

In the top region, the QPC-response just mimics the applied two-level pulse, indicating that here the charge on the dot remains constant throughout the pulse.

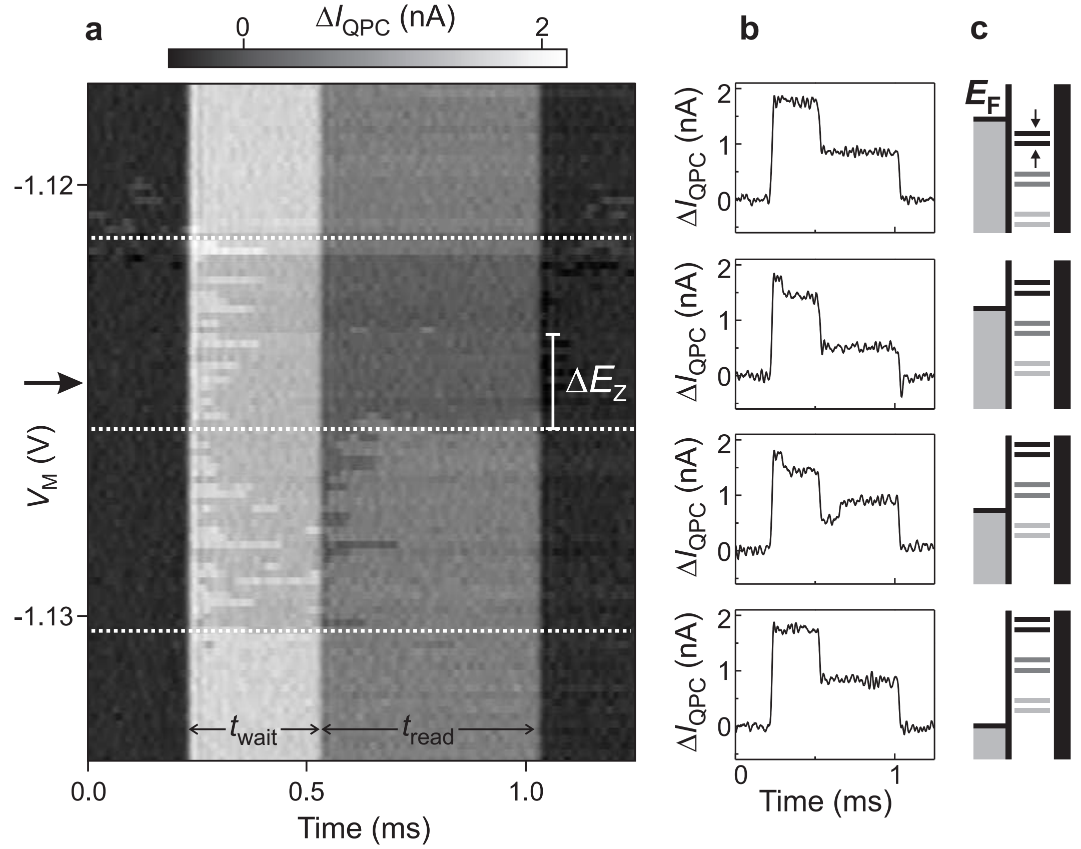

Figure 7.3: Tuning the quantum dot into the spin read-out configuration. We apply a two-stage voltage pulse as in Fig. 7.2a ($t_{wait} = 0.3$ ms, $t_{read} = 0.5$ ms), and measure the QPC-response for increasingly negative values of V_M. **(a)** QPC-response (in grey-scale) versus V_M. Four different regions in V_M can be identified (separated by white dotted lines), with qualitatively different QPC-responses. **(b)** Typical QPC-response in each of the four regions. This behaviour can be understood from the energy levels during all stages of the pulse. **(c)** Schematic energy diagrams showing $E_\uparrow$ and $E_\downarrow$ with respect to E_F before and after the pulse (black), during t_{wait} (light grey) and during t_{read} (dark grey), for four values of V_M. For the actual spin read-out experiment, V_M is set to the optimum position (indicated by the arrow in a).

This implies that $E_\uparrow$ remains below E_F for all stages of the pulse, thus the dot remains occupied with one electron. In the second region from the top, tunnelling occurs, as seen from the extra steps in ΔI_{QPC}. The dot is empty before the pulse, then an electron is injected during t_{wait}, which escapes after the pulse. This corresponds to an energy level diagram similar to before, but with $E_\uparrow$ and $E_\downarrow$ shifted up due to the more negative value of V_M in this region. In the third region from the top, an electron again tunnels on the dot during t_{wait}, but now it can escape already during t_{read}, irrespective of its spin. Finally, in the bottom region no electron-tunneling is seen, implying that the dot remains empty throughout the pulse.

Since we know the shift in V_M corresponding to shifting the energy levels by ΔE_Z, we can set V_M to the optimum position for the spin read-out experiment (indicated by the arrow). For this setting, the energy levels are as shown in Fig. 7.2c, i.e. E_F is approximately in the middle between $E_\uparrow$ and $E_\downarrow$ during the read-out stage.

7.4 Single-shot read-out of one electron spin

Fig. 7.4a shows typical experimental traces of the pulse-response recorded after proper tuning of the DC gate voltages (see Fig. 7.3). We emphasize that each trace involves injecting one particular electron on the dot and subsequently measuring its spin state. Each trace is therefore a single-shot measurement. The traces we obtain fall into two different classes; most traces qualitatively resemble the one in the top panel of Fig. 7.4a, some resemble the one in the bottom panel. These two typical traces indeed correspond to the signals expected for a spin-$\uparrow$ and a spin-$\downarrow$ electron (Fig. 7.2b), a strong indication that the electron in the top panel of Fig. 7.4a was spin-$\uparrow$ and in the bottom panel spin-$\downarrow$. The distinct signature of the two types of responses in ΔI_{QPC} permits a simple criterion for identifying the spin [28]: if ΔI_{QPC} goes above the threshold value (grey line in Fig. 7.4a and chosen as explained below), we declare the electron 'spin-down'; otherwise we declare it 'spin-up'. Fig. 7.4b shows the read-out section of twenty more 'spin-down' traces, to illustrate the stochastic nature of the tunnel events.

The random injection of spin-$\uparrow$ and spin-$\downarrow$ electrons prevents us from checking the outcome of any individual measurement. Therefore, in order to further establish the correspondence between the actual spin state and the outcome of our spin measurement, we change the probability to have a spin-$\downarrow$ at the beginning of the read-out stage, and compare this with the fraction of traces in which the electron is declared 'spin-down'. As t_{wait} is increased, the time between injection and read-out, t_{hold}, will vary accordingly ($t_{hold} \approx t_{wait}$). The probability for the spin to be $\downarrow$ at the start of t_{read} will thus decay exponentially to zero, since electrons in the excited spin state will relax to the ground state ($k_B T << \Delta E_Z$). For a set of 15 values of t_{wait} we take 625 traces for each t_{wait}, and count the fraction of traces in which the electron is declared 'spin-down' (Fig. 7.4c). The fact that the expected exponential decay is clearly reflected in the data confirms the validity of the spin read-out procedure.

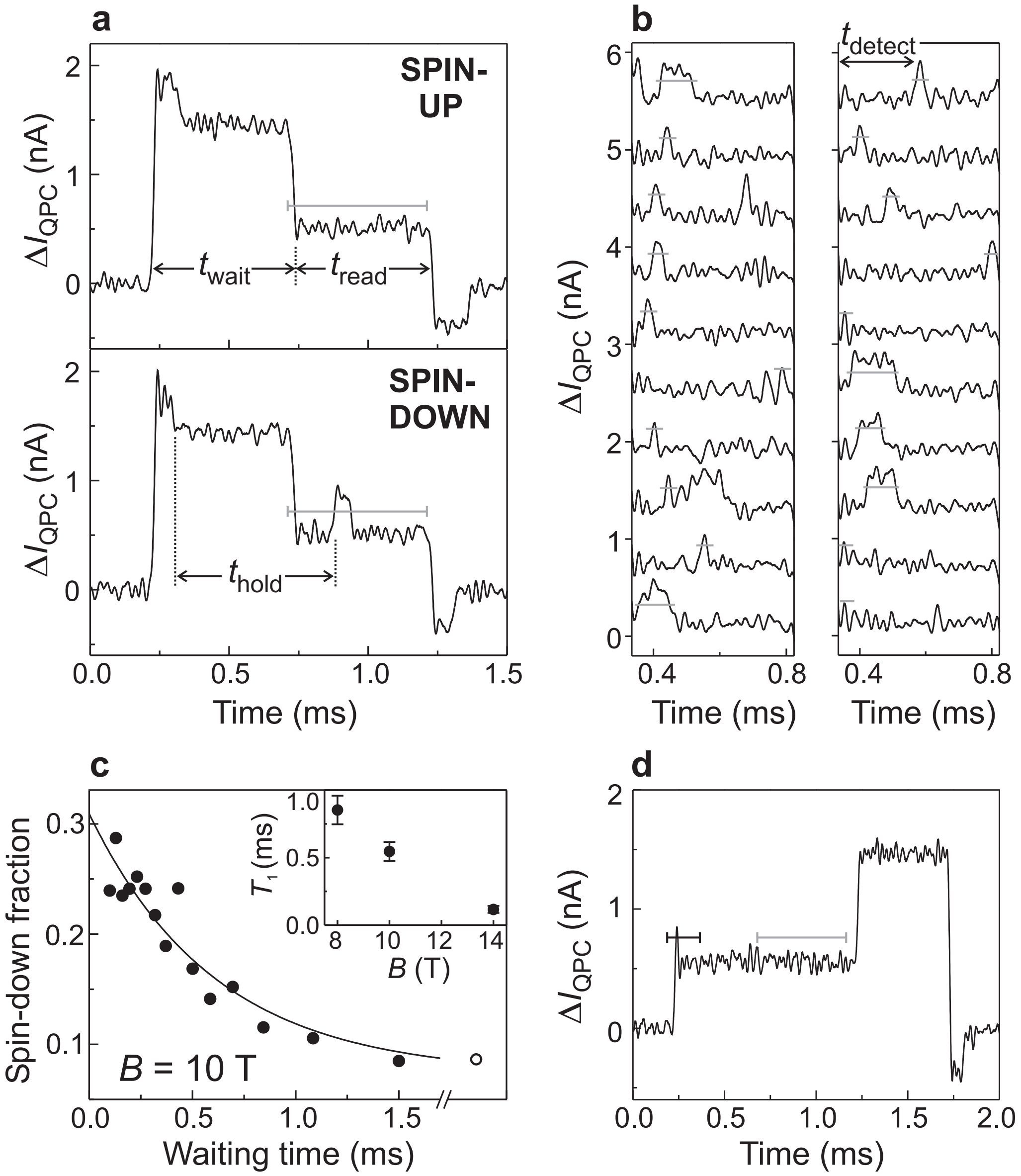

Figure 7.4: Single-shot read-out of one electron spin. **(a)** Time-resolved QPC measurements. Top panel: an electron injected during t_{wait} is declared 'spin-up' during t_{read}. Bottom panel: the electron is declared 'spin-down'. **(b)** Examples of 'spin-down' traces (for $t_{wait} = 0.1$ ms). Only the read-out segment is shown, and traces are offset for clarity. The time when ΔI_{QPC} first crosses the threshold, t_{detect}, is recorded to make the histogram in Fig. 7.7a. **(c)** Fraction of 'spin-down' traces versus t_{wait}, out of 625 traces for each waiting time. Open dot: spin-down fraction using modified pulse shape (d). Black solid line: exponential fit to the data. Inset: T_1 versus B. **(d)** Typical QPC-signal for a 'reversed' pulse, with the same amplitudes as in Fig. 7.2a, but a reversed order of the two stages. The grey threshold is used to obtain the open dot in (c), the black threshold is used in Fig. 7.7b (see text).

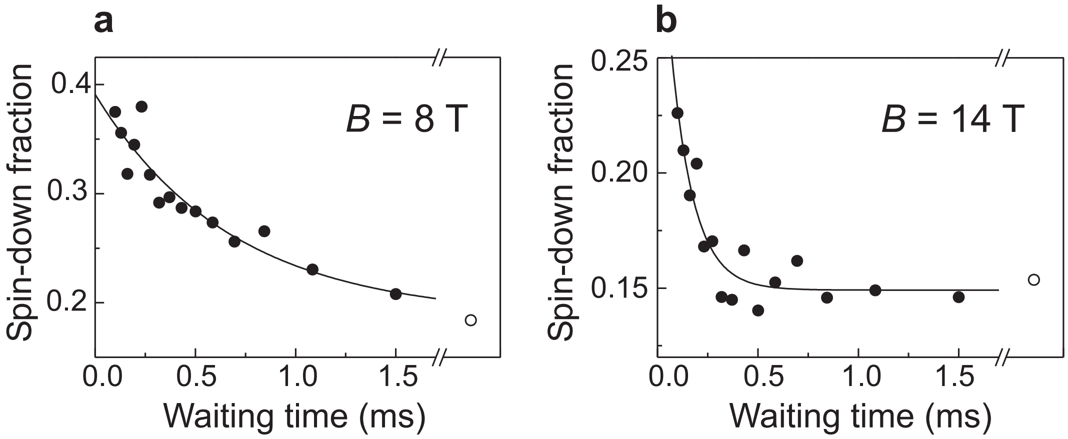

Figure 7.5: Measurement of the spin-relaxation time as in Fig. 7.4c, but at different magnetic fields. Averaging the results of an exponential fit (as shown) over three similar measurements yields **(a)**, $T_1 = (0.85 \pm 0.11)$ ms at 8 T and **(b)**, $T_1 = (0.12 \pm 0.03)$ ms at 14 T.

As an extra check that the observed decay is due to spin relaxation, we apply a pulse waveform where the two pulse stages are reversed (Fig. 7.4d). In this case injection takes place with $E_\uparrow$ below and $E_\downarrow$ above E_F (see Fig. 7.2c, third column), so that always a spin-↑ electron is injected. By comparing the signal with a threshold (grey line in Fig. 7.4d) as before, we find the fraction of spin-↑ electrons that is measured to be 'spin-down', which is nonzero due to measurement inaccuracy (see below). This fraction, indicated by the open dot in Fig. 7.4c, agrees very well with the value found for the longest waiting time (1.5 ms), demonstrating that here the electrons with spin-↓ indeed have relaxed to spin-↑.

We extract a single-spin energy relaxation time, T_1, from fitting the datapoints in Fig. 7.4c (and two other similar measurements) to $\alpha + C\exp(-t_{wait}/T_1)$, and obtain an average value of $T_1 \approx (0.55 \pm 0.07)$ ms at 10 Tesla. This is an order of magnitude longer than the lower bound on T_1 established earlier [21], and clearly longer than the time needed for the spin measurement (of order $1/\Gamma_\downarrow \approx 0.11$ ms). A similar experiment at 8 Tesla gives $T_1 \approx (0.85 \pm 0.11)$ ms and at 14 Tesla we find $T_1 \approx (0.12 \pm 0.03)$ ms (Fig. 7.5). More experiments are needed in order to test the theoretical prediction that relaxation at high magnetic fields is dominated by spin-orbit interactions [29, 30, 31], with smaller contributions resulting from hyperfine interactions with the nuclear spins [29, 32] (cotunnelling is insignificant given the very small tunnel rates). We note that the obtained values for T_1 refer to our entire device under active operation: i.e. a single spin in a quantum dot subject to continuous charge detection by a QPC.

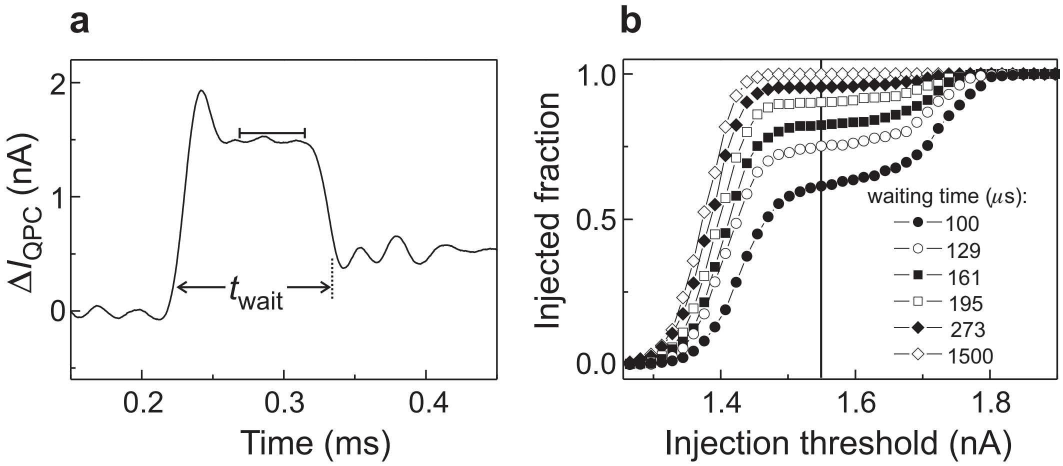

Figure 7.6: Setting the injection threshold. **(a)** Example of QPC-signal for the shortest waiting time used (0.1 ms). The horizontal line indicates the injection threshold. Injection is declared successful if the QPC-signal is below the injection threshold for a part or all of the last 45 μs before the end of the injection stage (t_{wait}). Traces in which injection was not successful, i.e. no electron was injected during t_{wait}, are disregarded. **(b)** Fraction of traces in which injection was successful, out of a total of 625 taken for each waiting time. The threshold chosen for analysing all data is indicated by the vertical line.

7.5 Measurement fidelity

For applications in quantum information processing it is important to know the accuracy, or fidelity, of the single-shot spin read-out. The measurement fidelity is characterised by two parameters, α and β (inset to Fig. 7.7a), which we now determine for the data taken at 10 T.

The parameter α corresponds to the probability that the QPC-current exceeds the threshold even though the electron was actually spin-$\uparrow$, for instance due to thermally activated tunnelling or electrical noise (similar to 'dark counts' in a photon detector). The combined probability for such processes is given by the saturation value of the exponential fit in Fig. 7.4c, α, which depends on the value of the threshold current. We analyse the data in Fig. 7.4c using different thresholds, and plot α in Fig. 7.7b.

The parameter β corresponds to the probability that the QPC-current stays below the threshold even though the electron was actually spin-$\downarrow$ at the start of the read-out stage. Unlike α, β cannot be extracted directly from the exponential fit (note that the fit parameter $C = p(1 - \alpha - \beta)$ contains two unknowns: $p = \Gamma_\downarrow/(\Gamma_\uparrow + \Gamma_\downarrow)$ and β). We therefore estimate β by analysing the two processes that contribute to it. First, a spin-$\downarrow$ electron can relax to spin-$\uparrow$ before spin-to-charge

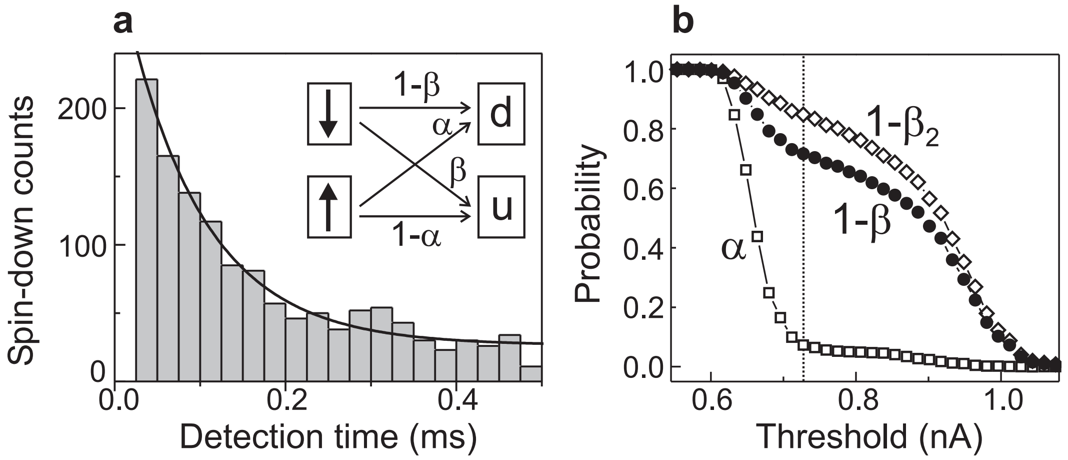

Figure 7.7: Measurement fidelity. **(a)** Histogram showing the distribution of detection times, t_{detect}, in the read-out stage (see Fig. 7.4b for definition t_{detect}). The exponential decay is due to spin-↓ electrons tunnelling out of the dot (rate = $\Gamma_\downarrow$) and due to spin flips during the read-out stage (rate = $1/T_1$). Solid line: exponential fit with a decay time $(\Gamma_\downarrow + 1/T_1)^{-1}$ of 0.09 ms. Given that $T_1 = 0.55$ ms, this yields $\Gamma_\downarrow^{-1} \approx 0.11$ ms. Inset: fidelity parameters. A spin-↓ electron is declared 'down' (d) or 'up' (u) with probability $1 - \beta$ or β, respectively. A spin-↑ electron is declared 'up' or 'down' with probability $1 - \alpha$ or α, respectively. **(b)** Open squares represent α, obtained from the saturation value of exponential fits as in Fig. 7.4c for different values of the read-out threshold. A current of 0.54 nA (0.91 nA) corresponds to the average value of ΔI_{QPC} when the dot is occupied (empty) during t_{read}. Open diamonds: measured fraction of 'reverse-pulse' traces in which ΔI_{QPC} crosses the injection threshold (black line in Fig. 7.4d). This fraction approximates $1-\beta_2$, where β_2 is the probability of identifying a spin-↓ electron as 'spin-up' due to the finite bandwidth of the measurement setup. Filled circles: total fidelity for the spin-↓ state, $1 - \beta$, calculated using $\beta_1 = 0.17$. The vertical dotted line indicates the threshold for which the visibility $1-\alpha-\beta$ (separation between filled circles and open squares) is maximal. This threshold value of 0.73 nA is used in the analysis of Fig. 7.4.

conversion takes place. This occurs with probability $\beta_1 = 1/(1 + T_1\Gamma_\downarrow)$. From a histogram (Fig. 7.7a) of the actual detection time, t_{detect} (see Fig. 7.4b), we find $\Gamma_\downarrow^{-1} \approx 0.11$ ms, yielding $\beta_1 \approx 0.17$. Second, if the spin-↓ electron does tunnel off the dot but is replaced by a spin-↑ electron within about 8 μs, the resulting QPC-step is too small to be detected. The probability that a step is missed, β_2, depends on the value of the threshold. It can be determined by applying a modified ('reversed') pulse (Fig. 7.4d). For such a pulse, we know that in each trace an electron is injected in the dot, so there should always be a step at the start of the pulse. The fraction of traces in which this step is nevertheless missed, i.e. ΔI_{QPC} stays below the threshold (black line in Fig. 7.4d), gives β_2. We plot $1-\beta_2$ in Fig. 7.7b (open diamonds). The resulting total fidelity for spin-↓ is given by $1-\beta \approx (1-\beta_1)(1-\beta_2)+(\alpha\beta_1)$. The last term accounts for the case when a spin-↓ electron is flipped to spin-↑, but there is nevertheless a step in ΔI_{QPC} due to the dark-count mechanism [33]. In Fig. 7.7b we also plot the extracted value of $1-\beta$ as a function of the threshold.

We now choose the optimal value of the threshold as the one for which the visibility $1-\alpha-\beta$ is maximal (vertical line in Fig. 7.7b). For this setting, $\alpha \approx 0.07$, $\beta_1 \approx 0.17$, $\beta_2 \approx 0.15$, so the measurement fidelity for the spin-↑ and the spin-↓ state is ~ 0.93 and ~ 0.72 respectively. The measurement visibility in a single-shot measurement is thus at present 65%.

Significant improvements in the spin measurement visibility can be made by lowering the electron temperature (smaller α) and especially by making the charge measurement faster (smaller β). Already, the demonstration of single-shot spin read-out and the observation of T_1 of order 1 ms are encouraging results for the use of electron spins as quantum bits.

We thank D. P. DiVincenzo, H. A. Engel, T. Fujisawa, V. Golovach, Y. Hirayama, D. Loss, T. Saku, R. Schouten, and S. Tarucha for technical support and helpful discussions. This work was supported by a Specially Promoted Research Grant-in-Aid from the Japanese Ministry of Education, the DARPA-QUIST program, the ONR, the EU-RTN network on spintronics, and the Dutch Organisation for Fundamental Research on Matter (FOM).

References

[1] J. J. Sakurai, Modern Quantum Mechanics. Addison-Wesley (Reading MA, USA, 1994).

[2] F. W. Wehrli, Physics Today **6**, 34 (1992).

[3] S. A. Wolf *et al.*, Science **294**, 1488-1495 (2001).

[4] R. Blatt and P. Zoller, Eur. J. Phys. **9**, 250-279 (1988).

[5] H. J. Mamin, R. Budakian, B. W. Chui and D. Rugar, Phys. Rev. Lett. **91**, 207604 (2003).

[6] D. Loss and D. P. DiVincenzo, Phys. Rev. A **57**, 120-126 (1998).

[7] B. E. Kane, Nature **393**, 133-137 (1998).

[8] L. M. K. Vandersypen *et al.*, in Quantum Computing and Quantum Bits in Mesoscopic Systems, Kluwer Academic/Plenum Publishers (New York, 2003). See also http://xxx.lanl.gov/abs/quant-ph/0207059 (2002).

[9] M. Xiao, I. Martin, and H. W. Jiang, Phys. Rev. Lett. **91**, 078301 (2003).

[10] M. Friesen *et al.*, Phys. Rev. Lett. **92**, 037901 (2004).

[11] H. A. Engel *et al.*, Phys. Rev. Lett. **93**, 106804 (2004).

[12] R. Ionicioiu *et al.*, http://xxx.lanl.gov/abs/quant-ph/0310047 (2003).

[13] A. D. Greentree *et al.*, http://xxx.lanl.gov/abs/cond-mat/0403449 (2004).

[14] L. P. Kouwenhoven, D. G. Austing and S. Tarucha, Rep. Prog. Phys. **64**, 701-736 (2001).

[15] W. Lu *et al.*, Nature **423**, 422 (2003).

[16] T. Fujisawa *et al.*, Appl. Phys. Lett. **84**, 2343 (2004).

[17] J. Weis *et al.*, Surf. Sci. **305**, 664 (1994).

[18] L. P. Kouwenhoven *et al.*, Science **278**, 1788 (1997).

[19] M. Ciorga *et al.*., Physica E **11**, 35 (2001).

[20] T. Fujisawa *et al.*, Nature **419**, 278-281 (2002).

[21] R. Hanson *et al.*, Phys. Rev. Lett. **91**, 196802 (2003).

[22] J. A. Folk *et al.*., Science **299**, 679 (2003).

[23] J. M. Elzerman *et al.*, Phys. Rev. B **67**, R161308 (2003).

[24] J. M. Elzerman *et al.*, Appl. Phys. Lett. **84**, 4617-4619 (2004).

[25] M. Field *et al.*, Phys. Rev. Lett. **70**, 1311 (1993).

[26] L. M. K. Vandersypen *et al.*, Appl. Phys. Lett. **85**, 4394 (2004).

[27] R. Hanson *et al.*, http://xxx.lanl.gov/abs/cond-mat/011414v1 (2003).

[28] The automated data analysis procedure first corrects for the offset of each trace. This offset, resulting from low-frequency interference signals or charge switches, is found by making a histogram of the QPC current during the read-out stage of a particular trace. The histogram typically displays a peak due to fluctuations around the average value corresponding to an occupied dot. The center of a gaussian fit to the histogram gives the offset. Then each trace is checked to make sure that an electron was injected during the injection stage, by evaluating if the signal goes below the injection threshold (dotted horizontal line in Fig. 7.6a). If not, the trace is disregarded. Finally, to determine if a trace corresponds to 'spin-up' or 'spin-down', we disregard

all points that lie below the previous point (since these could correspond to points on the falling pulse flank at the end of the injection stage), and check if any of the remaining points are above the threshold.

[29] A. V. Khaetskii and Y. V. Nazarov, Phys. Rev. B **64**, 125316 (2001).

[30] V. N. Golovach, A. Khaetskii and D. Loss, Phys. Rev. Lett. **93**, 016601 (2004).

[31] L. M. Woods, T. L. Reinecke and Y. Lyanda-Geller, Phys. Rev. B **66**, 161318(R) (2002).

[32] S. I. Erlingsson and Y. V. and Nazarov, Phys. Rev. B **66**, 155327 (2002).

[33] Let us assume there is a spin-$\downarrow$ electron on the dot at the start of the read-out stage. The probability that the $\downarrow$-electron tunnels out (i.e. that it does not relax to spin-$\uparrow$) is given by $1-\beta_1$. The probability that this tunnel event is detected (i.e. is not too fast) is given by $1-\beta_2$. Therefore, the probability that a spin-$\downarrow$ electron tunnels out and is detected, is $(1-\beta_1)(1-\beta_2)$. In addition, there is the possibility that the $\downarrow$-electron relaxes, with probability β_1, but a step in the QPC signal is nevertheless detected, with probability α, due to the 'dark count' mechanism. Therefore, the total probability that a spin-$\downarrow$ electron is declared 'spin-down' is given by $(1-\beta_1)(1-\beta_2)+(\alpha\beta_1)$ approximately.

Chapter 8

Single-shot read-out of two-electron spin states using spin-dependent tunnel rates

R. Hanson, L. H. Willems van Beveren, I. T. Vink,
J. M. Elzerman, W. J. M. Naber, F. H. L. Koppens,
L. P. Kouwenhoven and L. M. K. Vandersypen

We present a method for reading out the spin state of electrons in a quantum dot that is robust against charge noise and can be used even when the electron temperature exceeds the energy splitting between the states. The spin states are first correlated to different charge states using a spin dependence of the tunnel rates. A subsequent fast measurement of the charge on the dot then reveals the original spin state. We experimentally demonstrate the method by performing read-out of the two-electron spin states, achieving a single-shot visibility of more than 80%. We find very long triplet-to-singlet relaxation times (up to several milliseconds), with a strong dependence on in-plane magnetic field.

This chapter has been published in Physical Review Letters **94**, 196802 (2005).

8.1 Single-shot spin read-out using spin-dependent tunnel rates

The magnetic moment associated with the electron spin is tiny and therefore hard to measure directly. However, by correlating the spin states to different charge states and subsequently measuring the charge on the dot, the spin state can be determined [1]. Such a spin-to-charge conversion can be achieved by positioning the spin levels around the electrochemical potential of the reservoir μ_{res} as depicted in Fig. 8.1a, such that one electron can tunnel off the dot from the spin excited state, $|ES\rangle$, whereas tunneling from the ground state, $|GS\rangle$, is energetically forbidden. By combining this scheme with a fast (40 kHz bandwidth) measurement of the charge dynamics, we have recently performed read-out of the spin orientation of a single electron, with a single-shot visibility up to 65% [2]. (A conceptionally similar scheme has also allowed single-shot read-out of a superconducting charge qubit [3]). However, this energy-selective read-out (E-RO) has three drawbacks: (i) E-RO requires an energy splitting of the spin states larger than the thermal energy of the electrons in the reservoir. Thus, for a single spin the read-out is only effective at very low electron temperature and high magnetic fields (8 T and higher in Ref. [2]). Also, interesting effects occurring close to degeneracy, e.g. near the singlet-triplet crossing for two electrons [4], can not be probed. (ii) Since the E-RO relies on precise positioning of the spin levels with respect to the reservoir, it is very sensitive to fluctuations in the electrostatic potential. Background charge fluctuations [5], active even in today's most stable devices, can easily push the levels out of the read-out configuration. (iii) High-frequency noise can spoil the E-RO by inducing photon-assisted tunneling from the spin ground state to the reservoir. Since the QPC is a source of shot noise, this limits the current through the QPC and thereby the bandwidth of the charge detection [6]. A different read-out method is desired that does not suffer from these constraints.

In this work, we present a spin read-out scheme where spin-to-charge conversion is achieved by exploiting the difference in *tunnel rates* of the different spin states to the reservoir [7]. We outline the concept of this tunnel-rate selective read-out (TR−RO) in Fig. 8.1b. Assume that the tunnel rate from $|ES\rangle$ to the reservoir, Γ_{ES}, is much higher than the tunnel rate from $|GS\rangle$, Γ_{GS}, i.e. $\Gamma_{ES} \gg \Gamma_{GS}$. Then, we can read out the spin state as follows. At time t=0, we position the levels of both $|ES\rangle$ and $|GS\rangle$ far above μ_{res}, so that one electron is energetically allowed to tunnel off the dot regardless of the spin state. Then, at a time $t = \tau$, where $\Gamma_{GS}^{-1} \gg \tau \gg \Gamma_{ES}^{-1}$, an electron will have tunneled off the dot

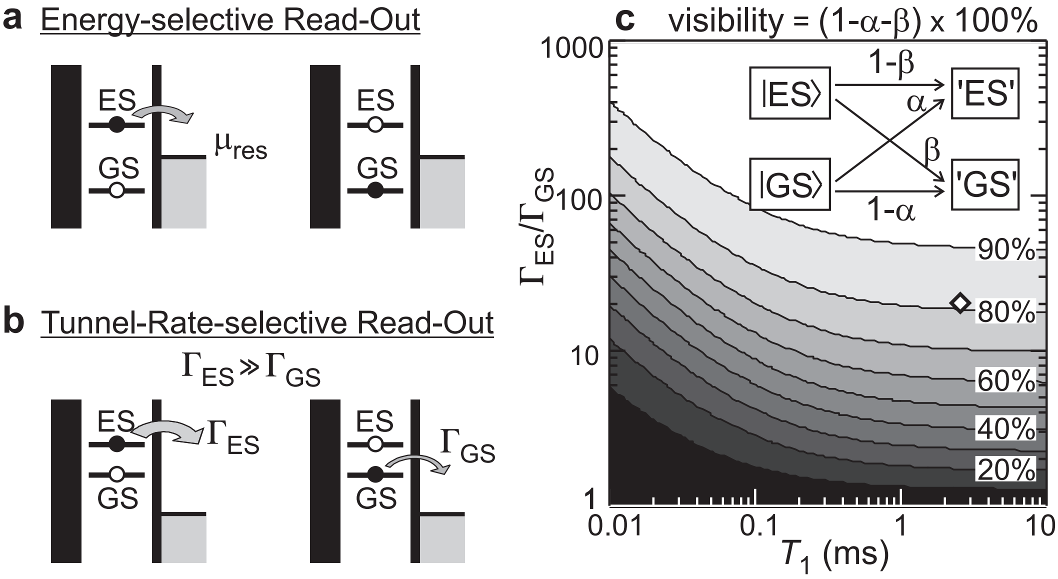

Figure 8.1: (a)-(b) Energy diagrams explaining two schemes for spin-to-charge conversion. (a) Energy-selective read-out. Tunneling is energetically allowed from $|ES\rangle$ (left diagram), but not from $|GS\rangle$ (right diagram). (b) Tunnel rate-selective read-out (TR-RO). One electron is allowed to tunnel off the dot, regardless of the spin state, but the tunnel rate depends strongly on the spin state: $\Gamma_{ES} \gg \Gamma_{GS}$. If a charge measurement after a time τ, where $\Gamma_{GS}^{-1} \gg \tau \gg \Gamma_{ES}^{-1}$, indicates that one electron has (not) tunneled, the state is declared $'ES'$ ($'GS'$). (c) Visibility of the TR-RO as a function of spin relaxation time T_1 and the ratio Γ_{ES}/Γ_{GS}, for $\Gamma_{GS} = 2.5$ kHz. The diamond corresponds to the read-out parameters of Fig. 8.2e. Inset: definition of the error rates α and β. If the initial state is $|GS\rangle$, there is a probability α that the measurement gives the wrong outcome, i.e. $'ES'$ (β is defined similarly).

with a very high probability if the state was $|ES\rangle$, but most likely no tunneling will have occurred if the state was $|GS\rangle$. Thus, the spin information is converted to charge information, and a measurement of the number of electrons on the dot reveals the original spin state.

A major advantage of this TR-RO scheme is that it does not rely on a large energy splitting between the spin states. Furthermore, it is robust against background charge fluctuations, since these cause only a small variation in the tunnel rates (of order 10^{-3} in Ref. [5]). Finally, photon-assisted tunneling is not important since here tunneling is energetically allowed regardless of the initial spin state. Thus, we see that TR-RO can overcome the constraints of E-RO.

8.2 Measurement visibility of the read-out

We first analyze the fidelity of the TR-RO theoretically using the error rates α and β as defined in the diagram of Fig. 8.1c (inset). Here, α is the probability that one electron has tunneled even though the initial state was $|GS\rangle$, and β the probability that no tunneling has occurred even though the initial state was $|ES\rangle$. The charge measurement itself is assumed to be perfect, and spin relaxation from $|ES\rangle$ to $|GS\rangle$ is modeled by a rate $1/T_1$. We find analytically

$$\alpha = 1 - e^{-\Gamma_{GS}\cdot\tau}, \tag{8.1}$$

$$\beta = \frac{(1/T_1)e^{-\Gamma_{GS}\cdot\tau} + (\Gamma_{ES}-\Gamma_{GS})\, e^{-(\Gamma_{ES}+1/T_1)\cdot\tau}}{\Gamma_{ES} + 1/T_1 - \Gamma_{GS}}, \tag{8.2}$$

where τ is the time at which we measure the number of electrons N [8]. The visibility of the read-out is $1-\alpha-\beta$.

The optimal value for the read-out time for given values of T_1 and the ratio Γ_T/Γ_S, τ_{max}, is found by solving $d(\text{visibility})/d\tau = 0$ for τ. We find

$$\tau_{max} = \frac{1}{\Gamma_{ES}+1/T_1-\Gamma_{GS}} \ln\left(\frac{\Gamma_{ES}+1/T_1}{\Gamma_{GS}}\right). \tag{8.3}$$

Inserting this expression into equations 8.1 and 8.2 yields the maximum visibility.

In Fig. 8.1c we plot the visibility for the optimal value of τ as a function of T_1 and the ratio of the tunnel rates Γ_{ES}/Γ_{GS}. (Here, Γ_{GS} is chosen to be 2.5 kHz, which is well within the bandwidth of our charge detection set up [6].) We see that for $\Gamma_{ES}/\Gamma_{GS} = 10$ and $T_1 = 0.5$ ms, the visibility is 65%, equal to the visibility obtained with E-RO in Ref. [2] for the same T_1. For $\Gamma_{ES}/\Gamma_{GS} > 60$ and $T_1 = 0.5$ ms, the visibility of TR-RO exceeds 90%.

The TR-RO can be used in a similar way if Γ_{ES} is much *lower* than Γ_{GS}. The visibility for this case can be calculated simply by replacing α and β in Eqs. 8.1-8.2 with $1-\alpha$ and $1-\beta$ respectively. Due to the symmetry in the equations, this visibility is the same as for the case $\Gamma_{ES} \gg \Gamma_{GS}$ whenever the relaxation rate, which is the only asymmetric parameter, is not dominant.

The main ingredient necessary for TR-RO is a spin dependence in the tunnel rates. For a single electron, this spin dependence can be obtained in the Quantum Hall regime, where a high spin-selectivity is induced by the spatial separation of spin-resolved edge channels [9, 10]. TR-RO can also be used for read-out of a two-electron dot, where the electrons are either in the spin-singlet ground state, denoted by $|S\rangle$, or in a spin-triplet state, denoted by $|T\rangle$. In $|S\rangle$, the two electrons both occupy the lowest orbital, but in $|T\rangle$ one electron is in the first excited orbital. Since the wave function in this excited orbital has more weight near the edge of the dot [11], the coupling to the reservoir is stronger than for the lowest orbital. Therefore, the tunnel rate from a triplet state to the reservoir Γ_T is much larger than the rate from the singlet state Γ_S, i.e. $\Gamma_T \gg \Gamma_S$ [12]. We use this spin-dependence in the following to experimentally demonstrate TR-RO for two electrons.

8.3 Single-shot read-out of the two-electron spin states

A quantum dot (white dotted circle in Fig. 8.2a) and a QPC are defined in a two-dimensional electron gas (2DEG) with an electron density of $4 \cdot 10^{15}$ m^{-2}), 60 nm below the surface of a GaAs/AlGaAs heterostructure from Sumitomo Electric, by applying negative voltages to gates L, M, T and Q. Gate P is used to apply fast voltage pulses. We completely pinch off the tunnel barrier between gates L and T, so that the dot is only coupled to the reservoir on the right. The conductance of the QPC is tuned to about e^2/h, making it very sensitive to the number of electrons on the dot. A voltage bias of 0.8 mV induces a current through the QPC, I_{QPC}, of about 30 nA.

We tune the dot to the $N = 1 \leftrightarrow 2$ transition in a small parallel field $B_{//}$ of 0.02 T. Here, the energy difference between $|T\rangle$ and the ground state $|S\rangle$, E_{ST}, is about 1 meV. From measurements of the tunnel rates [13], we estimate the ratio Γ_T/Γ_S to be on the order of 20. A similar ratio was found previously in transport measurements on a different device [12]. As can be seen in Fig. 8.1c, for $T_1 > 1$ ms this permits a read-out visibility $> 80\%$.

We implement the TR-RO by applying voltage pulses as depicted in Fig. 8.2b to gate P. Figure 8.2c shows the expected response of I_{QPC} to the pulse, together with the level diagrams in the three different stages. Before the pulse starts, there is one electron on the dot. Then, the pulse pulls the levels down so that a second electron can tunnel onto the dot ($N = 1 \rightarrow 2$), forming either a singlet or a triplet state with the first electron. The probability that a triplet state is formed is given by $3\Gamma_T/(\Gamma_S + 3\Gamma_T)$, where the factor of 3 is due to the degeneracy of the triplets. After a variable waiting time t_{wait}, the pulse ends and the read-out process is initiated, during which one electron can leave the dot again. The rate for tunneling off depends on the two-electron state, resulting in the desired spin-to-charge conversion. The QPC is used to detect the number of electrons on the dot. Due to the direct capacitive coupling of gate P to the QPC channel, ΔI_{QPC} follows the pulse shape. Tunneling of an electron on or off the dot gives an additional step in ΔI_{QPC} [2, 6, 14], as indicated by the arrows in Fig. 8.2c.

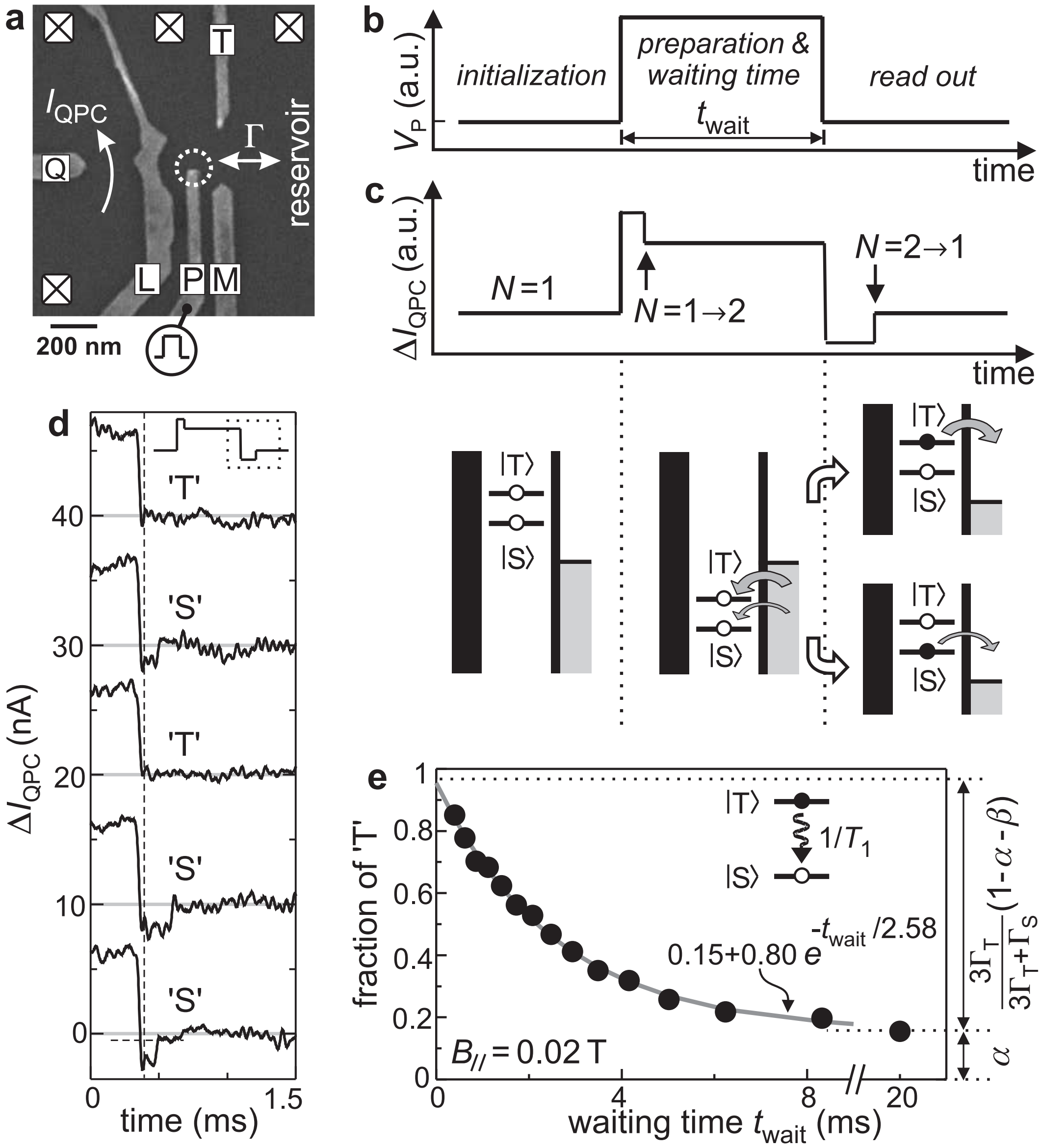

Figure 8.2: Single-shot read-out of $N = 2$ spin states. (a) Scanning electron micrograph of a device as used in the experiments. (b) Pulse waveform applied to gate P. (c) Response of the QPC-current to the waveform of (b). Energy diagrams indicate the positions of the levels during the three stages. In the final stage, spin is converted to charge information due to the difference in tunnel rates for states $|S\rangle$ and $|T\rangle$. (d) Real-time traces of ΔI_{QPC} during the last part of the waveform (dashed box in the inset), for $t_{wait} = 0.8$ ms. At the vertical dashed line, N is determined by comparison with a threshold (horizontal dashed line in bottom trace) and the spin state is declared $'T'$ or $'S'$ accordingly. (e) Fraction of $'T'$ as a function of waiting time at $B_{//} = 0.02$ T, showing a single-exponential decay with a time constant T_1 of 2.58 ms.

Now, Γ_S is tuned to 2.5 kHz, and Γ_T is therefore $\approx$ 50 kHz. In order to achieve a good signal-to-noise ratio in I_{QPC}, the signal is sent through an external 20 kHz low-pass filter. As a result, many of the tunnel events from $|T\rangle$ will not be resolved, but the tunneling from $|S\rangle$ should be clearly visible.

Figure 8.2d shows several traces of ΔI_{QPC}, from the last part (300 μs) of the pulse to the end of the read-out stage (see inset), for a waiting time of 0.8 ms. In some traces, there are clear steps in ΔI_{QPC}, due to an electron tunneling off the dot. In other traces, the tunneling occurs faster than the filter bandwidth. In order to discriminate between $|S\rangle$ and $|T\rangle$, we first choose a read-out time τ (indicated by a vertical dashed line in Fig. 8.2d) and measure the number of electrons on the dot at that time by comparing ΔI_{QPC} to a threshold value (as indicated by the horizontal dashed line in the bottom trace of Fig. 8.2d). If ΔI_{QPC} is below the threshold, it means $N = 2$ and we declare the state $'S'$. If ΔI_{QPC} is above the threshold, it follows that $N = 1$ and the state is declared $'T'$. Our method for determining the optimal threshold value and τ is explained below.

To verify that $'T'$ and $'S'$ indeed correspond to the spin states $|T\rangle$ and $|S\rangle$, we change the relative occupation probabilities by varying the waiting time. The probability that the electrons are in $|T\rangle$, P_T, decays exponentially with the waiting time: $P_T(t) = P_T(0)\, e^{-t_{wait}/T_1}$. Therefore, as we make the waiting time longer, we should observe an exponential decay of the fraction of traces that are declared $'T'$.

We take 625 traces similar to those in Fig. 8.2d for each of 15 different waiting times. Note that the two-electron state is formed on a timescale (of order $1/\Gamma_T$) much shorter than the shortest t_{wait} used (400 μs). To find the optimal read-out parameters, we scan a wide range of read-out times and threshold values using a computer program. For each combination of these two parameters, the program determines the fraction of traces declared $'T'$ for each of the waiting times, and fits the resulting data with a single exponential decay $A\, e^{-t_{wait}/T_1} + \alpha$. The prefactor A is given by $3\Gamma_T/(\Gamma_S{+}3\Gamma_T){\times}(1{-}\alpha{-}\beta)$. We see that A is proportional to the read-out visibility, and therefore the optimal read-out parameters can be determined simply by searching for the highest value of A. Here, we find the optimal values to be -0.4 nA for the threshold and 70 μs for τ (corresponding to t = 370 μs in Fig. 8.2d), and use these in the following.

In Fig. 8.2e, we plot the fraction of traces declared $'T'$ as a function of t_{wait}. We see that the fraction of $'T'$ decays exponentially, showing that we can indeed read out the two-electron spin states. A fit to the data yields a triplet-to-singlet relaxation time $T_1 = (2.58 \pm 0.09)$ ms, which is more than an order of magnitude longer than the lower bound found in Ref. [15]. As indicated on the right side of Fig. 8.2e, we can also extract α and β from the data. We find $\alpha = 0.15$ and $\beta = 0.04$ (taking $\Gamma_T/\Gamma_S = 20$). The single-shot visibility is thus 81%. These numbers agree well with the values predicted by the model ($\alpha = 0.14$, $\beta = 0.05$, visibility= 81%), as indicated by the diamond in Fig. 8.1c. Note that, since the visibility is insensitive to τ near the optimal value, it is not significantly reduced by the finite bandwidth of the charge measurement.

As an extra check of the read-out, we have also applied a modified pulse where during the preparation only the singlet state is energetically accessible. Here, the read-out should ideally always yield $'S'$, and therefore the measured probability for finding $'T'$ directly gives us α. We find a fraction of $'T'$ of 0.16, consistent with the value of α obtained from the fit. This again confirms the validity of the read-out method.

8.4 Magnetic field dependence of the triplet-to-singlet relaxation

We further study the relaxation between triplet and singlet states by repeating the measurement of Fig. 8.2e at different magnetic fields $B_{//}$. Figure 8.3a shows the decay of the fraction of $'T'$, normalized to the fraction of $'T'$ at $t_{wait} = 0$, on a logarithmic scale. The data follow a single-exponential decay at all fields. Figure 8.3b shows the relaxation rate $1/T_1$ as a function of $B_{//}$. The dominant relaxation mechanisms for large values of E_{ST} are believed to originate from

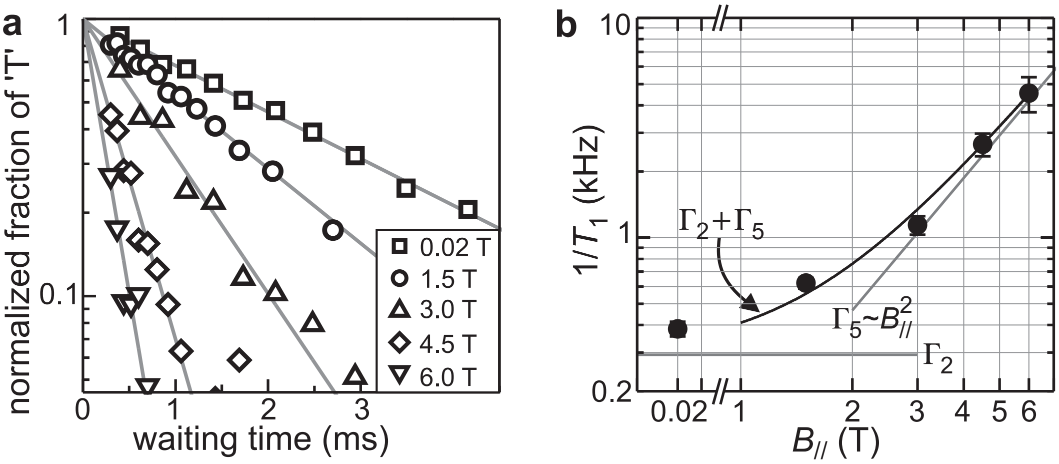

Figure 8.3: Triplet-to-singlet relaxation as a function of $B_{//}$. (a) Normalized fraction of $'T'$ vs. t_{wait} for different values of $B_{//}$. (b) Triplet-to-singlet relaxation rate $1/T_1$ as a function of $B_{//}$. The data is fit to with a second-order polynomial (see text).

the spin-orbit interaction [4, 16], but to our knowledge the case of an in-plane magnetic field has not been treated yet. A second-order polynomial fit to the data yields $1/T_1$ [kHz]= $(0.39 \pm 0.03) + (0.10 \pm 0.02) \cdot B_{//}^2$ [T], with a negligible linear term.

8.5 Read-out of nearly degenerate states

Now, we show that the TR-RO can still be used when $|S\rangle$ and $|T\rangle$ are almost degenerate. By mounting the device under a 45 degree angle with respect to the magnetic field axis, we can tune the singlet-triplet energy difference E_{ST} through zero [11]. In Fig. 8.4a we plot E_{ST} as a function of B, extracted from pulse spectroscopy measurements [13]. In these measurements, transitions are broadened both by the electron temperature in the reservoir and by fluctuations in the dot potential. We model these two effects by one effective electron temperature T_{eff}. For E_{ST} smaller than about 3.5 kT_{eff}, the energy splitting can not be resolved. As in previous transport and pulse spectroscopy measurements, we find here 3.5 $kT_{eff} \approx$ 60 μeV (see inset of Fig. 8.4a), and therefore it is impossible to use the E-RO method beyond $B \approx 3.9$ T. From extrapolation of the data, we find that the singlet-triplet ground state transition occurs at (4.25 ± 0.05) T.

We tune B to 4.15 T (see inset of Fig. 8.4a), so that we are very close to the degeneracy point, but still certain that $|S\rangle$ is the ground state. Here, we perform

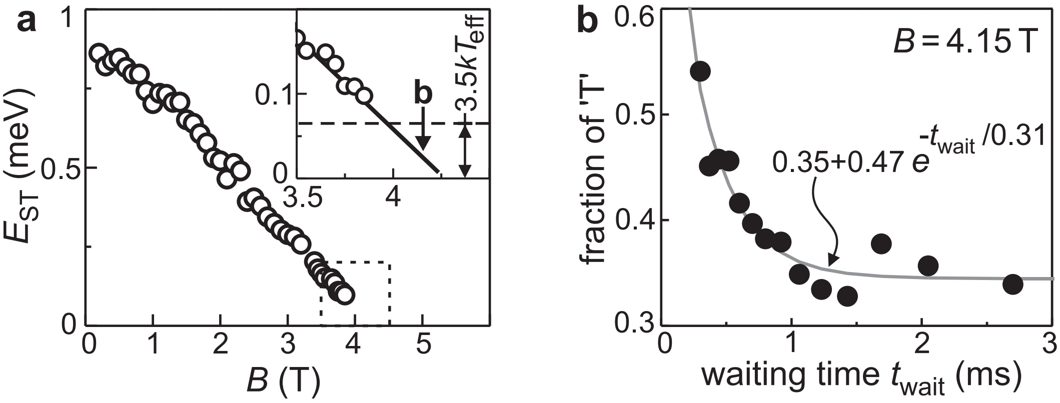

Figure 8.4: Single-shot read-out of nearly degenerate states. (a) Singlet-triplet energy difference E_{ST} as a function of magnetic field B, applied under a 45 degree angle to the 2DEG, showing a singlet-triplet ground state transition at 4.25 T. Inset: zoom-in of the transition region indicated by the dashed square. For $B > 3.9$ T, E_{ST} is smaller than the effective electron temperature. (b) Single-shot read-out at $B = 4.15$ T. This field value is indicated with 'b' in the inset of (a).

a read-out measurement similar to the one presented in Fig. 8.2e. Figure 8.4b shows the measured fraction of $'T'$ as a function of waiting time. Again, an exponential decay of the fraction of $'T'$ is observed, with a T_1 of (0.31 ± 0.07) ms. This demonstrates that even when the energy splitting E_{ST} is too small to resolve, we can still read out the spin states using TR-RO.

For a T_1 of 0.31 μs and a ratio Γ_T/Γ_S of 20, we expect a fidelity of about 75%. From the fit, we find that the decaying fraction of the data in Fig. 8.4b is 0.46. However, a detailed analysis of the fidelity is complicated by a number of factors, which we outline below.

First, the Zeeman splitting ΔE_Z ($\approx 70\mu$eV) is much larger than the temperature kT_{el}. Therefore, the dot will virtually always be in the one-electron spin-up state $|\uparrow\rangle$ at the end of the initialization phase (see Fig. 8.2b). This implies that the triplet $|T_-\rangle = |\downarrow\downarrow\rangle$ can not be occupied, since this would require a change in spin z-component of more than 1/2. The states $|T_+\rangle = |\uparrow\uparrow\rangle$ and $|T_0\rangle = (|\uparrow\downarrow\rangle + |\downarrow\uparrow\rangle)/\sqrt{2}$ are formed with a probability ratio 2:1 [17], if the tunnel rates do not depend on the spin of the tunneling electron. However, since such a spin-dependence has been observed in transport measurements in a perpendicular magnetic field [9, 10], this ratio is probably even larger.

Second, in a magnetic field the spin-orbit-induced decay from $|T_0\rangle$ to $|S\rangle$ is expected to be much slower than from $|T_+\rangle$ to $|S\rangle$ [16, 18]. If this is true, a relaxation measurement would yield a decay with two time constants: a very long T_1 due to relaxation from $|T_0\rangle$, and a shorter T_1 due to the relaxation from $|T_+\rangle$, as was observed in Ref. [19]. Note that close to zero field (as in Fig. 8.2e), these effects are not relevant since the Zeeman energy is negligible. Fitting to the data of Fig. 8.4b yields a single decay constant. It could be that the relaxation from $|T_0\rangle$ to $|S\rangle$ is so slow that the fraction of $|T_0\rangle$ that decays during the chosen waiting times is insignificant. The non-decaying fraction of the data is 0.35, which could be a combination of the error rate α for read-out of $|T_+\rangle$ states and a (virtually non-decaying) fraction of $|T_0\rangle$ states.

Finally, the occupation probability of $|S\rangle$ in thermal equilibrium could deviate significantly from 1, if the condition $E_{ST} \gg kT$ is not satisfied. This would decrease the decaying fraction of the data, leading to an underestimate of the fidelity. From Fig. 8.4a we find E_{ST} to be about 30 μeV, which is much more than the base temperature of the dilution fridge T_{base} ($kT_{base} < 2$ μeV), but not far from the electron temperature in the reservoir ($kT_{el} \approx 9$ μeV).

Since all of the above mentioned effects lead to an underestimate of the fidelity, we know that the fidelity is at least 0.46 (the decaying fraction), but probably much higher.

8.6 Conclusions

Concluding, we have demonstrated a novel read-out method for the N=2 spin states, based on the difference in tunnel rates between the spin states. In contrast to the E-RO, this read-out can also be used for states that are close to degeneracy, as we have experimentally shown. We finally note that read-out of single-electron spins should also be possible with TR-RO, as measurements have shown that a perpendicular magnetic field induces spin-selectivity in the tunnel rates, due to the spatial separation of the spin-resolved edge channels [9, 10].

We thank V. Golovach, S. I. Erlingsson and D. Loss for useful discussions. This work was supported by FOM, NWO, the DARPA-QUIST program, the ONR and the EU-RTN network on spintronics.

References

[1] D. Loss and D. P. DiVincenzo, Phys. Rev. A **57**, 120 (1998).

[2] J. M. Elzerman *et al.*, Nature **430**, 431 (2004).

[3] O. Astafiev *et al.*, Phys. Rev. B **69**, 180507 (2004).

[4] V. Golovach *et al.*, in preparation.

[5] S. W. Jung *et al.*, Appl. Phys. Lett. **85**, 768 (2004).

[6] L.M.K. Vandersypen *et al.*, Appl. Phys. Lett. **85**, 4394 (2004).

[7] Similarly, spin-dependent tunneling to a second dot can be used, see H. A. Engel *et al.*, Phys. Rev. Lett. **93**, 106804 (2004).

[8] The probability β that no tunnel event has occurred at $t = \tau$, even though the initial state was $|ES\rangle$, is the sum of β_1, the probability that the state is $|ES\rangle$, and β_2, the probability that the state is $|GS\rangle$. These are given by:

$$\begin{aligned} \beta_1 &= e^{-(\Gamma_{ES}+1/T_1)\cdot\tau}, \\ \beta_2 &= \int_0^{\tau} P_{rel}(t)\cdot P_{GS}(\tau-t)\ dt. \end{aligned}$$

Here, $P_{rel}(t)\,dt$ is the probability that $|ES\rangle$ relaxes to $|GS\rangle$ within the time interval $[t, t+dt]$, and $P_{GS}(\tau-t)$ is the probability that no tunneling has taken place from $|GS\rangle$ during a time $\tau - t$:

$$\begin{aligned} P_{rel}(t) &= 1/T_1\ e^{-(1/T_1+\Gamma_{ES})\cdot t} \\ P_{GS}(\tau-t) &= e^{-\Gamma_{GS}\cdot(\tau-t)}\ . \end{aligned}$$

[9] M. Ciorga *et al.*, Phys. Rev. B **61**, R16315 (2000).

[10] M. Ciorga *et al.*, Appl. Phys. Lett. **80**, 2177 (2002).

[11] L. P. Kouwenhoven, D. G. Austing, and S. Tarucha, Rep. Prog. Phys. **64** (6), 701 (2001).

[12] R. Hanson *et al.*, Proceedings of the 39th Rencontres de Moriond (La Thuile, 2004), see cond-mat/0407793.

[13] J. M. Elzerman *et al.*, Appl. Phys. Lett. **84**, 4617 (2004).

[14] R. Schleser *et al.*, Appl. Phys. Lett. **85**, 2005 (2004).

[15] T. Fujisawa *et al.*, Nature **419**, 278 (2002).

[16] A. V. Khaetskii and Y. V. Nazarov, Phys. Rev. B **61**, 12639 (2000).

[17] This can be seen by writing the state before tunneling as $|\uparrow S2\rangle$, where the $\uparrow$ denotes the spin-up electron on the dot and $S2$ the electron tunneling from the reservoir. The overlap of $|T_+\rangle$ with $|\uparrow\uparrow\rangle$ is 100%, whereas the overlap of $|T_0\rangle$ with $|\uparrow\downarrow\rangle$ is only 50%, leading to a ratio 2:1 in the tunneling probability.

[18] S. Dickmann and P. Hawrylak, cond-mat/0208223.

[19] S. Sasaki *et al.*, Phys. Rev. Lett. **95**, 056803 (2005).

Chapter 9

Current status and future directions for electron spin-based quantum computing

L. H. Willems van Beveren, R. Hanson, J. M. Elzerman,
F. H. L. Koppens, I. T. Vink,
L. P. Kouwenhoven and L. M. K. Vandersypen

In this chapter we review the progress towards the implementation of qubits with electron spins confined in few-electron lateral quantum dots, as described in the previous chapters. We evaluate the steps we have taken and the ones we still have to take, in terms of generally accepted criteria for any solid-state qubit implementation. We summarize current theoretical insight on the decoherence mechanisms and present concrete ideas on how to proceed towards coherent spin operations. Single-spin manipulation relies on a microfabricated wire located close to the quantum dot, and two-spin interactions are controlled via the tunnel barrier of a double quantum dot. We argue that experimental demonstration of single and- and two-qubit gates is easiest by using a QPC charge detection approach, without relying on transport measurements.

Some of the ideas in this chapter have been described in *Quantum Computing and Quantum Bits in Mesoscopic Systems*, Kluwer Academic, New York (2003) (see also quant-ph/0207059) and in cond-mat/0311414.

9.1 Introduction

In the previous chapters we have described experiments aimed at creating a quantum dot spin qubit according to the proposal by Loss and DiVincenzo [1]. In chapter 1 we have outlined the basic ingredients of this proposal. In this section, we will report the experimental progress on the spin qubit proposal using the five criteria of DiVincenzo's checklist [2] which must *all* be satisfied for any physical implementation of a quantum computer. We will first present the system in which we wish to implement our qubit and continue with schemes how to (i) initialize, (ii) read out and (iii) manipulate the qubit. Further requirements are (iv) long coherence times and (v) a set of universal quantum gates.

9.1.1 Qubit

The first of the five DiVincenzo requirements is to have a scalable physical system with well-characterised qubits. Well-characterized means that we know the properties of the system in which the qubit is encoded, the presence of and coupling to other states of the system, the interaction with other qubits, and the coupling to external control parameters.

In our case, the qubit is encoded in the spin orientation of a single electron in a static magnetic field B_0, where $|\uparrow\rangle$ serves as the logic $|0\rangle$, and $|\downarrow\rangle$ corresponds to the logic $|1\rangle$. The electron spin can not take on any value outside the two-dimensional Hilbert space spanned by $|\uparrow\rangle$ and $|\downarrow\rangle$. The interaction with other qubits and the coupling to external control fields will be discussed below in section 9.1.5.

Since the spin is carried by an electron confined in a quantum dot, we need to characterize this quantum dot as well. We have shown in section 3.4 that we can isolate a single electron in each of two coupled quantum dots [3]. The conventional way of characterizing dots is to measure the current through the dot as a function of applied bias voltage [4]. The smallest current that we can resolve is about 16 fA, which sets a lower bound on the tunnel rate to the reservoir, Γ, of about 16 fA/e= 100 kHz. For $\Gamma <$ 100 kHz, we can use the charge detection technique [5] developed in chapters 3 and 6 [3, 6], where a nearby quantum point contact (QPC) serves as an electrometer. Here the limitation arises from the bandwidth of our charge detection setup. This bandwidth can be extended by increasing the electrostatic coupling of the QPC to the dot using a different gate design [7]. Further improvements can be achieved by using a 'radio-frequency QPC' (RF-QPC), similar to the well-known RF-SET [8]. In this approach, the QPC is embedded in an LC circuit with a resonant frequency of $\sim$ 1 GHz. By measuring the reflection or transmission of a resonant carrier wave, it is estimated that it should be possible to read out the charge state of the nearby quantum dot in $\sim 1\ \mu$s, an order of magnitude faster than is currently attainable [9].

Both techniques allow a measurement of the absolute number of electrons on the dot, the discrete energy spectrum and the tunnel rate to the reservoir for the different transitions, thus providing a full characterization of a single quantum dot. We have used both techniques to identify the two basis states of the qubit, $|\uparrow\rangle$ and $|\downarrow\rangle$, and measured their energy splitting [10, 11, 6] (see chapters 4, 5 and 6).

The coupling between two quantum dots can be separated into a capacitive coupling and a tunnel coupling. The capacitive coupling can be easily inferred from the charge stability diagram (as shown in Fig. 3.9) [12]. The tunnel coupling can also be deduced from the stability diagram, either from the curvature of the lines in the 'honeycomb' diagram (see e.g. Ref. [13]) or from the charge distribution near the anti-crossing of the two single-dot ground states [14]. A more accurate value for the tunnel coupling can be found by performing photon-assisted tunneling spectroscopy. This method has been demonstrated both for transport measurements [15] and for measurements using only charge detection [14]. The double-dot exchange splitting J can in principle be determined from spectroscopy measurements [16], but in the regime of interest ($J \sim 1 - 30\ \mu$eV) we might not be able to resolve it due to thermal broadening. The value of J can always be found from the frequency of the two-spin oscillation (see section 9.3.1). Recently, J was measured using a QPC as charge detector in the spin-blockaded regime (by varying detuning and magnetic field), where hyperfine fields drive evolution between S and respective T states [17]. It should be noted that J in this experiment is enhanced significantly by the tunnel coupling. Nevertheless, detection of J in the spin-blockade regime at large detuning is much less limited by thermal broadening.

Thus all relevant parameters of a single and coupled quantum dot system can be determined without performing transport measurements. The essential advantage of the QPC technique is that it works even for a dot that is very weakly coupled to just a *single* reservoir. This gives us more freedom to design simple dots with fewer gates, which could therefore be easier to operate. At the same time it allows us to extend our present circuit to incorporate several more quantum dots, by making minor adjustments to the design of the surface gates. To study decoherence and demonstrating basic quantum algorithms a circuit containing about five to ten qubits is sufficient for the near future. In order to create a quantum computer consisting of, say, several hundreds of qubits, major revisions in the design and use of different fabrication techniques will most probably be necessary.

9.1.2 Initialization

Initialization of the qubits to a known (pure) state is required for two reasons. First, before the start of the computation the qubits have to be initialized to a known value. Second, for quantum error correction a continuous supply of (ancillary) qubits in a known pure state is needed [2].

Initialization of the spin to the pure state $|\!\uparrow\rangle$ – the desired initial state for most quantum algorithms [18] – can be achieved by waiting so long that energy relaxation will cause the the spin on the dot to relax to the $|\!\uparrow\rangle$ ground state (Fig. 9.1a). This is a very simple and robust initialization approach, which can be used for any magnetic field orientation (provided that $g\mu_B B > 5k_B T$). As it takes about $5T_1$ to reach equilibrium, it is also a very slow procedure, which might become problematic at the stage of quantum error correction [2].

A faster initialization method is to place the level $|\!\uparrow\rangle$ below and $|\!\downarrow\rangle$ above the Fermi energy of the reservoir (as in Fig. 9.1b). Then, a spin-up electron will stay on the dot, whereas a spin-down electron will tunnel out to the leads, to be replaced by a spin-up. After waiting a few times the sum of the typical tunnel times for spin-up and spin-down ($\sim 1/\Gamma_\uparrow + 1/\Gamma_\downarrow$), the spin will be with large probability in the $|\!\uparrow\rangle$ state. This initialization procedure can therefore be fast (< 1 ms), depending on the tunnel rates. A disadvantage is that the Zeeman energy splitting needs to be much larger than the electron temperature in the leads.

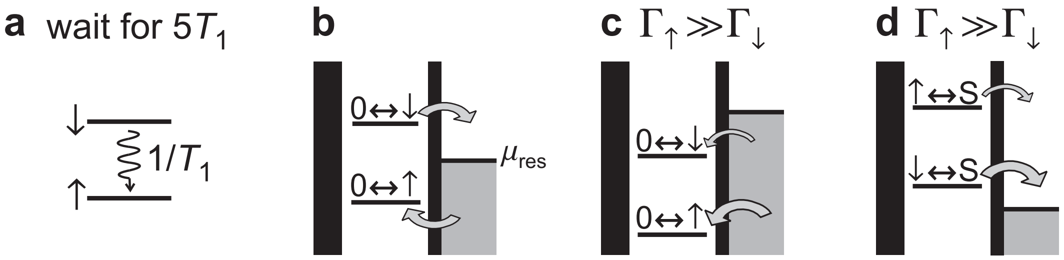
a wait for $5T_1$
↓
$1/T_1$
↑
b
$0\leftrightarrow\downarrow$
$0\leftrightarrow\uparrow$
μ_{res}
c $\Gamma_\uparrow \gg \Gamma_\downarrow$
$0\leftrightarrow\downarrow$
$0\leftrightarrow\uparrow$
d $\Gamma_\uparrow \gg \Gamma_\downarrow$
$\uparrow\leftrightarrow S$
$\downarrow\leftrightarrow S$

Figure 9.1: Different methods for initialization to (a)-(c)$|\!\uparrow\rangle$ and (d) $|\!\downarrow\rangle$. **(a)** Spin relaxation at a rate $1/T_1$ gives the state $|\!\uparrow\rangle$ after $\sim 5T_1$. **(b)** Energy-selective tunneling leads to $|\!\uparrow\rangle$ after a time $\sim 1/\Gamma_\uparrow + 1/\Gamma_\downarrow$. We use here explicit notations for the transitions between the zero-electron state and the one-electron spin states to avoid confusion with the transitions used in (d). **(c)** If $\Gamma_\uparrow \gg \Gamma_\downarrow$, tunneling into an empty dot will result in $|\!\uparrow\rangle$ with a probability $\Gamma_\uparrow/(\Gamma_\uparrow + \Gamma_\downarrow)$. **(d)** Initialization to $|\!\downarrow\rangle$ for $\Gamma_\uparrow \gg \Gamma_\downarrow$ by starting from the two-electron singlet state, denoted here by S.

A third possibility is to initialize using the large spin selectivity in the tunnel rates, i.e. $\Gamma_\uparrow \gg \Gamma_\downarrow$, which is present in a perpendicular field due to the spatial separation of the spin-resolved edge channels [19, 20]. Here, we first empty the dot, and then position both spin levels below μ_{res} (see Fig. 9.1c). The electron that will tunnel in will have spin-up with probability $\Gamma_\uparrow/(\Gamma_\uparrow + \Gamma_\downarrow)$, which is very close to unity for high spin selectivity.

For verifying read-out procedures and testing two-qubit operations (see section 9.3.1), we also need the ability to initialize to the spin-down state. The most straight-forward method is to initialize to $|\uparrow\rangle$ and rotate the spin by 180 degrees. However, controlled rotation of a single spin on a quantum dot has not yet been demonstrated. Fortunately, there are other ways to initialize to $|\downarrow\rangle$. If the tunnel rates are spin-selective as mentioned above, we can start from a two-electron singlet state $|S\rangle$=($|\uparrow\downarrow\rangle$-$|\downarrow\uparrow\rangle$)/$\sqrt{2}$, and allow one electron to tunnel off the dot. Since $\Gamma_\uparrow \gg \Gamma_\downarrow$, the probability that the tunneling electron has spin-up and therefore the remaining electron has spin-down is $\Gamma_\uparrow/(\Gamma_\uparrow + \Gamma_\downarrow)$ (see Fig. 9.1d). Thus, we can initialize to $|\uparrow\rangle$ and $|\downarrow\rangle$ with the same high fidelity.

In the absence of spin-selectivity in the tunnel rates (parallel magnetic fields) we can not initialize to $|\downarrow\rangle$, but we can initialize to a mixed state where the electron is probabilistically in $|\uparrow\rangle$ or $|\downarrow\rangle$, by first emptying the dot and then positioning both spin levels below μ_{res} (see chapter 7). The dot is then randomly filled with either a spin-up or a spin-down electron. This is very useful, e.g. to test two-spin operations (see section 9.3.1).

9.1.3 Read-out

Read-out determines the result at the end of the computation by measuring specific qubits. Many proposals exist for reading out the electron spin state on a quantum dot (see chapter 7 for an extensive list of references). In this thesis, we have demonstrated two methods. In both of them, the spin information is first converted to charge information, by making the number of electrons on the dot, N, dependent on the original spin state.

The first approach makes use of the large Zeeman energy splitting induced by an in-plane magnetic field. Here, the two spin levels are positioned such that an electron can tunnel off the dot only if it carries the high-energy spin (as in Fig. 9.1b). This is followed by real-time detection of single-electron tunneling events using the QPC as an electrometer. We have used this method in chapter 7 to perform single-shot read-out of the spin of a single electron [21]. Here, the measurement visibility was $\sim$ 65% at 10 T, limited mostly by the $\sim$ 40 kHz bandwidth of our current measurement setup, and also by thermal excitation of electrons out of the quantum dot, due to the (in this experiment) high effective electron temperature of ~ 300 mK. We estimate that we can improve the visibility of this energy-selective read-out (E-RO) technique to more than 90% by lowering the electron temperature below 100 mK, and especially by using a faster way to measure the charge on the dot (see section 9.1.1).

The second method that we have studied makes use of a difference in *tunnel rate* between the spin states. To read out the spin orientation of an electron on the dot, we simply raise both dot levels above μ_{res}, so that the electron can leave the dot. If the tunnel rate for spin-up electrons, $\Gamma_\uparrow$, is much larger than that for spin-down electrons, $\Gamma_\downarrow$, then after a time τ, where $\Gamma_\downarrow^{-1} \gg \tau \gg \Gamma_\uparrow^{-1}$, the dot will have a large probability to be already empty if the spin was up, but a very small probability to be empty if the spin was down. Measuring the charge on the dot at $t = \tau$ thus reveals the original spin state. In chapter 8 this tunnel-rate-selective read-out (TR-RO) method is used to read out the two-electron spin state, achieving a single-shot visibility of 81% [22]. We plan to use TR-RO also for a single electron by applying the magnetic field perpendicular to the 2DEG, so that $\Gamma_\uparrow \gg \Gamma_\downarrow$ [19, 20]. Note that in this case the tunnel-rate selectivity does not result form orbital differences, as was the case for the two-electron states. Nevertheless, we hope to achieve large spin-dependence of the tunnel rates, due to many-body exchange interactions leading to an enhanced g-factor in the reservoir [23].

As explained in chapter 8, TR-RO has some important advantages over E-RO. In contrast to E-RO, TR-RO does not require a large energy splitting between the spin states, which allows us to use lower frequencies for single-spin manipulation by ESR. Lower driving frequencies will also increase the coupling of the ESR-field to the electron spin. Moreover, the TR-RO method is robust against background charge fluctuations that shift the dot-levels with respect to the Fermi energy of the reservoir, μ_{res}. Finally, it is less sensitive to photon-assisted tunneling; a process which may interfere during driving of the qubit (see section 9.2.3). Which of the two read-out methods is preferable will also depend on the specific demands of the particular experiment.

9.1.4 Coherence

There are two time scales which are important for the success of the electron spin qubit. The first time scale is the longitudinal relaxation time T_1 corresponding to the time it takes for the excited state $|\downarrow\rangle$ to relax to the ground state $|\uparrow\rangle$. This process involves the emission of energy that should somehow be absorbed by the environment of the qubit (energy conservation), e.g. by phonons or the nuclear spins via the hyperfine interaction. For times larger than T_1 an arbitrary superposition state of the qubit will end up in the ground state and quantum coherence is lost. The second time scale is the transverse relaxation or dephasing time T_2 and corresponds to the time in which a quantum superposition loses its phase. At this point we loose track of the qubit state evolution on the Bloch sphere, unable to control it from outside.

In principle, loss of coherence (bit-flips and/or dephasing) can be entirely compensated for by performing quantum error correction [18]. It is estimated that if the error per operation is 10^{-4}, error correction can be successful and arbitrarily long computations can be performed. This ratio is sometimes referred to as the 'accuracy threshold'. It implies that also T_2 has to be at least 10^4 times larger than the gate operation time. However, for experiments in the near future, we only need to perform a few spin rotations within T_2, on the order of μs. This should be long enough to perform two-spin operations, which are likely to be much faster.

It is evident that the long-term potential of GaAs quantum dots as electron spin qubits clearly depends crucially on the spin coherence times T_1 and T_2. The electron spin was proposed as a candidate for a qubit, because the spin state was believed to be very stable. Relaxation measurements on a single spin (chapter 7 and Ref. [24]) and on two-electron spin states (chapter 8) have shown long spin relaxation times up to several milliseconds, suggesting that indeed the spin is only weakly perturbed by the environment. In contrast, the orbital degree of freedom of electrons has been measured to decay on a 10 nanosecond time scale [25], which is five orders of magnitude faster than the spin relaxation. The true figure of merit for quantum computing, however, is the coherence time. The value of T_2 for a single electron spin in a GaAs quantum dot has not yet been measured.

Over the past few years, theoretical insight into the electron spin relaxation and decoherence mechanisms has increased enormously. At present, the dominant mechanisms are believed to be the spin-orbit interaction [26, 27], and the hyperfine interaction with the nuclei [28, 29, 30, 31]. Recent theory suggests that the spin-orbit interactions, in leading order, do not affect the transverse components of the spin [27]. This would imply that the spin-orbit limited coherence time can not be shorter than the relaxation time T_1. In contrast, the nuclear spin system is expected to have a much more severe impact on T_2 than on T_1.

The hyperfine interaction of the electron spin with the surrounding nuclear spins leads to an additional effective magnetic field B_{nucl}, the so-called Overhauser field. The polarization of the nuclei will usually be negligible in our experiments and thus the absolute value of B_{nucl} will be small compared to the external field B_0. Anyway, a static polarization just adds a constant offset to B_0 and thus has no effect on the coherence. In contrast, the *fluctuations* in B_{nucl}, denoted ΔB_{nucl}, cause uncertainty in the total effective magnetic field and can therefore lead to significant decoherence of the electron spin.

The effect of the nuclear system on the coherence time of an electron in a quantum dot is discussed in detail in Ref. [30, 32]. The conclusion is that for zero magnetic field, the relevant dephasing time is set by the value of the statistical variation of B_{nucl}: $\Delta B_{nucl} \sim A/(\sqrt{N_{nucl}} g\mu_B)$, where A is the hyperfine constant ($A = 90$ μeV in GaAs [33]), and N_{nucl} is the number of nuclei with which the electron interacts. For N_{nucl}=10^5, we have ΔB_{nucl} ∼10 mT and a T_2 time on the order of 10 ns is expected. When a strong magnetic field is applied this timescale could be increased to about 100 μs [29, 30], if the value of B_{nucl} would be known exactly. In practice however, B_{nucl} is not known, and the relevant decoherence time is on the order of 10 ns. These considerations should be taken as a strong incentive to study the behavior of the nuclei in more detail experimentally.

For electrons in bulk n-type GaAs, an ensemble-averaged measurement has yielded a spin dephasing time T_2^* of 100 ns [34]. This value is larger than the dephasing time mentioned above. This can be explained by the following: an electron in the bulk interacts with many more nuclei (whereas for a quantum dot the electron wavefunction is localized), and since $\Delta B_{nucl} \propto 1/\sqrt{N}$ this leads to a lower decoherence rate. Therefore we conclude that the dephasing time measured in the bulk (or in a 2DEG) can not be considered as a lower bound for T_2 of an electron on a quantum dot.

Pioneering experiments in the group of Prof. Tarucha at the University of Tokyo have already uncovered some intriguing physics, occurring when electron transport through a vertical double dot is spin-blocked due to the Pauli exclusion principle [35]. Recently, the Pauli spin blockade was also observed in a lateral system in the group of Prof. Marcus at Harvard [36] as well as in our own group [37]. The extracted value of the dephasing time we measure in this experiment agrees very well with theory [38, 39].

The demonstration of a 180 ps $\sqrt{SWAP}$ operation (see section 9.3.1) has very recently been demonstrated by the Harvard group in a double quantum dot system using a QPC as sensitive charge detector in the spin-blockaded regime [17]. Here, the basis states of the qubit form the two-electron spin singlet state $|S_0\rangle$ and spin triplet state $|T_0\rangle$. The exchange interaction between the spins in each dot drives transitions between these states and coherence is limited by the fluctuating nuclear field. By a spin-echo technique the time-ensemble-averaged dephasing time (T_2^*) could be extended from ∼ 10 ns to a T_2 beyond 1 μs. This implies that the coherence time of the qubit using spin-echo exceeds the $\sqrt{SWAP}$ operation time by a factor of ∼7000.

The quest in the next years will be for a means to 'turn off' the fluctuations in the nuclear system on longer timescales, in so-called 'stopping points'. Since the decoherence arising during the precession of the electron spin in one nuclear configuration can be exactly canceled by a precession in the opposite nuclear configuration, flipping all nuclear spins with a period much faster than τ_1, the period of the nuclear spin precession in the hyperfine field of the electron, will greatly prolong the coherence. Alternatively, if the electron spin can be manipulated on timescales much shorter than τ_1, composite pulse techniques can be used [40]. In these cases, coherence can be preserved for a time of about 100 μs [30]. One ultimate possibility is to completely polarize the nuclear spin system, thus eliminating all fluctuations. Also, we can think of isolating the electron spin in a different host material where the nuclei possess no spin [41]. Most notably, Si/SiGe quantum dots [42, 43] and carbon nanotubes can in principle be purified to contain only spinless nuclei. Moreover, is expected that for quantum dots defined in two-dimensional hole gases (2DHG), the hyperfine interaction of holes with lattice nuclei is suppressed with respect to that of the conduction band (electrons), due to the p symmetry of the valence band leading to less overlap of the hole wavefunction with the nuclei [44]. However, the hole spin relaxation time is several orders of magnitude smaller than that for electrons, due to the strong spin-orbit coupling between the heavy-hole (HH) and light hole (LH) subbands [45]. These systems might one day exhibit the same excellent control over single-electrons that we have right now in GaAs structures.

To put the value of the coherence time in perspective, we need to compare it to the gate operation time, which we will estimate in the next section.

9.1.5 Universality

A set of quantum gates is called universal if every unitary operation on an arbitrary number of qubits can be decomposed into combinations of only these quantum gates. It has been proved that full single-qubit control combined with the two-qubit 'quantum XOR' (or 'CNOT'), suffice to implement all possible quantum algorithms [18].

For electron spins in quantum dots, both the single-qubit control fields as well as the interactions between neighboring qubits can be completely turned on and off at will. The two-qubit CNOT can be implemented by a combination of single-qubit rotations and two-spin exchange interactions [46]. In fact, the exchange interaction is even universal by itself, i.e. without single-qubit rotations, when the state of each qubit is encoded in the state of three electron spins [47].

We consider two schemes for single-spin rotations. In one approach, an oscillating magnetic field B_{ac} is applied perpendicular to the static field B_0 at the Larmor frequency $g\mu_B B_0/h$, with $g \approx -0.44$ and $\mu_B = 58$ μeV/T is the Bohr magneton. This induces spin rotations at a rate $f_{Rabi} = g\mu_B B_{ac}/h$, which is about 6 MHz for $B_{ac} = 1$ mT. This well-known electron spin resonance (ESR) technique has already been applied in the 1980s to GaAs/AlGaAs 2DEG electrons in the Quantum Hall regime (see e.g. Ref [48]). At dilution fridge temperatures, it is hard to reach values of B_{ac} exceeding 5 mT using current technology, in particular for high frequencies (see section 9.2.1). If we assume $B_{ac} < 5$ mT, then $f_{Rabi} < 30$ MHz and the single-qubit gate operation time will be at least $1/2f_{Rabi} \sim 15$ ns. As we have argued in the previous section, T_2 might be of the same order. Our efforts to demonstrate single-spin ESR will be discussed in section 9.2.

Alternatively, a spin rotation can be achieved by modulating the value of the electron g-factor at the Larmor frequency. This so-called g-tensor modulation has been experimentally demonstrated on electrons in an AlGaAs/GaAs/AlGaAs quantum well [49]. Here, a voltage on a backgate pulls the electron wave function from the GaAs central region, where g is -0.44, into the AlGaAs barrier region, where g is +0.4 [50]. Due to the anisotropy of the g-factor in these quantum wells, the orientation of the effective magnetic field also changes. By applying an oscillating electrical signal at the Larmor frequency to the backgate, the spin of electrons in the quantum well could be tipped by 2 degrees. For a single electron in a quantum dot, such oscillating electric fields might induce unwanted effects like photon-assisted tunneling. Furthermore, increasing the anisotropy such that it can produce rotations of 180 degrees seems challenging. Therefore, the ESR approach is likely to yield the first experimental demonstration of single-spin rotations and provide a value for T_2. Control over the g-factor might become useful to bring individual electron spins into resonance with a 'global' ESR field.

Two-spin operations are mediated by the exchange interaction, which leads to an effective Heisenberg Hamiltonian $J\,\vec{S}_1 \cdot \vec{S}_2$. Here, J is the strength of the exchange interaction and $\vec{S}_1$ and $\vec{S}_2$ denote the two spins. The value of J is related to the overlap of the electron wave functions, which varies exponentially with the voltage applied to the gate controlling the inter-dot tunnel barrier. Thus, by applying a (positive) voltage pulse with a certain amplitude and duration, we can temporarily turn on the exchange interaction. The two-spin operations are discussed in more detail in section 9.3.

The shortest electrical pulses applied to surface gates that can be precisely controlled are on the order of 100 ps [51], corresponding to a value of $J/h \sim 5$ GHz (for completely swapping the spin states). During the gate operation, fluctuations in the tunnel rate due to charge noise can lead to additional decoherence. It has been shown recently that background charge noise has only a very weak effect on the tunnel rate to the reservoir [52]. However, it can also lead to misalignment of the two single-dot levels, which will enhance J [53]. Since there are many factors that possibly influence the background charge noise, it is difficult to capture its effect on the coherence in a single number.

As in the case of a single spin, the nuclei can pose a significant threat: different Overhauser fields on the two dots (ΔB_{nucl} on the order of 10 mT) lead to a difference in the effective spin splitting δE of about 0.3 μeV. The error induced by δE is $(\delta E/2J)^2$ [54]; thus we can make the error small by performing the operation within a short time. For $J=$ 20 μeV (5 GHz), the error is of order 10^{-4}.

Concluding, current insight suggests that the single-qubit gate operation time (with our present technology in GaAs) is of the same order as the expected T_2. Single-qubit operation time might be drastically shortened using new electrical or optical techniques. For two-spin operations, the gate operation time could well be much shorter. If the decoherence rate turns out to be the same for one- and two-qubit operations, the two-qubit gate will be much closer to the accuracy threshold. In that case, the scheme where one qubit is encoded in the state of three electron spins [47] is more attractive than the original single-spin proposal [1], as single-spin rotations can then be completely left out.

9.1.6 Summary of the current status

Out of the five criteria for a scalable quantum computer, three have already been satisfied: well-defined qubits, initialization and read-out. The Harvard group has recently demonstrated the $\sqrt{SWAP}$ operation. Theoretical considerations suggest that the single-qubit operation time might be of the same order as the coherence time due to the hyperfine interaction with the nuclei, while for the two-spin operations the gate operation time is possibly much smaller.

Future experiments will focus on measuring the coherence time via the coherent manipulation of single spins and the coherent coupling and manipulation of spins in neighboring dots. In the next sections we will discuss these two research paths in more detail.

9.2 Single-spin rotations

In this section, our approach to the coherent rotation of a single electron spin using the above-mentioned ESR principle is outlined. We first discuss the on-chip generation of the required microwave field. Then we propose and critically analyze several schemes for the detection of ESR. Analogously, a bound on T_2 has been claimed for a single electron trapped near a Si-MOSFET channel, based on the linewidth of the observed electron spin resonance [60].

9.2.1 On-chip generation of the oscillating magnetic field

Excitation of ESR microwave magnetic fields commonly relies on microwave cavities, but unfortunately, a lot of power is dissipated in metallic cavities: for a rectangular cavity with a high Q-factor of 10^4, the power dissipation is over 1 Watt for $B_{ac} = 1$ mT at $f_0 = 30$ GHz and still about 100 μW for $B_{ac} = 0.01$ mT [55]. Superconducting cavities are not an option since B_0 is too large.

Instead, we intend to generate the oscillating magnetic field by sending an alternating current through an on-chip wire running close by the dot, as shown in Fig. 9.2a. Depending on the orientation of the static magnetic field that we prefer, the wire can be located next to the dot (for an in-plane magnetic field) or on top of the dot (for an in-plane or a perpendicular field). In the latter case, an insulating layer will separate the wire from the surface gate structure.

If the wire is placed well within one wavelength (which is a few mm at 30 GHz near the surface of a GaAs substrate) from the quantum dot, the dot is in the near-field regime and the electric and magnetic field distribution produced by the AC

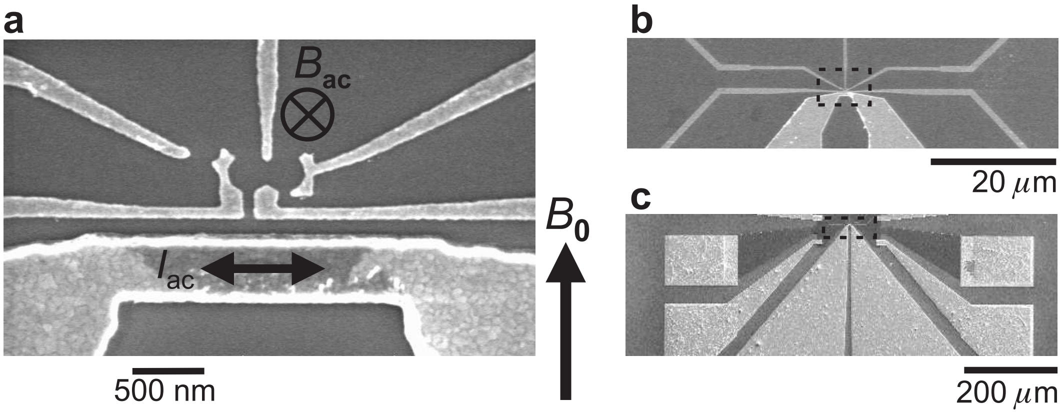

Figure 9.2: Scanning electron micrographs showing of the on-chip gold wire to apply microwaves to a nearby double quantum dot. This device was fabricated by Wouter Naber. **(a)** An AC current through the wire, I_{ac}, generates an oscillating magnetic field, B_{ac}, perpendicular to the plane. If the AC frequency is resonant with the Zeeman splitting induced by a large static in-plane magnetic field, B_0, an electron spin on the dot will rotate. **(b)-(c)** Zoom-outs of (a), showing the coplanar stripline which is designed to have 50 Ω impedance.

current should be the same as for a DC current [55]. The linearly oscillating field can be decomposed into a clockwise and an anti-clockwise component rotating at the same frequency. In the rotating frame, one of these components will be static (the resonant component), while the other one will be far off-resonance and can be disregarded. Note that this implies that only half of the applied oscillating field is actually effective. For a distance between the edge of the (500 nm wide and 200 nm high) wire and the centre of the dot of 200 nm, a current of ~ 2.5 mA should generate a magnetic field of about 1 mT and no electric field at the position of the dot [56, 57]. To minimize reflection and radiation losses, the wire is designed to be a shorted coplanar stripline (Fig. 9.2b) with a 50 Ω impedance. The total dissipation of the on-chip section (Au wire + Au waveguide) is estimated to be on the order of 10 μW for an oscillating field of 1 mT [57], which is well below the thermal budget at the mixing chamber of the dilution refrigerator (about 300 μW at 100 mK). For a field of 5 mT, the dissipation increases to about 250 μW.

9.2.2 Detection of Continuous Wave ESR

In the simplest schemes for detecting ESR, the microwave field B_{ac} is continuously on. Engel *et al.* have proposed a setup in which spin rotations on the dot [58] lead to a current flowing through the dot. This scheme is depicted in Fig. 9.3a-b for a single electron on the dot. If the ESR field is off resonance, the dot is in its ground state $|\uparrow\rangle$ and there is no current due to Coulomb blockade (Fig. 9.3a). In contrast, if the ESR field rotates the spin on the dot to $|\downarrow\rangle$, the electron has enough energy to escape to the right lead (Fig. 9.3b). A resonant current now flows via $|\downarrow\rangle$ until $|\uparrow\rangle$ becomes occupied. The current is then again blocked until the spin is rotated. In Fig. 9.3c a simulation (using the model of Ref. [58]) shows the expected current trace versus gate voltage, for two different values of B_{ac}. From the linewidth in frequency (or magnetic field) of the resonance, a lower bound on the single-electron T_2 can be derived.

A similar setup has been proposed where the ESR-induced change in the average occupation of the dot is measured [59]. Recently, measurement of a spin resonance signal using this setup from an electron in a Si MOSFET impurity trap has been reported [60].

Although these schemes are conceptually simple, it is quite hard to prove that a signal in the current as shown in Fig. 9.3c is indeed due to single-spin rotations on the dot. We discuss here two relevant parasitic effects that can lead to a similar resonance feature.

First, it is virtually impossible to completely eliminate the electrical component of the oscillating field. This electrical component can induce a photon-

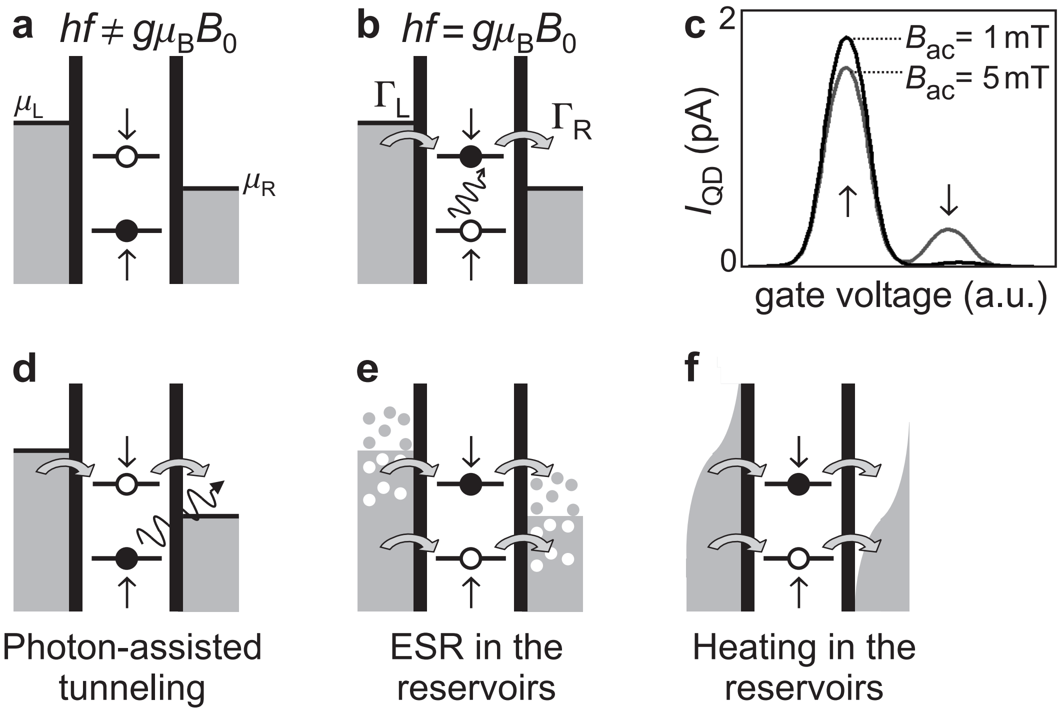

Figure 9.3: Detection of Continuous Wave (CW) ESR. **(a)-(b)** Scheme for detecting CW ESR. **(a)** The electron can not leave the dot if it is in in $|\uparrow\rangle$. **(b)** If the electron is in $|\downarrow\rangle$ due to a spin rotation, it can tunnel off the dot and contribute to the current. **(c)** Simulation of the expected current as a function of gate voltage, using the model of Ref. [58]. The symbols ↑ and ↓ indicate the gate voltage at which the levels for ↑ and ↓ lie within the bias window (i.e. are between μ_L and μ_R). The ESR-induced peak is about 20 fA (400 fA) for B_{ac}= 1 mT (5 mT). We have used the following parameter values: T_1=1 ms, T_2=100 ns, Γ_L=50 MHz, Γ_R=15 MHz, B_0=5 T. Curves similar to (c) can result from the unwanted effects of **(d)** photon-assisted tunneling, **(e)** ESR in the reservoirs, or **(f)** heating of the electrons in the reservoir.

assisted tunnel event from $|\uparrow\rangle$ to the leads (see Fig. 9.3d). This so-called photo-ionization process leads to exactly the same situation as in Fig. 9.3b. Also, for even higher electric fields a current can flow where every tunnel event involves photon-absorption (pure photon-assisted tunneling). This will induce peaks on both sides of the main peak.

Second, if the ESR resonance frequency of electrons in the *leads* is the same as the expected resonance frequency for the electron on the dot (see Fig. 9.3e), a current will flow through the dot independent of whether the spin on the dot is actually rotated. Clearly, under these conditions there is no way to prove that spin rotations occur on the dot. (A similar effect is present when the electrons in the leads are heated by the microwave field (Fig. 9.3f), but the frequency and magnetic field dependence of the heating process and ESR will generally be different). Both the photo-ionization process and ESR in the reservoirs can not be circumvented by changing the magnetic field, making single-spin ESR on the dot hard to prove.

9.2.3 Detection of pulsed ESR

The problems mentioned in the previous section can be avoided by separating the spin rotation and the read-out in time: B_{ac} is turned on when the levels are well in the Coulomb blockade regime, and B_{ac} is off when the spin state is read out. In between, we allow enough time for any excitation in the reservoirs to disappear (note that the relaxation times in the leads are much shorter than T_1 on the dot). This way, photon-assisted tunneling does not provide enough energy for the electron to tunnel out, and the read-out is performed when the reservoirs are (again) in thermal equilibrium.

In the long run, we would like to combine ESR with single-shot read-out. In order to find the resonance condition and obtain first evidence of single-spin rotation, it is more convenient and much faster to apply a voltage pulse train and measure the read-out signal averaged over many cycles. In Fig. 9.4a we show the pulse amplitude V_P and the amplitude of the microwave field B_{ac} as a function of time. The spin is rotated when the levels are in Coulomb blockade (Fig. 9.4b). After the spin rotation, some time is allowed for the excitations in the leads to disappear (Fig. 9.4c). Then the levels are brought into the read-out configuration. In the transport scheme of Fig. 9.4d, the electron can tunnel out and contribute to the current only if its spin has been rotated. The two read-out configurations shown in Figs. 9.4e and 9.4f both rely on charge detection with the QPC. In the scheme of Fig. 9.4e, an electron can tunnel off the dot only if its spin was rotated. Thus, temporarily the number of electrons will be zero, reducing the average charge on the dot, which in turn affects I_{QPC}. In the scheme of Fig. 9.4f the tunneling is fast if the electron has spin-up, but becomes very slow if the spin was rotated. If the difference in tunnel rates is large enough, and $\Gamma_\uparrow \gg f_{rep}/2 \sim \Gamma_\downarrow$, then during a large part of the read-out stage there will be one electron on the dot if the electron was spin-down, and zero electrons if the electron was spin-up. Again, with the QPC we can measure this difference in charge.

We now estimate the minimum field strength of B_{ac} necessary to observe the resonance signal using transport as in Fig. 9.4d. The peak in the current has to exceed about 16 fA (the smallest detectable current in our setup). The current

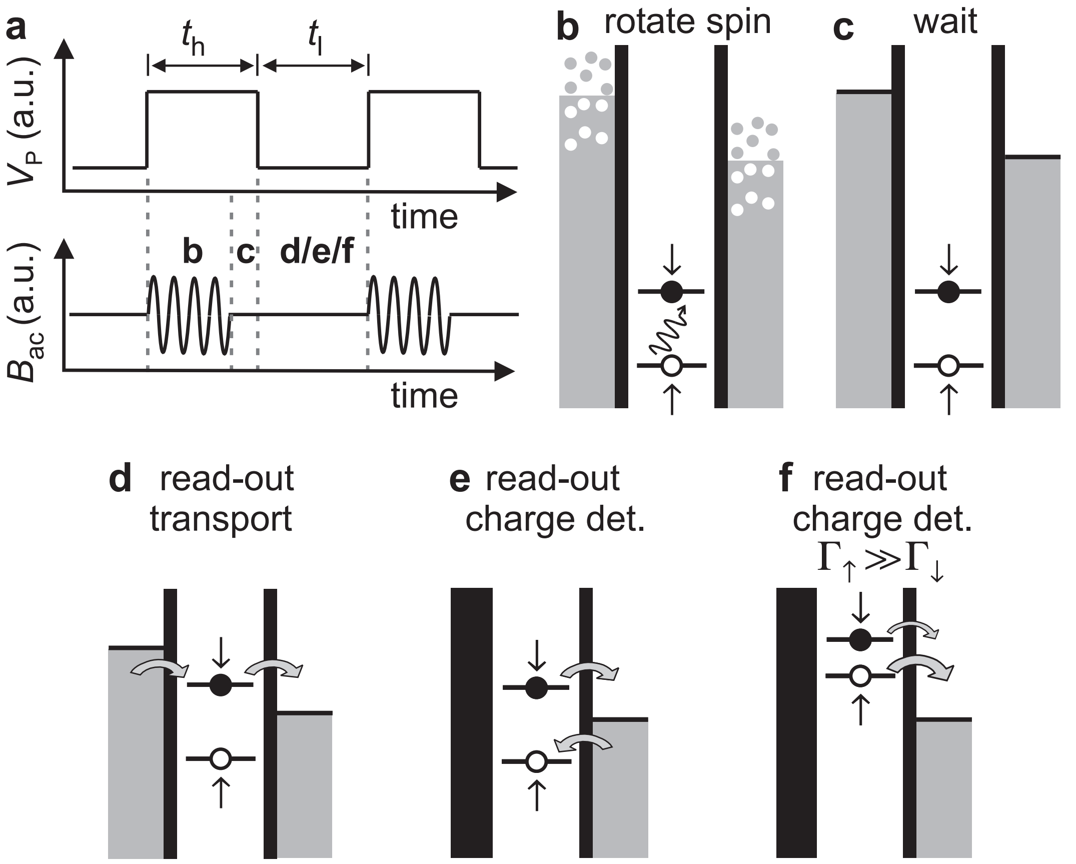
a
t_h
t_l
V_P (a.u.)
time
b
c
d/e/f
B_{ac} (a.u.)
time
b rotate spin
c wait
d read-out transport
e read-out charge det.
f read-out charge det.
$\Gamma_\uparrow \gg \Gamma_\downarrow$

Figure 9.4: Detection of pulsed ESR. **(a)** The pulse amplitude V_P and the applied microwave field B_{ac} as a function of time. **(b)** The spin is rotated by B_{ac} when the levels are in Coulomb blockade. **(c)** Then B_{ac} is turned off, and the excited electrons in the leads relax. In the last part, the levels are brought in the read-out configuration. If the spin was rotated it results in **(d)** a change in the current due to a difference in energy, or in a change in the average charge on the dot caused by **(e)** a difference in energy or **(f)** a difference in tunnel rate.

can be written as

$$I = e <n> f_{rep} = e\ P_\downarrow\ n_\downarrow\ f_{rep}, \tag{9.1}$$

where f_{rep} is the pulse repetition frequency and $<n>$ the average number of electrons transported per pulse cycle, which is the product of $P_\downarrow$, the probability that the spin is down at the start of the read-out stage, and $n_\downarrow$, the average number of electrons transported during the read-out stage for $P_\downarrow = 1$. Assuming we apply B_{ac} for 20 ns, which is on the order of the expected T_2, then wait 10 ns for the excitations to disappear, and use 70 ns for the read-out stage, the repetition frequency of the pulse train will be 10 MHz. The tunnel rate for spin-down in

Fig. 9.4d has to be least 50 MHz, to make sure the electron will have enough time to tunnel off the dot during the read-out stage. Then, $<n>$ needs to be at least 16 fA/(ef_{rep})=0.01. If $\Gamma_\uparrow = \Gamma_\downarrow$, $n_\downarrow$ will be of order 1, and therefore $P_\downarrow$ has to exceed 0.01, implying that the spin has to be rotated over an angle of about 6 degrees within 20 ns (assuming every cycle starts with a spin-up electron). The Rabi frequency f_{Rabi} then has to be at least 6/(360·20 ns)≈ 0.8 MHz, corresponding to a value for B_{ac} of about 0.13 mT. If B_{ac} is 1 mT, the expected current is 64 times as high (1 pA).

If the tunnel rates are spin-dependent ($\Gamma_\uparrow > \Gamma_\downarrow$), the signal can be increased by performing the experiment at the 1↔2 electron transition. The scheme is completely similar, except that for the same f_{Rabi}, $<n>$ will be larger because $n_\uparrow$, the equivalent of $n_\downarrow$, can be much larger than 1.

In both schemes using charge detection, we can increase the signal-to-noise ratio by using lock-in detection of I_{QPC} at the pulse repetition frequency (see chapter 6). The drawback is that the pulse repetition frequency is then limited to the bandwidth of the wiring in our dilution fridge, which is about 100 kHz. More analysis is needed to find the resulting strength of the ESR signal for these charge detection schemes.

Finally, we would like to detect ESR using single-shot read-out. Finding the resonance this way is very time-consuming and can be more easily done using one of the techniques described above. However, at the resonance the single-shot measurement will allow us to map out the Rabi oscillation in time, and perform more advanced rotations such as a spin-echo.

9.3 Two-spin experiments

9.3.1 Two-spin quantum gate: SWAP

The goal of the two-spin experiments is to demonstrate the operation of the SWAP gate, which exchanges ('swaps') the states of the two spins. This two-spin operation can be explored independently of the single-spin rotations. Only for the demonstrating of a quantum-CNOT gate [1], we will need both $\sqrt{\text{SWAP}}$ operations and single-spin rotations.

The SWAP gate can be conveniently understood as follows. The two spins are initially uncoupled and reside in the single dot orbital eigenstates. When the tunnel coupling becomes nonzero due to a voltage pulse on a gate, the new eigenstates are the two-electron spin singlet state $|S\rangle = (|\uparrow\downarrow\rangle - |\downarrow\uparrow\rangle)/\sqrt{2}$ and the spin triplets $|T_+\rangle = |\uparrow\uparrow\rangle$, $|T_0\rangle = (|\uparrow\downarrow\rangle + |\downarrow\uparrow\rangle)/\sqrt{2}$ and $|T_-\rangle = |\downarrow\downarrow\rangle$. Here, the orbital part of the wave function is built up from combinations of the single-dot orbitals (see e.g. Ref. [53]). The energy difference between the singlet and the triplets is the (time-dependent) Heisenberg exchange energy $J(t)$. Now, if initially the electrons had opposite spin, we can write the two-electron spin state as

$$|\uparrow\downarrow\rangle = (|\uparrow\downarrow\rangle - |\downarrow\uparrow\rangle + |\uparrow\downarrow\rangle + |\downarrow\uparrow\rangle)/2 = (|S\rangle + |T_0\rangle)\sqrt{2}. \tag{9.2}$$

Thus the spins start in a superposition of a singlet and a triplet state. The relative phase between the two parts of the superposition will change according to their energy difference $J(t)$ (i.e. the state precesses in the new eigenbasis):

$$(|S\rangle + |T_0\rangle)/\sqrt{2} \rightarrow (|S\rangle + e^{-i\int J(t)dt/\hbar}\,|T_0\rangle)/\sqrt{2}. \tag{9.3}$$

After a time t_{SWAP}, defined by $\int_0^{t_{SWAP}} J(t)/\hbar\, dt = \pi$, the state has evolved to

$$(|S\rangle + e^{-i\pi}|T_0\rangle)/\sqrt{2} = (|S\rangle - |T_0\rangle)/\sqrt{2} = |\downarrow\uparrow\rangle, \tag{9.4}$$

and the states of the two spins have been swapped. The whole period between $t = 0$ and $t = t_{SWAP}$, the two spins are entangled. Note that the important parameter here is the *integral* over $J(t)$, not its maximum value. If the two spins initially carry the same spin, they are already in a two-spin eigenstate ($|T_+\rangle$ or $|T_-\rangle$), and the SWAP operation does not change the spin states, so entanglement will arise.

The scheme for measuring the coherent oscillation between the spins follows straightforwardly from the above. We prepare qubit 1 in state $|\uparrow\rangle$ and qubit 2 in $|\downarrow\rangle$. Measurement of qubit 1 should then always give $|\uparrow\rangle$, while measurement of qubit 2 should give $|\downarrow\rangle$. Now, we pulse the tunnel barrier separating the two dots for a specified time t_{pulse}, and read out the spin states. On repeating this measurement for many values of t_{pulse}, we will find the probabilities of qubit 1 and 2 to be in $|\uparrow\rangle$ and $|\downarrow\rangle$ respectively to oscillate in phase with the frequency J/h as a function of t_{pulse}. (The control measurements for the other combinations of initial spin states can be done similarly.) These two-spin operations will yield the coherence time, the value of J, and most importantly, the basic resource for quantum computing: entanglement of electrons!

9.4 Conclusions

The experimental research on using electron spins as quantum bits, which started only about three years ago, has already produced a number of exciting results, including isolation and read-out of a single electron spin. Experiments are now aimed at controlling the coherent properties of single spins as well as at creating and detecting entanglement between two spins. The ideas laid out in this chapter provide a detailed guide for experiments in the near future.

The question remains whether we will ever see a quantum computer based on electron spins in quantum dots. There are a number of fundamental issues, e.g. the hyperfine interaction and the scaling to more than ten qubits, that need to be resolved before we can start thinking about a true large-scale quantum computer. However, as these problems are being attacked, new theoretical ideas and experimental techniques will be developed, which are not only extremely valuable for future research on a spin quantum computer, but at the same time will yield more interesting and exciting physics.

We thank C. J. P. M. Harmans, S. de Franceschi, D. P. DiVincenzo, S. Tarucha, T. Fujisawa, H. -A. Engel, V. Golovach, G. Burkard, D. Loss and M. Blaauboer for useful discussions. We acknowledge financial support from FOM, NWO, the DARPA-QUIST program, the ONR and the EU-RTN network on spintronics.

References

[1] D. Loss and D. P. DiVincenzo, Phys. Rev. A **57**, 120 (1998).

[2] D. P. DiVincenzo, Fortschr. Phys. **48**, 771 (2000).

[3] J. M. Elzerman *et al.*, Phys. Rev. B. **67**, 161308(R) (2003).

[4] L. P. Kouwenhoven, G. Schön, and L. L. Sohn, in *Mesoscopic Electron Transport*, Vol. 345 of *NATO Advanced Study Institute, Series E*, edited by L. L. Sohn, L. P. Kouwenhoven, and G. Schön (Kluwer Academic Publishers, Dordrecht, 1997).

[5] M. Field *et al.*, Phys. Rev. Lett. **70**, 1311 (1993).

[6] J. M. Elzerman *et al.*, Appl. Phys. Lett. **84**, 4617 (2004).

[7] L.-X. Zhang *et al.*, Appl. Phys. Lett. **85**, 2628 (2004).

[8] R. J. Schoelkopf *et al.*, Science **280**, 1238 (1998).

[9] L. M. K. Vandersypen *et al.*, Appl. Phys. Lett. **85**, 4394 (2004).

[10] L. H. Willems van Beveren *et al.*, New J. Phys. **7**, 182 (2005).

[11] R. Hanson *et al.*, Phys. Rev. Lett. **91**, 196802 (2003).

[12] W. G. van der Wiel *et al.*, Rev. Mod. Phys. **75**, 1 (2003).

[13] M. Pioro-Ladrière *et al.*, Phys. Rev. Lett. **91**, 026803 (2003).

[14] J. R. Petta *et al.*, Phys. Rev. Lett. **93**, 186802 (2004).

[15] T. H. Oosterkamp *et al.*, Nature **395**, 873 (1998).

[16] V. N. Golovach and D. Loss, Phys. Rev. B **69**, 245327 (2004).

[17] J. R. Petta *et al.*, Science Express, published online 1 September 2005 (10.1126/science.1116955).

[18] M. A. Nielsen and I. L. Chuang, *Quantum Computation and Quantum Information*, (Cambridge Universty Press, Cambridge, England, 2000).

[19] M. Ciorga *et al.*, Phys. Rev. B **61**, R16315 (2000).

[20] M. Ciorga *et al.*, Appl. Phys. Lett. **80**, 2177 (2002).

[21] J. M. Elzerman *et al.*, Nature **430**, 431 (2004).

[22] R. Hanson *et al.*, Phys. Rev. Lett. **94**, 196802 (2005).

[23] T. Englert *et al.*, Surface Science **113**, 295 (1982).

[24] M. Kroutvar *et al.*, Nature **432**, 81 (2004).

[25] T. Fujisawa *et al.*, Nature **419**, 278 (2002).

[26] A. V. Khaetskii and Y. V. Nazarov, Phys. Rev. B **61**, 12639 (2000); A. V. Khaetskii and Y. V. Nazarov, Phys. Rev. B **64**, 125316 (2001).

[27] V. N. Golovach, A. Khaetskii and D. Loss, Phys. Rev. Lett. **93**, 016601 (2004).

[28] S. I. Erlingsson and Y. V. Nazarov, Phys. Rev. B **66**, 155327 (2002).

[29] A. V. Khaetskii, D. Loss and L. Glazman, Phys. Rev. Lett. **88**, 186802 (2002).

[30] I. A. Merkulov, Al. L. Efros and M. Rosen, Phys. Rev. B **65**, 205309 (2002).

[31] R. de Sousa and S. Das Sarma, Phys. Rev. B **67**, 033301 (2003).

[32] W. A. Coish and D. Loss, Phys. Rev. B **70**, 195340 (2004).

[33] D. Paget *et al.*, Phys. Rev. B **15**, 5780 (1977).

[34] J. M. Kikkawa and D. D. Awschalom, Phys. Rev. Lett. **80**, 4313 (1998).

[35] K. Ono *et al.*, Science **297**, 1313 (2002); K. Ono and S. Tarucha, Phys. Rev. Lett. **92**, 256803 (2004).

[36] A. C. Johnson *et al.* cond-mat/0410679 (2004).

[37] F. H. L. Koppens *et al.*, Science **309**, 1346 (2005).

[38] O. N. Jouravlev and Y. V. Nazarov, cond-mat/0507680 (2005).

[39] W. A. Coish and D. Loss, comd-mat/0506090 (2005).

[40] L. M.K . Vandersypen and I. L. Chuang, Rev. Mod. Phys. 76, 1034 (2004).

[41] CRC *Handbook of Chemistry and Physics* eds. D. R. Lide and H. P. R. Frederikse (CRC Press, Boca Baton, 1996).

[42] T. Berer *et al.*, cond-mat/0508260 (2005).

[43] K. A. Slinker *et al.*, cond-mat/0508107 (2005).

[44] D. V. Bulaev and D. Loss, cond-mat/050318 (2005).

[45] Al. L. Efros and M. Rosen, Phys. Rev. B **58**, 7120 (1998).

[46] G. Burkard, D. Loss and D. P. DiVincenzo, Phys. Rev. B **59**, 2070 (1999).

[47] D. P. DiVincenzo *et al.*, Nature **408**, 339 (2000).

[48] M. Dobers, K. v. Klitzing and G. Weimann, Phys. Rev. B **38**, 5453 (1988).

[49] Y. Kato *et al.*, Science **299**, 1201 (2003).

[50] G. Salis *et al.*, Nature (London) **414**, 619 (2001).

[51] T. Hayashi *et al.*, Phys. Rev. Lett. **91**, 226804 (2003).

[52] S.W. Jung *et al.*, Appl. Phys. Lett. **85**, 768 (2004).

[53] G. Burkard, Ph.D. thesis '*Quantum Computation and Communication using Electron Spins in Quantum Dots and Wires*, University of Basel (2001).

[54] X. Hu, R. de Sousa and S. Das Sarma, Phys. Rev. Lett. **86**, 918 (2001).

[55] J.D. Jackson, *Classical electrodynamics*, Wiley, New York (1998).

[56] L. M. K. Vandersypen *et al.*, in *Quantum Computing and Quantum Bits in Mesoscopic Systems*, Kluwer Academic, New York (2003) (see also quant-ph/0207059).

[57] J. J. Wever, M. Sc. thesis, Delft University of Technology (2003).

[58] H. A. Engel and D. Loss, Phys. Rev. Lett. **86**, 4648 (2001); H. A. Engel and D. Loss, Phys. Rev. B **65**, 195321 (2002).

[59] I. Martin, D. Mozyrsky, and H.W. Jiang, Phys. Rev. Lett. **90**, 018301 (2003).

[60] M. Xiao *et al.*, Nature **430**, 435 (2004).

[61] D. Loss and E.V. Sukhorukov, Phys. Rev. Lett. **84**, 1035 (2000).

[62] M. Blaauboer and D. P. DiVincenzo (unpublished).

[63] A. C. Johnson *et al.*, Phys. Rev. B **71**, 115333 (2005).

[64] A. C. Johnson *et al.*, Nature **435**, 925 (2005).

Appendix A

Fabrication recipes

In this Appendix, we summarize the fabrication process for lateral quantum dot devices with coplanar stripline and a dielectric layer as a recipe.

A.1 Alignment markers

Preparation:

- acetone clean (5')
- IPA rinse (30")
- N_2 (g) dry
- oven 120°C (10')

Resist:

- 400 nm copolymer: 500 rpm (5") / 2000 rpm (55")
- pre-bake at hot plate: 180°C (15')
- 90 nm 950PMMA (2%): 500 rpm (5") / 5000 rpm (55")
- pre-bake at hot plate: 180°C (15')

Exposure:

- positive-tone process
- e-beam dose: 650 μC/cm^2
- spot size / beam current: 152 nm / 311 nA

Developing:

- 1:3 MIBK / IPA (90")
- IPA stop (60")

- N_2 (g) dry

Evaporation:

- 50 nm Ti, rate 1 nm/sec
- 150 nm Au, rate 0.4 nm/sec

Lift-off:

- acetone (24h) / acetone spray
- IPA rinse (30")
- N_2 (g) dry

A.2 Mesa etching

Preparation:

- acetone clean (5')
- IPA rinse (30")
- N_2 (g) dry
- oven 120°C (10')

Resist:

- 120 nm 950PMMA (2%): 500 rpm (5") / 3000 rpm (55")
- pre-bake at hot plate: 180°C (15')

Exposure:

- positive-tone process
- e-beam dose: 550 μC/cm^2
- spot size / beam current: 152 nm / 311 nA

Developing:

- 1:3 MIBK / IPA (90")
- IPA stop (60")
- N_2 (g) dry

Etching:

- oxide removal: 1:5 H_2SO_4 / H_2O (30")
- H_2O rinse (30")

- N_2 (g) dry
- wet etch in 1:5:25 H_2O_2 / H_2SO_4 / H_2O: 10°C (40”), rate 3 nm/sec
- H_2O rinse (30”)
- IPA rinse (30”)
- N_2 (g) dry

Lift-off:

- acetone (24h)
- IPA rinse
- N_2 (g) dry

A.3 Ohmic contacts

Preparation:

- acetone clean (5’)
- IPA rinse (30”)
- N_2 (g) dry
- oven 120°C (10’)

Resist:

- 400 nm copolymer: 500 rpm (5”) / 2000 rpm (55”)
- pre-bake at hot plate: 180°C (15’)
- 90 nm 950PMMA (2%): 500 rpm (5”) / 5000 rpm (55”)
- pre-bake at hot plate: 180°C (15’)

Exposure:

- positive-tone process
- e-beam dose: 650 μC/cm^2
- spot size / beam current: 152 nm / 311 nA

Developing:

- 1:3 MIBK / IPA (90”)
- IPA stop (60”)
- N_2 (g) dry

Evaporation:

- 5 nm Ni, rate 0.2 nm/sec
- 150 nm AuGe, rate 1.2 nm/sec
- 25 nm Ni, rate 0.2 nm/sec

Lift-off:

- acetone (24h) / acetone spray
- IPA rinse (30")
- N_2 (g) dry

Rapid thermal annealing: recipe name H2440C60

- ramp from 20°C to 440° (42")
- stay at 440° (60")
- cool down from 440°C to below 80°C (30")

A.4 Fine gates

Preparation:

- plasma strip (10')
- acetone clean (5')
- IPA rinse (30")
- N_2 (g) dry
- oven 120°C (10')

Resist:

- 90 nm 3:2 OEBR-1000 (100 cp) / OFPR-800: 500 rpm (3") / 4000 rpm (50")
- pre-bake at hot plate: 180°C (15')

Exposure:

- positive-tone process
- e-beam dose: 650-800 μC/cm^2
- spot size / beam current: 4 nm / 509 pA

Developing:

- 1:3 MIBK / IPA (90")
- IPA stop (60")

- N_2 (g) dry

Evaporation:

- oxide removal: 1:5 H_2SO_4 / H_2O (60")
- H_2O rinse (30")
- IPA rinse (30")
- N_2 (g) dry
- 10 nm Ti, rate 1 nm/sec
- 20 nm Au, rate 0.4 nm/sec

Lift-off:

- acetone (24h) / acetone spray
- IPA rinse (30")
- N_2 (g) dry

A.5 Large gate / CPS and ESR wire

Preparation:

- acetone clean (5')
- IPA rinse (30")
- N_2 (g) dry
- oven 120°C (10')

Resist:

- 500 nm OEBR-1000 (200 cp): 500 rpm (5") / 2000 rpm (55")
- pre-bake at hot plate: 180°C (15')
- 90 nm 950PMMA (2%): 500 rpm (5") / 5000 rpm (55")
- pre-bake at hot plate: 180°C (15')

Exposure:

- positive-tone process
- e-beam dose: 600 μC/cm^2
- spot size / beam current: 100 nm / 236 nA

Developing:

- 1:3 MIBK / IPA (90")

- IPA stop (60”)
- N_2 (g) dry

Evaporation normal metal:

- 50 nm Ti, rate 1 nm/sec
- 400 nm Au, rate 0.4 nm/sec

Sputtering superconductor:

- 320 nm NbTiN, rate 1 nm/sec

Lift-off:

- acetone (24h) / acetone spray
- IPA rinse (30”)
- N_2 (g) dry

A.6 Dielectric layers

A.6.1 SiO / SiO_2

Preparation:

- acetone clean (5’)
- IPA rinse (30”)
- N_2 (g) dry
- oven 120°C (10’)

Resist:

- 500 nm OEBR-1000 (200 cp): 500 rpm (5”) / 2000 rpm (55”)
- pre-bake at hot plate: 180°C (15’)
- 90 nm 950PMMA (2%): 500 rpm (5”) / 5000 rpm (55”)
- pre-bake at hot plate: 180°C (15’)

Exposure:

- positive-tone process
- e-beam dose: 650 $\mu C/cm^2$
- spot size / beam current: 152 nm / 311 nA

Developing:

- 1:3 MIBK / IPA (90")
- IPA stop (60")
- N_2 (g) dry

Evaporation SiO_2:

- 100 nm SiO_2, rate 1 nm/sec

Sputtering SiO:

- 100 nm SiO, rate 1 nm/sec

Lift-off:

- acetone (24h) / acetone spray
- IPA rinse (30")
- N_2 (g) dry

A.6.2 PMGI / SF7

Preparation:

- acetone clean (5')
- IPA rinse (30")
- N_2 (g) dry
- oven 120°C (10')

Resist:

- 400 nm PMGI: 500 rpm (5") / 2600 rpm (60")
- pre-bake at hot plate: 200°C (5')
- 90 nm 950PMMA (2%): 500 rpm (5") / 5000 rpm (55")
- pre-bake at hot plate: 180°C (15')

Exposure:

- positive-tone process
- e-beam dose: 650 $\mu C/cm^2$
- spot size / beam current: 152 nm / 311 nA

Developing top layer (PMMA):

- 1:3 MIBK / IPA (60")

- IPA stop (60”)
- N_2 (g) dry

Developing bottom layer (PMGI):

- MF-321 (or 322) (90”)
- H_2) rinse (30”)
- IPA rinse (5”)
- N_2 (g) dry

A.6.3 HSQ / FOx-12

Preparation:

- acetone clean (5’)
- IPA rinse (30”)
- N_2 (g) dry
- oven 120°C (10’)

Resist:

- 100-140 nm FOx-12: 500 rpm (5”) / 3000 rpm (55”)
- pre-bake at hot plate: 150°C (2’) / 200°C (2’)

Exposure:

- negative-tone process
- e-beam dose: 600 μC/cm^2
- spot size / beam current: 100 nm / 236 nA

Developing:

- MF-322 (90”)
- IPA stop (60”)
- N_2 (g) dry

A.6.4 Calixarene

Preparation:

- acetone clean (5')
- IPA rinse (30")
- N_2 (g) dry
- oven 120°C (10')

Resist:

- 80 nm calixarene (5%): 500 rpm (5") / 2000 rpm (55")
- pre-bake at hot plate: 180°C (15')

Exposure:

- negative-tone process
- e-beam dose: 7500 μC/cm^2
- spot size / beam current: 152 nm / 311 nA

Developing:

- xylene (30")
- IPA rinse (30")
- N_2 (g) dry

Summary

Electron spins in few-electron lateral quantum dots

This thesis describes a series of experiments in order to understand and control the behavior of the spin and charge degree of freedom of single electrons, confined in semiconductor lateral quantum dots.

This research work is motivated by the prospects of using the electron spin, rather than its charge, as a quantum bit (qubit), the basic building block of a quantum computer. The spin lifetime of a single electron confined in a quantum dot is expected to be long lived, as the dominant electron spin relaxation mechanism for localized carriers is suppressed. In the spin qubit proposal, the envisioned basis states (logical 0 and 1) of the qubit are the two possible orientations of the spin in a magnetic field: 'spin-up' (parallel to the field) and 'spin-down' (anti-parallel to the field). Coherent superpositions of these basis states can in principle be realized by the technique of electron spin resonance (ESR).

In this thesis, a number of important steps towards the use of electron spins as qubits are reported: the fabrication process of lateral quantum dots, the isolation of single electrons in (double) quantum dots, energy spectroscopy of few-electron spin states, development of a new technique to probe a nearly-isolated quantum dot, 'single-shot' read-out of the electron spin orientation, measurements of the spin relaxation time, and increased understanding of the interaction of the electron spin with its environment.

A quantum dot can be thought of as a small 'box' filled with a controllable number of electrons. The box is coupled via tunnel barriers to reservoirs, with which electrons can be exchanged, and is coupled capacitively to one or more gate electrodes that allow the number of electrons on the dot to be varied. Due to the small dot size (typically $\sim$ 50 nm), comparable to the Fermi wavelength of the electrons, it exhibits a discrete energy spectrum. The lateral quantum dot devices studied in this work are defined in a two-dimensional electron gas (2DEG) of a GaAs/AlGaAs heterostructure, by applying negative voltages to metallic gate electrodes that have been fabricated on top of the semiconductor

by electron beam lithography.

In this thesis, a number of important steps towards the use of electron spins as qubits are reported: the fabrication process of lateral quantum dot devices, the isolation of single electrons in (double) quantum dots, energy spectroscopy of few-electron spin states, development of a new technique to probe a nearly-isolated quantum dot, 'single-shot' read-out of the electron spin orientation, measurements of the spin relaxation time, and increased understanding of the interaction of the electron spin with its environment.

There are two ways to probe the electronic properties of a (double) quantum dot. In the first (conventional) method the transport of electrons through the dot is monitored as a function of bias voltage applied over the device and the voltage applied to the gate electrodes. This method provides detailed information on the energy level spectrum and the coupling of the different states to the reservoirs. The second method relies on charge detection using an electrostatically coupled quantum point contact (QPC). A QPC is a narrow channel in the 2DEG, of which the conductance can be made very sensitive to the electrostatic environment. By applying a bias voltage over the constriction, and measuring the resulting current flowing through it, the QPC is operated as an electrometer and allows the detection of changes in the number of electrons on the nearby quantum dot.

Both charge detection and transport measurements allow complete control over the number of electrons (down to zero) on a double quantum dot. Even in the few-electron regime, the coupling between the two dots as well as the coupling to the reservoirs remain fully tunable. By increasing the bandwidth of the electrometer to about 40 kHz, single-electron tunneling on and off the dot is observed in real time.

The spin states of a few-electron quantum dot can be investigated using transport measurements. By applying a large magnetic field parallel to the 2DEG, the Zeeman energy splitting of the orbital states is measured directly. By combining the observation of the Zeeman energy splitting with knowledge of the absolute number of electrons on the dot, we are able to determine the ground state spin configuration for one up to five electrons occupying the dot. For four electrons, we find a ground state spin configuration with total spin $S = 1$, in agreement with Hund's first rule. Furthermore, by applying short voltage pulses, we can populate the excited spin state for a single electron on the dot and find a lower bound on the spin relaxation time of 50 μs at a magnetic field of 7.5 T.

Then, a new technique is developed for extracting all relevant parameters of the quantum dot using the QPC as an electrometer. The number of electrons on the dot and the tunnel rate between the dot and the reservoir can be determined even in the regime of very weak coupling of the dot to only one reservoir (this regime is inaccessible to transport measurements). The excited states can be identified by the changes they cause in the effective tunnel rate, allowing the complete energy level spectrum to be obtained.

Two methods are presented for reading out the electron spin state on a quantum dot, both relying on 'spin-to-charge' conversion. Here, the spin information is first converted to charge information by making the number of electrons on the dot dependent on the initial spin state. A subsequent fast measurement of the number of electrons on the dot using the QPC thus reveals the spin state.

The first method for spin-to-charge conversion relies on a large energy difference between the spin states, induced by an applied magnetic field. The levels are aligned such, that a spin-up electron is trapped on the dot, whereas a spin-down electron has enough energy to escape. Using this technique, read-out of an individual electron spin is performed, with a single-shot measurement visibility up to 65%.

Alternatively, spin-to-charge conversion can be induced by spin-dependent tunnel rates. This method is applied to read out the two-electron spin state. Here, tunneling from a triplet state is about twenty times as fast as tunneling from a singlet state, resulting in a single-shot measurement visibility of more than 80%.

The read-out techniques also allow the spin relaxation times to be extracted. Both for a single spin and for the two-electron spin states, the relaxation is found to be very slow (relaxation times up to milliseconds). These long times, five orders of magnitude longer than the typical orbital relaxation time for an electron in a dot, indicate that the electron spin degree of freedom is well isolated from the environment. A strong magnetic field dependence suggests that the spin-orbit interaction is the dominant relaxation mechanism.

Finally, the progress on the 'electron spin qubit' proposal is reviewed and the important problems are identified and critically analyzed. A number of key experiments are proposed for the demonstration of coherent control over the spin state and the presence of entanglement.

Laurens Willems van Beveren
September 2005

Samenvatting

Elektron spins in enkele-elektron laterale quantum dots

Dit proefschrift beschrijft een reeks experimenten die het doel hebben om het gedrag van de spin- en ladingsvrijheidsgraad van enkele elektronen, opgesloten in halfgeleider laterale quantum dots, te begrijpen en onder controle te krijgen. De motivatie voor dit onderzoek is de mogelijke toepassing van de spin van een elektron, in plaats van de lading, als quantum bit (of qubit), de elementaire bouwsteen van een quantum computer. Men verwacht een lange levensduur voor de spin van een enkel elektron opgesloten in een quantum dot, omdat het overheersende spin relaxatie mechanisme onderdrukt wordt in het geval van gelokaliseerde ladingsdragers. In het spin qubit voorstel, komen de beoogde basistoestanden van de qubit (de logische 0 en 1) overeen met de twee mogelijke richtingen van de spin van een elektron in een magneetveld: 'spin-omhoog' (parallel aan het magneetveld) en 'spin-omlaag' (antiparallel aan het magneetveld). Coherente superposities van deze basistoestanden kunnen in principe tot stand worden gebracht door middel van de elektron spin resonantie (ESR) techniek.

In dit proefschrift wordt verslag gedaan van een aantal belangrijke stappen richting het gebruik van de spin van elektronen als qubits: het fabricage proces van laterale quantum dots, opsluiting van enkele elektronen in (dubbele) quantum dots, energie spectroscopie van de spintoestanden van enkele elektronen, de ontwikkeling van een nieuwe techniek waarmee een bijna-geïsoleerde quantum dot kan worden onderzocht, uitlezing van de spintoestand van een elektron in een enkele meting, en toegenomen kennis over de interactie van de spin van het elektron met de omgeving.

Een quantum dot kan worden beschouwd als een klein 'doosje' gevuld met een regelbaar aantal elektronen. Dit doosje is via tunnel barrières gekoppeld aan reservoirs, waarmee elektronen kunnen worden uitgewisseld, en het is capacitief gekoppeld aan één of meer 'gate' elektroden waarmee het elektronenaantal op de dot gevarieerd kan worden. Vanwege de kleine afmetingen van de dot (typisch ~ 50 nm), vergelijkbaar met de Fermi golflengte van de elektronen, vertoont de dot een discreet energie spectrum. De in dit werk bestudeerde laterale quantum dots zijn gedefinieerd in een tweedimensionaal elektronengas (2DEG) van een GaAs/AlGaAs heterostruktuur, door negatieve voltages aan te brengen op metalen 'gate' elektroden die bovenop de halfgeleider zijn gefabriceerd door middel van elektron bundel lithografie.

Er zijn twee manieren om de elektronische eigenschappen van een (dubbele) quantum dot te bestuderen. In de eerste (conventionele) methode wordt gekeken naar het transport van elektronen door de dot als functie van het spanningsverschil dat wordt aangelegd over de structuur en de spanning op de 'gate' elektroden. Deze methode geeft gedetailleerde informatie over het spectrum van energieniveaus en de tunnelkoppeling naar de reservoirs. De tweede methode is gebaseerd op ladings detectie door gebruik te maken van een elektrostatisch gekoppeld quantum puntcontact (QPC). Een QPC is een nauw kanaaltje in het 2DEG, waarvan de geleiding erg gevoelig gemaakt kan worden voor de elektrostatische omgeving. Door een spanningsverschil aan te leggen over het kanaaltje, en de resulterende stroom die er doorheen loopt te meten, kan de QPC worden gebruikt als een ladingsmeter en kunnen veranderingen in het aantal elektronen op de vlakbij gelegen dot worden gedetecteerd.

Volledige controle over het aantal elektronen (tot aan nul) op een dubbele quantum dot kan worden aangetoond, zowel met ladingsmetingen als met transportmetingen. Zelfs met nog maar een paar elektronen op de dots blijven zowel de tunnelkoppeling tussen de dots als de tunnelkoppeling naar de reservoirs volledig instelbaar. Met een verhoogde bandbreedte van de ladingsmeter (ongeveer 40 kHz) is het tunnelen van een enkel elektron naar en van de dot geobserveerd in 'real-time'.

De spintoestanden in een quantum dot met enkele elektronen kunnen worden onderzocht met transportmetingen. In een sterk magneetveld, aangelegd in het vlak van het 2DEG, is de Zeemanenergie splitsing van de orbitaal toestanden op een directe manier gemeten. Door het combineren van de observatie van Zeemanenergie splitsing met de kennis van het absolute aantal elektronen op de dot, is het mogelijk om de spin configuratie van de grondtoestand vast te stellen voor één tot en met vijf elektronen op de dot. Verder kunnen we, door gebruik te maken van korte spannings pulsen, de aangeslagen spin toestand van één elektron op de dot bezetten en hebben we voor de spinvervaltijd een ondergrens van 50 microseconden gevonden in een magnetisch veld van 7.5 T.

Vervolgens is een nieuwe techniek ontwikkeld waarmee alle relevante parameters van de quantum dot te bepalen zijn door een QPC te gebruiken als elektrometer. Het aantal elektronen op de dot en de tunnelfrequentie tussen de dot en het reservoir kunnen ermee worden bepaald, zelfs in het regime waarin de dot zeer zwak gekoppeld is naar maar één reservoir, een regime dat niet toegankelijk is voor conventionele transportexperimenten. De aangeslagen toestanden kunnen worden geïdentificeerd door de verandering die ze veroorzaken in de effectieve tunnelfrequentie te meten, zodat het complete energiespectrum kan worden verkregen.

Twee methodes worden gepresenteerd waarmee de spintoestand op de quantum dot kan worden uitgelezen, beiden gebruik makend van 'spin-naar-lading conversie'. Hierin wordt de spininformatie eerst omgezet naar ladingsinformatie, door het aantal elektronen op de dot afhankelijk te maken van de initiële spintoestand. Vervolgens onthult een snelle meting van het aantal elektronen op de dot met behulp van de QPC de spintoestand.

De eerste methode voor 'spin-naar-lading conversie' berust op een groot verschil in energie tussen de spintoestanden als gevolg van een aangelegd magneetveld. De niveaus van de spintoestanden worden zo gepositioneerd dat een elektron vastzit op de dot als het 'spin-omhoog' heeft, terwijl een elektron de dot kan verlaten als het 'spin-omlaag' heeft. Met deze techniek is het gelukt de spinrichting van een enkel elektron uit te lezen, met een enkele-meting nauwkeurigheid tot aan 65%.

De 'spin-naar-ladings conversie' kan op een andere manier worden gerealiseerd met behulp van tunnelfrequenties die afhangen van de spintoestand. Deze methode is toegepast op de uitlezing van de spintoestand van twee elektronen. De tunnelfrequentie van een spin-triplet is twintig maal zo hoog als die van een spin-singlet, wat resulteert in een enkele-meting nauwkeurigheid boven de 80%.

Met deze uitleestechnieken kunnen ook de spinvervaltijden worden bepaald. Zowel voor een enkele spin als voor de spintoestanden van twee elektronen is een zeer langzaam verval gevonden (vervaltijden tot aan milliseconden). Deze vervaltijden, vijf ordegroottes langer dan de typische baanvervaltijden van een elektron in een dot, geven aan dat de spinvrijheidsgraad van een elektron goed geïsoleerd is van de omgeving. De sterke magneetveldafhankelijkheid suggereert dat spin-baan interactie het dominante vervalmechanisme is.

Tot slot is een overzicht gegeven van de vooruitgang op het 'elektron spin qubit' gebied, en zijn de belangrijkste problemen geïdentificeerd en kritisch bekeken. Een aantal sleutelexperimenten is voorgesteld voor het aantonen van coherente controle over de spintoestand en de aanwezigheid van verstrengelde toestanden.

Laurens Willems van Beveren
september 2005

Curriculum Vitae

Laurens Henry Willems van Beveren

23-11-1976	Born in Assen, the Netherlands.
1989-1995	Grammar school at the Dr. Nassau College in Assen.
1995-2001	M.Sc. Applied Physics, University of Groningen. Graduate research in the group of Prof. dr. ir. B. J. van Wees. Subject: Nanofabrication of mechanically controllable break junctions.
2001	Internship at Tokyo University, Japan. under supervision of Prof. dr. S. Tarucha. Subject: Fabrication and transport properties of diluted magnetic semiconductor (Ga,Mn)As metal oxide field effect transistor devices. Including device measurements at NTT Basic Research Labs, Japan.
2001-2005	Ph.D. research at Delft University of Technology under supervision of Prof. dr. ir. L. P. Kouwenhoven. Subject: Electron spins in few-electron lateral quantum dots. Including device fabrication at NTT Basic Research Labs, Japan.

List of publications

1. *A quantum dot as a high frequency shot noise detector*
   E. Onac, F. Balestro, L. H. Willems van Beveren, U. Hartmann, Y. V. Nazarov and L. P. Kouwenhoven,
   Submitted to Physical Review Letters.
2. *Control and detection of singlet-triplet mixing in a random nuclear field*
   F. H. L. Koppens, J. A. Folk, J. M. Elzerman, R. Hanson, L. H. Willems van Beveren, I. T. Vink, H. P. Tranitz, W. Wegscheider, L. P. Kouwenhoven and L. M. K. Vandersypen,
   Science **309**, 1346 (2005).
3. *Spin filling of a quantum dot derived from excited-state spectroscopy*
   L. H. Willems van Beveren, R. Hanson, I. T. Vink, F. H. L. Koppens, L. P. Kouwenhoven and L. M. K. Vandersypen,
   New Journal of Physics **7**, 182 (2005), Part of *Focus on Solid State Quantum Information.*
4. *Single-shot read-out of electron spin states in a quantum dot using spin-dependent tunnel rates*
   R. Hanson, L. H. Willems van Beveren, I. T. Vink, J. M. Elzerman, W. J. M. Naber, F. H. L. Koppens, L. P. Kouwenhoven and L. M. K. Vandersypen,
   Physical Review Letters **94**, 196802 (2005).
5. *Experiments and simulations on a few-electron quantum dot circuit with integrated charge read-out*
   R. Hanson, J. M. Elzerman, L. H. Willems van Beveren, L. M. K. Vandersypen, L.-X. Zhang, P. Matagne, J. P. Leburton and L. P. Kouwenhoven,
   Proceedings of the 27th International Conference on the Physics of Semiconductors (2004).
6. *Semiconductor few-electron quantum dots as spin qubits*
   J. M. Elzerman, R. Hanson, L. H. Willems van Beveren, S. Tarucha, L. M. K. Vandersypen and L. P. Kouwenhoven,
   in *Quantum Dots: a Doorway to Nanoscale Physics*, Series: Lecture Notes in Physics, Vol. 667, Heiss, WD. (Ed.), Springer (2005).

7. *Semiconductor few-electron quantum dot operated as a bipolar spin filter*
R. Hanson, L. M. K. Vandersypen, L. H. Willems van Beveren, J. M. Elzerman, I. T. Vink and L. P. Kouwenhoven,
Physical Review B **70**, 241304(R) (2004).

8. *Semiconductor few-electron quantum dots as spin qubits*
J. M. Elzerman, R. Hanson, L. H. Willems van Beveren, L. M. K. Vandersypen and L. P. Kouwenhoven,
To appear in *Quantum Computation: solid state systems*, Kluwer Academic/Plenum Publishers (due 2005).

9. *Electron spin qubits in quantum dots*
R. Hanson, J. M. Elzerman, L. H. Willems van Beveren, L. M. K. Vandersypen and L. P. Kouwenhoven,
Technical Digest of the 2004 IEEE International Electron Devices Meeting.

10. *Real-time detection of single electron tunneling using a quantum point contact*
L. M. K. Vandersypen, J. M. Elzerman, R. N. Schouten, L. H. Willems van Beveren, R. Hanson and L. P. Kouwenhoven,
Applied Physics Letters **85**, 4394 (2004).

11. *Tunable few-electron double quantum dots with integrated charge read-out*
J. M. Elzerman, R. Hanson, J. S. Greidanus, L. H. Willems van Beveren, S. De Franceschi, L. M. K. Vandersypen, S. Tarucha and L. P. Kouwenhoven,
Physica E **25**, 135 (2004).

12. *Determination of the tunnel rates through a few-electron quantum dot*
R. Hanson, I. T. Vink, D. P. DiVincenzo, L. M. K. Vandersypen, J. M. Elzerman, L. H. Willems van Beveren and L. P. Kouwenhoven,
To appear in Proceedings of XXXIXth Rencontres de Moriond (2004).
See also http://xxx.lanl.gov/abs/cond-mat/0407793 (2004).

13. *Single shot read-out of an individual electron spin in a quantum dot*
J. M. Elzerman, R. Hanson, L. H. Willems van Beveren, B. Witkamp, L. M. K. Vandersypen and L. P. Kouwenhoven,
Nature **430**, 431 (2004).

14. *Excited-state spectroscopy on a nearly-closed quantum dot via charge detection*
J. M. Elzerman, R. Hanson, L. H. Willems van Beveren, L. M. K. Vandersypen and L. P. Kouwenhoven,
Applied Physics Letters **84**, 4617 (2004).

15. *Zeeman energy and spin relaxation in a one-electron quantum dot*
R. Hanson, B. Witkamp, L. M. K. Vandersypen, L. H. Willems van Beveren, J. M. Elzerman and L. P. Kouwenhoven,
Physical Review Letters **91**, 196802 (2003).

16. *Few-electron quantum dot circuit with integrated charge read-out*
J. M. Elzerman, R. Hanson, J. S. Greidanus, L. H. Willems van Beveren, S. De Franceschi, L. M. K. Vandersypen, S. Tarucha and L. P. Kouwenhoven,
Physical Review B **67**, 161308 (2003).

17. *Quantum computing with electron spins in quantum dots*
L. M. K. Vandersypen, R. Hanson, L. H. Willems van Beveren, J. M. Elzerman, J. S. Greidanus, S. De Franceschi and L. P. Kouwenhoven,
in *Quantum Computing and Quantum Bits in Mesoscopic Systems*, Chapter 22, Kluwer Academic/Plenum Publishers (2003).
See also http://xxx.lanl.gov/abs/quant-ph/0207059 (2002).